

# UNIVERSITY OF LONDON THESIS

Degree PhD Year 2007 Name of Author RUMP, Owen James

# Non-rotating and rotating free surface flows over topography

Owen James Rump

*Department of Mathematics*
*University College London*
*University of London*

A thesis submitted for the degree of
*Doctor of Philosophy*

Supervisors

Prof. E.R. Johnson &

Dr. J.G. Esler

June 2007





ProQuest LLC
789 East Eisenhower Parkway
P.O. Box 1346
Ann Arbor, MI 48106-1346

## Abstract

An important effect in atmosphere and ocean dynamics is the drag exerted by topography, in the form of mountain ranges and individual mountains, on incident flows. Because the scale of topographic variations are usually small compared to the resolution of global-scale numerical models, drag effects must often be parameterised. This thesis aims to understand topographic drag in highly idealised numerical models with a view to demonstrating where efforts in parameterisation may be best directed.

Specifically, the thesis considers single-layer and one and one half layered flow (where a single layer lies below an infinitely deep layer of slightly lower density) over topography, inspired by a series of rotating tank experiments. The flow behaviour is strongly affected by the Froude number $F$ of the flow - the ratio of the oncoming flow to the speed of long free gravity waves.

The transcritical regime $F \sim 1$, in which there is a close analogy with compressible gas dynamics, is investigated as a novel limit of the Shallow-Water Equations. Scaling laws for the drag are verified against numerical integrations and various flow regimes for rotating and non-rotating flows delineated.

Supercritical flow ($F > 1$) is also investigated, focusing on both the drag and breaking waves in the far-field, which in the rotating case is shown to depend on a single parameter.

# Acknowledgements

Without the support of my supervisors, Professor E. R. Johnson and Dr. J. G. Esler, and my family, this enterprise would simply not have been possible. Thanks are also due to Laurie Carver, Tim Ham, Fern Scott and Tim Edwards, for countless helpful conversations - mathematical and otherwise.

Some of the results presented here derive from the direct input of Dr. Esler and Professor Johnson, and appear in our joint publications.

The derivation of the 'equivalent aerofoil' description of transcritical flow in Chapter 2, and results presented in Chapter 4 appear in Esler, Rump & Johnson (2007a).

Aspects of the discussion of rotating flow over a ridge in Chapter 5 appear in Esler, Rump & Johnson (2005).

The description of transcritical, rotating flow over three-dimensional topography in Chapter 6 appears in Esler, Rump & Johnson (2007c).

The description of supercritical, rotating flow over three-dimensional topography in Chapter 7 appears in Esler, Rump & Johnson (2007b).

The rotating tank experiments described in Chapter 8, are presented in Johnson, Esler, Rump, Sommeria & Vilenski (2006).

# Contents

# List of Figures

# List of Tables

# Chapter 1

# Introduction

Our interest in weather forecasting and global climate models ranges from the frivolous to the potentially life-saving. Modern Formula 1 teams employ their own meteorologists in the hope that they might predict the weather with sufficient accuracy to glean an advantage over their rivals. On the other hand, an ability accurately (and sufficiently in advance) to predict extreme weather events can certainly save lives. Further to the traditional desire to predict weather conditions, alarms over the effects of 'global warming' as a result of human activity have led to an explosion of interest in constructing global climate models.

The sheer complexity of the equations required adequately to describe our environment on a global scale necessitates resort to numerical modelling. When compared to the grid resolution of such global-scale numerical models, it is usual for topographic variations, the subject of this thesis, to occur at a sub-grid scale. If it were the case that topographic variations merely effect the local details of flows, not much would be lost in the context of a global scale model. This is not so. In fact, as noted by Baines (1995), the form drag exerted by topographic features on atmospheric flow accounts for

approximately 50% of the drag exerted by the Earth's surface and has a substantial influence on the circulation of the atmosphere. Therefore such effects must be included in global-scale circulation models as accurately as possible. The incorporation of the nett contribution of dynamical effects occurring at a sub-grid scale is referred to as *parameterisation.*

When addressing environmental concerns such as air quality and the distribution of pollutants, it is also sometimes important to predict the details of the flow itself in the neighbourhood of topography.

Many different equations to describe fluid flow over topography, of varying degrees of complexity, can - and have - been studied. To which should we turn? In a book review for the American Mathematical Society, (Albert, 1997), John Albert opens with the following:

> "Some native peoples of the North are reluctant to mention the ocean by name, reasoning that it is not wise to refer off-handedly to something that is so big. The vast topic of wave motion should perhaps be approached in the same spirit. Following the lead of the book under review, let us confine our attention here to a few human-sized features of the subject."

Echoing these sentiments, the majority of this thesis will describe topographically induced waves in the context of perhaps the most simple of geophysically relevant paradigms - the shallow-water equations. Though this is a highly idealised representation of the physical problem, it is hoped that results presented here might at least serve to suggest where future efforts in the parameterisation of drag might best be directed, and also offer some insight into the qualitative behaviour of flows observed in the 'real world', the laboratory, and more sophisticated mathematical models. To further

focus our treatment of the problem, throughout the majority of this work it is taken that the topography is isolated and that the flow is steady.

Before proceeding to a discussion of the shallow-water equations, a few examples of geophysical phenomena that have been described with a degree of success within the shallow-water paradigm are touched upon.

## 1.1 Observed Geophysical Phenomena

### 1.1.1 *Guadalupe Island, CA*

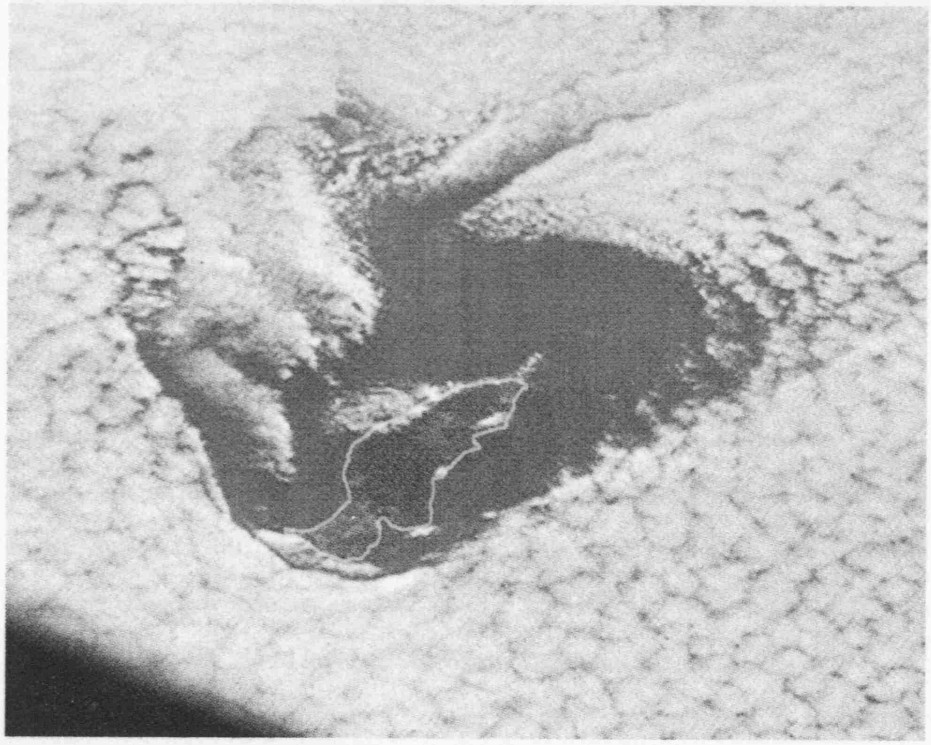

Figure 1.1: Low-layer stratocumulus cloud moving at 6-10 kts past Guadalupe Island, Baja California, Mexico. A bow wave spreads from the north end of the island. Taken during Gemini flight $V$, August 21, 1965.

Among the many observations of cloud patterns near topography, some stand out as showing stationary disturbances upwind of the topography.

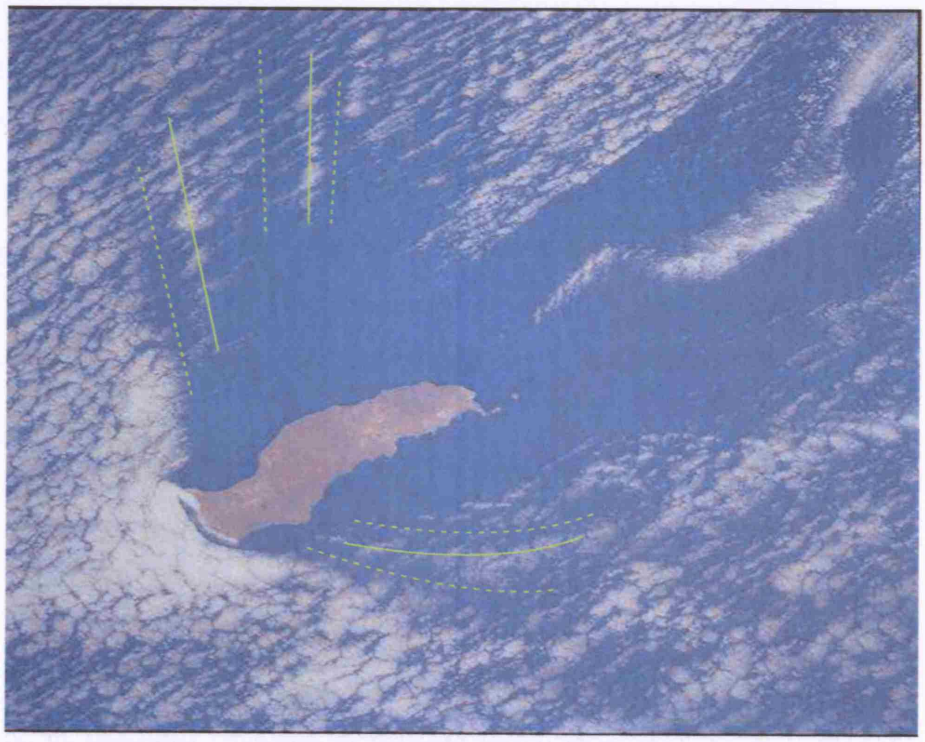

Figure 1.2: The wave field over Guadalupe island, Baja California on 11th July 2001. Solid and dotted lines have been added to highlight wave crests and wave troughs respectively.

Figure 1.1 reproduces a NASA photograph of Guadalupe island, Baja California, taken during the Gemini-V flight on August 21st, 1965 and described by Stevenson (1969). A layer of stratocumulus cloud is moving at 6-10 knots past the island, whose peaks reach 4500 ft and thereby project through, and interfere with, the cloud layer. Stevenson (1969) notes that a 'shock' or 'bow' wave spreads from the north end of the island, "similar to waves formed by a ship moving through water". As will be seen later, 'bow' waves are characteristic of solutions to the shallow-water equations; by implication, then, Stevenson (1969) suggests that the observed phenomena might be described within the shallow-water paradigm.

Stevenson (1969) reports that similar cloud features were photographed

during four further Gemini flights, so that these cloud features must be considered climatic features of the Guadalupe island marine atmosphere, as opposed to merely transient events. Figure 1.2 reproduces a rather more recent NASA photograph of Guadalupe island, having been taken on 11th July 2001. Again, the 'bow' wave at the north end of the island is clearly visible, amply bearing out Stevenson's observation that it is a climatic feature. The technology may have moved on in the interim, but the clouds have not.

Considering Figure 1.2 a little more closely, however, offers a first indication of effects that, as will be seen, are not captured in the shallow-water paradigm. To clarify the wave field of Figure 1.2 solid lines have been added to indicate wave crests, and dashed lines to indicate wave troughs; behind the initial bow wave, a series of alternate crests and troughs can readily be identified. Johnson & Vilenski (2004) show that, by extending the shallow-water equations to include weak non-hydrostatic effects, the single isolated bow waves of the shallow-water paradigm split into multiple parallel crests similar to those of Figure 1.2. A brief discussion of the effects of non-hydrostatic dispersion in the context of the current work is given in Chapter 8.

### 1.1.2 *Monterey - Big Sur, CA*

Burk & Haack (1999), amongst others, describe similar cloud features extending away from the Monterey - Big Sur coastline of central California. Figure 1.3 reproduces a GOES-9 (Geostationary Operational Environmental Satellite ) visible image, taken on 23rd June, 1996. White lines in the figure serve to highlight the coastline.

Burk & Haack (1999) note that it is the orographic forcing and stationary

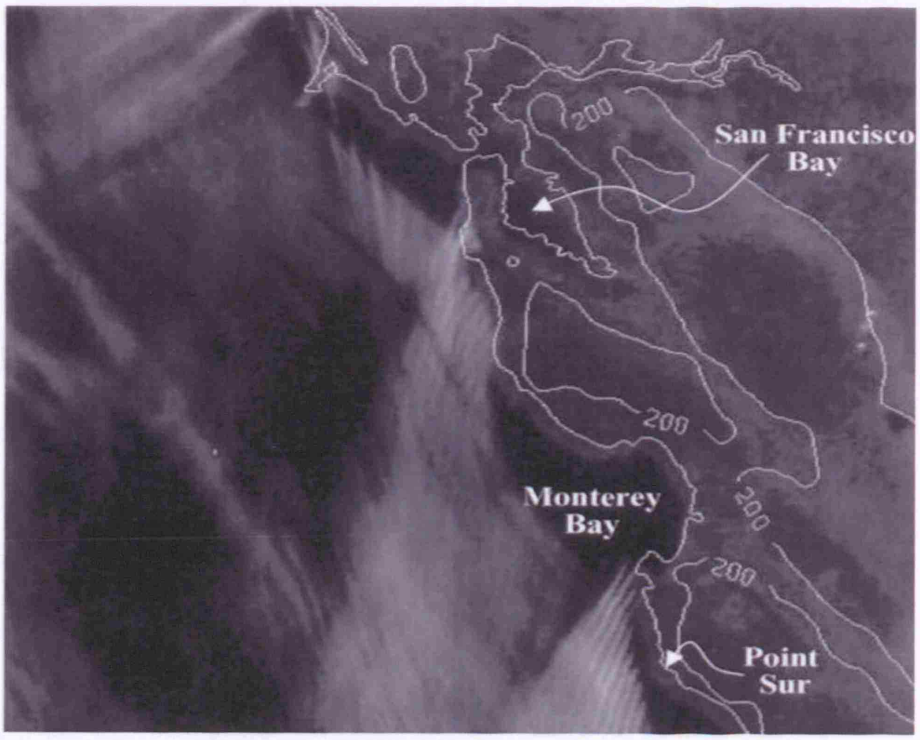


Figure 1.3: A GOES-9 visible image from 23rd June 1996, reproduced from Burk & Haack (1999), showing wave clouds extending away from the Monterey-Big Sur coastline of central California. White lines highlight the coastline.

appearance in GOES image loops (with frames every 15 minutes) that set these waves apart from propagating wave phenomena. They present a convincing interpretation of the observed cloud features based on isolated single attached and detached shocks forced by obstacles in supercritical shallow-water flow.

## 1.2 Theoretical Modelling

### 1.2.1 *Physical scenario and governing equations*

From a geophysical perspective, the relevant physical scenario to which solutions presented in this thesis apply is that of a 'one-and-a-half' layer fluid, consisting of a layer of undisturbed depth $H$ and uniform density $\rho_2$ underlying a less dense layer (density $\rho_1$) of inifinite vertical extent. This is illustrated in Figure 1.4. It is taken that $(\rho_2 - \rho_1)/\rho_2 \ll 1$ in order that the

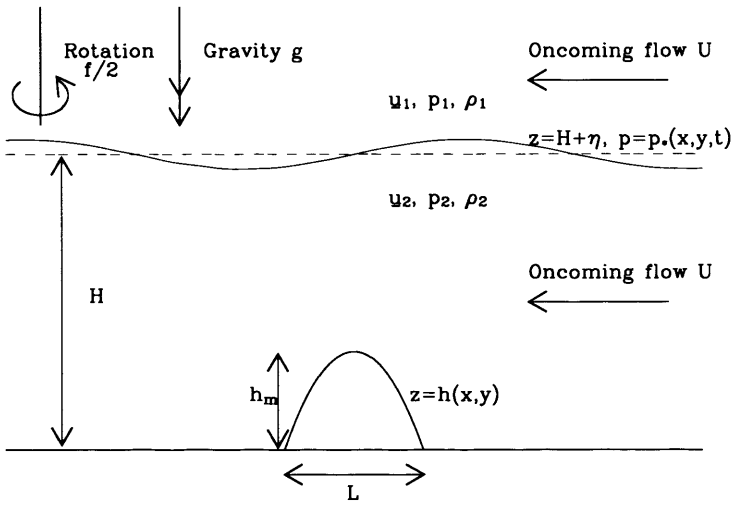


Figure 1.4: Schematic showing the physical scenario of oncoming 'one-and-a-half' layer flow, described in the text.

Boussinesq approximation can be made. The fluid is rotating with angular frequency $f/2$, is acted on by gravity $g$ and both layers are flowing with an initially uniform speed $U$, from right to left, over an obstacle with maximum height $h_m$ and horizontal scale $L$. Further, we specify *a priori* that the upper layer is dynamically passive, so that $\mathbf{u}_1 = (-U, 0, 0)$ for all time.

The Euler equations for the flow scenario described above are

$$\begin{aligned} \frac{D\mathbf{u}_i}{Dt} + f\mathbf{k} \times \mathbf{u}_i &= -\frac{\nabla p_i}{\rho_i} - g\mathbf{k}, \\ \nabla.\mathbf{u}_i &= 0, \end{aligned} \tag{1.1}$$

for $i = 1, 2$, with $i = 2$ denoting the lower layer and $i = 1$ the upper layer. The boundary conditions at the interface are the continuity of normal velocity and pressure,

$$w_i = \frac{D_H \eta}{Dt}, \quad p_1 = p_2 = p_*(x, y, t) \quad \text{at} \quad z = H + \eta(x, y, t), \tag{1.2}$$

whilst the kinematic condition at the lower boundary requires

$$w_2 = \mathbf{u}_{2_H}.\nabla h \quad \text{at} \quad z = h(x, y), \tag{1.3}$$

where the subscript $H$ indicates quantities that are purely horizontal.

### 1.2.2 *Shallow-water Approximation*

For the majority of this work, studies will focus on the shallow-water equations, a reduction of the Euler equations (1.1) appropriate when the aspect ratio $\delta = H/L$ of the flow is small.

One approach to deriving the shallow-water equations from the full Euler equations (1.1) is to specify *a priori* that the pressures are hydrostatic; that is

$$\frac{\partial p_i}{\partial z} = -g\rho_i \tag{1.4}$$

for $i = 1, 2$. The utility of the hydrostatic assumption is that it is immediately clear that horizontal velocities become $z$-independent. Considering the $x$-momentum equation for the lower layer for example, the forcing term is

now given by $p_{2x} = p_{*x} + \rho_2 g\eta_x$; thus it follows that, provided $u_2$ is initially independent of $z$, which is indeed the case here since $u_2 = -U$ upstream of the topography, it remains so for all time. Thus the shallow-water equations offer the advantage of a reduction of dimension over the Euler equations.

Consider first the lower layer, introducing the lower layer thickness defined by

$$\sigma = H + \eta - h. \tag{1.5}$$

In order that the equations have a meaningful solution, we must have $\sigma > 0$. Since horizontal velocities are independent of $z$, it follows from the lower-layer continuity equation that $w_2$ must be a linear function of $z$. In order that the kinematic boundary conditions be satisfied, we thus deduce that

$$w_2 = \left(\frac{z-h}{\sigma}\right)\frac{D_H\eta}{Dt} + \left(\frac{\sigma+h-z}{\sigma}\right)\mathbf{u_{2_H}}.\nabla h, \tag{1.6}$$

so that

$$w_{2z} = \frac{1}{\sigma}\frac{D_H\sigma}{Dt}. \tag{1.7}$$

Combining this with the lower layer continuity equation then reveals the shallow-water thickness equation

$$\sigma_t + \nabla.(\sigma\mathbf{u}_{2_H}) = 0. \tag{1.8}$$

Now consider the momentum equations. Integrating the hydrostatic pressure relation (1.4) in $z$ from the interface where $p = p_*(x, y, t)$ reveals the following:

$$p_2 = p_* + \rho_2 g(H + \eta - z); \tag{1.9}$$

$$p_1 = p_* + \rho_1 g(H + \eta - z). \tag{1.10}$$

In order that the upper layer be dynamically inactive, flowing from right to left with speed $U$ for all time, $\nabla p_1$ must achieve a force balance in the upper layer momentum equations. Hence,

$$\nabla p_1 = \rho_1 f U \mathbf{j} \tag{1.11}$$

so that

$$\nabla_H p_2 = \rho_1 f U \mathbf{j} + (\rho_2 - \rho_1) g \nabla_H \eta. \tag{1.12}$$

Substituting into the lower layer momentum equations then reveals

$$\frac{D_H \mathbf{u}_{2_H}}{Dt} + f\mathbf{k} \times \mathbf{u}_{2_H} = -g' \nabla_H \eta - \frac{\rho_1}{\rho_2} f U \mathbf{j}, \tag{1.13}$$

where

$$g' = g \frac{\rho_2 - \rho_1}{\rho_2} \tag{1.14}$$

is called the *reduced gravity.* Finally, we make the Boussinesq approximation, setting $\rho_1/\rho_2 = 1$. Equations (1.5), (1.8) and (1.13) comprise the shallow-water equations for a one-and-a-half layer flow, and are a closed partial differential equation system for $\mathbf{u}_{2_H}$, $\sigma$ and $\eta$.

Following the above procedure, no indication of the expected range of validity of the shallow-water theory is afforded. An approximation has been made - namely that the pressure is hydrostatic (1.4) - but what this assumption might mean in terms of the physical parameters of the system is not immediately obvious; indeed the shallow-water theory was initially regarded with a degree of scepticism. The problem was resolved by K.O. Friedrichs in an appendix to Stoker (1948), who demonstrated that shallow-water theory may be derived as the lowest order in a formal perturbation expansion of the Euler equations in the aspect ratio $\delta$. Shallow-water theory retains terms

up to $O(\delta^2)$, and may be expected to be accurate for $\delta \ll 1$.

Taking the horizontal scale to be $L$, the horizontal velocity scale to be $c \equiv \sqrt{g'H}$ (the long interfacial gravity wave speed), the time scale to be $L/c$, and the layer thickness scale to be $H$ (and dropping the subscripts '2' and '$H$'), the shallow-water equations describing the motion of the lower fluid layer may be written in non-dimensional form as

$$\begin{aligned} u_t + (u-F)u_x + vu_y - \sqrt{B}v &= -\eta_x, \\ v_t + (u-F)v_x + vv_y + \sqrt{B}u &= -\eta_y, \\ \sigma_t + [(u-F)\sigma]_x + [v\sigma]_y &= 0, \end{aligned} \tag{1.15}$$

where $\sigma = 1+\eta-Mh$ is the layer thickness, and the total horizontal velocity is $\mathbf{u} = (-F+u, v)$. The non-dimensional parameters appearing in (1.15) are defined by:

$$F = \frac{U}{c}; \quad M = \frac{h_m}{H}; \quad B = \frac{f^2L^2}{c^2}. \tag{1.16}$$

$F$ is the Froude number of the oncoming flow, measuring the ratio of the oncoming flow speed to the long interfacial gravity wave speed. When $F > 1$, the flow is termed supercritical, critical when $F = 1$ and subcritical when $F < 1$. $M$ describes the non-dimensional obstacle height. $B$ may be recognised as an inverse Burger number, measuring the square of the ratio of the obstacle length scale $L$ to the Rossby radius of deformation $L_R = c/f$.

Equations (1.15) also apply to an 'experimental scenario' (see Figure 1.5) in which an obstacle is towed through a single layer of rotating fluid which is otherwise quiescent. However, since the rotating shallow-water equations describing flow of a single layer are not Galilean invariant, the set (1.15)

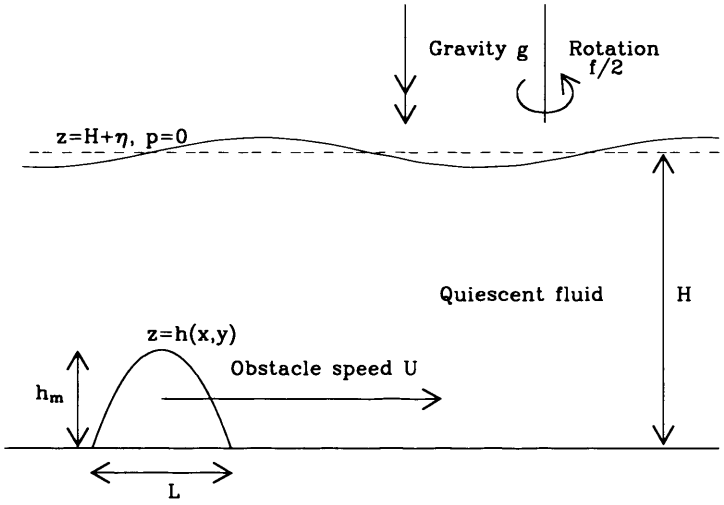


Figure 1.5: Schematic showing the 'experimental scenario', in which an obstacle is towed through an otherwise quiescent fluid at speed $U$, described in the text.

does not apply directly to the oncoming flow of a single layer over a fixed obstacle. In the single layer oncoming flow scenario, the fluid surface tilts so that the Coriolis force is balanced by a pressure gradient. The long gravity wavespeed $c = \sqrt{gH}$ and Froude number $F = U/\sqrt{gH}$ are then functions of the cross-stream ordinate $y$.

In the absence of rotation however, the shallow-water equations *are* Galilean invariant, so that non-rotating solutions presented throughout this thesis also apply directly to single-layer flows.

### 1.2.3 *Hydraulic jumps*

Familiar to anyone who has tried to fill a bowl of water rather rapidly is the phenomenon of a 'hydraulic jump'. This term describes the abrupt increase

in the depth of the water observed, which stands in a near-circle a uniform distance from where the water hits the bowl. Often this depth increase may be seen to induce a very turbulent mixing of the surrounding water, so that we surmise that significant energy loss must occur at such a jump. When such a jump is in motion, it is referred to as a bore, a famous example of which is that periodically observed on the River Severn.

Waves in the shallow-water system (1.15) travel with a speed proportional to the layer thickness $c = \sqrt{\sigma}$. Thus waves have a tendency to steepen as they travel, to the point at which the profile must eventually overturn. This corresponds to the physically observed wave breaking described above, but our equations (1.15) fail us at this point, since solutions become multi-valued.

In order to model the situation at breaking waves, it is usual to regularise solutions to (1.15) by including the possibility of mass and (lower layer) momentum conserving hydraulic jumps, across which the fluid depth and normal velocity jump discontinuously between distinct (but finite) values. In two dimensions in the absence of rotation, providing that the curvature of the jump is not too great, such jumps satisfy (see e.g. Johnson, 1997)

$$-V[\sigma]_-^+ + [\sigma \mathbf{u}.\mathbf{n}]_-^+ = 0, \tag{1.17}$$

$$-V[\sigma \mathbf{u}.\mathbf{n}]_-^+ + [\sigma(\mathbf{u}.\mathbf{n})^2 + \frac{1}{2}\sigma^2]_-^+ = 0, \tag{1.18}$$

where $\mathbf{n}$ is a horizontal unit vector normal to the jump, $V$ is the jump velocity in the direction of $\mathbf{n}$, $\mathbf{u} = (u - F, v)$ is the full velocity, and for any quantity $q$

$$[q]_-^+ = [q]_{upstream} - [q]_{downstream}. \tag{1.19}$$

Across such a jump energy is lost, so that there is an implicit assumption

that an unspecified dissipation acts on the (unresolved) horizontal scale of the jumps (see e.g. Jiang & Smith, 2000) and therefore energy is not a globally conserved quantity of the shallow-water equations when jumps are present.

In the case of one-dimensional rotating flow, Baines & Leonard (1989), following Houghton (1969), argue that, since an hydraulic jump may be considered to take place across a very short distance compared to the Rossby radius of deformation ($L_R = c/f$), rotation may be considered to have a negligible effect on its internal dynamics. A similar argument may be applied to the two-dimensional system, so that jumps satisfy the conditions of the non-rotating system as given above.

Although the closure in which the lower layer is taken to suffer an energy loss across an hydraulic jump is the usual one, it should be noted that for the particular case of a one-and-a-half layer flow this is not the only possible closure. In particular Klemp *et al.* (1997) argue that, in this case, it may be appropriate to formulate a condition at a travelling bore in which the lower layer conserves energy, whilst momentum is transferred to the upper layer across the bore.

## 1.3 Overview of Shallow-Water Flow Over Topography

### 1.3.1 *Steady, non-rotating, shallow-water flow over a two-dimensional ridge*

The problem of steady shallow-water flow over a two-dimensional ridge is well understood and has been discussed in detail by Baines (1995). Here, it will be of value briefly to review this problem, as it serves to contextualise

much of the work presented in this thesis.

The possible flow configurations and the regions of obstacle height, Froude number $(M, F)$ space in which they are encountered, are given in Figure 1.6. In *regime I* the flow is everywhere supercritical; the flow field is symmetric, with the layer depth increasing over the obstacle, achieving its maximum at the obstacle crest. In *regime IIa*, the flow is transcritical over the obstacle, with critical flow occurring exactly at the obstacle crest. Jumps propagate at constant speed to $x = \pm\infty$. In *regime IIb*, similarly to regime IIa, the flow over the obstacle is transcritical, with a jump propagating at constant speed upstream toward $x = +\infty$. However, the downstream recovery jump (DRJ) is now stationary on the lee side of the obstacle. In *regime III* the flow is purely subcritical; the flow field is again symmetric, with the layer depth decreasing over the obstacle and achieving its minimum over the obstacle crest. In *regime IV*, the obstacle is sufficiently high to completely block the oncoming flow.

In the context of flow over an infinite ridge, the shallow-water equations become $y$-independent, so that the set (1.15) reduces to

$$u_t + (u - F)u_x = -(\sigma + Mh)_x, \tag{1.20}$$

$$\sigma_t + [(u - F)\sigma]_x = 0, \tag{1.21}$$

where $F$ is the Froude number of the oncoming flow, and the ridge profile is described by $h(x)$. The relevant upstream conditions are $x \to \infty$, $\sigma \to 1$, $u \to 0$.

If the resulting flow is assumed steady, and solutions are sought that are purely a function of $x$, the thickness equation (1.21 ) may be integrated to

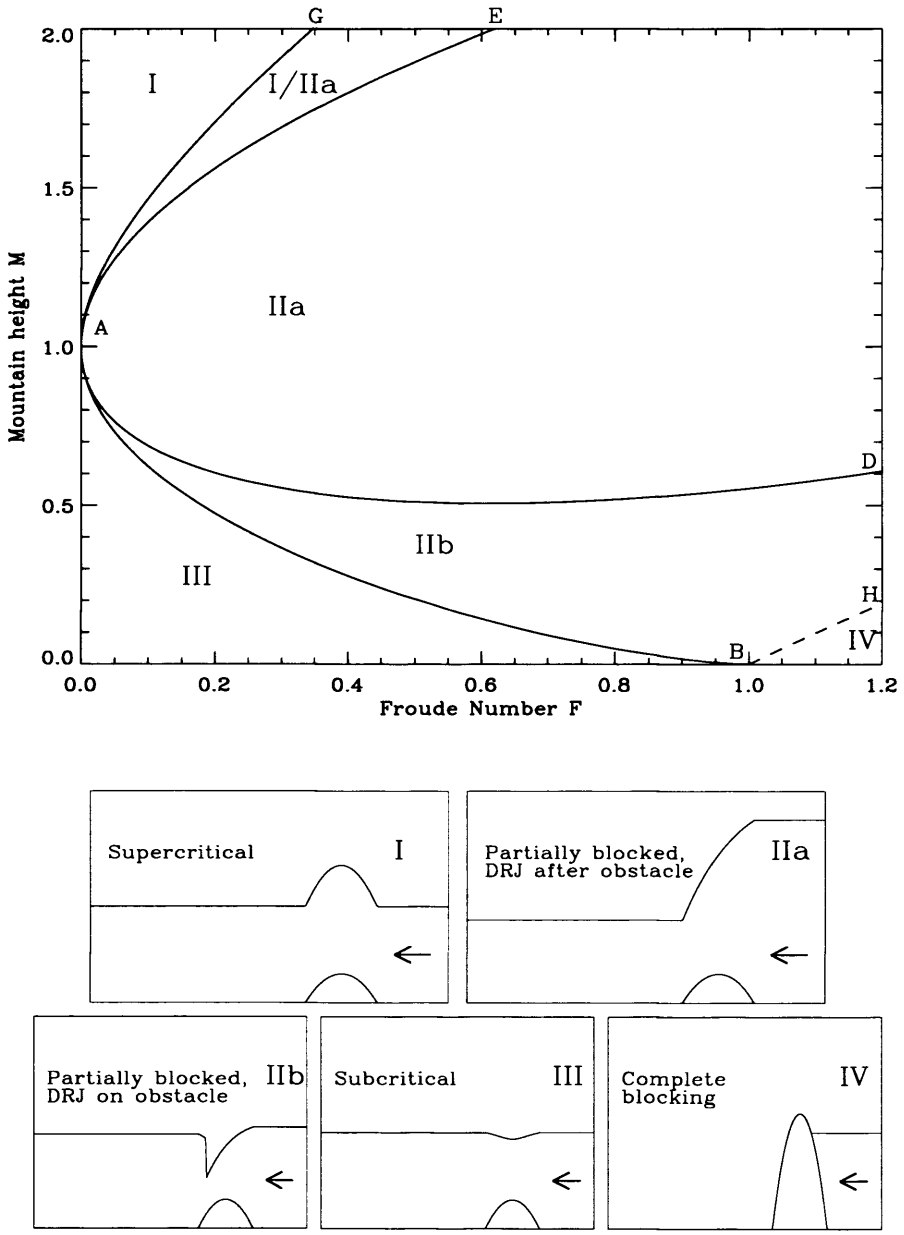


Figure 1.6: $(M, F)$ regime diagram for quasi-steady flow over a two-dimensional obstacle. The regimes are as follows. (I) Supercritical flow everywhere. (IIa) Transcritical flow over the obstacle with upstream and downstream propagating jumps. (IIb) Transcritical flow over the obstacle with an upstream propagating jump and a stationary recovery jump on the obstacle. (III) Subcritical flow everywhere. (IV) Complete blocking of the flow. The region I/IIa is an hysteresis region where more than one solution is possible.

give

$$(F-u)\sigma = F.$$

This allows $u$ to be eliminated from (1.20) to give the single equation

$$\left(\sigma + \frac{F^2}{2\sigma^2}\right)_x = -Mh_x \tag{1.22}$$

for the layer depth $\sigma$. The velocity $u$ may be recovered from the layer depth $\sigma$ via

$$u = F - \frac{F}{\sigma}.$$

Equation (1.22) may be integrated to give

$$\sigma + \frac{F^2}{2\sigma^2} + Mh = K. \tag{1.23}$$

However, the range of validity of (1.23) is limited, as can be seen by performing the differentiation on the left hand side to reveal

$$\left(\frac{F^2}{\sigma^3} - 1\right)\sigma_x = Mh_x. \tag{1.24}$$

At the crest of a single-humped obstacle of the type discussed here, since $h_x = 0$ we must have either that $\sigma_x = 0$ also, or that the layer depth is exactly $\sigma = F^{2/3}$. In the latter case, the local Froude number, defined by $F_l^2 = (u-F)^2/\sigma$ is exactly unity, so that this requirement is often referred to as 'critical' control.

If a given oncoming flow is to remain entirely sub/supercritical, then in light of the above discussion, equation (1.23) must posses two distinct real roots at the obstacle crest (h=1), the condition for which is given by

(recalling the discriminant for a cubic polynomial)

$$K > M + \frac{3}{2}F^{2/3}. \tag{1.25}$$

In this case, the flow contains no hydraulic jumps, so that in the absence of such a dissipative mechanism we must have that $K = 1 + F^2/2$ throughout (i.e. the upstream value of the undisturbed flow). For a transcritical solution, the condition of critical control requires that the flow at the obstacle crest is exactly critical, so that two roots of equation (1.23) must coalesce at that point. This requires equality in equation (1.25), so that the condition on the obstacle height for which a purely sub/supercritical solution is allowed is given by $M \leq M_0$ where

$$M_0 = 1 + \frac{F^2}{2} - \frac{3}{2}F^{2/3}. \tag{1.26}$$

This equation defines the curve BAE in Figure 1.6.

As discussed by Baines (1995), in the case that $M$ is sufficiently large that condition (1.26) is violated we must, in principle, return to a time-dependent formulation of the problem to establish details of the flow. However, guided by previous studies and laboratory experiments, we may assume *ab initio* that an upstream travelling jump exists, thereby simplifying our analysis. Throughout regime II then, we have an upstream travelling jump, which acts to relieve the partial blocking of the flow by the obstacle. The speed at which this upstream propagating jump travels depends on the values of $F$ and $M$, and eventually falls to zero relative to the oncoming flow. The limiting case thus consists of a stationary hydraulic jump located at the upstream edge of the obstacle. In this case, from (1.24) the flow must be critical at the obstacle crest, so that $K = M + 3/2F^{2/3}$. Employing the

jump conditions at the obstacle edge, where $\sigma = 1$, and then substituting into equation (1.23) reveals that

$$\frac{1}{2}\left(\sqrt{8F^2+1}-1\right)+\frac{2F^2}{(\sqrt{8F^2+1}-1)^2}=M_1+\frac{3}{2}F^{2/3},$$

which may be rearranged as

$$M_1=\frac{(8F^2+1)^{3/2}+1}{16F^2}-\frac{1}{4}-\frac{3}{2}F^{2/3}. \tag{1.27}$$

This defines curve AG in the regime diagram of Figure 1.6.

At this point we note the curious fact that curve AG lies to the left of curve AE - which we previously took to be the boundary between purely subcritical and transcritical flows. Thus throughout region AGE we surmise that two steady states are possible, belonging to either regime I or IIa. In fact, recent work by Baines & Whitehead (2003) has demonstrated that there are *three* possible steady states in region AGE - the upstream jump could lie over the obstacle; however, this last possibility is shown to be unstable, so is unlikely to be observed either numerically or in an hydraulic lab. This phenomenon is known as *hysteresis*: the steady state achieved is dependent on the details of the time development of the flow.

Throughout regime II the flow is critically controlled at the obstacle crest; downstream, Houghton & Kasahara (1968) showed that the flow may take on one of two possible configurations. Flow on the lee side of the obstacle is supercritical and is followed by an hydraulic jump that may either be stationary over the obstacle or propagate downstream at a constant speed. In order that the flow after this lee-side jump can be connected with the initial flow state, a time-dependent downstream propagating rarefaction wave must be added to complete the solution.

The limiting case, which defines curve AD, is that in which a stationary hydraulic jump stands exactly at the downstream edge of the obstacle. Curve AD may be established by solving the following set of equations numerically using the secant method:

$$\begin{aligned}
\mathcal{F} &= \sigma_0 F - (\sigma_0 - 1)\sqrt{\frac{1}{2}\sigma_0(\sigma_0+1)}; \\
\sigma_0^3 - \left(M + \frac{3}{2}\mathcal{F}^{2/3}\right) + \frac{1}{2}\mathcal{F}^2 &= 0, \quad \sigma_0 > 1; \\
\sigma_1^3 - \left(M + \frac{3}{2}\mathcal{F}^{2/3}\right)\sigma_1^2 + \frac{1}{2}\mathcal{F}^2 &= 0, \quad 0 < \sigma_1 < 1; \\
\sigma_+ &= \frac{1}{2}\sigma_1\left(\sqrt{\frac{8\mathcal{F}^2}{\sigma_1^3}+1} - 1\right); \\
\frac{\mathcal{F}}{\sigma_+} - 2\sqrt{\sigma_+} &= F - 2.
\end{aligned}$$

The first of them determines the effective oncoming mass flux $\mathcal{F}$ of the flow at a given station upstream of the obstacle once the upstream propagating jump has passed by, in terms of the layer thickness at the obstacle edge $\sigma_0$. The second and third equations state that the flow is critically controlled. The fourth is simply a rearrangement of the jump conditions (1.17) & (1.18), whilst the fifth guarantees that the flow after the jump may be connected to the undisturbed flow via a rarefaction wave.

If $M$ is sufficiently large, total blocking occurs. In this case the mass flux over the obstacle $\mathcal{F}$ is zero. From the first two equations of the above set, we find that the curve BH bounding the blocking region is given by

$$F = (M-1)\sqrt{\frac{M+1}{2M}}. \tag{1.28}$$

### 1.3.2 *Steady, rotating, shallow-water flow over a two-dimensional ridge*

Although steady shallow-water flow over a two-dimensional ridge is well understood in the absence of rotation, its rotating analogue is less well appreciated. Queney (1948) and Pierrehumbert (1984) discuss linear solutions, but solutions involving the direct extension of the full nonlinear equations were not considered until Baines & Leonard (1989). They demonstrate that, as in the non-rotating case, critical conditions over the obstacle serve to control the flow. However, the presence of rotation causes upstream propagating bores either to become arrested at a fixed distance ahead of the obstacle, or, in the case of subcritical oncoming flow, to disappear completely in the steady state. When the oncoming flow is supercritical, Baines & Leonard (1989) demonstrate that finite-amplitude inertia-gravity wavetrains are generated downstream of the obstacle. Rotation is also found to reduce the size of the region of parameter space allowing transcritical flow over the obstacle.

Esler *et al.* (2005) construct semi-analytic solutions for the particular case of flow over a parabolic ridge, aspects of which are reviewed in Chapter 5.

### 1.3.3 *Steady, non-rotating, shallow-water flow over three-dimensional topography*

General analytical solutions to the full nonlinear shallow-water equations in two dimensions are not available; hence previous studies have been numerical. Consequently, solutions of the full nonlinear equations have a rather short history, apparently not having been considered until Lamb & Britter (1984), Schär & Smith (1993a) and Schär & Smith (1993b). All three studies consider situations in which the environmental flow is subcritical i.e. $F < 1$;

Lamb and Britter consider a cone-shaped obstacle and Schär and Smith a 'Witch of Agnesi' obstacle of the form $h = h_m(1 + x^2/a^2 + y^2/a^2)^{-\frac{3}{2}}$.

Lamb & Britter (1984) present both numerical and experimental results for flow over a cone-shaped obstacle. Of particular concern in their numerical investigations is the development with increasing 'three-dimensionality' of the obstacle of the transition from purely subcritical to transcritical flow. By comparing numerically established transition points in $(M, F)$ space with the corresponding curve for flow over a two-dimensional ridge (curve BAE of Figure 1.6), Lamb & Britter (1984) demonstrate that, for a given flow speed $F$, the obstacle height $M$ required for transition to occur increases as the obstacle is changed from a two-dimensional ridge, to a 'truncated ridge', to the fully three-dimensional cone-shaped obstacle. Both to confirm and extend their numerical study, Lamb & Britter (1984) performed towing tank experiments in which a cone-shaped obstacle was towed through two layers of density contrasting fluid, thereby exciting waves at the interface between the two fluids. A related set of experiments, but in which rotation also plays a part, are described in Chapter 8. Lamb & Britter (1984) were able to demonstrate experimentally that the flow regimes encountered in their numerical simulations correspond well with those that occur in a real fluid, although they note that flow separation and turbulent effects in the lee of the obstacle constitute important qualitative differences. In both the numerical integrations and experiments however, the presence of impermeable horizontal boundaries rather near to the obstacle edges requires that the results presented be treated with some caution as examples of flow over *isolated* topography.

The subsequent two-part study of subcritical shallow-water flow over an isolated three-dimensional obstacle comprising Schär & Smith (1993a),

Schär & Smith (1993b) constitutes a major contribution to the topic, and may be considered to account in essence for our current level of understanding of this problem. The studies were motivated by phenomena which, though germane to the current work, will in fact not be discussed in detail here. Schär & Smith (1993a) note that "atmospheric vortex streets behind major isolated topographic obstacles are one of the most spectacular features in the earth's atmosphere", and it is these that they aim to interpret. Perhaps the most important results of their studies are the following. First, in Schär & Smith (1993a) it is demonstrated that the vorticity of which these vortex streets are comprised may be generated by a 'pseudoinviscid' mechanism, as opposed to the explicitly viscous mechanism of surface drag. The closure of the shallow-water equations in which mass and momentum conserving hydraulic jumps are taken to regularise the system at the onset of wave breaking, makes no explicit assumptions about the nature of the dissipation acting across the jump, except that it exists. This is what is meant in Schär & Smith (1993a) by 'pseudoinviscid': the presence of an hydraulic jump can serve to introduce vorticity to the flow, with no special requirements concerning the nature of the dissipation invoked at the jump. Secondly, in Schär & Smith (1993b) it is demonstrated that, these potential vorticity anomalies having been introduced, the flow is potentially susceptible to barotropic instabilities, and the resulting wake may consist of a periodic vortex street similar to those observed in the atmosphere.

More closely related to the material of the current work is the description of the various possible flow regimes in Schär & Smith (1993a). To establish regime boundaries in $(M, F)$ space, they integrated the shallow-water equations numerically for flow over a 'Witch of Agnesi' obstacle of the form $h = M(1 + x^2 + y^2)^{-\frac{3}{2}}$, with the simulations confined to being

symmetrical about the obstacle centreline to suppress the emergence of the periodic vortex street. For a fixed $F < 1$ and sufficiently small $M$, the flow remains entirely subcritical throughout the domain. The flow exhibits fore-aft symmetry and is well described by linear theory. As the obstacle height $M$ is increased, the flow becomes critical over part of the obstacle and an hydraulic jump of finite length forms toward the lee side of the obstacle. On further increasing the obstacle height $M$, Schär & Smith (1993a) identify a further transition at which flow reversal along $y = 0$ and flow separation are encountered. Finally, for sufficiently large $M$, the obstacle may project through the layer, just as in the two-dimensional case.

A more detailed description of these studies, together with some discussion of in what circumstances these flows might in reality become dominated by viscous effects is given by Baines (1995). The regime diagram in $(M, F)$ space depicting the various flow configurations described above may also be found there (Fig. 2.30, p.85).

The above studies assume that the oncoming flow is subcritical ($F < 1$). Jiang & Smith (2000) considered the supercritical regime ($F > 1$), identifying three possible flow configurations based on a large number of numerical simulations with $1.2 < F < 2.0$, $0 < M < 3$ for flow over the 'Witch of Agnesi' obstacle of Schär & Smith (1993a), Schär & Smith (1993b). If the obstacle is sufficiently small and the Froude number of the oncoming flow sufficiently far from unity (in a sense that will be made clear in Chapter 2), Jiang & Smith (2000) describe the resulting purely supercritical flow field as belonging to the 'V-wave regime'. Both the drag and flow in this regime are well described by linear theory. As $M$ is increased with $F$ fixed, the flow eventually becomes transcritical in character, containing an embedded region of subcritical flow. In this case, a stationary 'bow' hydraulic jump

is encountered ahead of the obstacle, through which the flow transitions abruptly to subcritical near the centreline of the obstacle. Following this initial jump, the flow is accelerated back to supercritical smoothly, before decelerating back to its upstream speed via an oblique jump at the trailing edge of a V-wave. Jiang & Smith (2000), adopting an additive nomenclature, describe this structure as belonging to the 'Bow-wave and V-wave regime'. Finally, just as in the case of subcritical oncoming flow, for sufficient obstacle height they discover a 'flow splitting regime' in which the flow is pierced by the obstacle.

Jiang & Smith (2000) also derive the supercritical, linear drag exerted by the obstacle on the flow, for the particular case of their 'Witch of Agnesi' obstacle, which is found to offer good agreement with nonlinear computations for sufficiently large $F$ (or small $M$). Further, they discuss the generation of vorticity by both the bow jump and V-wave, noting that the vorticity produced is much less, often by a factor of 100, than that produced by a jump in subcritical flow (Schär & Smith (1993a)).

### 1.3.4 *Steady, rotating, shallow-water flow over three-dimensional topography*

To the best of the author's knowledge, the problem of rotating shallow-water flow over a three-dimensional obstacle has received little or no attention. Vilenski & Johnson (2004) recently considered the related problem in which the first effects of non-hydrostatic dispersion are retained in the context of the rotating Kadomtsev-Petviashvili equation (Kadomtsev & Petviashvili, 1970). Solutions presented correspond to rotating flow over a Gaussian obstacle that is asymptotically elongated in the cross-stream direction; several representative flow patterns are identified and the effects of rotation on the

drag exerted by the obstacle are discussed.

## 1.4 Thesis outline

In Chapter 2 asymptotic theories, valid for small obstacle height $M$, are introduced to describe the transcritical (Froude number $F$ close to unity) and supercritical (Froude number (significantly) larger than unity) regimes of shallow-water flow over an isolated obstacle. It is well known that the shallow-water equations are isomorphic to the isentropic equations of gas dynamics (see e.g. Johnson, 1997) when the 'ratio of specific heats' $\gamma = 2$. Although for a real gas, '$\gamma = 2$' cannot in fact be realised, much of the literature of gas dynamics is extremely relevant to a discussion of the shallow-water equations. Jiang & Smith (2000) describe the phenomena they observe in their numerical simulations in the language of gas dynamics, describing flow patterns as consisting of 'bow-shocks' and 'V-waves'. The transcritical theory presented in Chapter 2 makes this analogy precise, showing that transcritical flow over an obstacle of small height is isomorphic to the problem of flow past a thin aerofoil.

In a broader geophysical context, the transcritical regime describes that in which the topographic forcing acts to near-resonantly excite a free wave mode of the flow. When dispersive effects are negligible, the result of this resonance is the generation of hydraulic jumps, whilst in the case that dispersion is important (discussed in Chapter 8) nonlinear dispersive waves (solitons) replace the hydraulic jumps of non-dispersive flow.

The example flow patterns given in Section 1.1 are entirely characteristic of the transcritical regime, and Rottman & Einaudi (1993) carefully argue that transcritical conditions are in fact likely to be ubiquitous in both the atmosphere and oceans. As will be highlighted in the course of this thesis,

the maximum drag exerted on a flow by an obstacle occurs in the transcritical regime, so that a proper understanding of the behaviour of drag in this regime must be considered essential to effective parameterisations in global-scale circulation models.

Chapter 3 reviews the numerical techniques, developed by researchers in the field of compressible gas dynamics, employed to solve the asymptotic equation describing the transcritical regime derived in Chapter 2. In Chapter 4, non-rotating transcritical flows are discussed, comparing results from the asymptotic theory with solutions to the shallow-water equations with finite obstacle height $M$. Drag predictions from the asymptotic theory are particularly highlighted.

The second major theme of this thesis is the effects of rotation on topographically forced flows. For an excellent introduction to wave motions that are influenced by rotation, the reader is recommended to consult the review by Grimshaw *et al.* (1998). Their introduction analyses in detail the circumstances in which the effects of rotation play an important role in establishing geophysical phenomena, a complete discussion of which is beyond the scope of the current work. However, for the following reason, it seems likely that flows on the geophysical mesoscale associated with atmospheric flow around isolated islands or over mountain ranges might be sensitive to even 'weak' rotation.

The effects of rotation on flow past an isolated obstacle become important when the Rossby radius of deformation, $L_R = c/f$, becomes comparable to the transverse scale of the obstacle wake. A feature of the transcritical regime, highlighted by the choice of $y$-scale in the next chapter, is that the transverse scale of disturbances generated by an obstacle can be much greater than the length scale of the obstacle itself. Thus it is expected that

in applying analyses of the transcritical regime to 'real world' flows, it is important first to assess the effects of the Earth's rotation.

As discussed by Grimshaw *et al.* (1998) waves generated by topography in the presence of rotation can be quite distinct from their non-rotating counterparts. A particularly striking example is the finite-amplitude inertia-gravity waves (see also Shrira (1986), and Plougonven & Zeitlin (2003) for a discussion of the corresponding waves in a two-fluid system). In order to highlight the generation of these 'new' waves, and other qualitative effects of rotation in the transcritical regime, the problem of flow over a two-dimensional ridge governed by the shallow-water equations is discussed in Chapter 5. A weakly nonlinear theory analogous to that of Chapter 2 is also considered, offering further insight into the validity of weakly nonlinear reductions to describe water waves.

In Chapter 6, rotating flow over a three-dimensional obstacle is considered, both under the transcritical limit introduced in Chapter 2 and for finite obstacle height $M$ solutions of the shallow-water equations.

Jiang & Smith (2000) argue that the supercritical flow regime ($F > 1$) is also of geophysical interest, because flow conditions in the marine atmospheric boundary layer in the neighbourhood of coastal topography may often be supercritical. Further, they highlight the fact that shallow rivers and even ocean currents such as those in the Long Island Sound might be considered to belong to the supercritical regime.

The second asymptotic theory introduced in Chapter 2 aims to describe the behaviour of the supercritical regime. The predictions of the resulting theory in the absence of rotation are discussed toward the end of Chapter 4. Of greater interest is the case in which rotation is included, discussed in Chapter 7. In this case, it is shown that the qualitative nature of the

shallow-water flow (at least for small obstacle height $M$) depends on a single parameter. Further, it is demonstrated that both in the asymptotic theory and finite obstacle height $M$ shallow-water computations, rotation can act to suppress the wave breaking observed in its absence.

Chapter 8 offers a qualitative comparison between the non-dispersive results presented in the majority of this thesis and the corresponding flows in which the first effects of dispersion are retained. Rotating towing tank experiments performed at the LEGI-Coriolis Institute in Grenoble are reported, and it is hoped that the reader will agree that at least some of the qualitative effects discussed in this thesis can be observed in the experiments.

Finally, Chapter 9 presents both conclusions and possible extensions to the work presented. The effect of obstacle anisotropy and variable oncoming flow direction on the drag exerted on the flow is highlighted. A possible extension of the asymptotic theory of Chapter 2, in which a 'genuinely' two-layered fluid is modelled, is proposed.

# Chapter 2

# Transcritical and supercritical theories for flow over topography in the shallow-water limit

Asymptotic theories, valid for small obstacle height $M$, are introduced to describe the transcritical and supercritical regimes of shallow-water flow over a three-dimensional obstacle. The analysis to follow relates to that described in Esler *et al.* (2007*a*), in which the effects of (weak) dispersion are retained by considering the full Euler equations in the small aspect ratio limit. However, whilst Esler *et al.* (2007*a*) consider non-rotating flows, here the effects of (weak) rotation are included. The introduction of rotation breaks the symmetry of the flow about the centreline $y = 0$; the subtleties associated with this require some consideration.

Throughout this chapter, the physical scenario to be considered is that

of the oncoming flow of a 'one-and-a-half' layer fluid discussed in Chapter 1 - or, equally, the 'experimental scenario' discussed therein. In this case shallow-water dynamics apply in the dynamically active layer, so that the governing equations are

$$\begin{aligned} u_t + (u-F)u_x + vu_y - \sqrt{B}v &= -\eta_x, \\ v_t + (u-F)v_x + vv_y + \sqrt{B}u &= -\eta_y, \\ \sigma_t + [(u-F)\sigma]_x + [v\sigma]_y &= 0, \end{aligned} \tag{2.1}$$

where $\sigma = 1 + \eta - Mh$ is the layer thickness. Recall that the three non-dimensional parameters in the above are as follows: the Froude number $F = U/c$; an inverse Burger number $B$, the square of the ratio of the obstacle scale to the Rossby radius of deformation $B = f^2L^2/c^2 = (L/L_R)^2$, and the non-dimensional obstacle height $M = h_m/H$. As discussed in Chapter 1, the set (2.1) is complemented by the conditions for mass and momentum conserving hydraulic jumps, namely

$$\begin{aligned} -V[\sigma]_-^+ + [\sigma \mathbf{u}.\mathbf{n}]_-^+ &= 0, \\ -V[\sigma \mathbf{u}.\mathbf{n}]_-^+ + [\sigma(\mathbf{u}.\mathbf{n})^2 + \frac{1}{2}\sigma^2]_-^+ &= 0, \end{aligned} \tag{2.2}$$

where $\mathbf{n}$ is a horizontal unit vector normal to the jump, $V$ is the jump velocity in the direction of $\mathbf{n}$, and $\sigma = 1 + \eta - Mh$ is the layer thickness.

The following discussion is restricted to axisymmetric obstacles. The radial height profile of the obstacle is described by a non-dimensional function $h(r)$ where $r$ is a radial coordinate in the horizontal plane, scaled with $L$, measuring distance from the centre of the obstacle. Without loss of generality, $h(0)$ is taken to be unity and the volume $\mathcal{V}$ of the obstacle is set

according to

$$\mathcal{V} = 2\pi \int_0^\infty rh(r)\, dr = \frac{\pi}{2}. \tag{2.3}$$

These restrictions on $h(r)$ are not strictly necessary to the development of the theory outlined; however, stipulating the above conditions ensures that comparisons between different obstacles presented in subsequent chapters are for obstacles of identical height and volume. Thus the effects of obstacle *shape* are highlighted.

Next, an equation describing the asymptotic regime for small obstacle height $M$ is derived, which is valid for transcritical flow when the Froude number $F$ is close to unity.

## 2.1 Transcritical flow: the equivalent aerofoil regime

The relevant scaling regime for rotating transcritical flow over an obstacle with small height $M \ll 1$ is suggested by Esler *et al.* (2007*a*) together with the derivation of the rotating Kadomtsev-Petviashvili equation (Grimshaw & Melville, 1989). Based on these previous works, the non-dimensional parameters

$$\Gamma = (F-1)M^{-2/3}, \qquad \nu = \sqrt{B}M^{-1/3}, \tag{2.4}$$

are taken to be of order unity. Following Esler *et al.* (2007*a*), the parameter $\Gamma$ will be referred to as the transcritical similarity parameter and is the relevant measure of the degree of supercriticality ($F > 1$, $\Gamma > 0$) or subcriticality ($F < 1$, $\Gamma < 0$) of the flow for a given obstacle height $M$. The similarity parameter $\nu$ is a measure of the importance of rotation in the transcritical regime, with the non-rotating limit corresponding to $\nu = 0$, and the weakly rotating limit given by $\nu \to 0$. Both positive and negative values of $\nu$ are permissible, depending on the sense of the rotation.

Introducing a small parameter $\epsilon = M^{2/3}$, and seeking solutions of (2.1) that evolve on a 'slow' time scale $\tau = \epsilon t$, the variables $(u, v)$ and $\eta$ may be expanded in powers of $\epsilon^{1/2}$ as follows

$$\begin{aligned} u &= \epsilon\left(u_0 + \epsilon^{1/2}u_1 + \epsilon u_2 + ....\right) \\ v &= \epsilon^{3/2}\left(v_0 + \epsilon^{1/2}v_1 + \epsilon v_2 + ....\right) \\ \eta &= \epsilon\left(\eta_0 + \epsilon^{1/2}\eta_1 + \epsilon\eta_2 + ....\right). \end{aligned} \tag{2.5}$$

The expansions (2.5) are used to match leading order asymptotic solutions of (2.1) in two separate regions defined by their cross-stream distance from the centre of the obstacle at $y = 0$.

### 2.1.1 *Inner region*

In the inner region, which describes flow on streamlines that pass over or near to the obstacle, the cross-stream coordinate is taken to be $y$. Denoting inner region variables with the superscript $i$ and inserting the expansions (2.5) in (2.1), at leading order it is established that

$$u_0^i = \eta_0^i(x). \tag{2.6}$$

The leading order solution is therefore described by an (as yet) undetermined $y$-independent function $\eta_0^i(x)$, except for the leading order cross-stream velocity $v_0^i$. At the next order in the expansion

$$u_1^i = \eta_1^i(x, y), \qquad v_{0y}^i = -h_x. \tag{2.7}$$

Integrating the second condition in $y$ gives

$$v_0^i(x,y) = V(x) - \int_0^y h_x(x,\hat{y})\, d\hat{y}, \tag{2.8}$$

where $V(x)$ is an undetermined function. The velocity $v_0^i$ is related to the free surface height through

$$-v_{0x}^i + \nu\eta_0^i = -\eta_{1y}^i. \tag{2.9}$$

Proceeding to higher order, it becomes clear that $\eta_0^i(x)$ will not be determined by the inner region expansion alone. Furthermore, the solution becomes invalid away from the obstacle where $|y| \sim O(\epsilon^{-1/2})$. At these distances, higher order terms in the series expansion become comparable to those at leading order. This indicates that $\eta_0^i$ must be determined by matching with an outer region solution which is valid for $|y| \sim O(\epsilon^{-1/2})$.

### 2.1.2 *Outer region*

In the outer region, the variable $Y = \epsilon^{1/2}y$ is introduced to capture the cross-stream scale on which the leading order free surface height and streamwise velocity vary in the direction perpendicular to the oncoming flow. The influence of the obstacle is experienced through the boundary condition at $Y = 0$ only. Throughout the rest of the domain in the rescaled coordinates the bottom boundary is taken to be flat. In the outer region far-field asymptotic solutions are sought, denoted by superscript $o$, of (2.1) by substituting

$$u_0 = u_0^o(x,Y,\tau) \quad \text{etc.}$$

for each term in the series expansion (2.5). At leading order

$$u_0^o = \eta_0^o(x, Y), \tag{2.10}$$

together with

$$v_{0x}^o = \eta_{0Y}^o + \nu\eta_0^o. \tag{2.11}$$

At the next order, $u_1^o$, $v_1^o$, $\eta_1^o$ are found to satisfy an identical set of equations to (2.10-2.11), and hence may be set to zero without loss of generality. To obtain an equation for $\eta_0^o$ it is necessary to proceed to $O(\epsilon^2)$, thereby introducing nonlinear terms.

From the $x$-momentum and continuity equations, the following relations between the $O(\epsilon^2)$ terms are obtained:

$$\begin{aligned} u_{2x}^o - \eta_{2x}^o &= -\nu v_0^o + \eta_{0\tau}^o - \Gamma\eta_{0x}^o + \eta_0^o\eta_{0x}^o; \\ u_{2x}^o - \eta_{2x}^o &= -v_{0Y}^o - \eta_{0\tau}^o + \Gamma\eta_{0x}^o - 2\eta_0^o\eta_{0x}^o. \end{aligned}$$

Equating the above expressions to eliminate $u_2^o$, $\eta_2^o$, and employing the relation (2.11) from leading order subsequently to eliminate terms involving $v_0^o$, the following equation is revealed

$$(2\eta_{0\tau}^o + 3\eta_0^o\eta_{0x}^o - 2\Gamma\eta_{0x}^o)_x - \nu^2\eta_0^o + \eta_{0YY}^o = 0. \tag{2.12}$$

Equation (2.12) is the (dispersionless) rotating Kadomtsev-Petviashvili (rKP) equation (Kadomtsev & Petviashvili (1970); Grimshaw & Melville (1989)), as might be anticipated for the outer region. The novel component introduced in Esler *et al.* (2007*a*) is the derivation of the appropriate boundary condition on $Y = 0$, which is obtained by matching with the inner solution as follows.

### 2.1.3 *Matching conditions - the equivalent aerofoil*

Matching between the inner and outer regions results in the following conditions

$$\begin{aligned} \eta_0^i(x) &= \lim_{Y\to 0} \eta_0^o(x,Y), \\ \lim_{y\to\pm\infty} \eta_{1y}^i(x,y) &= \lim_{Y\to 0^\pm} \eta_{0Y}^o(x,Y), \\ \lim_{y\to\pm\infty} v_0^i(x,y) &= \lim_{Y\to 0^\pm} v_0^o(x,Y). \end{aligned} \tag{2.13}$$

Using (2.8) and (2.9) the matching conditions may be replaced by the single condition

$$[\eta_{0Y}^o]_-^+ = -\int_{-\infty}^{\infty} h_{xx}(x,\hat{y})\, d\hat{y}, \tag{2.14}$$

where the square brackets denote the difference between evaluation at $Y \to 0^+$ and $Y \to 0^-$. For obstacles symmetric about $y = 0$, including the axisymmetric obstacles considered here, the boundary condition (2.14) for equation (2.12) can be replaced by a 'line-charge' forcing term on the right-hand side of (2.12) of the form

$$F(x,Y) = -2\delta(Y)K_{xx}(x), \quad \text{where } K(x) = \int_0^{\infty} h(x,\hat{y})\, d\hat{y} \tag{2.15}$$

and $\delta(Y)$ is the Dirac delta function.

The system involving (2.12) and (2.15) is symmetric in $\eta_0^o$ about $Y = 0$, and it is therefore convenient to solve the equation in the half-plane $Y \geq 0$. In order to exploit numerical methods from the field of gas dynamics, we introduce

$$\phi(x,Y) = \int_x^{\infty} \eta_0^o(\hat{x},Y)\, d\hat{x},$$

allowing (2.12) to be integrated once to give the following system, valid in

the half-plane $Y \geq 0$,

$$(-2\Gamma - 3\phi_x)\,\phi_{xx} - \nu^2\phi + \phi_{YY} = 0, \quad \text{with} \quad \phi_Y(x,0) = K_x(x) \quad \text{on} \quad Y = 0. \tag{2.16}$$

On setting $\nu = 0$, this equation may be recognised as the transonic small disturbance (TSD hereafter) equation, or Kármán-Guderley equation, for flow over a thin symmetric aerofoil with half-thickness $\epsilon K(x)$, where the aerofoil profile $K(x)$ describes the streamwise development of (half) the cross-sectional area of the topography. For rotating flows over topography, when $\nu \neq 0$, this equation will be referred to as the rotating transcritical small disturbance (rTSD hereafter) equation.

### 2.1.4 *Jump conditions for the rTSD equation*

In order to model the physical situation of breaking waves, the shallow-water equations (2.1) are regularised by including mass and momentum conserving hydraulic jumps which satisfy (2.2). To obtain the corresponding closure of the rTSD equation (2.16), it is necessary to derive the asymptotic form of the shallow-water jump conditions (2.2).

For steady flow, the jump velocity $V = 0$, so that (2.2) reduce to

$$\left[\sigma \mathbf{u}.\mathbf{n}\right]_-^+ = 0, \tag{2.17}$$

$$\left[\sigma(\mathbf{u}.\mathbf{n})^2 + \frac{1}{2}\sigma^2\right]_-^+ = 0, \tag{2.18}$$

which are complemented by the kinematic condition that the component of velocity tangential to the jump is continuous:

$$[\mathbf{u} \times \mathbf{n}] = 0. \tag{2.19}$$

In the above, as previously, $\mathbf{n}$ is a horizontal unit vector normal to the jump, $\sigma = 1+\eta-Mh$ is the layer thickness and $\mathbf{u} = (u-F, v)$ is the total velocity.

Consider a jump described by

$$\mathcal{S}(x,y) = x - s(y) = 0. \tag{2.20}$$

Then, in the outer region, the unit vector normal to the jump is given by

$$\begin{aligned} \mathbf{n} = \frac{\nabla\mathcal{S}}{|\nabla\mathcal{S}|} &= \frac{\mathbf{i} - \epsilon^{1/2}s'(Y)\mathbf{j}}{\sqrt{1+\epsilon s'(Y)^2}} \\ &\approx \left(1 - \frac{1}{2}\epsilon\tilde{s}^2 + \cdots\right)\mathbf{i} + \left(\epsilon^{\frac{1}{2}}\tilde{s} + \cdots\right)\mathbf{j} \end{aligned} \tag{2.21}$$

where $\tilde{s} = -s'(Y)$ has been introduced for notational convenience.

To obtain the jump condition for the rTSD equation, the expansions (2.5) and (2.21) may be substituted into equations (2.17-2.19), to reveal the following relations:

$$\tilde{s}\left[\eta_0^o\right]_-^+ = \left[v_0^o\right]_-^+; \tag{2.22}$$

$$\left[u_2^o - \eta_2^o + \eta_0^{o2} - \Gamma\eta_0^o + \tilde{s}v_0^o\right]_-^+ = 0; \tag{2.23}$$

$$\left[2(u_2^o - \eta_2^o) + \frac{1}{2}\eta_0^{o2} - \tilde{s}^2\eta_0^o + 2\tilde{s}v_0^o\right]_-^+ = 0. \tag{2.24}$$

Eliminating $u_2^o$, $\eta_2^o$ between (2.23), (2.24), and subsequently using (2.22) yields the single condition

$$\left[2\Gamma\eta_0^o - \frac{3}{2}\eta_0^{o2}\right]_-^+ - \tilde{s}\left[v_0^o\right]_-^+ = 0. \tag{2.25}$$

On introducing the 'solution' variable $\phi$ and employing the relation (2.11)

(with $\nu = 0$), the jump condition for the rTSD equation (2.16) is given by

$$\big[ -2\Gamma\phi_x - \frac{3}{2}\phi_x^2 \big]_-^+ - s'(Y)\big[\phi_Y\big]_-^+ = 0, \tag{2.26}$$

which corresponds to the conservation form

$$\left( -2\Gamma\phi_x - \frac{3}{2}\phi_x^2 \right)_x + \big(\phi_Y\big)_Y - \nu^2\phi = 0 \tag{2.27}$$

of the rTSD equation (see e.g. Whitham, 1974, pp31-32).

### 2.1.5 *Interpretation and Discussion*

Before proceeding to a more general discussion of the transcritical asymptotic theory, the subtleties due to the presence of rotation alluded to at the beginning of the chapter are discussed.

First note that the centreline interface displacement $\eta_0^i(x)$ and the cross-stream velocity $V(x)$ in equation (2.8) with $\nu \neq 0$ remain at this stage unknown, and must be determined from the solution to equation (2.16) itself *a posteori*. In the absence of rotation however, the problem becomes entirely symmetric about the centreline $y = 0$, so in fact it is immediate that $V = 0$ in equation (2.8) since flow cannot cross the centreline; in this case the leading order transverse velocity $v_0^o$ is seen to be antisymmetric about $Y = 0$. Thus, in the absence of rotation, solving (2.16) in the half-plane exactly recovers the solution for flow over a half-obstacle when an infinite wall is present along $y = 0$.

In the presence of rotation however, (2.11) reveals that the leading order transverse velocity $v_0^o$ is not antisymmetric about $Y = 0$ as it is in the non-

rotating problem. Explicitly, in terms of the solution variable $\phi$ we have

$$v_0^o = -\phi_Y - \nu\phi. \tag{2.28}$$

Thus it follows that, in the rotating problem, the cross-stream velocity $V(x)$ on the inner region centreline $y = 0$, determined by (2.8), will in general be non-zero. From (2.28) it is also clear that, whereas the leading order surface displacement $\eta_0^o$ is unchanged under a change in sign of rotation, the leading order velocity $v_0^o$ is reflected about $Y = 0$. As recognised by Grimshaw & Melville (1989), the implication of non-zero $V(x)$ on $y = 0$ is that, despite the superficial appearance of reflectional symmetry in surface displacement height, solving (2.16) for $\eta_0^o$ in the half-plane does not recover the solution for flow over a half-obstacle when an infinite sidewall is present along $y = 0$. The physical reason for this is that the introduction of rotation introduces a 'new' wave, a Kelvin wave, into the problem. The half-obstacle / sidewall problem will then have two quite different solutions depending on the sign of the rotation.

The transcritical asymptotic theory presented above has the advantageous effect of reducing the three-parameter ($M$, $F$, $B$) problem for flow over an obstacle of arbitrary height to a two-parameter problem ($\Gamma$, $\nu$) valid for small obstacles $M \ll 1$. Small modifications to the highly developed existing algorithms for the non-rotating TSD equation result in robust, efficient numerical methods for the rTSD equation. The addition of the rotation term to the TSD equation may also be of interest to engineers and aerodynamicists, representing the effect of a general low-wavenumber dispersion on transonic flows over aerofoils.

The drag on the obstacle, given by

$$\mathcal{D} = M \int_{-\infty}^{\infty} \int_{-\infty}^{\infty} p(x, y, h)\, h_x(x, y)\; dx\, dy,$$

with dimensional units $\rho_0 g H^2 L$, can be shown at leading order to be equal to

$$\mathcal{D} = M^{5/3} \int_{-\infty}^{\infty} \eta_0^o(x, 0) K_x(x)\; dx = M^{5/3} D(\Gamma)$$

i.e. $M^{5/3}$ times the non-dimensional drag on the equivalent aerofoil in the rTSD solution, which is denoted $D(\Gamma)$ for a fixed value of $\nu$. In the absence of rotation, by examining the equivalent-aerofoil thickness profile $K(x)$ of a given obstacle, insight from engineering studies of flow over aerofoils might be used to anticipate both the resulting flow patterns and the consequent drag exerted on the flow by an obstacle. In the presence of rotation, the rTSD equation offers a simplified setting in which to examine the effects of rotation on the drag exerted on the flow by obstacles in the transcritical regime.

A further aspect of shallow-water flow over three-dimensional obstacles that has received considerable attention in the context of non-rotating flow (Schär & Smith, 1993a; Baines, 1995, Fig. 2.30 therein) is the location of the boundaries between transcritical and supercritical flow, and transcritical and subcritical flow, as plotted on an ($M$, $F$) regime diagram (cf Chapter 1). Recall that a transcritical flow in this sense simply describes a supercritical flow containing an embedded region of subcritical flow, or a subcritical flow with an embedded region of supercritical flow. The boundaries in ($M$, $F$) parameter space described above are boundaries at which the embedded region appears or vanishes. In the transcritical limit, for fixed $\nu$, the boundaries must exist at fixed values of $\Gamma = \Gamma_- < 0$ and $\Gamma = \Gamma_+ > 0$ since the

rTSD equation (2.16) depends only on the single parameter $\Gamma$ for fixed $\nu$. Hence for small obstacle height $M$, the transcritical theory predicts that the regime boundaries occur at

$$F = 1 + \Gamma_- M^{2/3}, \quad \text{and} \quad F = 1 + \Gamma_+ M^{2/3}, \qquad (\Gamma_- < 0 < \Gamma_+), \quad (2.29)$$

for fixed $\nu$, where $\Gamma_-$ and $\Gamma_+$ are constants that must be determined from numerical solutions of (2.16) for an obstacle's equivalent aerofoil $K(x)$. The rTSD equation then, offers a simplified setting in which to investigate the effects of rotation on the location of regime boundaries in $(M, F)$ space, a topic that so far seems not to have been much discussed in the literature.

## 2.2 Supercritical Flow

Jumping ahead of ourselves briefly, in Chapter 4 it will be seen that the transcritical similarity theory described above breaks down for for $\Gamma \gtrsim 1.5$, and must be replaced by a theory more suited to the supercritical flow regime. In the present section, an asymptotic theory to describe the supercritical flow regime is derived, which is formally valid for $M \ll 1$, $F - 1 \gg M^{2/3}$ (or $\Gamma \gg 1$ in the terms of the previous section). As with transcritical flow, the asymptotic theory is obtained by matching between an inner region near the obstacle and an outer far field.

### 2.2.1 *Inner region*

For non-rotating and weakly rotating flow with $\sqrt{B} \sim M^{1/2}$, the inner region solution of (2.1) in the vicinity of the obstacle is given by non-rotating linear theory and has been discussed by Baines (1995) and Jiang & Smith (2000).

Introducing $\varepsilon = M$ to be a small parameter and expanding

$$\begin{aligned} u &= \varepsilon\left(u_0 + \varepsilon^{1/2}u_1 + \varepsilon u_2 + ....\right) \\ v &= \varepsilon\left(v_0 + \varepsilon^{1/2}v_1 + \varepsilon v_2 + ....\right) \\ \eta &= \varepsilon\left(\eta_0 + \varepsilon^{1/2}\eta_1 + \varepsilon\eta_2 + ....\right), \end{aligned} \tag{2.30}$$

the leading order solution is found to satisfy

$$(F^2 - 1)\eta^l_{0xx} - \eta^l_{0yy} = F^2 h_{xx}, \tag{2.31}$$

where the superscript $l$ has been introduced to denote the inner region solution for the supercritical problem. Using Green's function techniques, Jiang and Smith obtained the general solution (adapted here for right-to-left flow)

$$\eta^l_0(x,y) = -\frac{F^2}{2\gamma}\left\{\int_{-\infty}^{y} h_x(x+\gamma(y-\tilde{y}),\tilde{y})\,d\tilde{y} + \int_{y}^{\infty} h_x(x-\gamma(y-\tilde{y}),\tilde{y})\,d\tilde{y}\right\}, \tag{2.32}$$

where $\gamma = \sqrt{F^2-1}$. It is useful at this stage to introduce a rotated coordinate system $(\mathcal{X}_\pm, \mathcal{Y}_\pm) = (x \pm \gamma y, y \mp \gamma x)/F$ for the regions $y > 0$ and $y < 0$ respectively. In $y > 0$, the new coordinate system is rotated anti-clockwise through an angle $\tan^{-1}\gamma$, so that $\mathcal{X}_+$ measures distance perpendicular to the Mach lines, $x + \gamma y =$ constant, and $\mathcal{Y}_+$ the distance along these Mach lines. A similar, but clockwise, rotation occurs for the coordinates in $y < 0$. In terms of these new coordinates, Johnson & Vilenski (2004) noted that, provided the obstacle height decays sufficiently rapidly at large distances, then as $y \to \pm\infty$ the solution (2.32) converges to

$$\lim_{y\to\pm\infty}\eta^l_0(x,y) = -\frac{F^2}{2\gamma^2}\int_{-\infty}^{\infty}\begin{cases} h_x\left(\xi, \frac{(F\mathcal{X}_+ - \xi)}{\gamma}\right)d\xi & y \to +\infty \\ h_x\left(\xi, \frac{(\xi - F\mathcal{X}_-)}{\gamma}\right)d\xi & y \to -\infty \end{cases}. \tag{2.33}$$

Equation (2.33) shows that the linear solution away from the obstacle tends to a function of the single coordinate $\mathcal{X}_{\pm}$, with sign taken according to whether we are looking at $y \to \pm\infty$. For definiteness, the upper half-plane $y > 0$ will be considered hereafter (the lower half-plane solution being identical), and the subscript + will be dropped.

For the particular case of an axisymmetric obstacle $h = h(r)$, a change of variables (discussed in Chapter 9) in the expression (2.33) results in

$$\eta_0^l(\mathcal{X}) \to -\frac{1}{\gamma}\mathcal{X}G(\mathcal{X}) \quad \text{where} \quad G(\mathcal{X}) = \int_{|\mathcal{X}|}^{\infty} \frac{h'(r)}{\sqrt{r^2 - \mathcal{X}^2}}\, dr. \tag{2.34}$$

### 2.2.2 *Outer region*

Supercritical flows are linear only in the vicinity of the obstacle, as can be seen by seeking 'far-field' steady solutions of (2.1). In order to determine the behaviour of the solution further from the obstacle, 'stretched' variables $(\mathcal{X}_*, \mathcal{Y}_*) = \varepsilon(\mathcal{X}, \mathcal{Y})$ can be introduced. Expanding (2.1) in powers of $\varepsilon$ according to (2.30), derivatives in the $\mathcal{X}$ and $\mathcal{Y}$ directions are found to appear at different orders, and it is thereby natural to seek solutions of the form $\eta = \eta^f(\mathcal{X}, \mathcal{Y}_*)$ etc. The superscript $f$ denotes the supercritical far-field solutions. To ensure that rotation enters the problem at the correct order, it is taken that the variable

$$\hat{\nu} = (B/M)^{1/2} \tag{2.35}$$

is of order unity. At leading order, (2.1) is satisfied by

$$u_0^f = \frac{\eta_0^f}{F}, \quad v_0^f = \frac{\gamma\eta_0^f}{F}.$$

At the next order, the relations

$$u^f_{1\mathcal{X}} + \hat{\nu} v^f_0 = \frac{\eta^f_{1\mathcal{X}}}{F}, \quad v^f_{1\mathcal{X}} - \hat{\nu} u^f_0 = \frac{\gamma \eta^f_{1\mathcal{X}}}{F} \tag{2.36}$$

are revealed. In the absence of rotation ($\hat{\nu} = 0$), the above relations are identical to those found at leading order and hence without loss of generality may be set to zero. Equivalently, as in Esler *et al.* (2007*a*), the expansions (2.30) may be taken in Integer powers of $\varepsilon$. In the presence of rotation however, equations (2.36) are required in order to eliminate $u^f_1$ and $v^f_1$ from the next order of equations.

To find an equation for $\eta^f_0$, it is necessary to proceed to order $O(\varepsilon^2)$, thereby introducing nonlinear terms, where it can be shown from (2.1) that

$$\frac{1}{F}\eta^f_{2\mathcal{X}} - u^f_{2\mathcal{X}} = -\frac{1}{F}\eta^f_0 \eta^f_{0\mathcal{X}} + \hat{\nu} v^f_1, \tag{2.37}$$

$$\frac{\gamma}{F}\eta^f_{2\mathcal{X}} - v^f_{2\mathcal{X}} = -F\eta^f_{0\mathcal{Y}_*} - \frac{\gamma}{F}\eta^f_0 \eta^f_{0\mathcal{X}} - \hat{\nu} u^f_1, \tag{2.38}$$

$$\frac{1}{F}u^f_{2\mathcal{X}} - \eta^f_{2\mathcal{X}} + \frac{\gamma}{F}v^f_{2\mathcal{X}} = -\gamma\eta^f_{0\mathcal{Y}_*} - 2\eta^f_0 \eta^f_{0\mathcal{X}}. \tag{2.39}$$

Taking (2.37)$+\gamma$(2.38)$+F$(2.39) serves to eliminate $\eta^f_2, u^f_2, v^f_2$; subsequently relations (2.36) may be used to eliminate $u^f_1$ and $v^f_1$ from the resulting equation, so that the far-field equation for the leading order free surface displacement $\eta^f_0$ is obtained,

$$(2\gamma\eta^f_{0\mathcal{Y}_*} + 3\eta^f_0 \eta^f_{0\mathcal{X}})_{\mathcal{X}} - \hat{\nu}^2 \eta^f_0 = 0. \tag{2.40}$$

Equation (2.40) is the Ostrovsky-Hunter equation (Ostrovsky (1978), Hunter (1990)), with the 'stretched' space variable $\mathcal{Y}_*$ assuming the role of the time-like variable.

The 'initial' condition for (2.40) is determined by the matching condition

with the inner solution (2.32),

$$\lim_{\mathcal{Y}_* \to 0^+} \eta_0^f = \lim_{y \to +\infty} \eta_0^l,$$

or, from (2.33),

$$\eta_0^f(\mathcal{X}, 0) = -\frac{1}{\gamma}\mathcal{X}G(\mathcal{X}), \tag{2.41}$$

with $G(\mathcal{X})$ defined by (2.34). Vilenski & Johnson (2004) have previously derived the dispersive analogue of equation (2.40) (the Ostrovsky equation) for the case of supercritical flow over an elongated ridge in the weakly dispersive, weakly rotating, limit where the flow is described by the rKP equation. Here, it has been shown that the solution applies equally to the more general problem of supercritical flow over a small isolated obstacle ($M \ll 1$) at all Froude numbers satisfying $F > 1$, $F - 1 \gg M^{2/3}$.

### 2.2.3 *Jump conditions for the Ostrovsky-Hunter equation*

As in the case of transcritical flow, it is necessary to obtain the appropriate form of the jump conditions for the Ostrovsky-Hunter equation (2.40). As before, consider a jump described by (2.20). Then, in the outer region, the unit normal to the jump is given by

$$\mathbf{n} \approx \frac{1}{F}\left(1 - \varepsilon\gamma\tilde{s} - \frac{\varepsilon^2\tilde{s}^2}{2} + \cdots\right)\mathbf{i} + \frac{1}{F}\left(\gamma + \varepsilon\tilde{s} - \frac{\gamma\varepsilon^2\tilde{s}^2}{2}\right)\mathbf{j}, \tag{2.42}$$

where $\tilde{s} = -s'(\mathcal{Y}_*)$. Substituting the expansions (2.30) and (2.42) into equations (2.17-2.19) reveals the following relations:

$$\begin{aligned}
\frac{1}{F}\left[\gamma u_2^f - v_2^f\right]_-^+ + \tilde{s}[\eta_0^f]_-^+ &= 0; \\
\frac{1}{F}\left[u_2^f + \gamma v_2^f - F\eta_2^f\right]_-^+ + [\eta_0^{f2} + \gamma\tilde{s}\eta_0^f]_-^+ &= 0; \\
\frac{2}{F}\left[u_2^f + \gamma v_2^f - F\eta_2^f\right]_-^+ + [\frac{1}{2}\eta_0^{f2}]_-^+ &= 0.
\end{aligned}$$

Eliminating $\eta_2^f$, $v_2^f$, $u_2^f$ yields the jump condition

$$-2\gamma s'(\mathcal{Y}_*)[\eta_0^f]_-^+ + [\frac{3}{2}\eta_0^{f2}]_-^+ = 0,$$

corresponding to the conservation form of the Ostrovsky-Hunter equation (2.40)

$$2\gamma\eta_{0\mathcal{Y}_*}^f + \left(\frac{3}{2}\eta_0^{f2}\right)_{\mathcal{X}} = \hat{\nu}^2 \int^{\mathcal{X}} \eta_0^f(\hat{\mathcal{X}}, \mathcal{Y}_*) d\hat{\mathcal{X}}. \tag{2.43}$$

## 2.3 Discussion

Asymptotic theories, valid for small obstacle height $M$, have been derived to describe the transcritical and supercritical regimes of rotating shallow-water flow over topography.

In Chapter 4, both are discussed in the absence of rotation. Two separate numerical models are employed to investigate the range of validity of the asymptotic theories by comparison with nonlinear behaviour at finite obstacle height $M$.

Chapter 6 discusses transcritical, rotating flow governed by the rTSD equation (2.16), whilst Chapter 7 is devoted to supercritical, rotating flow governed by the Ostrovsky-Hunter equation (2.40).

# Chapter 3

# Numerical solution of the rTSD equation

## 3.1 Introduction

The transcritical theory of the previous chapter led to the rTSD equation, which in conservation form reads

$$\left( -2\Gamma\phi_x - \frac{3}{2}\phi_x^2 \right)_x + \left(\phi_Y\right)_Y - \nu^2\phi = 0, \tag{3.1}$$

together with the 'equivalent aerofoil' boundary condition

$$\phi_Y(x,0) = K_x(x) \quad \text{on} \quad Y = 0. \tag{3.2}$$

Here, the numerical procedure implemented to solve (3.1) is detailed. The techniques discussed were developed for the non-rotating TSD equation; since the introduction of rotation introduces only a minor change to algorithms for the TSD equation, the extra terms required are included without further comment. Before proceeding, it should be noted that the algorithms

described here produce flow over an aerofoil from left to right - the opposite direction to that adopted elsewhere in this thesis. Since the flow field is symmetric about $Y = 0$, the contour plots throughout this thesis may be produced simply by switching the sense of the streamwise ordinate $x$.

Numerical solutions of the TSD equation were first obtained in a landmark paper by Murman & Cole (1971). By introducing the concept of 'type-dependent differencing', Murman and Cole provided major impetus to the field of computational aerodynamics - and indeed to computational fluid dynamics (CFD) as a whole. Rapid progress followed throughout the remainder of the '70's and into the '80's, attention focusing not only on the TSD equation but also the full potential, Euler and Navier-Stokes equations. Writing of the full potential equation, Hirsch (1988) notes that "presently [the] problem can be considered as solved, and three-dimensional potential codes are operational tools in industry and applied systematically in preliminary design stages [of aircraft]".

This chapter briefly considers some of the work that may be considered as signal in the development of the modern field of CFD. For a comprehensive account, the interested reader is recommended to consult the review paper by Holst (2000).

### 3.1.1 *Historical Perspective*

The difficulty in constructing finite difference methods for the solution of the TSD equation stems from the fact that the equation is of mixed type. For regions in which the local flow speed remains subcritical, the governing equation is elliptic. Here, relaxation schemes similar to those used for Laplace's equation are effective. When the local flow speed becomes supercritical however, the governing equation is of hyperbolic type; in these

regions, a typical elliptic differencing scheme will violate the physically correct domain of dependence of the flow. The result is that an elliptic type scheme will diverge even if there is only one supercritical point in the flow domain. Thus it is necessary to introduce the concept of type-dependent differencing: the computational finite difference stencil must change in accordance with the flow being locally subcritical or supercritical. Since the nature of the flow is not known *a priori*, tests must be devised to decide whether a given point is elliptic, hyperbolic, parabolic or a shock point.

Perhaps the best way to understand the issues involved - and the thought processes through which they were resolved - is to quote the historical account reported by Hall (1981).

> "Earll Murman had been working for a year or so at Boeing on finite difference methods for integrating the compressible Navier-Stokes equations when, in 1968, Julian Cole arrived on a one-year visit. Cole writes: 'it was Goldberg who suggested that transonic flow was a timely subject. I decided on a joint analytical and numerical approach and he said that Earll and I could work together (since my programming was feeble)'. Our approach was founded on several bits of previous experience.
>
> i) The fact that Lax-Wendroff could give the correct shock-jumps (had) made a deep impression and I (had) learned about artificial viscosity, diffusion and dispersion in difference schemes. Yosh (Yoshihara) was convinced that steady flows could not be calculated directly but I decided while at Boeing to try using a conservative scheme (*á la* Lax) in order to catch shocks.
>
> ii) I was aware of Howard Emmon's very early 'successful' relax-

ation calculations of mixed flows in nozzles and decided to try a relaxation method.

iii) I had studied the fundamentals of small disturbance theory ..... rather extensively earlier. I knew it had all the essential difficulties and could even be a good approximation. It was clear that it would make the numerical work easier.

Murman writes that Cole

..... spent several months systematically deriving a small disturbance theory from the complete Euler equations. It laid the theoretical groundwork for our later developments.

In January 1969 we started some computations solving Laplace equations and then the TSP [1] using centred differences. By April we found that we could not get the calculations to converge for supercritical flow. It was in the following several months that we hit upon the idea of switching and type dependent schemes. I believe that the idea grew out of an afternoon brainstorming session when we were discussing finite difference methods for elliptic and hyperbolic problems and how the two were basically different. Julian, I believe, threw out a comment that maybe we could combine them somehow.

I have often reflected back on that event to realise how important it is in research to be open-minded, imaginative, and receptive to unconventional suggestions.

Cole adds:

I knew enough numerical analysis to know that hyperbolic schemes

[1]Transonic potential - referred to as the TSD equation in the current work

> were unstable if the domain of dependence was incorrect. Even though the time-like direction was unclear I thought that perhaps we should have only downstream influence. So we decided to switch schemes: explicit hyperbolic was ruled out by the CFL condition near the sonic line.
>
> Murman continues
>
> My experience the previous year on the Navier-Stokes computations allowed us to make rapid progress. It was clear that we should maintain conservation form to calculate shock waves. Unfortunately we missed the essential point of the shock point operator. For stability reasons, the hyperbolic operator had to be implicit. This naturally led to a line relaxation algorithm so that the method would work in the limits of both purely supersonic and purely subsonic flow. In July we programmed up the first code and it worked almost immediately."

Thus the type-dependent differencing concept was born.

## 3.2 Engquist and Osher's Scheme

Although Murman and Cole's type dependent differencing provided a major breakthrough in the computation of transcritical flows, further refinements were necessary consistently to obtain physically meaningful solutions. Jameson (1986) demonstrated that the Murman-Cole scheme could permit entropy-violating shocks as solutions; additionally, in Ballhaus & Goorjian (1977) and Krupp & Cole (1976) instabilities were reported even when schemes should be stable according to linear analysis. Engquist & Osher (1980) introduce modifications to the original scheme of Murman and Cole

which guarantee that non-physical shocks cannot occur. Further, they are able to prove nonlinear stability for the resulting scheme. Their modified scheme is described below, and is employed to produce solutions throughout this thesis.

Let $\tilde{u} = \phi_x$ and $\tilde{v} = \phi_Y$, and define the convex function

$$f(\tilde{u}) = 2\Gamma\tilde{u} + \frac{3}{2}\tilde{u}^2, \tag{3.3}$$

so that the rTSD equation (3.1) in conservation form may be written

$$-\big(f(\tilde{u})\big)_x + \tilde{v}_Y - \nu^2\phi = 0. \tag{3.4}$$

Introduce the sonic speed $\bar{u} = -\frac{2}{3}\Gamma$ so that (3.4) is hyperbolic for $\tilde{u} > \bar{u}$ and elliptic for $\tilde{u} < \bar{u}$. Here and in the following, for any grid function $\psi_{i,j}$, we define the forward ($\delta_x^+$) and backward ($\delta_x^-$) first derivative operators by

$$\delta_x^+\psi_{i,j} = \frac{\psi_{i+1,j} - \psi_{i,j}}{\Delta x}, \qquad \delta_x^-\psi_{i,j} = \frac{\psi_{i,j} - \psi_{i-1,j}}{\Delta x},$$

with $\delta_Y^\pm\psi_{i,j}$ defined analogously. Then taking backward differences

$$\tilde{u}_{i,j} = \delta_x^-\phi_{i,j}, \quad \tilde{v}_{i,j} = \delta_Y^-\phi_{i,j}$$

the difference scheme of Engquist and Osher may be written

$$-\delta_x^- f(\max(\tilde{u}_{i,j}, \bar{u})) - \delta_x^+ f(\min(\tilde{u}_{i,j}, \bar{u})) + \delta_Y^+\tilde{v}_{i,j} - \nu^2\phi_{i,j} = 0. \tag{3.5}$$

This scheme is is in fact identical to that of Murman and Cole in regions of purely subcritical or supercritical flow, the only differences occurring at shock and critical points. The discretisation is of second order accuracy in

$\Delta x$ in regions of subcritical flow, reducing to first order when the flow is supercritical.

The proof that the above discretisation prevents the occurrence of non-physical shock solutions and satisfies nonlinear stability criteria is beyond the scope of the current work, and the interested reader is referred to the original paper (Engquist & Osher, 1980).

## 3.3 Solution of the difference equations

The success of the Murman-Cole scheme lay not only in the formulation of a type-dependent differencing scheme, but additionally in the use of a generalisation of the line relaxation method of elliptic problems to solve the nonlinear difference equations - successive line over relaxation ('SLOR'). The details of the SLOR scheme are discussed by Jameson (1986). Ballhaus *et al.* (1978) demonstrate that it is possible to improve on the convergence rate of the SLOR algorithm by using implicit approximate factorisation ('AF') algorithms. Indeed, for the second of the algorithms they present, 'AF-2', convergence is of the order of ten times faster than with SLOR for certain cases. Their study, however, is based upon the Murman-Cole switching scheme. Goorjian & Van Buskirk (1981) present an implicit approximate factorisation algorithm, 'MAF' (monotonic approximate factorisation), using the Engquist and Osher switching described above. The increased stability of the Engquist and Osher scheme leads to a convergence rate that is approximately 35% faster than the corresponding AF-2 scheme. The MAF algorithm is implemented to produce solutions throughout this thesis.

### 3.3.1 *The MAF algorithm*

Numerical schemes solving the TSD equation are often implemented on non-uniform grids. This stems from the fact that aerodynamiscists are most interested in evaluating aerodynamic loads along the surface of an aerofoil, so that solutions need be well resolved only in the immediate vicinity of the aerofoil. In the current work however, we would like solutions to be equally well resolved throughout the computational domain, particularly solutions to the rTSD equation where interesting flow features often extend some distance downstream and to the sides of the aerofoil. Therefore, solutions are obtained on a uniform rectangular grid, and the algorithm described is particular to the case of uniform grids.

It is standard practice to present iterative schemes for solving nonlinear difference equations in 'residual-correction' form. In the $(n+1)$th cycle of the iterative procedure the residual $R_{i,j}$ at grid point $(i,j)$ is evaluated by inserting the values $\phi_{i,j}^{(n)}$ of the $n$th cycle into the difference equations. Then the correction at level $n+1$ is given by $C_{i,j} = \phi_{i,j}^{(n+1)} - \phi_{i,j}^{(n)}$. $C_{i,j}$ is calculated by solving an equation of the form

$$NC_{i,j} = -\sigma R_{i,j}, \tag{3.6}$$

where $N$ is a discrete operator acting on $C_{i,j}$ and $\sigma$ is a scaling factor, used to control both the convergence rate and the stability of the iterative scheme. The operator $N$ represents a simplified form of the full nonlinear operator; in the SLOR method for example, $N$ is linear and of lower triangular form so that the elements of $C_{i,j}$ may be determined sequentially. The underlying idea of the AF type schemes is to construct $N$ as a product of two or more

factors

$$N = N_1 N_2 ... N_k,$$

each of which is of a form in which the algebraic equations may be solved easily.

The MAF algorithm of Goorjian & Van Buskirk (1981), which employs the switching (3.5) due to Engquist & Osher (1980), in residual-correction form may be written (letting $\sigma = \alpha\omega$)

$$NC_{i,j} \equiv (\alpha - (A_{i,j}\bar{D}_x) - \nu^2)(\delta_{YY} - \alpha\delta_x^-)C_{i,j} = -\alpha\omega R_{i,j},$$

and is implemented via the following two-step procedure:

Step 1:

$$(\alpha - (A_{i,j}\bar{D}_x) - \nu^2)f_{i,j} = -\alpha\omega R_{i,j}$$

Step 2:

$$(\delta_{YY} - \alpha\delta_x^-)C_{i,j} = f_{i,j}.$$

Each step results in a tridiagonal matrix equation, which can easily be solved using Gaussian elimination. The terms appearing in the above are defined

as follows:

$$\begin{aligned}
R_{i,j} &= ((A_{i,j}\bar{D}_x)\delta_x^- + \delta_{YY} - \nu^2)\phi_{i,j}^{(n)};\\
A_{i,j}\bar{D}_x &= \breve{A}_{i,j}\delta_x^+ + \hat{A}_{i,j}\delta_x^-;\\
\breve{A}_{i,j} &= -2\Gamma - \frac{3}{2}(\breve{u}_{i+1,j} + \breve{u}_{i,j});\\
\hat{A}_{i,j} &= -2\Gamma - \frac{3}{2}(\hat{u}_{i,j} + \hat{u}_{i-1,j});\\
\breve{u}_{i,j} &= \min(\bar{u}, \tilde{u}_{i,j});\\
\hat{u}_{i,j} &= \max(\bar{u}, \tilde{u}_{i,j});\\
\bar{u} &= -\frac{2}{3}\Gamma;\\
\tilde{u}_{i,j} &= \delta_x^- \phi_{i,j}^n.
\end{aligned}$$

$\delta_{YY}$ is the second centred difference operator in the $Y$ direction, which for a grid function $\psi_{i,j}$ is defined as

$$\delta_{YY}\psi_{i,j} = \frac{\psi_{i,j+1} - 2\psi_{i,j} + \psi_{i,j-1}}{(\Delta Y)^2}.$$

The scaling factor $\sigma$ in equation (3.6) naturally splits into two components, $\omega$ and $\alpha$, both of which may be 'tuned' to accelerate the convergence of the scheme.

### 3.3.2 *Multigrid Acceleration*

The multigrid technique was originally developed for the numerical solution of elliptic equations, but has subsequently proved effective for a wide range of problems. Jameson (1979) successfully applied the technique to the computation of transcritical flows, noticing significant improvements in the convergence rate compared to the standard SLOR and AF type schemes. The majority of relaxation schemes, such as SLOR or AF, prove extremely

efficient in damping high-frequency errors but are less efficient in damping low-frequency errors. The idea behind the multigrid method is to solve the problem on a sequence of grids ranging from fine to coarse. Since the high-frequency error on the coarsest grid is actually the lowest-frequency error existing in the problem, the low-frequency error may be efficiently dealt with on the coarsest grid with the result that very little computational effort is expended in removing it from the solution. The result is a tremendous improvement in the convergence rate compared with solution on a single fine grid.

Implementation of Brandt's Full Approximate Storage Algorithm (FAS) (Brandt, 1977) multigrid scheme is now described, following the presentation in Press *et al.* (2001).

The rTSD equation (3.1) is written symbolically in the form

$$\mathcal{L}(\phi) = 0. \tag{3.7}$$

Suppose that (3.7) is suitably discretised relative to some fine grid with $\Delta x = \Delta Y = h$, so that the exact (discrete) solution $\phi_h$ satisfies

$$\mathcal{L}_h(\phi_h) = 0. \tag{3.8}$$

In the course of the multigrid algorithm, equations of the form (3.8) will be generated with a non-zero right-hand side (c.f. equation (3.10), overleaf); we denote this right-hand side by $f_h$ so that we allow

$$\mathcal{L}_h(\phi_h) = f_h. \tag{3.9}$$

Denote by $\tilde{\phi}_h$ the approximate solution to equation (3.9). First, a few steps

of the MAF algorithm are applied on this grid, with the effect of smoothing high-frequency errors. Denote the improved approximation to equation (3.9) by $\bar{\phi}_h$. We now seek to smooth lower-frequency errors by applying further steps of the MAF algorithm on a coarser grid with spacing $H > h$. We seek a correction, $v_h$, which solves

$$\mathcal{L}(\bar{\phi}_h + v_h) = f_h,$$

so that

$$\mathcal{L}(\bar{\phi}_h + v_h) - \mathcal{L}_h(\bar{\phi}_h) = -R_h,$$

where $R_h$ is the residual on the $h$-grid. The left-hand side is now transferred to the coarser $H$-grid, to give

$$\mathcal{L}_H(\phi_H) - \mathcal{L}_H(\mathcal{R}\bar{\phi}_h) = -\mathcal{R}R_h.$$

Here, $\mathcal{R}$ denotes the restriction operator, which is used to restrict a given grid function from a given grid to the next coarser grid. A further few iterations of the MAF algorithm are used to solve

$$\mathcal{L}_H(\phi_H) = \mathcal{L}_H(\mathcal{R}\bar{\phi}_h) - \mathcal{R}R_h \tag{3.10}$$

on the coarse grid, with the effect of damping low-frequency errors to the initial approximation $\bar{\phi}_h$. Denoting by $\bar{\phi}_H$ the resulting approximate solution to (3.10), the computed coarse grid correction is given by

$$v_H = \bar{\phi}_H - \mathcal{R}\bar{\phi}_h.$$

The fine grid solution is now updated by the prolongation of the coarse grid

correction to the fine grid to give

$$\bar{\phi}_h^{new} = \bar{\phi}_h + \mathcal{P}(\bar{\phi}_H - \mathcal{R}\tilde{\phi}_h),$$

where $\mathcal{P}$ is the prolongation operator, which interpolates from the $H$ grid to the $h$ grid. Finally $\tilde{\phi}^{new}$ is computed by applying a further few iterations of the MAF algorithm to $\bar{\phi}_h^{new}$.

As discussed by Press *et al.* (2001), several choices are possible for the restriction $\mathcal{R}$ and prolongation $\mathcal{P}$ operators. Here, simple bilinear interpolation for $\mathcal{P}$ and 'half-weighted' restriction $\mathcal{R}$ have proved effective.

Though the above describes iteration between two grids, the process may be extended with corrections being sought on progressively coarser grids, so that ultimately as few as two grid points in each direction span the computational domain.

The question remains as to how many iterations of the MAF algorithm should be performed on a given grid before proceeding to the next. Brandt (1977) employed a recursive approach, with the decision to proceed to the next grid, be it coarser or finer, based on the rate at which the residual is being reduced on the current grid. Here a simple fixed strategy, similar to that advocated by Jameson (1979) has proved effective. Each cycle begins on the finest grid; five iterations of the MAF algorithm are then applied on each grid until the coarsest grid is reached. Then the MAF algorithm is performed five times on each grid going back up to the second finest, the cycle terminating with the interpolation of the correction from the second finest grid to the finest. A complete cycle of this form is usually referred to as a 'V-cycle' (see, e.g. Press *et al.*, 2001).

## 3.4 Boundary Conditions and Numerical Implementation

The boundary of the computational domain must be truncated at some finite distance from the aerofoil, and far-field boundary conditions must be supplied which are consistent with the problem. The boundary conditions differ according to whether the oncoming flow is subcritical or supercritical.

In the case of subcritical oncoming flow, disturbances from the aerofoil potentially reach all parts of the flow, and the appropriate boundary conditions are calculated via an asymptotic analysis of the rTSD equation (3.1) at large distances from the aerofoil. In the absence of rotation, the solution decays as $(1/r)$, and the far-field solution may be approximated by (see, e.g. Cole & Cook, 1986)

$$\phi_{ff} \sim \left(\frac{\mathcal{D}}{2\pi\sqrt{-2\Gamma}}\right)\left(\frac{x - x_m}{(x - x_m)^2 - 2\Gamma Y^2}\right),$$

where $x_m$ denotes the midpoint of the aerofoil, and the doublet strength, $\mathcal{D}$, is given by

$$\mathcal{D} = 2\int_0^c K(x)dx + \frac{3}{2}\int\int \tilde{u}^2(x,Y)dxdY.$$

$K(x)$ describes the shape of the aerofoil, of chord $c$. The second term represents the effects of nonlinearity in the far field and must be updated based on the developing solution. If $\mathcal{D}$ is updated too frequently during the course of the solution, convergence may be difficult to achieve. Here, updating the doublet strength $\mathcal{D}$ at the end of each multigrid V-cycle has proved effective.

In the presence of rotation, the far-field solution decays exponentially

with distance from the aerofoil, so that it is sufficient to set $\phi = 0$ on (suitably distant) lateral boundaries.

For supercritical oncoming flows, no disturbance is felt sufficiently far ahead of the aerofoil, so that we may set $\phi = 0$ on the upstream boundary. On the upper and downstream boundaries, outflow conditions are implemented.

*Aerofoil boundary condition*

The aerofoil boundary condition (3.2) is introduced to the discretisation through the second $Y$ derivative of $\phi$ at points $i,j = 1$ on the aerofoil surface along the $x$ axis. Introducing the fictive point $j = 0$, symmetric of $j = 1$ about the $x$-axis, gives

$$\delta_{YY}\phi_{i,1} = \frac{\phi_{i,2} - 2\phi_{i,1} + \phi_{i,0}}{(\Delta Y)^2}.$$

The value of $\phi_{i,0}$ is recovered by expressing the aerofoil boundary condition as a centred difference

$$\tilde{v}_{i,1} = \frac{\phi_{i,2} - \phi_{i,0}}{2\Delta Y} = K'(x_i) = K'_i$$

so that the second $Y$ derivative becomes

$$\delta_{YY}\phi_{i,1} = \frac{2(\phi_{i,2} - \phi_{i,1} - \Delta Y K'_i)}{(\Delta Y)^2}.$$

## 3.5 Examples

Many example flow patterns for both TSD and rTSD solutions can be found throughout the remainder of this work, so it is unnecessary to present them

here.

In lieu of example flow fields, Figure 3.1 takes the normalised pressure coefficient $C_p$ ($\propto -\phi_x$) along the surface of the parabolic arc aerofoil

$$K(x) = 2(x - x^2) \qquad 0 < x < 1, \tag{3.11}$$

derived from solutions to the TSD equation (3.1) with spatial resolution $\Delta x = \Delta Y = 0.01$, and compares it with both experimental results and approximate linear theories.

In the upper panel, for which $\Gamma = -1.632$, the flow is purely subcritical and thus we expect the flow field to be symmetric. Examining the TSD solution (solid curve), we see that the computed pressure coefficient does indeed exhibit a high degree of symmetry about the aerofoil mid-point $x = 0.5$. The dashed curve derives from an approximate linear theory due to Spreiter *et al.* (1958), whilst the stars indicate the results of wind-tunnel experiments performed by Knechtel (1959). The agreement between the linear theory, experimental results and TSD solution is close.

In the lower panel, for which $\Gamma = 0.642$, the flow is transcritical. Ahead of the aerofoil stands a bow jump, through which the flow transitions to subcritical. Over the aerofoil the flow accelerates smoothly to supercritical, the normalised pressure coefficient passing through its critical value ($C_{p_{cr}} \approx 0.164$, dotted line in the figure). At the trailing edge of the aerofoil is a supercritical leap (visible in the figure). The dashed line derives from an approximate linear theory, in this case from Spreiter & Alksne (1958), and the stars indicate the results of further wind-tunnel experiments by Knechtel (1959). In this case the TSD solution compares well with the approximate linear solution, but consistently over predicts the experimentally determined

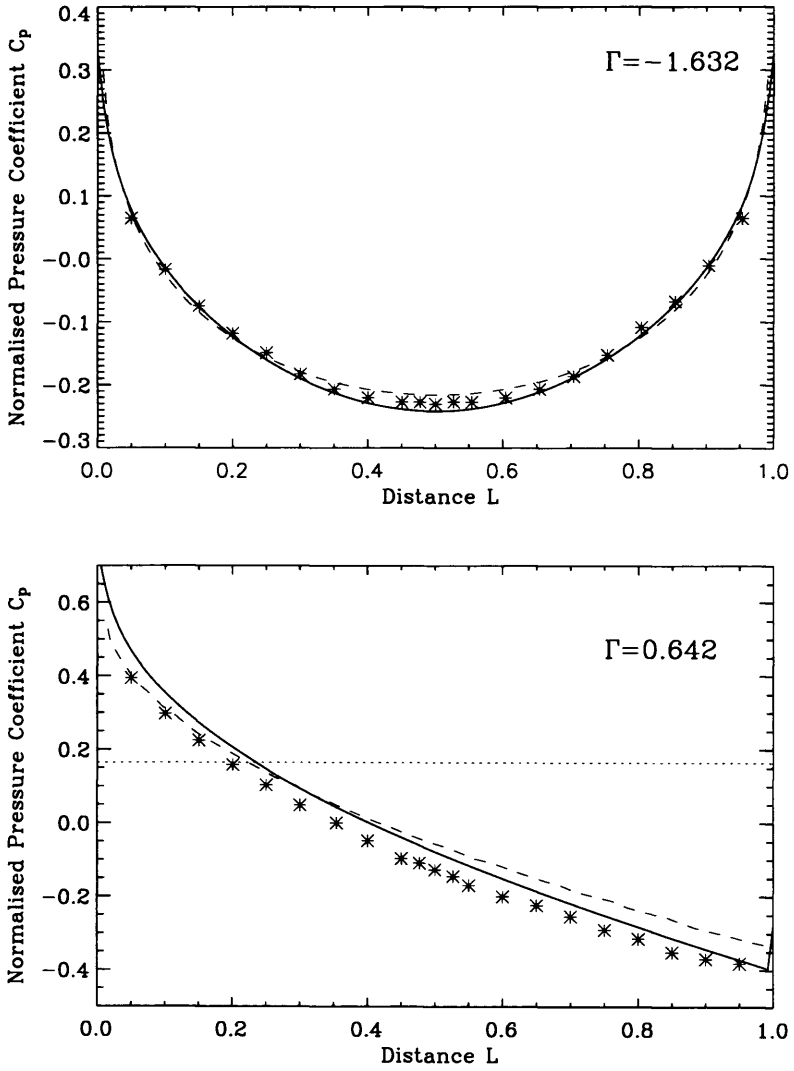


Figure 3.1: Normalised pressure coefficients for flow over the parabolic arc aerofoil (3.11). Solid curves indicate the results of TSD computations, dashed lines derive from approximate linear theories and stars from wind-tunnel experiments (see text). The dotted line in the lower panel indicates the critical pressure coefficient $C_{p_{cr}} \approx 0.164$.

pressure coefficients.

Figure 3.2 demonstrates the enhancement in convergence rate obtained by employing multigrid acceleration. Flow over the equivalent aerofoil corresponding to the 'Witch of Agnesi' obstacle introduced in the next chapter was computed for subcritical oncoming flow (transcritical similarity parameter $\Gamma = -0.6$) on a 513x513 grid (resolution $\Delta x = \Delta Y \approx 0.04$) using the MAF algorithm on a single fine grid. The computation was then repeated, using multigrid acceleration on a sequence of nine grids. Figure 3.2 plots the logarithm of the maximum residual in the computational domain against the number of 'work units' - the number of iterations on the fine grid - performed. The multigrid acceleration is clearly effective.

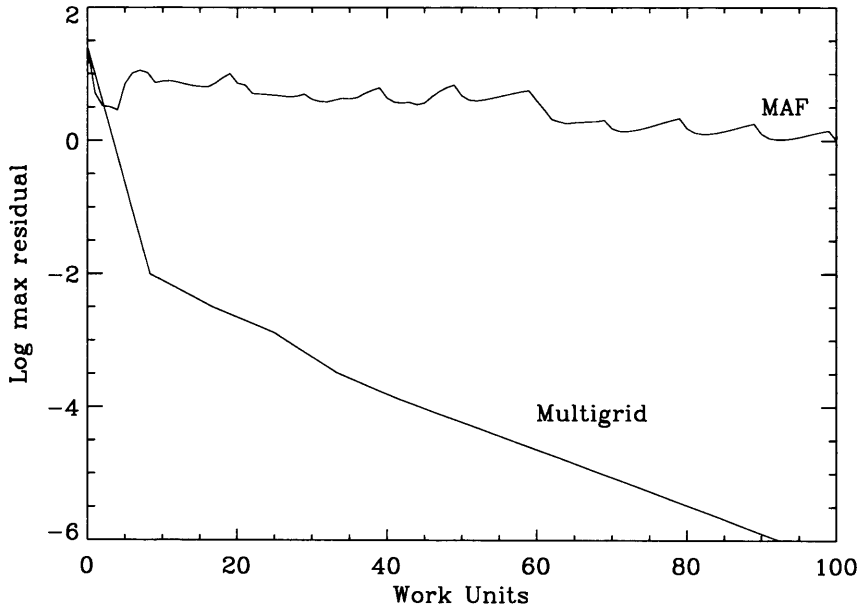


Figure 3.2: Logarithm of the maximum residual versus work units (iterations on the fine grid) for the MAF algorithm with and without multigrid acceleration, see text.

# Chapter 4

# Non-rotating shallow-water flow over topography

In Chapter 2, asymptotic theories were introduced to describe transcritical and supercritical flows in the limit of small obstacle height $M$. In this chapter, two separate numerical models are used to investigate the range of validity of the asymptotic theories by comparison with nonlinear behaviour at finite obstacle height $M$. Much of the work presented here appears in Esler *et al.* (2007*a*).

The numerical model employed to solve the TSD equation ((2.16) with $\nu = 0$) has been described in detail in the previous chapter. For the shallow-water equations (1.15), the model chosen is the CLAWPACK finite volume code (Conservation LAWs PACKage, LeVeque (2002)), which is a generic solver for hyperbolic systems of equations. The advantage of the finite volume technique is that, once the shallow-water equations have been written in conservation form, the speed of propagation of jump discontinuities satisfying (1.17) & (1.18) can be accurately captured. Solving the shallow-water equations using CLAWPACK has been discussed in detail by LeVeque

(2002); here the unforced equations (i.e. (1.15), without the terms due to rotation or topography) are solved using Roe's approximate Riemann solver (Roe (1981)) together with Godunov's upwind method, whilst the contribution due to the forcing terms is handled using the method of Strang splitting and standard finite-difference methods. These techniques are discussed in detail by LeVeque (2002).

By employing different numerical techniques for the solution of the shallow-water and TSD equations, the comparison of the asymptotic and full theories is to some degree independent of the vagaries of a particular numerical model.

In practice, as critical flow is approached, ($F \to 1$, $\Gamma \to 0$), a progressively larger computational domain, and progressively longer time-scale of integration, is required to obtain solutions that are steady in the vicinity of the obstacle. There are two main reasons which prevent steady solutions, where they exist, being found for near-critical oncoming flow:

1. Propagation of the solution at sufficient amplitude to the upstream boundary, thereby invalidating the inflow condition; overcoming this problem necessitates increasing the size of the domain in the $x$-direction as $F$ approaches unity ($\Gamma \to 0$);

2. Propagation of the solution at sufficient amplitude to the lateral boundaries, causing reflected waves or hydraulic jumps to interfere with the solution in the vicinity of the obstacle; to prevent this, the size of the domain in the $y$-direction must also be increased as $F$ approaches unity ($\Gamma \to 0$).

For these reasons, a range of domain sizes is used with each model. In all of the numerical calculations, care is taken on a case-by-case basis to

ensure that the flow patterns and calculated drags are unaffected by further increases in domain size, that the flow field in the vicinity of the obstacle is sufficiently steady, and that adequate convergence with respect to spatial resolution occurs.

For both the TSD and shallow-water equations, symmetry considerations permit solutions to be calculated in the half-plane $y \geq 0$. Under the considerations above, shallow-water solutions are obtained on domains ranging in size from $10L \times 10L$ to $60L \times 45L$, with grid-spacing ranging between $\delta x = 0.1L$ (low resolution) to $\delta x = 0.01L$ (high resolution). TSD solutions are obtained on domains ranging in size from $40L \times 40\epsilon^{-1/2}L$ to $60L \times 60\epsilon^{-1/2}L$, with grid spacing between $\delta x = 0.1L$ (low resolution) and $\delta x = 0.01L$ (high resolution).

Before proceeding to a discussion of the transcritical asymptotic theory, it is important briefly to note that, as pointed out by Schär & Smith (1993b), the assumption of symmetry about $y = 0$ would be inappropriate if there were a possibility that the obstacle wake might be unstable. However this is not the case for the results presented here.

## 4.1 Transcritical flow over topography

In Chapter 2 it was shown that, in the limit of small $M$, transcritical shallow-water flow over topography is described by the TSD equation ( (2.16) with $\nu = 0$) together with the equivalent aerofoil boundary condition. For convenience, both the equation and boundary condition are restated below:

$$(-2\Gamma - 3\phi_x)\,\phi_{xx} + \phi_{YY} = 0, \quad \text{with} \quad \phi_Y(x,0) = K_x(x) \quad \text{on } Y = 0. \tag{4.1}$$

| Obstacle | $h(r)$ | $K(x)$ |
|---|---|---|
| Witch of Agnesi | $\frac{a^3}{(a^2+r^2)^{3/2}}$ | $\frac{a^3}{a^2+x^2}$ |
| $(a = 1/2)$ | | |
| Gaussian | $\exp\{-\frac{r^2}{a^2}\}$ | $\frac{\sqrt{\pi}a}{2}\exp\{-\frac{x^2}{a^2}\}$ |
| $(a = 1/\sqrt{2})$ | | |
| Cone | $1-\frac{r}{a}$ | $\frac{\sqrt{a^2-x^2}}{2} - \frac{x^2}{2a}\log\left\{\frac{\sqrt{a^2-x^2}+a}{\lvert x\rvert}\right\}$ |
| $(a = \sqrt{3/2})$ | $(r < a)$ | $(\lvert x\rvert < a)$ |
| Hemi-ellipsoid | $\sqrt{1-\frac{r^2}{a^2}}$ | $\frac{\pi}{4a}(a^2-x^2)$ |
| $(a = \sqrt{3}/2)$ | $(r < a)$ | $(\lvert x\rvert < a)$ |
| Paraboloid | $1-r^2$ | $\frac{2}{3}(1-x^2)^{\frac{3}{2}}$ |
| | $(r < 1)$ | $(\lvert x\rvert < 1)$ |

Table 4.1: Obstacle shapes investigated and their equivalent aerofoils (see text). The five obstacles have unit height and are normalised to have the same volume as the paraboloid ($\mathcal{V} = \pi/2$) using the given value of the non-dimensional constant $a$.

### 4.1.1 *Topographies and their 'equivalent aerofoils'*

First, what does an 'equivalent aerofoil' look like? Table 4.1 introduces five different axisymmetric topographies as examples, namely an obstacle with a 'Witch of Agnesi'-like profile (Jiang & Smith, 2000), a Gaussian, a cone, a hemi-ellipsoid and a paraboloid. As discussed in Chapter 2, the maximum height of each obstacle $h(0)$ is unity, and the volume $\mathcal{V}$ of the obstacle, determined by the non-dimensional parameter $a$, is set according to

$$\mathcal{V} = 2\pi \int_0^\infty r h(r) dr = \frac{\pi}{2}. \tag{4.2}$$

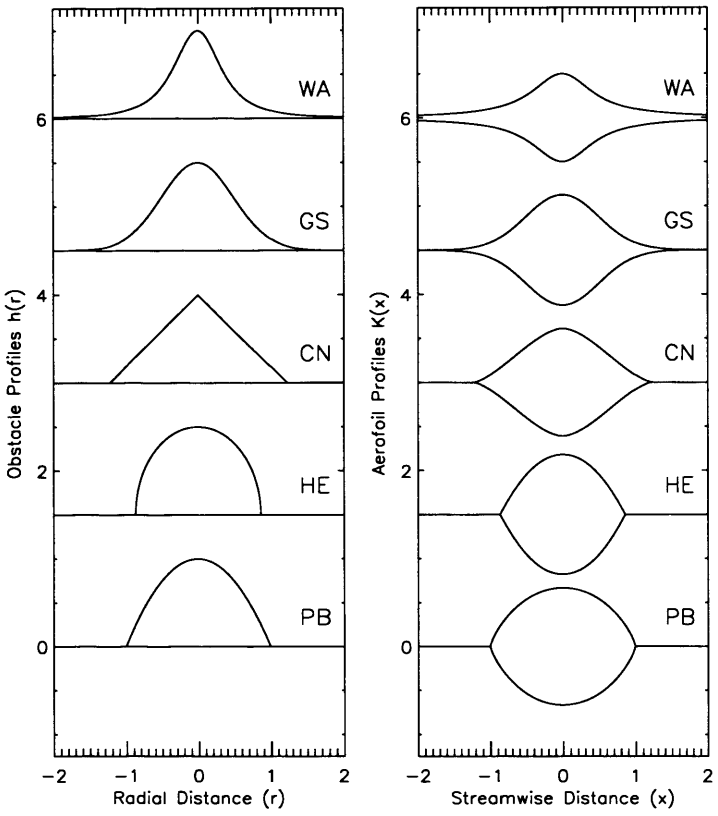


Figure 4.1: Left hand column: obstacle profiles $h(r)$ for the 'Witch of Agnesi' obstacle (WA), the Gaussian (GS), the cone (CN), the hemi-ellipsoid (HE) and the paraboloid (PB). Right hand column: the corresponding obstacle equivalent aerofoils $K(x)$. See Table 4.1 for details.

The above restrictions were introduced to ensure that, in the following, comparisons are made between obstacles with identical height and volume; thus the effects of obstacle *shape* are highlighted.

Figure 4.1 illustrates the obstacle profiles and corresponding equivalent aerofoils introduced in Table 4.1. The left hand column shows the radial height profiles $h(r)$ for the 'Witch of Agnesi' (WA), the Gaussian (GS), the cone (CN), the hemi-ellipsoid (HE) and the paraboloid (PB). The right hand column shows the corresponding equivalent aerofoils $K(x)$.

Although TSD results will be presented for all the above obstacles, comparisons with finite obstacle height $M$ shallow-water computations will be made only for the 'Witch of Agnesi' and paraboloid obstacles. The 'Witch of the Agnesi' is considered partly for 'historical' reasons: Lamb & Britter (1984), Schär & Smith (1993b), Jiang & Smith (2000), to name but a few, considered flow over such an obstacle. The paraboloid is considered with half an eye on the material in the following chapter - where semi-analytic solutions to the problem of rotating flow over a parabolic ridge will be discussed. Most importantly, however, these choices allow for flow over obstacles of infinite support and compact support to be compared and contrasted.

### 4.1.2 *Example results from the equivalent aerofoil theory*

Although essentially included only for visualisation purposes, Figure 4.1 allows for an *a priori* estimate of the maximum drag exerted on the flow by each obstacle.

During the late 1940's and early 1950's, much activity in the aircraft industry was concerned with designing aircraft capable of achieving stable flight at transonic and supersonic speeds. The problem was that the marked increase in drag for classical wing-body combinations in the transonic range prevented prototypes from achieving their expected speeds. Pioneering work by a young NASA-Ames scientist, Richard T. Whitcomb, identified the solution to the problem. Through physical insight and extensive wind tunnel testing, Whitcomb realised that the peak drag experienced in the transonic regime is directly related to the axial development of the cross-sectional areas normal to the air-stream. Thus reducing the maximum rate of change of the cross-sectional area normal to the air-stream would reduce the drag on a given wing-body combination. Attempts to adhere

to this law led to the idiosyncratic 'pinching' of the fuselage at the point at which the wings are joined on many post war aircraft. By pinching the fuselage at this point, the rate of change of cross-sectional area is reduced without compromising wingspan. Whitcomb's findings are reported in Whitcomb (1956) and an interesting historical account can be found online at http://history.nasa.gov/SP-4219/Chapter5.html.

Since the equivalent aerofoil $K(x)$ describes the stream-wise development of (half) the cross-sectional area of the topography, referring to Figure 4.1 and appealing to Whitcomb's area rule, one might anticipate that the hemi-ellipsoid topography will exert the highest peak drag, followed by the paraboloid topography, and so on.

The upper panel of Figure 4.2 shows the drag function $D(\Gamma)$ calculated from a series of steady numerical solutions of the TSD equation (4.1), with values of $\Gamma$ in the range $[-1.5, 1.5]$, for each of the five equivalent aerofoils $K(x)$ corresponding to the five obstacles in Table 4.1. The shape of the drag curves is observed to be remarkably similar amongst the different aerofoils: at least for the aerofoils considered, the following description is generic. As $\Gamma$ increases from $-1.5$, the drag function $D(\Gamma)$ first becomes non-zero with the onset of transcritical flow; the appearance of an hydraulic jump and embedded region of supercritical flow acts to break the symmetry of purely subcritical flow. Recall from Chapter 2, that the boundary between purely subcritical and transcritical flow determines the functional $\Gamma_-$ (2.29). Thus non-zero drag is first encountered when $\Gamma = \Gamma_- \approx -1.2$. As $\Gamma$ increases further, the drag increases rapidly until a value close to the peak drag $D_m$ is attained, which is subsequently maintained for $|\Gamma| \lesssim 0.8$. For $\Gamma > 0.8$, the drag is seen to decrease at a rather gentler rate than the rapid increase for $\Gamma < 0$. Eventually, the flow becomes everywhere supercritical when the

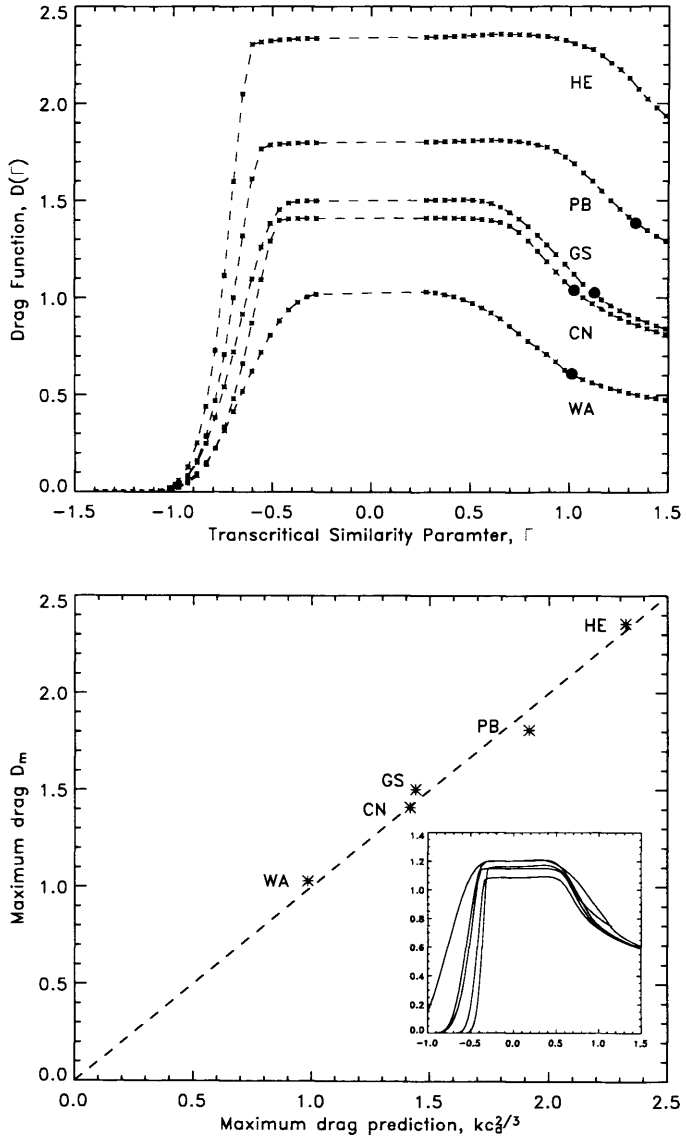


Figure 4.2: The drag function $D(\Gamma)$ as a function of the transcritical similarity parameter $\Gamma$, calculated from a series of steady numerical solutions of the TSD equation (4.1). The upper panel shows results for the five obstacles detailed in Table 4.1 ('Witch of Agnesi' (WA), Gaussian (GS), cone (CN), paraboloid (PB) and hemi-ellipsoid (HE)). The solid dot on each curve shows the location of $\Gamma_+$; for the dashed region of each curve there is no numerical data because of the difficulty in obtaining results for $F$ close to unity. The lower panel plots the correlation between the rescaled supercritical drag coefficient $kc_d^{2/3}$ and the maximum transcritical drag $\mathcal{D}_m$ for the five obstacles. The inset shows the extent to which the five drag curves collapse onto a single profile after application of the scaling described in the text.

| Obstacle | $D_m$ | $\Gamma_-$ | $\Gamma_+$ | $c_d$ |
|---|---|---|---|---|
| Witch of Agnesi | 1.030 | -1.236 | 1.012 | $\frac{\pi a}{2}$ |
| $(a = 1/2)$ | | | | (0.7854) |
| Gaussian | 1.504 | -1.225 | 1.100 | $a\left(\frac{\pi}{2}\right)^{3/2}$ |
| $(a = 1/\sqrt{2})$ | | | | (1.3921) |
| Cone | 1.411 | -1.237 | 1.034 | $\frac{4a}{3}(2c_t - 1)$ |
| $(a = \sqrt{3/2})$ | | | | (1.3585) |
| Hemi-ellipsoid | 2.356 | -1.208 | 1.739 | $\frac{\pi^2 a}{3}$ |
| $(a = \sqrt{3}/2)$ | | | | (2.8491) |
| Paraboloid | 1.810 | -1.214 | 1.333 | $\frac{32}{15}$ |
| | | | | (2.1333) |

Table 4.2: Numerically calculated values of maximum drag coefficient $D_m$ for each obstacle in the transcritical regime (Max $[D] = D_m M^{5/3}$), and values of the transcritical similarity parameter $\Gamma$ marking the boundary between subcritical and transcritical flow ($\Gamma_-$) and supercritical and transcritical flow ($\Gamma_+$). $c_d$ is the linear supercritical drag coefficient discussed in the text. $c_t$ is Catalan's constant ($\approx 0.916$).

functional $\Gamma_+$ (2.29), indicated by the solid dot on each curve, is reached. Typically, when $\Gamma = \Gamma_+$ the drag is in the region of $60 - 70\%$ of its peak value $D_m$.

The values of the functionals $\Gamma_-$, $\Gamma_+$ and the peak drag $D_m$ for each obstacle are given in Table 4.2. The value of the functional $\Gamma_-$ marking the boundary between subcritical and transcritical flow is remarkably close between the obstacles; indeed to two significant figures $\Gamma_- = -1.2$ for all the obstacles considered. Much greater variation is shown in the values $\Gamma_+$, which lie in the range $1.0 - 1.75$. The peak drag $D_m$ also exhibits significant variation, with compact obstacles such as the hemi-ellipsoid and paraboloid

exerting greater drag on the flow compared to distributed obstacles such as the 'Witch of Agnesi'. Indeed, the hemi-ellipsoid exerts a peak drag on the flow over twice that exerted by the 'Witch of Agnesi' obstacle.

At this point we allow ourselves a brief digression from discussing the transcritical regime to pose the question: is it possible to relate drags calculated for the transcritical regime to drag in the supercritical regime? Esler *et al.* (2007*a*) show that the linear supercritical drag on a general axisymmetric obstacle is given by

$$\mathcal{D} = c_d \frac{M^2}{F\sqrt{F^2-1}}, \tag{4.3}$$

where the constant $c_d$ is given by

$$c_d = 2\int_{-\infty}^{\infty} \mathcal{X}^2 G(\mathcal{X})^2 \, d\mathcal{X}. \tag{4.4}$$

Here, $G(\mathcal{X})$ is the 'initial condition' functional derived in Chapter 2 (2.34). The derivation will not be discussed further here, since the above is simply a special case of the more general form for flow over an elliptical obstacle at an angle of attack derived in Chapter 9 (obtained by setting the eccentricity parameter $\mathcal{E} = 1$).

The strong degree of similarity between the shapes of the five curves in the upper panel of Figure 4.2 suggests that some simple rescaling arguments may be useful. Changes in the transcritical drag can be seen to be closely related to changes in the supercritical drag coefficient $c_d$, defined in equation (4.4). As $c_d$ increases (see Table 4.2), $D_m$ and the range of $\Gamma$ for which $D(\Gamma)$ is uniformly large both increase. One possibility is that the drag curves $D(\Gamma)$ collapse to some 'universal' drag curve under the rescaling $\Gamma \to \tilde{\Gamma} c_d^{\beta_*}$, $M \to \tilde{M} c_d^{\alpha_*}$. Consistency with (4.3) in the limit $M \to 0$, $F \to 1 + \Gamma M^{2/3}$

requires $5\alpha_*/3 + \beta_*/2 = 1$. This leaves an arbitrary choice for $\alpha_*$, and the value giving the best fit empirically is found to be $\alpha_* = 2/5$ yielding, since drag scales with $M^{5/3}$,

$$\mathcal{D}_m \approx k c_d^{2/3}, \tag{4.5}$$

with $k$ a constant, which can be estimated from a least squares fit for the five obstacles to be $k = 1.156$. $D_m$ is plotted against $kc_d^{2/3}$ in the lower panel of Figure 4.2, and the extent to which the rescaled drag curves collapse to a single curve is shown in the inset. It is to be emphasised that the above relation is entirely empirical, and has not been tested other than for the five obstacles under discussion. Nevertheless, it may prove to be of use in understanding and developing drag parameterisations for oceanic and atmospheric topography.

Figure 4.3 shows steady state free surface displacement fields $\eta$ derived from numerical solutions of the TSD equation (4.1) for flow around the aerofoils corresponding to the 'Witch of Agnesi' (WA), Gaussian (GS), hemi-ellipsoid (HE) and paraboloid (PB) obstacles. In the left-hand panels, the oncoming flow is subcritical ($\Gamma = -0.6$), and the shading indicates regions of supercritical flow. In the right-hand panels, the oncoming flow is supercritical ($\Gamma = 0.6$) and the shading indicates regions of subcritical flow. The features of the flow are broadly similar for all the aerofoils considered. For subcritical oncoming flows (left-hand panels), fluid accelerates smoothly to supercritical around the upstream side of the aerofoil, then abruptly returns to subcritical through an hydraulic jump toward the rear of the aerofoil. For supercritical oncoming flows (right-hand panels), a curved hydraulic jump, or 'bow wave', marks the upstream boundary of the region of embedded subcritical flow, ahead of which the flow is undisturbed.

For subcritical oncoming flows the lateral extent of the disturbance

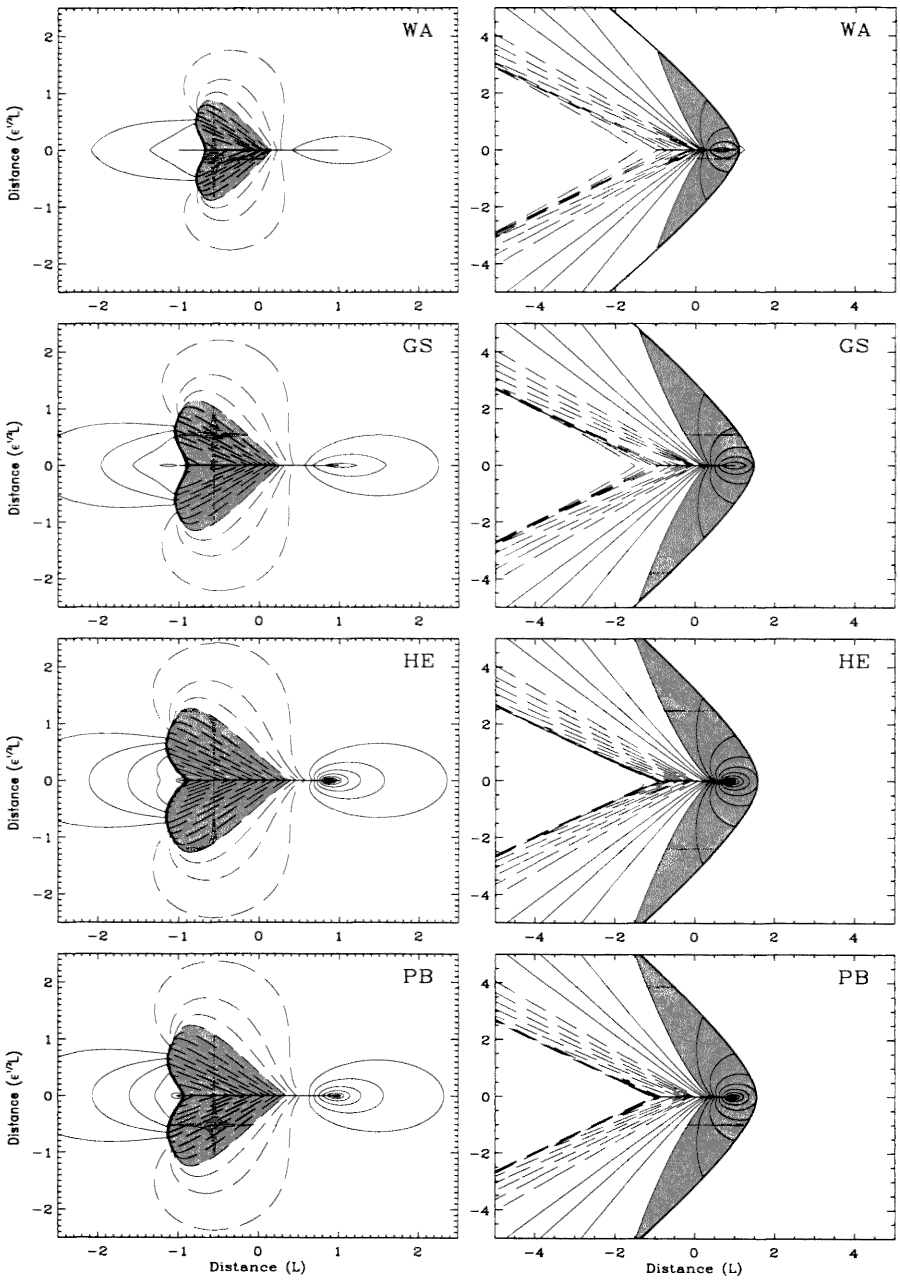


Figure 4.3: Free surface displacement fields derived from numerical solutions of the TSD equation, with spatial resolution $\delta x = \delta y = 0.01L$. Contour intervals are $0.1\epsilon H$ in each panel ($\epsilon = M^{2/3}$). In the left-hand panels $\Gamma = -0.6$; the oncoming flow is subcritical, and shading indicates regions of supercritical flow. In the right-hand panels $\Gamma = 0.6$; the oncoming flow is supercritical, and shading indicates regions of subcritical flow. Displacement fields shown are for the 'Witch of Agnesi' (WA), Gaussian (GS), hemi-ellipsoid (HE) and paraboloid (PB) obstacles.

caused to the flow by an obstacle is seen to relate closely to the drag exerted on the flow by the obstacle. For example, the disturbance to the flow caused by the aerofoil corresponding to the paraboloid obstacle (PB) is of significantly greater lateral extent than that caused by the aerofoil corresponding to the 'Witch of Agnesi' obstacle (WA). This is in agreement with the drag curves of Figure 4.2, where it is observed that this results in the drag exerted on the flow by the paraboloid obstacle being considerably greater than that exerted by the 'Witch of Agnesi' obstacle.

For supercritical oncoming flows, although there is some deviation in the position and angle of the bow wave, the flow fields are qualitatively similar in the half-plane $x > 0$. In $x < 0$ however, a distinction between compact and non-compact obstacles can be made. For the compact obstacles, the V-wave to the rear of the aerofoil is strong, with a clearly defined location. For the distributed obstacles, the V-wave is weaker and less clearly localised.

### 4.1.3 *Assessment of the equivalent aerofoil theory and behaviour at finite obstacle height M*

As a starting point for an assessment of the accuracy of the transcritical theory, drag curves $D(\Gamma)$ calculated numerically from the TSD equation (4.1) may be compared with the corresponding shallow-water computations with finite $M$. In Figure 4.4, the particular cases of the 'Witch of Agnesi' (upper panel) and the paraboloid (lower panel) are considered. In each case, the drag curve $D(\Gamma)$ is plotted along with the drag $\mathcal{D}$, scaled by $M^{5/3}$, calculated from the corresponding shallow-water calculations with $M = 0.05$ (triangles), $M = 0.1$ (diamonds) and $M = 0.4$ (squares). As $M \to 0$, the shallow-water drags $\mathcal{D}$ are seen to converge to the transcritical drag curves $D(\Gamma)$ in both cases. However, this convergence is by no means uniform: the

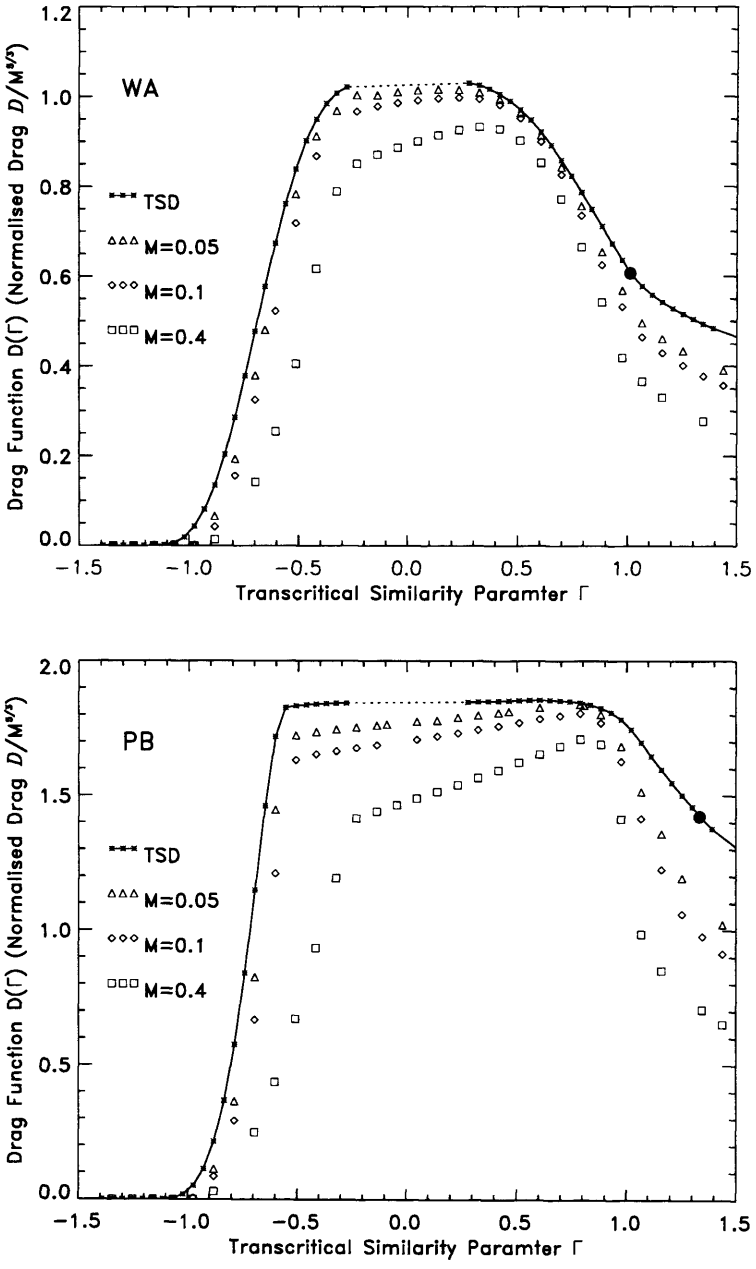


Figure 4.4: The drag function $D(\Gamma)$ as a function of the transcritical similarity parameter $\Gamma$, calculated from a series of steady numerical solutions of the TSD equation (4.1). The upper and lower panels correspond to the 'Witch of Agnesi' (WA) and paraboloid (PB) results respectively. The corresponding normalised drags $\mathcal{D}/M^{5/3}$ from the shallow-water model numerical calculations are plotted on these panels for comparison. Results for obstacle heights $M = 0.05$, 0.1 and 0.4 are shown.

shallow-water results converge considerably more rapidly for supercritical oncoming flow ($\Gamma > 0$) than for subcritical oncoming flow ($\Gamma < 0$). Quantitatively, for $M \lesssim 0.4$, the transcritical theory accurately predicts the peak drag $\mathcal{D}_m$, which occurs in the shallow-water flow for $\Gamma \approx 0.7 - 0.9$, to within an accuracy of 10%. On the subcritical side however, the prediction is in error by as much as 50% in the case of the paraboloid.

Figure 4.5 illustrates the self-similarity of flows over the 'Witch of Agnesi' obstacle at constant values of $\Gamma$. The upper panels show the TSD flow around the equivalent aerofoil, the middle panels results for obstacle height $M = 0.05$, and the lower panels results for $M = 0.4$. Note that the $y$-axis in each panel has been scaled with $\epsilon^{1/2} = M^{1/3}$, and contour intervals have been scaled with $\epsilon$ for consistency with the transcritical asymptotic theory. Hence the obstacle, where plotted, appears elliptical in the lower panels. In the left-hand panels the oncoming flow is subcritical ($\Gamma = -0.6$), and the shading indicates an isolated embedded region of supercritical flow, beginning on the obstacle (or aerofoil) and extending to an hydraulic jump toward its rear. In the right-hand panels, the oncoming flow is supercritical ($\Gamma = 0.6$), and the shading indicates a region of subcritical flow. At the upstream boundary of the subcritical region is an hydraulic jump, ahead of which the flow is undisturbed. As might be anticipated in light of the drag curves in Figure 4.4, for $M = 0.05$ the transcritical theory performs well, the TSD and $M = 0.05$ pictures being nearly identical for both subcritical and supercritical oncoming flows. For the $M = 0.4$ case however, some differences are apparent as the asymptotic theory becomes inaccurate. Considering the supercritical flows, the bow wave in the $M = 0.4$ shallow-water flow exhibits less curvature than its TSD counterpart, indicating that the disturbance to the $M = 0.4$ shallow-water flow remains strong at greater lat-

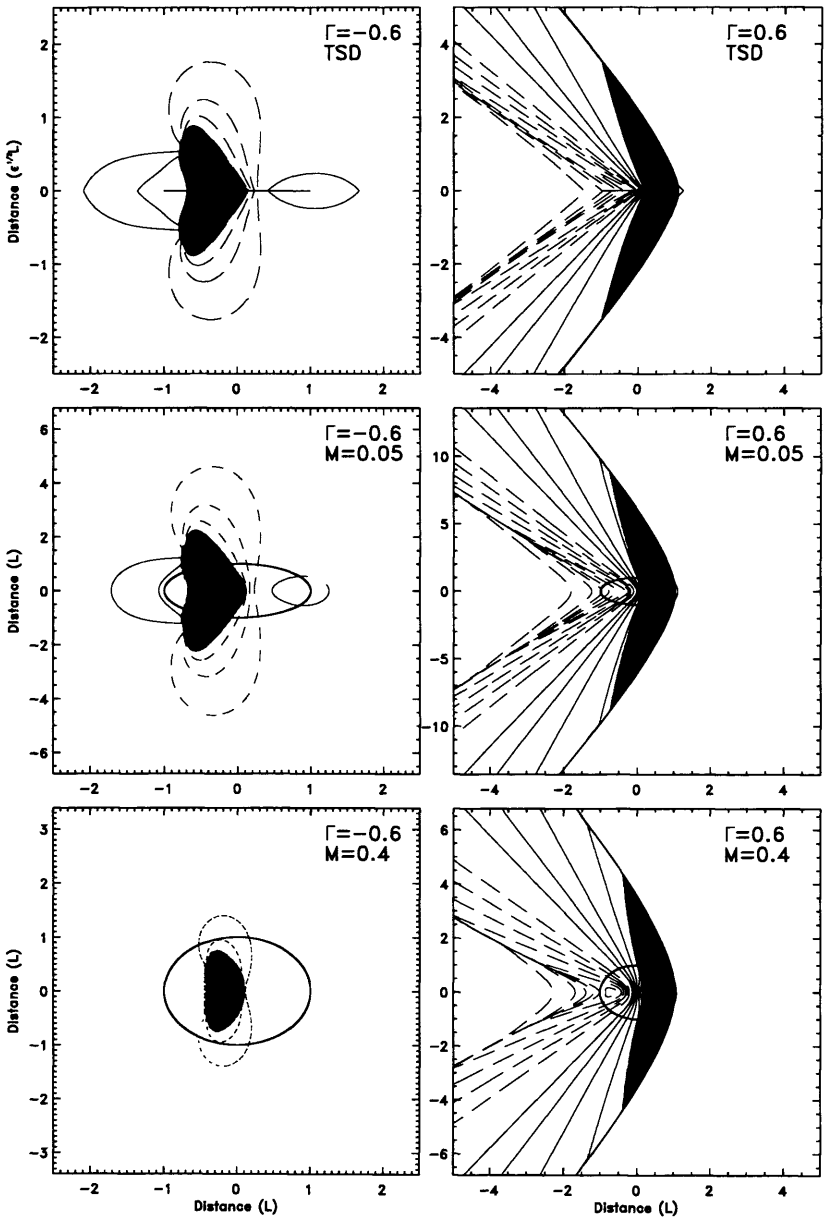


Figure 4.5: Steady state free surface displacement fields illustrating the transcritical similarity theory for flow over the 'Witch of Agnesi' obstacle. Upper panels show results derived from numerical solutions of the TSD equation ((4.1), with spatial resolution $\delta x = 0.01L$ and domain size $40L \times 40\epsilon{-}1/2L$); the remaining panels are derived from numerical solutions of the shallow-water equations ((1.15), with spatial resolution and domain size: Left: $\delta x = 0.05L$, $60L \times 45L$ Right: $\delta x = 0.01L$, $10L \times 10L$) for obstacle heights $M = 0.05$ and $M = 0.4$. Left panels show subcritical flow with the transcritical similarity parameter $\Gamma = -0.6$, and right panels supercritical flow with $\Gamma = 0.6$. Contour intervals are $0.1\epsilon H$ in each panel ($\epsilon = M^{2/3}$), and the $y$-axis on each panel extends from $-5\epsilon^{-1/2}L$ to $5\epsilon^{-1/2}L$. Regions of supercritical flow (left panels) and subcritical flow (right panels) are shaded.

eral extent than predicted by the asymptotic theory. Further, the region of undisturbed fluid in the lee of the obstacle is reduced in the $M = 0.4$ shallow-water flow relative to its TSD counterpart. Differences in flow pattern are much more pronounced for the subcritical oncoming flows, the disturbance to the shallow-water flow being confined to a much smaller region, in the vicinity of the obstacle, than its TSD counterpart. It appears that, as $M$ increases, the overlap between the 'inner' region flow, describing flow along streamlines passing over or near to the obstacle, and the 'outer' flow region away from the obstacle (where the TSD equation is anticipated to be accurate) is much greater for subcritical flow. Thus one of the key assumptions of the transcritical theory - that it is appropriate to divide the flow into 'inner' and 'outer' regions - becomes invalid at lower values of $M$ for subcritical flow than supercritical flow. This observation also serves to explain the more rapid convergence of the shallow-water drag $\mathcal{D}$ to the transcritical drag $D(\Gamma)$ for supercritical oncoming flow compared to subcritical oncoming flow noted in Figure 4.4.

Figure 4.6 is a plot of drag $\mathcal{D}$, scaled this time by $M^2$, against the Froude number $F$ of the oncoming flow. The upper panel shows results for the 'Witch of Agnesi' obstacle and the lower panel results for the paraboloid. Replotting the numerical results in this form serves to emphasise the different regions of validity of the transcritical and supercritical theories introduced in Chapter 2. The thick dashed line in each picture is the linear supercritical drag (4.3), and the series of solid curves shows the TSD prediction for the transcritical drag, as previously plotted in Figure 4.4, for the obstacle heights $M = 0.05, 0.1$ and $0.4$. The TSD drag curves are plotted for $\Gamma_- < \Gamma < 1.5$ in each case, with $\Gamma_+$ indicated by a solid dot on each curve. The shallow-water numerical results for obstacle heights $M = 0.05$, $0.1$ and

0.4 are plotted as symbols (triangles, diamonds, squares respectively). For both obstacles, for Froude numbers $F$ satisfying $\Gamma_- < \Gamma \lesssim \Gamma_+$ the calculated drags follow the TSD predictions reasonably closely, as described previously in relation to Figure 4.4. Again, the greater divergence for subcritical flows and $M = 0.4$ flows, as well as the better approximation to flows over the 'Witch of Agnesi' obstacle compared to the paraboloid, are evident. Of particular interest however, is the transition from transcritical to supercritical drag laws. For $\Gamma \approx \Gamma_+$, the calculated drags begin to diverge from the TSD predictions, but rapidly converge to the supercritical linear prediction given by the thick dashed curve thereafter. For values of $F$ satisfying $\Gamma \gtrsim 1.6$, the supercritical drag curve is accurate - for both obstacles and for each value of $M$ considered. The fact that the transition between the realms of validity of the transcritical and supercritical theories occurs rapidly indicates that, together, they constitute a complete description of the behaviour at obstacle heights up to $M = 0.4$.

As discussed in Chapter 1, a particular topic of interest concerns the construction of regime diagrams in $(M, F)$ space to anticipate the flow configurations found for flow over three-dimensional topography. In Chapter 2 it was noted that the 'equivalent aerofoil' theory predicts that the transitions from purely sub/supercritical flow to transcritical flow occur at

$$F = 1 + \Gamma_- M^{2/3}, \qquad F = 1 + \Gamma_+ M^{2/3}, \quad (\Gamma_- < 0 < \Gamma_+) \tag{4.6}$$

respectively, where $\Gamma_-$, $\Gamma_+$ are constants determined from numerical solutions of the TSD equation (4.1) for each equivalent aerofoil $K(x)$. In the TSD problem of flow over a thin aerofoil, the boundary between the transcritical and supercritical flow regimes is easily calculated by varying the

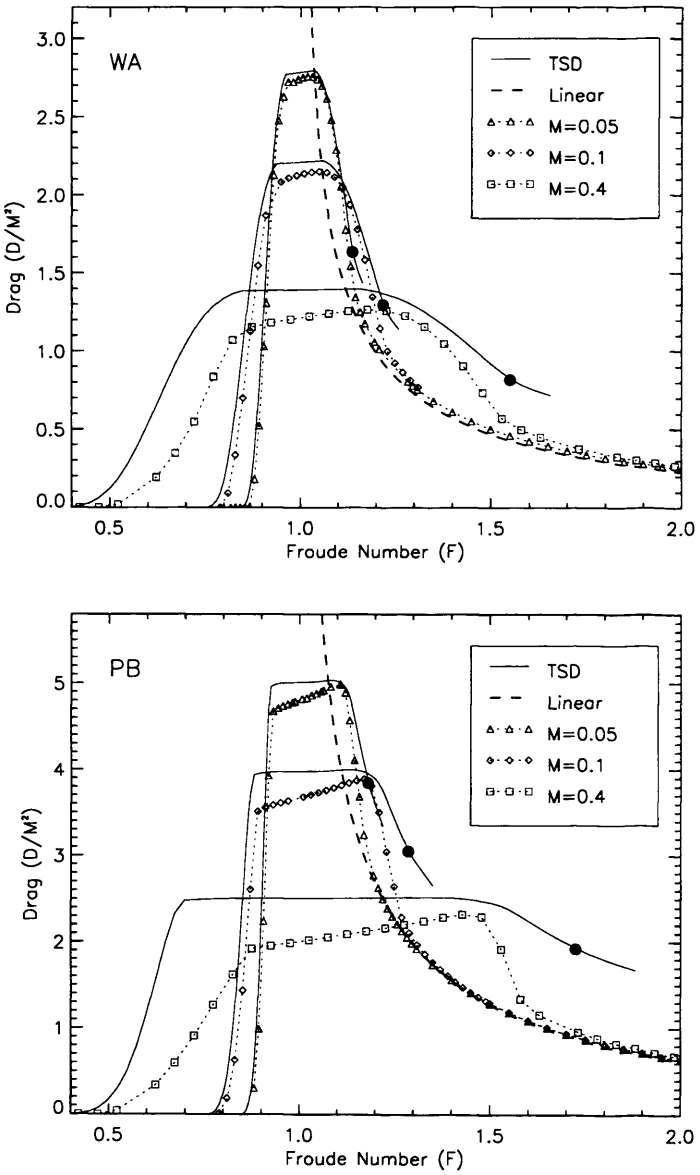


Figure 4.6: Drag $\mathcal{D}$, scaled by obstacle height $M^2$, as a function of Froude number $F$ for flow over the 'Witch of Agnesi' obstacle (WA) and the paraboloid obstacle (PB). Triangles, diamonds and squares mark the results of shallow-water model results for $M = 0.05$, 0.1 and 0.4 respectively. The solid lines show the transcritical similarity theory predictions for the drag in each case, as derived from the TSD numerical results, with the Froude number corresponding to $\Gamma = \Gamma_+$ marked as a solid circle. The dashed curve shows the drag in linear supercritical flow as given by (4.3).

parameter $\Gamma$ until the subcritical region in the vicinity of the obstacle vanishes. In shallow-water flow over the corresponding axisymmetric obstacle however, the situation can sometimes be more complicated, as the isolated region of subcritical flow can split into two regions, located on the flanks of the obstacle.

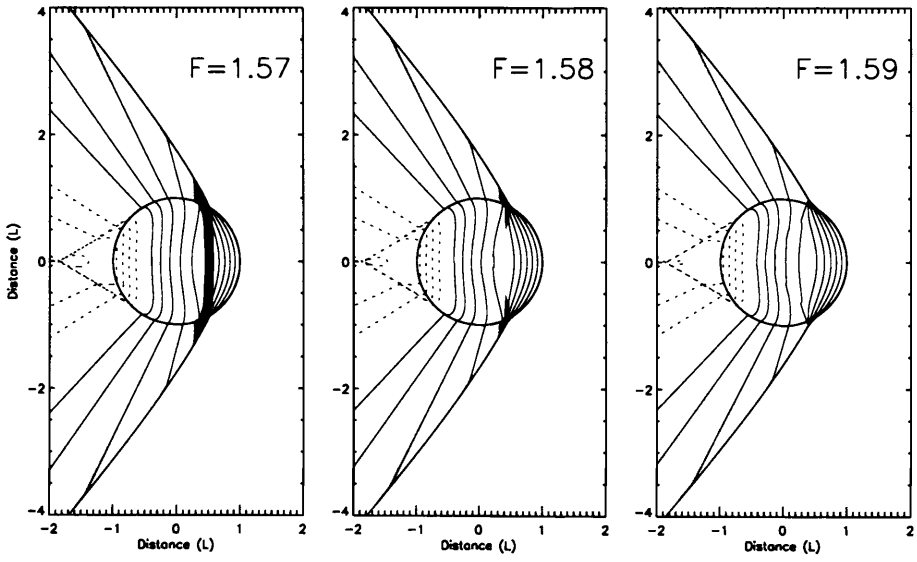


Figure 4.7: Steady state free surface displacement fields illustrating the transition, occurring for flow over the paraboloid obstacle with $M = 0.4$, between (left, $F = 1.57$) supercritical flow with a single embedded region of subcritical flow (shaded), (centre, $F = 1.58$) two separate regions of subcritical flow, and (right, $F = 1.59$) purely supercritical flow. The contour interval is 0.1 $\epsilon H$ in each panel.

Figure 4.7 illustrates this more complicated variety of transition from transcritical to supercritical flow, solutions presented being for the paraboloid obstacle. The three panels show the steady flow free surface displacement field for $M = 0.4$ and $F = 1.57$, $F = 1.58$, and $F = 1.59$ respectively. At $F = 1.57$ a single 'bow' hydraulic jump is situated over the obstacle, behind which is a region of subcritical flow (shaded). As $F$ is increased to $F = 1.58$,

the bow jump at the centreline $y = 0$ weakens and then disappears, and the subcritical region divides into two regions located at the flanks of the obstacle (middle panel). As $F$ is increased further to $F = 1.59$ (right panel), the bow jump has divided into two entirely supercritical 'flank' jumps to the sides of the obstacle and the flow is entirely supercritical throughout the domain. Thus for the case of the paraboloid, two separate transition points in $(M, F)$ space may be identified: the first when the flow along the centreline $y = 0$ becomes everywhere supercritical; the second where the flow becomes supercritical throughout the flow domain. However, further numerical results indicate that the parameter values of the two transitions remain close together, even for larger obstacle heights.

The 'two-step' transition from transcritical to supercritical flow described above is not generic to shallow-water flow over three-dimensional obstacles. The above discussion refers to the paraboloid; for flow over the 'Witch of Agnesi' obstacle this type of supercritical transition is not observed; when the flow along the centreline of the 'Witch of Agnesi' obstacle becomes everywhere supercritical, the flow is everywhere supercritical throughout the domain.

Figure 4.8 shows the calculated regime diagrams for both the 'Witch of Agnesi' (upper panel) and paraboloid (lower panel) obstacles. The region of parameter space where entirely supercritical flow is found is labelled SPC, subcritical flow SBC and transcritical flow TC. The locations in $(M, F)$ space where transition has been found to occur in shallow-water numerical calculations are labelled on Figure 4.8 with stars, whereas diamonds mark the locations where the subcritical region of the paraboloid flow field is found to split into two. The predictions (4.6) from the transcritical theory, expected to be valid for small $M$, are plotted as solid curves. The dotted

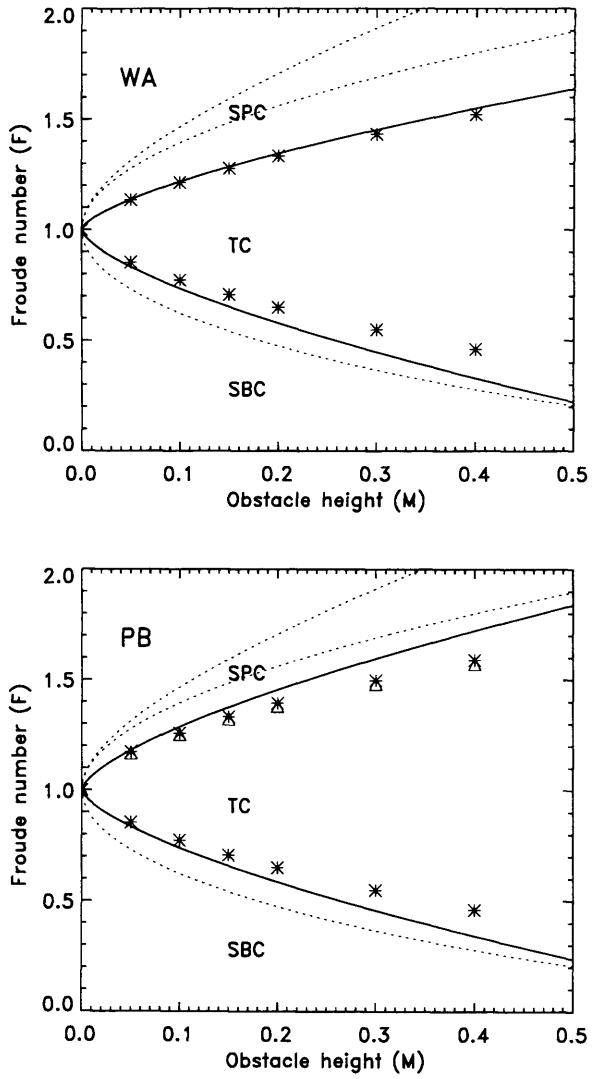


Figure 4.8: Illustrating the flow regimes (SBC - subcritical, TC - transcritical, SPC - supercritical), in obstacle height - Froude number ($M$,$F$) parameter space, for flow over the 'Witch of Agnesi' (WA) and paraboloid (PB) obstacles. The solid lines show the predictions (4.6) from transcritical theory, formally valid for $M \ll 1$. The dotted curves show the corresponding results for one-dimensional obstacles, valid for all $M$. The stars show the location of the actual transitions found in each case from a sequence of steady numerical solutions of the shallow-water equations (1.15). The triangles in the paraboloid panel mark the transition from a single subcritical region to two distinct subcritical regions as illustrated in Figure 4.7.

curves show the corresponding curves (valid for all M) for flow over two-dimensional obstacles discussed in Chapter 1.

The calculated locations of transitions in the shallow-water equations are seen to diverge somewhat from the transcritical theory (solid curves) for values of $M$ approaching 0.5. This is consistent with previous observations of drag and flow predictions, particularly in light of the fact that the transcritical theory has been observed to become less accurate (for fixed $M$) when $|\Gamma|$ is large, as is necessarily the case in the vicinity of the transition curves. Again, as before, the transcritical theory is more accurate for supercritical oncoming flows than for subcritical oncoming flows, and is more accurate for the 'Witch of Agnesi' obstacle than for the paraboloid.

The regime diagram in Figure 4.8 is of course by no means complete. As discussed in Chapter 1, many further interesting regimes exist for $M > 0.5$. However, the behaviour for $M$ close to zero and $F$ close to unity is captured.

## 4.2 Supercritical flow over topography

Further to introducing the transcritical theory, in Chapter 2 it was shown that in the limit of small $M$, the steady flow pattern away from the obstacle in non-rotating, supercritical shallow-water flow over topography is described by the Hopf equation

$$2\gamma\eta_{0}^{f}{}_{\mathcal{Y}_*} + 3\eta_{0}^{f}\eta_{0}^{f}{}_{\mathcal{X}} = 0, \tag{4.7}$$

together with the 'initial' condition

$$\eta_{0}^{f}(\mathcal{X},0) = -\frac{1}{\gamma}\mathcal{X}G(\mathcal{X}), \quad \text{where} \quad G(\mathcal{X}) = \int_{|\mathcal{X}|}^{\infty} \frac{h'(r)}{\sqrt{r^2-\mathcal{X}^2}}\,dr. \tag{4.8}$$

| Obstacle | $h(r)$ | $G(\mathcal{X})$ | $\mathcal{A}$ |
|---|---|---|---|
| Witch of Agnesi | $\frac{a^3}{(a^2+r^2)^{3/2}}$ | $\frac{-2a^3}{(\mathcal{X}^2+a^2)^2}$ | $1/2$ |
| $(a = 1/2)$ | | | |
| Gaussian | $\exp\{-\frac{r^2}{a^2}\}$ | $-\frac{\sqrt{\pi}}{a}\exp\{-\frac{\mathcal{X}^2}{a^2}\}$ | $\sqrt{\frac{\pi}{8}}$ |
| $(a = 1/\sqrt{2})$ | | | |
| Cone | $1-\frac{r}{a}$ | $-\frac{1}{a}\cosh^{-1}\left\{\frac{a}{\lvert\mathcal{X}\rvert}\right\}$ | $\sqrt{\frac{3}{8}}$ |
| $(a = \sqrt{3/2})$ | $(r < a)$ | $(\lvert\mathcal{X}\rvert < a)$ | |
| Hemi-ellipsoid | $\sqrt{1-\frac{r^2}{a^2}}$ | $-\frac{\pi}{2a}$ | $\pi\frac{\sqrt{3}}{8}$ |
| $(a = \sqrt{3}/2)$ | $(r < a)$ | $(\lvert\mathcal{X}\rvert < a)$ | |
| Paraboloid | $1-r^2$ | $-2\sqrt{1-\mathcal{X}^2}$ | $2/3$ |
| | $(r < 1)$ | $(\lvert\mathcal{X}\rvert < 1)$ | |

Table 4.3: Obstacle shapes considered, functions $G(\mathcal{X})$ and non-dimensional N-wave amplitudes $\mathcal{A}$.

The function $G(\mathcal{X})$ for each of the obstacles considered is given in Table 4.3. The initial condition $-\mathcal{X}G(\mathcal{X})$ corresponding to each obstacle is plotted in Figure 4.9. The left column shows the radial height profiles $h(r)$ for the 'Witch of Agnesi' (WA), the Gaussian (GS), the cone (CN), the hemi-ellipsoid (HE) and the paraboloid (PB); the right hand column shows the corresponding supercritical, linear, far-field wake free surface displacement field $-\mathcal{X}G(\mathcal{X})$.

The structure of solutions to the Hopf equation as $\mathcal{Y}_*$ increases away from the obstacle has been discussed in detail by Whitham (1974). As $\mathcal{Y}_*$ increases, wave breaking eventually occurs so that solutions become multi-valued, and must be regularised by hydraulic jumps, which, in order to

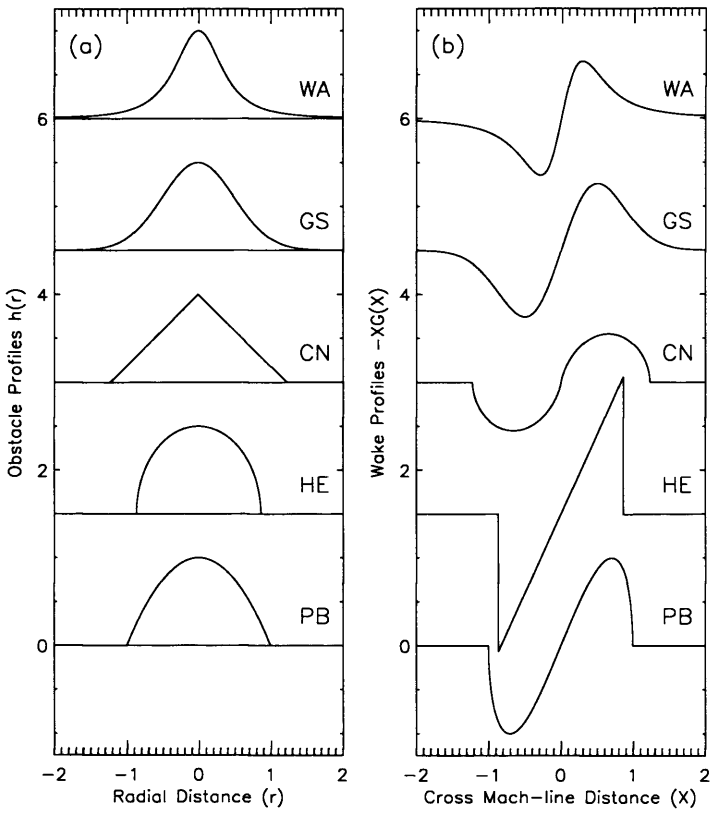


Figure 4.9: (a) Obstacle profiles $h(r)$ for the 'Witch of Agnesi' obstacle (WA), the Gaussian (GS), the cone (CN), the hemi-ellipsoid (HE) and the paraboloid (PB). (b) The supercritical, linear, far-field wake height fields $-\mathcal{X}G(\mathcal{X})$. See Table 4.3 for details.

conserve mass and momentum in the flow, must obey an 'equal areas' rule. Regardless of the exact form of the topographic initial condition, far enough from the obstacle the solution develops into an '$N$-wave', in which the free surface displacement field is linear between two hydraulic jumps. For an antisymmetric initial condition such as (4.8), the $N$-wave is centred on the Mach line $\mathcal{X} = 0$, and as $\mathcal{Y}_*$ increases the distance of each jump from the Mach line increases uniformly. The $N$-wave asymptotic solution for the

current problem is given by

$$\eta_0^f(\mathcal{X},\mathcal{Y}_*) \to \begin{cases} \frac{2\gamma}{3}\frac{\mathcal{X}}{\mathcal{Y}_*} & \text{for} \quad |\mathcal{X}| \le \sqrt{\frac{3\mathcal{A}\mathcal{Y}_*}{F^2-1}} \\ 0 & \text{for} \quad |\mathcal{X}| > \sqrt{\frac{3\mathcal{A}\mathcal{Y}_*}{F^2-1}} \end{cases} \quad \text{with} \quad \mathcal{A} = -\int_0^\infty \mathcal{X}G(\mathcal{X})\,d\mathcal{X}. \tag{4.9}$$

The parameter $\mathcal{A}$ is a measure of both the extent and the amplitude of the $N$-wave at a fixed distance far from the obstacle. The values obtained for each obstacle are given in Table 4.3. Since these values do not differ greatly between the obstacles, the amplitude of the $N$-wave far from the obstacle is relatively insensitive to the details of obstacle shape for obstacles of fixed volume. This is in contrast to the transcritical regime, where the structure of the flow field has been seen to be markedly different for different obstacles.

Figure 4.10 shows the steady state free surface displacement field from a shallow-water calculation with the 'Witch of Agnesi' obstacle and $M = 0.1$, $F = 1.3$. The transcritical similarity parameter is therefore $\Gamma = 1.392 > \Gamma_+ = 1.012$ for this obstacle. Hence supercritical theory might be expected to be accurate in describing this flow. The solid dots marked on the figure show the asymptotic prediction for the locations of the hydraulic jumps marking the boundaries of the $N$-wave given by (4.9). Although $\Gamma$ is not significantly larger than $\Gamma_+$ - at which the flow might be expected to switch between transcritical and supercritical regimes - the supercritical theory is seen to be accurate. This reinforces the impression from the drag curves of Figure 4.6 that, at least for small $M$, the region of parameter space for which neither transcritical nor supercritical theory is accurate is rather small.

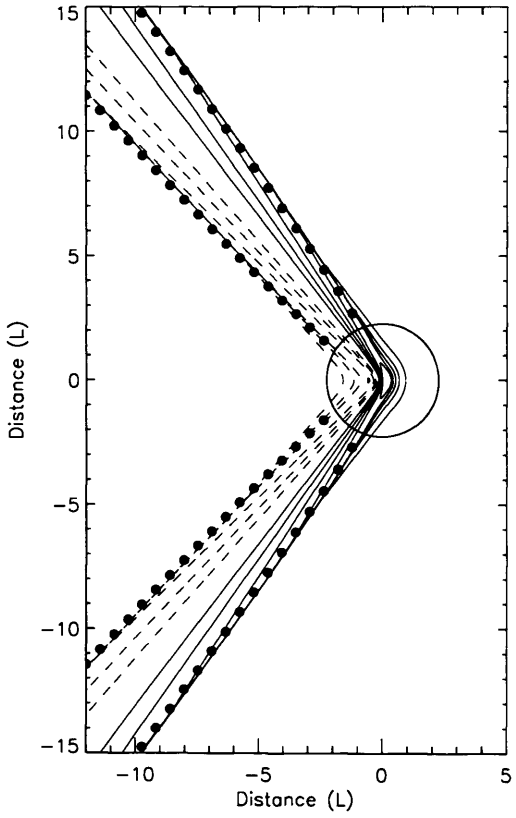


Figure 4.10: The steady state free surface displacement field for flow over the 'Witch of Agnesi' obstacle with $M = 0.1$, $F = 1.3$. The contour interval is $0.1H$, with positive displacements given by solid contours and negative displacements by dashed contours. The zero contour is omitted. The solid dots show the Whitham prediction (4.9) for the location of the hydraulic jumps associated with the front and rear of the $N$-wave.

## 4.3 Discussion

The transcritical and supercritical asymptotic theories introduced in Chapter 2 have been examined in the absence of rotation.

The transcritical theory has been demonstrated to describe most aspects of the full shallow-water flow accurately up to obstacle height $M = 0.4$. In particular, the peak drag exerted on the flow by the obstacle is well approximated, and typically occurs for supercritical oncoming flow with $\Gamma \approx 0.7 - 0.8$. For certain aspects however, particularly the flow patterns and drag for subcritical oncoming flow, the transcritical predictions diverge from the shallow-water results at somewhat lower values of $M$. Further, the involved nature of the supercritical transition identified for the paraboloid topography is not captured by the transcritical theory.

The supercritical theory, though less thoroughly investigated, appears to be accurate even in the vicinity of the anticipated change of realms of validity from supercritical to transcritical theories. Although linear supercritical drag shows a marked dependence on the details of obstacle shape, the supercritical far fields, characterised by the $N$-wave pattern, are relatively insensitive to obstacle shape.

Taken together, the transcritical and supercritical theories appear to offer a complete description of the behaviour of shallow-water flows over obstacles of height up to $M = 0.4$.

# Chapter 5

# Steady rotating flows over a ridge

In this chapter we take up the second major theme of the thesis - the effects of rotation on topographically forced flows. The scenario to be discussed first is that of steady rotating flow over a two-dimensional ridge. Since rotation induces a flow parallel to the ridge, solutions presented necessarily apply to the case of an infinite ridge without sidewalls. However, in common with the corresponding non-rotating flows discussed in Chapter 1, solutions are still effectively one-dimensional, being independent of the along-ridge coordinate. Esler *et al.* (2005) consider the specific case of flow over a parabolic obstacle of the form

$$h(x) = \begin{cases} 4x(1-x) & 0 < x < 1, \\ 0 & x \leq 0, x \geq 1, \end{cases} \tag{5.1}$$

for which much analytical progress can be made. Steady state solutions are derived for a range of parameters $F$, $M$, $B$ exhibiting the possible flow configurations that may be encountered for both subcritical and supercritical ambient flows, and the corresponding regime diagrams are constructed.

These solutions and regime diagrams may be described as 'semi-analytic' in this sense: explicit analytic expressions are available for several of the regime diagram transition curves and for the flow variables on certain branches of the solution curves in phase space; when exact closed-form analytic expressions are not available, the recourse to numerical techniques is limited to simple fourth order Runge-Kutta and secant methods.

It is not the purpose of this chapter to reconsider in detail the construction of solutions to the shallow-water equations discussed in Esler *et al.* (2005); rather, it is to contextualise the results for transcritical, rotating flow over three-dimensional obstacles discussed in the next chapter. To facilitate such a comparison, an equation appropriate to the rotating transcritical limit is introduced (the one-dimensional analogue of the rTSD equation derived in Chapter 2), solutions to which are then constructed using the methodology introduced in Esler *et al.* (2005). In particular, we would like to establish whether rotation has a robust, predictable effect on the flow patterns in topographically forced flows, which persists regardless of the geometry of the obstacle.

First, regime diagrams describing the possible flow configurations for steady rotating flows over a ridge are derived following the methodology of Esler *et al.* (2005); but, whereas Esler *et al.* (2005) discuss solutions for the parabolic obstacle (5.1), here it is consistent to derive solutions for an obstacle with cross section corresponding to the paraboloid obstacle of the previous (and next) chapters. Thus the obstacle considered is of the form

$$h(x) = \begin{cases} 1 - x^2 & -1 < x < 1, \\ 0 & x \leq -1, x \geq 1. \end{cases} \tag{5.2}$$

This change of obstacle is equivalent to the substitution $B \to 4B$ in the

results of Esler *et al.* (2005), and so adds nothing new to the analysis therein.

Secondly, similar regime diagrams for a 'Witch of Agnesi' ridge profile are constructed numerically. Although analytic progress is possible for the parabolic obstacle (5.2), no guarantees are provided that solutions particular to this parabolic obstacle are generic to all single-crested obstacles. In particular, in the previous chapter, it was noted that the supercritical transition for the paraboloid obstacle had a character distinct from that of the 'Witch of Agnesi' obstacle, which might give us cause for concern. By presenting results for the 'Witch of Agnesi' obstacle, we hope to gain some insight into the importance of obstacle shape.

Thirdly, to facilitate comparison with the results to be presented in the following chapter, flow patterns and the regime diagram for flow over the parabolic obstacle are discussed in terms of similarity parameters in the transcritical, $M \to 0$ limit, in an analogous way to the theory of Chapter 2. Finally, finite obstacle height $M$ solutions to the shallow-water equations are compared and contrasted with those of the weakly nonlinear theory.

## 5.1 Steady rotating shallow-water flow over a ridge

Solutions to the nonlinear rotating shallow-water equations have a relatively short history, apparently having first been considered in a brief report by Sambuco & Whitehead (1976). They present an approximate treatment of the case of transcritical flow over an obstacle, noting in particular that although the flow is still 'hydraulically controlled' in the manner of the non-rotating scenario (cf Chapter 1), the critical point need no longer occur at the obstacle crest. Rotating towing tank experiments are also reported, but are of only limited interest to our problem of flow over an infinitely long ridge, since the width of their towing tank is rather narrow.

A considerable advance in our understanding of the problem of rotating flow over an infinitely long ridge was made by Baines & Leonard (1989), comprising numerical solutions to the time-dependent initial value problem with a 'semi-analytic' (in a sense similar to that of the methods employed here) approach to the steady problem.

Initially, Baines & Leonard (1989), consider the case in which the height of the ridge is much greater than the height of the oncoming fluid layer, so that the former might be well approximated as a vertical barrier. In this case, both linear solutions for small Froude number $F$ and numerical integrations for $F$ closer to unity, indicate that the height of the fluid surface grows at a constant rate at the edge of the barrier. The approximation of a tall (yet finite) ridge as a vertical barrier thus breaks down in finite time - eventually, the fluid surface reaches a sufficient height that it may surmount, and flow over, any finite height ridge. Thus, in the steady state, *rotating* flow over a ridge is never completely blocked, in contrast to the non-rotating scenario (cf Chapter 1) in which total blocking is possible.

Further numerical integrations, employing both a symmetric parabolic obstacle and a semi-infinite plateau-shaped obstacle (with a parabolic nose and flat top) offer further insight into the structure of steady state solutions. In the case of transcritical flow in which the oncoming flow is subcritical, the upstream propagating bore, which propagates unattenuated and at constant speed in the non-rotating problem, exhibits both decreasing amplitude and propagation speed (relative to the obstacle) as the solution develops, such that it is entirely absent in the steady state. For supercritical oncoming flows, the upstream travelling bore again exhibits decreasing amplitude as it travels upstream, but in this case comes to rest a finite distance upstream of the obstacle. Thus in the case of rotating flow, not only is it not possible

for the flow to become completely blocked, but no upstream blocking whatsoever is possible, in the sense that the mass flux is constant throughout the fluid layer in the steady state. Further numerical simulations highlight the generation of finite-amplitude inertia-gravity waves downstream of the obstacle in initially supercritical flow, which attain their limiting amplitude after an hydraulic jump downstream of the obstacle.

Baines & Leonard (1989) complement these numerical investigations with semi-analytic solutions of the steady-state equations, employing some of the techniques used in Esler *et al.* (2005) and the current work. They detail a procedure for integrating the equations in the neighbourhood of the obstacle, and further highlight the governing equation for the finite-amplitude inertia-gravity waves found downstream of the ridge in their numerical simulations.

In Esler *et al.* (2005) the discussion of Baines & Leonard (1989) is extended by the presentation of exact solutions for the specific case of flow over the parabolic ridge (5.1), and it is these solutions (but for the obstacle (5.2)) that are discussed in the following section. The study of Baines & Leonard (1989) leaves certain questions open. What controls the position and occurrence of a downstream hydraulic jump? Under what circumstances does the wavetrain of finite-amplitude inertia-gravity waves downstream of the obstacle achieve its limiting amplitude? Does the region of hysteresis allowed for in non-rotating flows still occur in rotating flows?

### 5.1.1 *Flows over a parabolic ridge*

Before proceeding to a description of flow over the parabolic ridge (5.2), it is worth recalling the equations to which solutions are presented. In the context of flow over an infinite ridge the shallow-water equations become

$y$-independent, so that the set (1.15) reduces to

$$\begin{aligned} u_t + (u-F)u_x - \sqrt{B}v &= -(\sigma + Mh)_x, \\ v_t + (u-F)v_x + \sqrt{B}u &= 0, \\ \sigma_t + [(u-F)\sigma]_x &= 0, \end{aligned} \tag{5.3}$$

where, as before, $F$ is the Froude number of the oncoming flow and $B$ is the inverse Burger number; the ridge profile is described by $h(x)$. The relevant upstream conditions are $x \to \infty$, $\sigma \to 1$, $u \to 0$.

If the resulting flow is assumed steady, and solutions are sought that are purely a function of $x$, the thickness equation may be integrated to give

$$(F-u)\sigma = F.$$

This allows $u$, and subsequently $v$ to be eliminated from (5.3) to give the single equation

$$\left(\sigma + \frac{F^2}{2\sigma^2}\right)_{xx} + B(1-\sigma) = -Mh_{xx} \tag{5.4}$$

for the layer depth $\sigma$. The velocity components may be recovered from the layer depth $\sigma$ via

$$u = F - \frac{F}{\sigma}, \quad v = \frac{1}{\sqrt{B}}\left\{Mh_x + \sigma_x\left(1 - \frac{F^2}{\sigma^3}\right)\right\}.$$

For the particular case of the parabolic obstacles (5.1, 5.2), equation (5.4) may be integrated, allowing for the construction of semi-analytic solutions and the regime diagrams to be discussed. It is useful at this point explicitly to note why it is that rotating solutions, in contrast to their non-rotating counterparts, are sensitive to obstacle *shape* as opposed to depending merely

on the obstacle height $M$. Eliminating $u$ from the $x-$momentum equation of (5.3) reveals the following

$$\left(1-\frac{F^2}{\sigma^3}\right)\sigma_x = \sqrt{B}v - Mh_x.$$

When $B = 0$, we recognise the hydraulic alternative of non-rotating hydraulics: at the obstacle crest ($h_x = 0$), either $\sigma = F^{2/3}$ and the flow is critically controlled, or $\sigma_x = 0$. When $B \neq 0$, the critical point occurs not at the obstacle summit ($h_x = 0$) but where

$$\sqrt{B}v = Mh_x.$$

Thus the shape of the obstacle may now affect the character of the solution.

*Flow regimes*

The possible flow configurations that may be encountered are discussed in Esler *et al.* (2005). Figure 5.1 plots numerically evaluated (using the CLAWPACK finite volume code) solutions for each of the eight possible flow configurations identified. The regimes, which are labelled in such a way as to be consistent with those used in the next chapter, are as follows.

In *regime VI* the flow is everywhere supercritical. The layer thickness increases over the obstacle, downstream of which an inifinite wavetrain of finite-amplitude inertia-gravity waves is found.

In *regime V* the flow over the obstacle, as in regime VI, is entirely supercritical. However, the topographic forcing is larger than that required to generate the limiting amplitude inertia-gravity wave. Therefore, an hydraulic jump must appear downstream of the obstacle, after which the flow describes inertia-gravity waves of limiting amplitude.

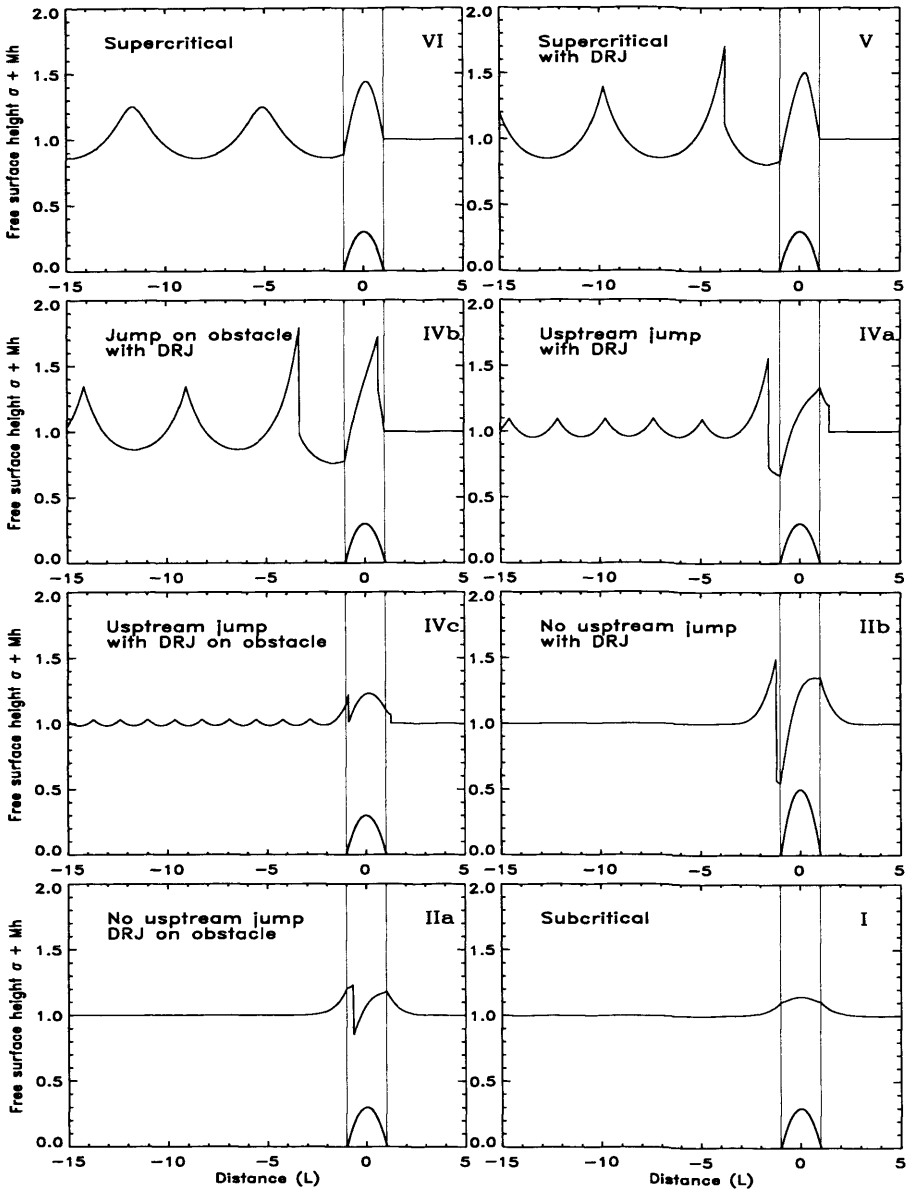


Figure 5.1: Numerically evaluated solutions illustrating possible flow configurations for steady, rotating flow over a ridge. The regimes are as follows. (VI) Supercritical flow everywhere. (V) Supercritical flow over the obstacle with a stationary downstream recovery jump (DRJ). (IVb) Transcritical flow over the obstacle with a jump on the obstacle and a DRJ. (IVa) Transcritical flow over the obstacle with an upstream jump, and a DRJ after the obstacle. (IVc) Transcritical flow over the obstacle with with an upstream jump and a DRJ on the obstacle. (IIb) Transcritical flow over the obstacle with no upstream jump and a DRJ after the obstacle. (IIa) Transcritical flow over the obstacle with no upstream jump and a DRJ on the obstacle. (I) Subcritical flow everywhere.

Throughout regime IV, two hydraulic jumps are observed. In each case, after the downstream jump the flow describes inertia-gravity waves of limiting amplitude. It is the location of these jumps relative to the obstacle that leads to a subdivision of regime IV. In *regime IVa* both hydraulic jumps lie off the obstacle, one upstream and the other downstream. In *regime IVb* the upstream jump now stands over the obstacle, whilst the downstream jump occurs off the obstacle. In *regime IVc*, the upstream jump lies ahead of the obstacle whilst the downstream jump has moved onto the rear of the obstacle.

Regime II describes transcritical flows in which the oncoming flow is subcritical. In this case, as discussed previously, the upstream propagating jump is entirely absent from the steady state solution, and the flow returns rapidly to its undisturbed state after a downstream jump. *Regime IIa* describes the case in which the downstream jump lies on the obstacle, whereas in *regime IIb* the jump lies downstream of the obstacle.

In *regime I* the flow is everywhere subcritical. The solution is symmetric about $x = 0$, the layer depth increasing immediately before and after the obstacle, and decreasing over the obstacle.

*Regime diagrams and transitions*

Regime diagrams in obstacle height/Froude number $(M, F)$ space for flow over the parabolic obstacle (5.2) with rotation rates $B = \frac{1}{2}$ and $B = 2$ are presented in Figure 5.2. These rotation rates are chosen to illustrate best the development of different regimes of solution from the non-rotating scenario described in Chapter 1. Further, as discussed below, for the case when $B = \frac{1}{2}$ a region of hysteresis is found to exist in a similar fashion to that of non-rotating flow.

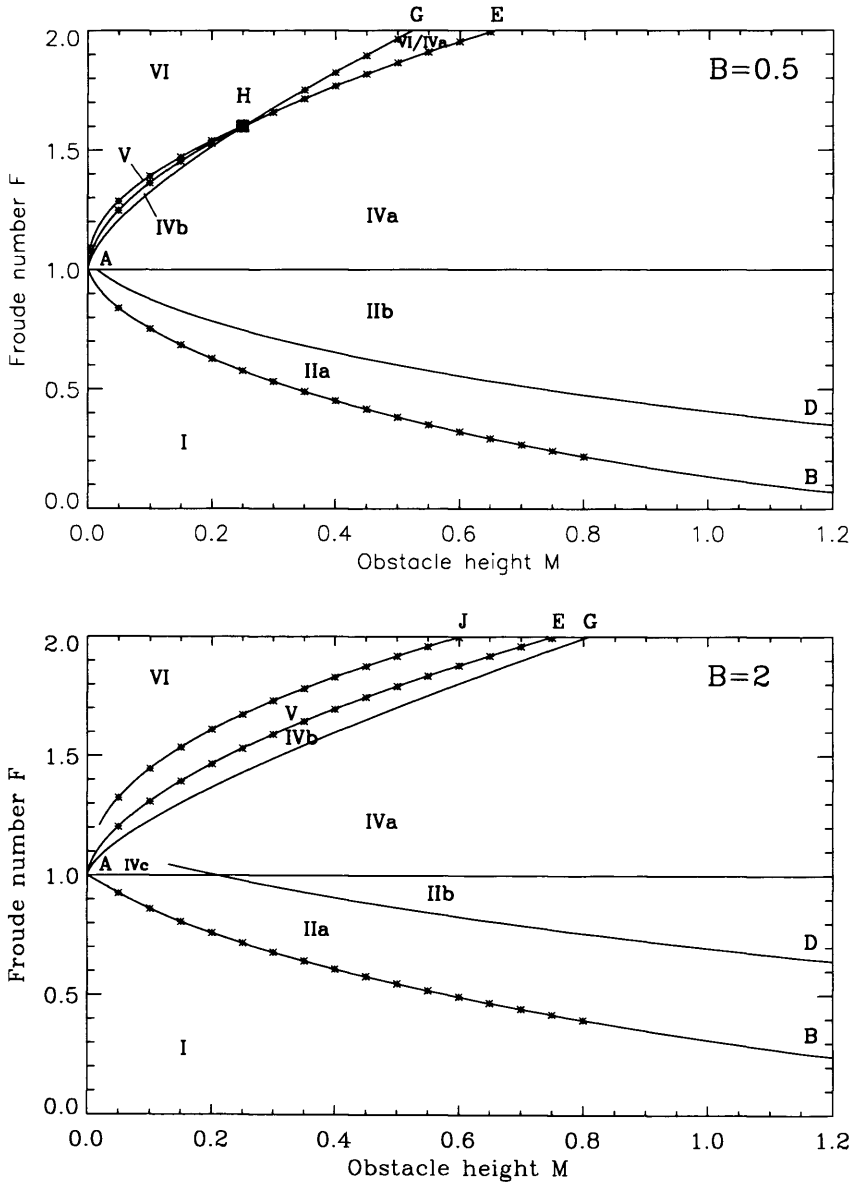


Figure 5.2: Obstacle height / Froude number $(M, F)$ regime diagrams for steady solutions of flow over the parabolic obstacle (5.2) in the presence of rotation with $B = \frac{1}{2}$ (upper panel) and $B = 2$ (lower panel). Examples of the flow configurations encountered within each regime are given in Figure 5.1. The stars along each curve indicate transition points derived from numerical solution of the shallow-water equations with spatial resolution $\delta x = 0.05$.

The nature of the supercritical transition between the different flow regimes depends crucially on the obstacle inverse Burger number $\mathcal{B}_m$ defined as

$$\mathcal{B}_m = \frac{B}{M} = \frac{f^2 L^2}{g h_m}$$

where $h_m$ is the maximum (dimensional) height of the obstacle. The different types of supercritical transition are now described in turn.

First consider the supercritical transition when the rotation rate is sufficiently rapid that the obstacle inverse Burger number $\mathcal{B}_m > 2$. In the regime diagrams of Figure 5.2, this corresponds to the left side of the point $H$ in the upper panel ($B = \frac{1}{2}$) and everywhere in the lower panel ($B = 2$).

Let us begin with a purely supercritical flow, belonging to regime VI on each diagram, and gradually decrease the Froude number of the oncoming flow. Initially then, the flow is everywhere supercritical, with finite-amplitude inertia-gravity waves generated downstream of the obstacle. As the Froude number is reduced, the amplitude of these inertia-gravity waves gradually increases, until waves of limiting amplitude are achieved along the curve AJ (AH in the upper panel). Along AJ, an hydraulic jump of initially infinitesimal amplitude appears downstream of the obstacle. As the Froude number is further reduced, the amplitude of this hydraulic jump grows; throughout regime V a wavetrain of limiting amplitude inertia-gravity waves is present downstream of the hydraulic jump. On further decreasing the Froude number, an upstream jump of initially infinitesimal amplitude appears on the obstacle, just ahead of the critical point ($\sigma = F^{2/3}$), as the curve AE is encountered. Progressing through regime IVb, the upstream jump grows in amplitude and moves upstream until it reaches the edge of the obstacle, at which point the maximum amplitude of the upstream jump is achieved. Thereafter as F is further decreased, the upstream jump decreases

in amplitude as it moves further ahead of the obstacle, finally reaching zero amplitude when $F = 1$ where the flow evolves smoothly into a regime IIb solution described above.

Now consider the supercritical transition in the case that $\mathcal{B}_m < 2$, which holds to the right of point H in the upper panel of Figure 5.2 ($B = \frac{1}{2}$). It is clear that this transition is markedly different, as curves AE and AG are encountered in the opposite order with decreasing Froude number.

Just as in the non-rotating case discussed in Chapter 1, region HGE describes a region of hysteresis in which more than one solution is possible, the type of solution, belonging to regime VI or IVa, that emerges depending on how the flow is initiated. If the Froude number $F$ is subsequently changed so as to leave the hysteresis region, the flow can undergo an abrupt, finite-amplitude transition to the opposite solution, in marked contrast to the smooth transitions observed when $\mathcal{B}_m > 2$. As noted in Esler *et al.* (2005) a third solution is possible in region HGE (identified in non-rotating experiments by Baines & Whitehead (2003)), belonging to regime IVb; but this solution can be demonstrated to be unstable.

The convergence to different steady states within the region of hysteresis may be explicitly demonstrated via time-dependent numerical simulations. The shallow-water equations are integrated forward in time (again using the CLAWPACK finite volume implementation), with a spatial resolution of $\delta x = 0.01$ with different initial conditions. Figure 5.3 shows the time evolution of the flow with $B = \frac{1}{2}$, $F = 1.79$, and $M = 0.4$ with two different initial conditions. In each panel, both the free surface height $\sigma + Mh$ and the along-ridge component of velocity $v$ are plotted. To demonstrate the time evolution, each panel shows the steady-state solution as a thick solid line, together with solutions at $t = 1, 8$ as dashed and dash-dot lines respectively.

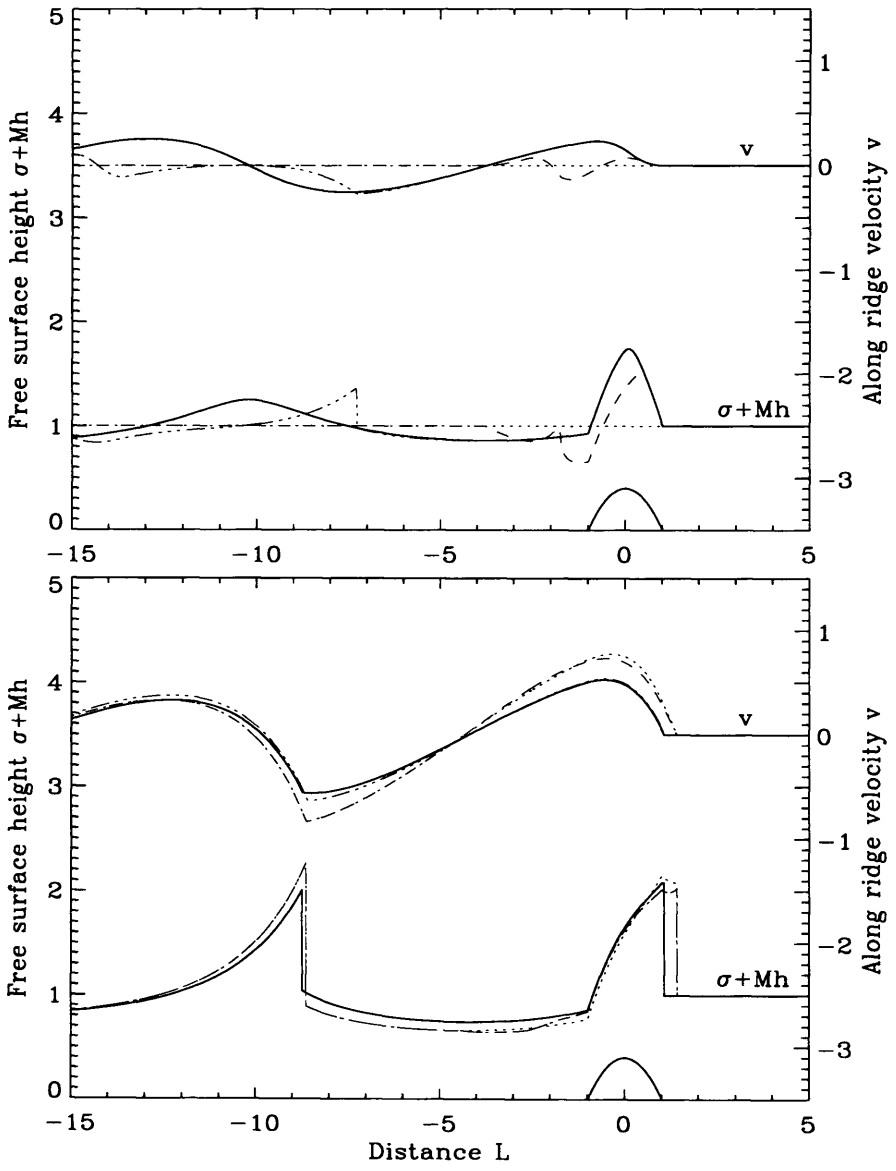


Figure 5.3: Convergence to different stable steady solutions within the hysterysis region ($B = \frac{1}{2}$,$M = 0.4$,$F = 1.79$). The upper panel shows the flow evolving toward the supercritical steady solution (regime VI, thick black curve) from initial conditions of a flat surface (dotted line) and uniform oncoming flow. The evolution of both the free-surface height $\sigma + Mh$ (lower curves) and the along-ridge velocity $v$ (upper curves) are shown in each case. The dashed lines in each panel indicate the time-dependent solution at nondimensional times $t = 1$ (dashed lines) and $t = 8$ (dash-dot lines). The lower panel shows the solution evolving toward the transcritical solution IVa, from an initial condition as described in the text (dotted curve).

In the upper panel, the initial conditions (dotted lines in each panel) are that of a flat surface and uniform oncoming flow and the solution converges to the purely supercritical solution of regime VI. In the lower panel, the initial conditions consist of the steady state obtained from a prior integration, with the larger obstacle height $M = 0.6$. In this case the solution converges to the transcritical solution of regime IVa.

### 5.1.2 *Regime diagram for a 'Witch of Agnesi' obstacle*

Rotating shallow-water flow over an infinite ridge is sensitive to the details of obstacle shape. In the previous chapter it was seen that the nature of the supercritical transition for non-rotating flow over a three-dimensional paraboloid obstacle exhibited behaviour distinct from that of flow over a 'Witch of Agnesi' type obstacle. Thus it is desirable to make some effort to ensure that the results discussed above are of some generality; that the parabolic obstacle is not a singular example.

Figure 5.4 presents numerically established regime diagrams corresponding to those of Figure 5.2, but in this case for a 'Witch of Agnesi' obstacle ridge-profile

$$h(x) = (1 + ((3/2)x)^2)^{-3/2}, \tag{5.5}$$

which has been normalised to have maximum height unity and the same 'volume' as the parabolic obstacle (5.2) discussed thus far. In order to verify the accuracy of the numerically established transition points, transitions were first calculated for the parabolic obstacle, and have been added to the regime diagrams of Figure 5.2 as stars. A spatial resolution of $\delta x = 0.05$ was found sufficient to produce good agreement between the analytic and numerical transitions for the paraboloid obstacle.

Since the 'Witch of Agnesi' is not compact, the subdivision of regimes

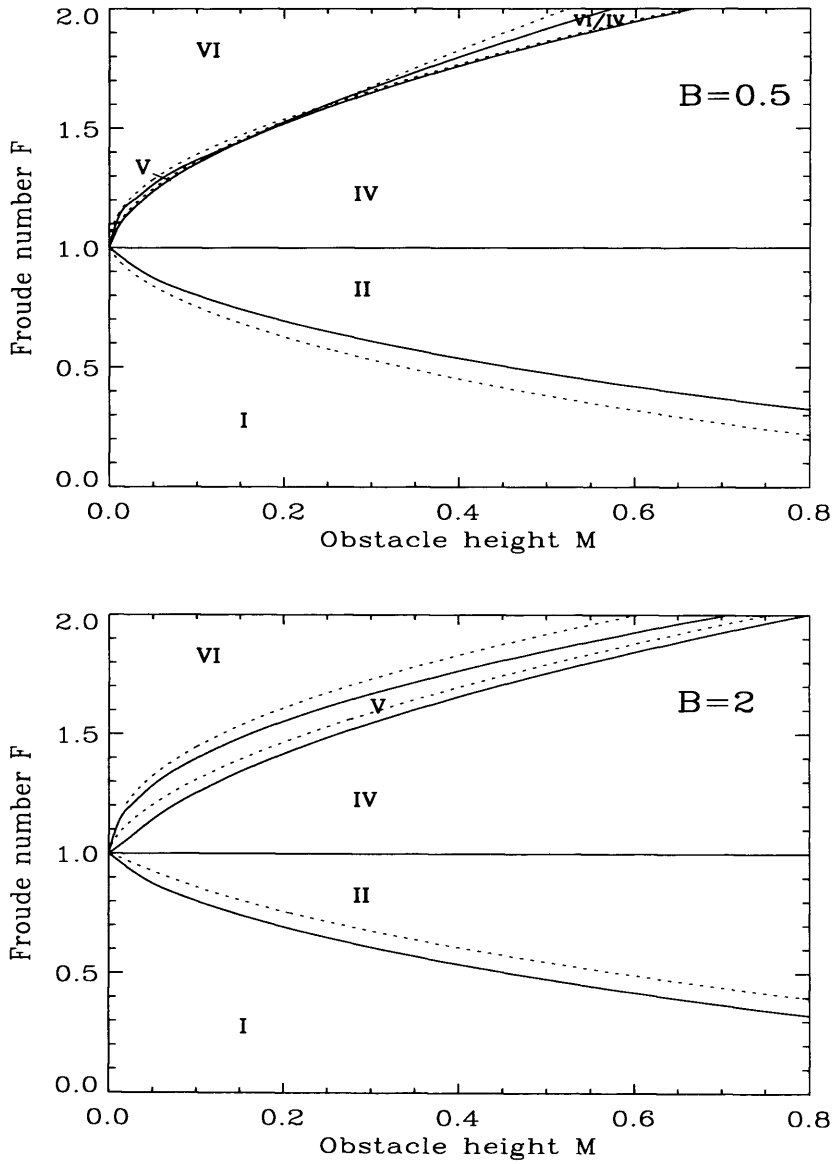


Figure 5.4: Obstacle height / Froude number $(M, F)$ regime diagrams for steady solutions of flow over the 'Witch of Agnesi' obstacle (5.5) in the presence of rotation with $B = 1/2$ (upper panel) and $B = 2$ (lower panel). Regime boundary curves are derived from numerical solutions of the shallow-water equations with spatial resolution $\delta x = 0.05$. Dotted curves are the corresponding regime boundaries for the parabolic obstacle (5.2).

according to whether jumps are located on or off the obstacle is not possible. Also, here the definition of regime V solutions (previously 'supercritcal flow over the obstacle with a stationary downstream jump') is slightly modified, being 'supercritcal flow in $x > 0$ with a stationary jump in $x < 0$'. In fact, the numerically established transition points for the parabolic obstacle (Figure 5.2) have been obtained subject to this condition, so that it is clear that these definitions are equivalent.

Solid curves in Figure 5.4 indicate regime boundaries for the 'Witch of Agnesi' obstacle (5.5), whilst dotted curves describe the corresponding regime boundaries for the parabolic obstacle (5.2). First, it is clear that the parabolic obstacle (5.2) is not a singular example; the flow regimes are qualitatively similar between the two obstacles. Secondly, the dependence of rotating flows on obstacle shape is highlighted.

## 5.2 Steady solutions for rotating flow over a parabolic ridge in the transcritical limit

Although the results discussed above are valid for all $(M, F, B)$, a particularly useful way of presenting the results for small $M$ is to find similarity parameters which entirely determine the flow pattern in the limit $M \to 0$. This enables us first to make a more direct comparison with the corresponding regime diagrams for the rTSD equation discussed in the next chapter, and secondly to assess further the limitations of the 'weakly nonlinear' framework.

Writing

$$\bar{\Gamma} = \frac{F-1}{M^{1/2}}, \qquad \bar{\nu} = \frac{B^{1/2}}{M^{1/4}} \tag{5.6}$$

and setting $\sigma = 1 + M^{1/2}\phi$, at leading order in $M$ equation (5.4) reduces to

$$\left( -2\bar{\Gamma}\phi + \frac{3}{2}\phi^2 \right)_{xx} - \bar{\nu}^2\phi = -h_{xx}. \tag{5.7}$$

Equation (5.7) describes the leading order nonlinear behaviour of the steady flow described by (5.4) in the weakly rotating, transcritical limit $M, B \to 0$, $F \to 1$ in which $\bar{\Gamma}, \bar{\nu}$ remain finite. Therefore, for small $M$, the problem is seen to be characterised by the two similarity parameters $(\bar{\Gamma}, \bar{\nu})$ as in the problem of flow over three-dimensional obstacles discussed in Chapter 2. Note that the appropriate scalings for the velocity components $(u, v)$ are $(M^{1/2}, M^{3/4})$ respectively, and that under these scalings the leading order velocity fields $(\tilde{u}, \tilde{v})$ are related to $\phi$ by

$$\tilde{u} = \phi, \qquad \tilde{v} = \frac{1}{\nu}\left[ h - 2\bar{\Gamma}\phi + \frac{3}{2}\phi^2 \right]_x. \tag{5.8}$$

Equation (5.7) is susceptible to analytic treatment in a manner similar to that of the full equation (5.4) described by Esler *et al.* (2005).

### 5.2.1 *Discontinuities*

Two types of discontinuity must be accounted for in solutions to (5.7). The first corresponds to the hydraulic jumps of the full nonlinear equations, given by equations (1.17). To leading order in $M$, continuity of momentum across an hydraulic jump reduces to

$$\left[ \frac{3}{2}\phi^2 - 2\bar{\Gamma}\phi \right]_-^+ = 0,$$

which can be rearranged as

$$\phi_+ = \frac{4}{3}\bar{\Gamma} - \phi_-, \tag{5.9}$$

whilst the condition of continuity of $v$ across a jump reduces to

$$\left[\phi_x(3\phi - 2\bar{\Gamma})\right]_-^+ = 0. \tag{5.10}$$

Conservation of mass is implicit in the derivation of (5.7). If we are to solve (5.7) for the parabolic obstacle (5.2), it is necessary to consider the behaviour where the obstacle gradient $h_x$ is discontinuous (the edges of the parabola). Integrating (5.7) in the streamwise direction across such a discontinuity (at $x = x_e$ say), requires that

$$\int_{x_e+\epsilon}^{x_e-\epsilon} \left\{ \left( -2\bar{\Gamma}\phi + \frac{3}{2}\phi^2 \right)_{xx} - \bar{\nu}^2\phi + h_{xx} \right\} dx = 0.$$

Assuming that $\phi$ is continuous at $x = x_e$, in the limit $\epsilon \to 0$, the gradient $\phi_x$ must experience a finite jump at $x = x_e$ given by

$$(3\phi - 2\bar{\Gamma})[\phi_x]_-^+ = -[h_x]_-^+ \quad \text{at} \quad x = x_e. \tag{5.11}$$

### 5.2.2 *Solution Methodology*

Here, solutions are discussed for the parabolic obstacle (5.2), recalled below:

$$h(x) = \begin{cases} 1 - x^2 & -1 < x < 1, \\ 0 & x \leq -1, x \geq 1. \end{cases} \tag{5.12}$$

In this case, the governing equation (5.7) becomes

$$\left(-2\bar{\Gamma}\phi+\frac{3}{2}\phi^2\right)_{xx}-\bar{\nu}^2\phi=\begin{cases}2 & -1<x<1,\\ 0 & x<-1, x>1,\end{cases} \tag{5.13}$$

with the conditions at the edges of the obstacle being

$$(3\phi-2\bar{\Gamma})[\phi_x]^+_-=\begin{cases}2 & \text{at } x=1,\\ 2 & \text{at } x=-1.\end{cases} \tag{5.14}$$

Following Esler *et al.* (2005), equation (5.13) may be integrated once to reveal

$$\begin{aligned}&(\phi_x)^2(3\phi-2\bar{\Gamma})^2-\bar{\nu}^2(2\phi^3-2\bar{\Gamma}\phi^2)\\ &\qquad=\begin{cases}K_0 & x>1,\\ K_1+2(3\phi^2-4\bar{\Gamma}\phi) & -1<x<1,\\ K_2 & x<-1.\end{cases}\end{aligned} \tag{5.15}$$

Equation (5.15) may be used to construct solutions in the phase plane $(\phi,\phi_x)$ in the following manner. In the phase plane, solutions follow contours of constant $K_i$ $(i=0,1,2)$ until they meet either the edge of the obstacle or a stationary hydraulic jump; at this point the solution jumps in phase space, according to either (5.9) and (5.10) if an hydraulic jump is met, or (5.14) if the edge of the obstacle is met.

Assuming for now that it is the obstacle edge that is met first, the solution can be constructed in the following way. First the constant $K_0$ is evaluated using the upstream conditions ($\phi=\phi_x=0$); the solution then follows the "outside obstacle" contour until $x=1$, where $\phi=\phi_1$. At this point, the solution jumps to a new position in phase space according to

(5.14). The constant $K_1$ is now evaluated, and subsequently the solution follows the "above obstacle" set of contours until the second obstacle edge, $x = -1$, is met. At $x = -1$, $\phi = \phi_{-1}$ may be determined by noting that the condition

$$x(\phi_1) - x(\phi_{-1}) = 2 \tag{5.16}$$

must be satisfied; that is, that the obstacle has length $2L$. Here $x(\phi)$ is determined from

$$x(\phi) = \int_{\phi_1}^{\phi} \frac{d\phi}{\mathcal{G}(\phi; K_1)}, \tag{5.17}$$

where $\mathcal{G}(\phi; K_1)$ is obtained by a rearrangement of (5.15):

$$\begin{aligned} \phi_x &= \mathcal{G}(\phi; K_1) \\ &= \pm \frac{1}{3\phi - 2\bar{\Gamma}} \left( K_1 + 2(3\phi^2 - 4\bar{\Gamma}\phi) + \bar{\nu}^2(2\phi^3 - 2\bar{\Gamma}\phi^2) \right)^{1/2}. \end{aligned}$$

Since $\phi$ need not necessarily be monotonic above the obstacle, the sign taken for the function $\mathcal{G}$ must be appropriately modified when solutions cross the $\phi_x = 0$ axis.

In a similar fashion, the shape of solutions after the obstacle may be determined from the equation

$$x(\phi) = \int_{\phi_{-1}}^{\phi} \frac{d\phi}{\mathcal{F}(\phi; K_2)}, \tag{5.18}$$

where $\mathcal{F}(\phi; K_2)$ is given by

$$\mathcal{F}(\phi; K_2) = \pm \frac{1}{3\phi - 2\bar{\Gamma}} \left( K_2 + \bar{\nu}^2(2\phi^3 - 2\bar{\Gamma}\phi^2) \right)^{1/2}. \tag{5.19}$$

The shape of solutions before the obstacle may also be determined using (5.18), with $K_0$ and the upstream value of $\phi$ replacing $K_2$ and $\phi_{-1}$. In prac-

tice, when evaluating the integral expressions (5.17), (5.18), it is convenient first to identify a local maximum (minimum) of $\phi$ (at which, for example, $\mathcal{G}(\phi; K_1) = 0$) and then to evaluate the integral in two parts heading away from this maximum (minimum).

In the weakly nonlinear limit, transcritical flow occurs when $\phi = \frac{2}{3}\bar{\Gamma}$ somewhere in the domain. Inspection of the phase-plane diagrams in Figures 5.6 & 5.7 shows that the solution space is effectively divided in two by a vertical line at $\phi = \frac{2}{3}\bar{\Gamma}$, with supercritical flow to the left and subcritical flow to the right. A single curve on both the "above obstacle" and "away from obstacle" solutions passes through the $\phi = \frac{2}{3}\bar{\Gamma}$ dividing line. These are the transcritical curves, and are plotted as thick solid and thick dotted grey curves on each phase-space panel. The values $K_i = K_{ic}$ corresponding to the transcritical curves, obtained by substituting $\phi = \frac{2}{3}\bar{\Gamma}$ into equation (5.15) are given by:

$$K_{0c} = K_{2c} = \frac{8}{27}\bar{\Gamma}^3\bar{\nu}^2, \tag{5.20}$$

$$K_{1c} = \frac{8}{27}\bar{\Gamma}^3\bar{\nu}^2 + \frac{8}{3}\bar{\Gamma}^2. \tag{5.21}$$

The equations of the transcritical curves are essential in the construction of the solutions described below.

Each of the characteristic solutions to the fully nonlinear equation (5.4), depicted in Figure 5.1, are captured in the weakly nonlinear limit governed by (5.7). Figure 5.5 shows the regime diagram in $(\bar{\Gamma}, \bar{\nu})$ parameter space for solutions to the weakly nonlinear equation (5.7) for the particular case of the parabolic obstacle (5.2). We now discuss the construction of representative solutions from each flow regime encountered (except for regime IVc, which is sufficiently similar to regime IVa as to be repetitious), together with the

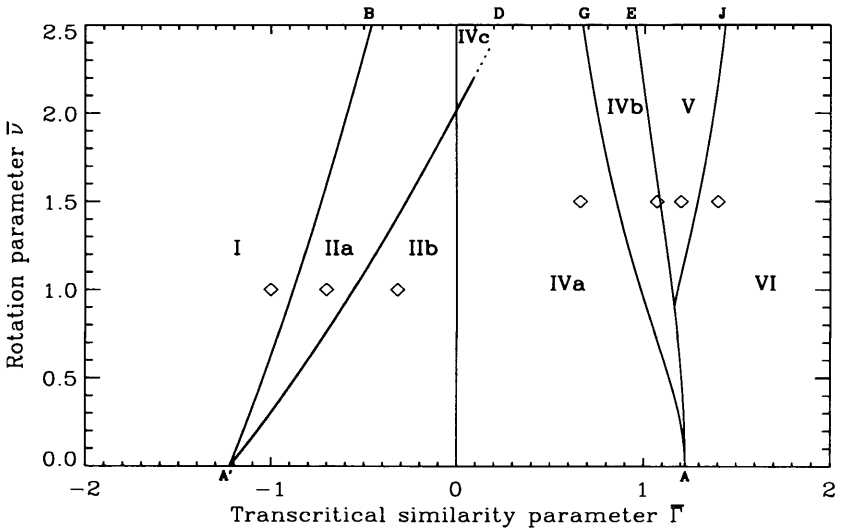


Figure 5.5: Transcritical similarity parameter/rotation parameter $(\bar{\Gamma}, \bar{\nu})$ regime diagrams for flow over the parabolic obstacle (5.2) in the weakly nonlinear limit (governed by equation (5.7)). The regimes are as follows. (VI) Supercritical flow everywhere. (V) Supercritical flow over the obstacle with a stationary downstream recovery jump (DRJ). (IVb) Transcritical flow over the obstacle with a jump on the obstacle and a DRJ. (IVa) Transcritical flow over the obstacle with an upstream jump, and a DRJ after the obstacle. (IVc) Transcritical flow over the obstacle with with an upstream jump and a DRJ on the obstacle. (IIb) Transcritical flow over the obstacle with no upstream jump and a DRJ after the obstacle. (IIa) Transcritical flow over the obstacle with no upstream jump and a DRJ on the obstacle. (I) Subcritical flow everywhere.

derivation of the regime boundaries of Figure 5.5. The location of each representative flow solution in $(\bar{\Gamma}, \bar{\nu})$ parameter space is indicated in Figure 5.5 by a diamond.

*Regime VI solution*

In this case, $\bar{\Gamma} = 1.4$, $\bar{\nu} = 1.5$, and the solution is described by the top panels of Figure 5.6.

For each of the supercritical solutions, for which $\bar{\Gamma} > 1$ ahead of the

obstacle or initial jump, the flow is supercritical and inertia-gravity waves cannot propagate upstream. Hence $\phi = \phi_x = 0$ up to the edge of the obstacle at $x = 1$ or an initial hydraulic jump.

In the present case, the flow is purely supercritical and contains no upstream jump so that $\phi = \phi_x = 0$ up to the upstream edge of the obstacle at $x = 1$. At the obstacle edge ($x = 1, \phi_1 = 0$), the solution jumps in phase space according to (5.14) to the point A, which lies on the "above obstacle" solution curve with $K_1 = K_{1o}$ where

$$K_{1o} = 4. \tag{5.22}$$

The solution then follows this curve in phase space until it reaches the point B, where $x = -1$, and $\phi = \phi_{-1}$ may be determined by the condition

$$x(\phi_1) - x(\phi_{-1}) = 2 \tag{5.23}$$

on the length of the obstacle. Here, $x(\phi)$ may be determined via the integral (5.17). As mentioned earlier, it is convenient to evaluate the integral from the maximum $\phi = \phi_m$ which, on this branch of the solution, is given by the largest real root of

$$\bar{\nu}^2(2\phi_m^3 - 2\bar{\Gamma}\phi_m^2) + 2(3\phi_m^2 - 4\bar{\Gamma}\phi_m) + K_{1o} = 0. \tag{5.24}$$

Having thus established $\phi_{-1}$, the layer depth displacement at the downstream edge of the obstacle, the solution again jumps in phase space according to (5.14) at which point the constant $K_2$ is calculable.

In the present case, it is found that $K_2 < K_{2c}$, so that a contour of constant $K_2$ forms a closed orbit as illustrated in Figure 5.6. The shape of

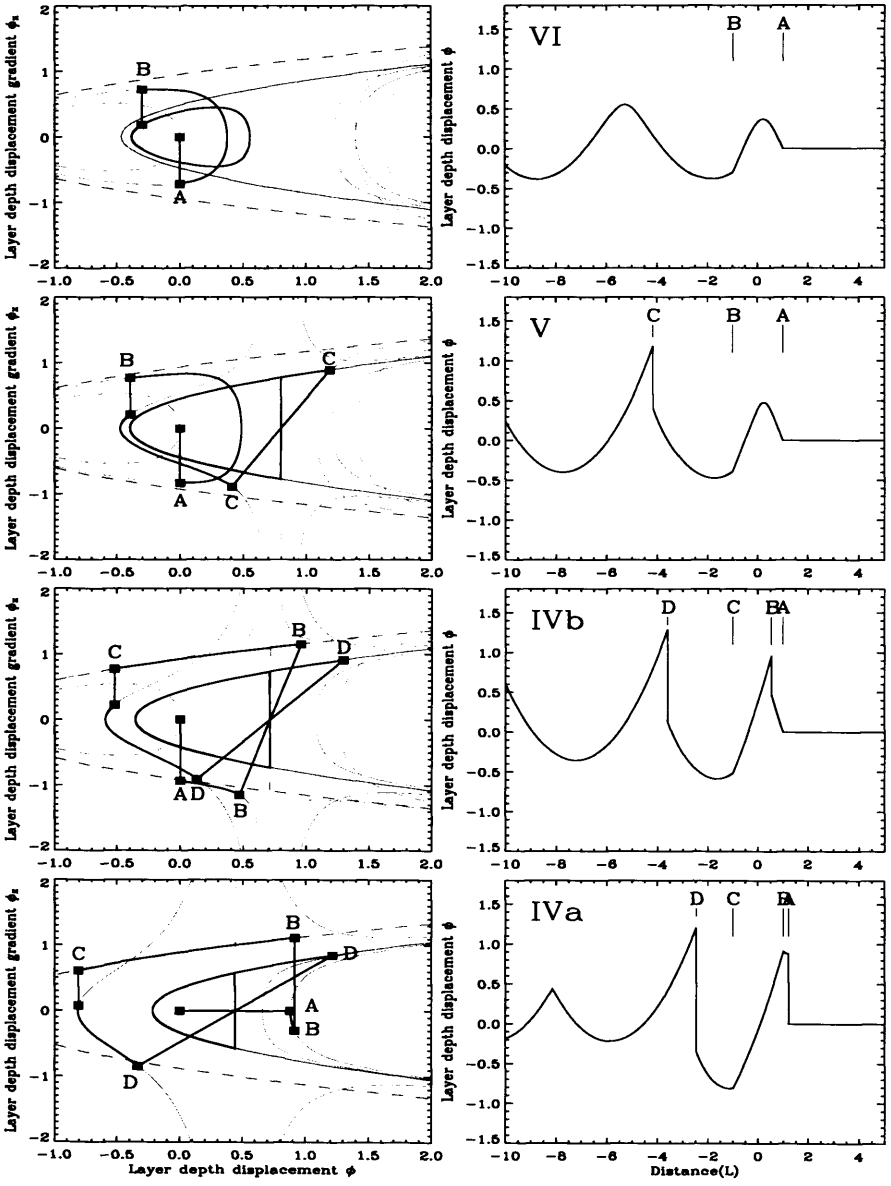


Figure 5.6: Illustrating the steady solutions as they appear in $(\phi, \phi_x)$ phase space (left-hand panels) and the layer depth displacement $\phi$ (right-hand panels) near to the obstacle. The values of the transcritical similarity parameter are as follows: (VI) $\bar{\Gamma} = 1.4$; (VI) $\bar{\Gamma} = 1.2$; (VI) $\bar{\Gamma} = 1.07$; (VI) $\bar{\Gamma} = 0.66$. In each case, the rotation parameter is given by $\bar{\nu} = 1.5$. In the phase-space panels, the dashed grey contours are contours of constant $K_1$, and the solid grey contours of constant $K_0$ ($K_2$), with transcritical curves emphasised in bold. The thick black curve indicates the solution itself.

the solution along this curve may be determined using the integral expression (5.18), and reveals (the weakly nonlinear analogue of) a wavetrain of finite-amplitude inertia-gravity waves downstream of the obstacle.

*Regime V solution*

In this case, $\bar{\Gamma} = 1.2$, $\bar{\nu} = 1.5$, and the solution is described by the second-from-top panels of Figure 5.6.

The construction of the regime V solution proceeds in an analogous manner until the downstream edge of the obstacle is reached. In this instance, upon evaluating the constant $K_2$ it is found that $K_2 > K_{2c}$. Similarly to the fully nonlinear case discussed in Esler *et al.* (2005), the solution can no longer follow a closed orbit after the obstacle and must undergo an hydraulic jump to subcritical flow at some point downstream of the obstacle. After the jump, the solution must lie on the transcritical curve with $K_2 = K_{2c}$, since this is the only curve that allows the solution to return to supercritical thereafter. This requirement serves uniquely to determine the point C at which the jump must occur, downstream of which the solution describes (the weakly nonlinear analogue of) inertia-gravity waves with limiting amplitude.

Along this branch of the solution, an analytic solution for $x(\phi)$ is possible, since when $K_2 = K_{2c}$ each term in equation (5.15) may be divided by $(3\phi - 2\bar{\Gamma})^2$. The resulting equation can be integrated to reveal

$$x - x_0 = \frac{3\sqrt{2}}{\nu}\left(\phi + \frac{1}{3}\bar{\Gamma}\right)^{1/2}, \tag{5.25}$$

(c.f. Grimshaw *et al.*, 1998, equation (53)).

*Regime boundary AJ*

The limiting case defining the regime boundary between the above solutions, at which a downstream hydraulic jump of initially infinitesimal amplitude first appears, is that in which $K_2 = K_{2c}$. This corresponds to the curve AJ in Figure 5.5, which may be derived by solving iteratively for the value of $\bar{\Gamma}$ for which $K_2 = K_{2c}$ at fixed values of $\bar{\nu}$.

*Regime boundary AE*

In each of the above solutions, the flow over the obstacle remains entirely supercritical. This is possible only if $K_{1o} \leq K_{1c}$, or

$$4 \leq \frac{8}{27}\bar{\Gamma}^3\bar{\nu}^2 + \frac{8}{3}\bar{\Gamma}^2.$$

Curve AE in Figure 5.5, marking the onset of critical control conditions over the obstacle, is defined by equality in the above equation, which may be rearranged to yield

$$\bar{\nu}^2 = \frac{3}{2}\left(\frac{9 - 6\bar{\Gamma}^2}{\bar{\Gamma}^3}\right). \tag{5.26}$$

*Regime IVb solution*

In this case, $\bar{\Gamma} = 1.07$, $\bar{\nu} = 1.5$, and the solution is described by the second-from-bottom panels of Figure 5.6.

Here, it is found that $K_{1o} > K_{1c}$. Examining the relevant phase-space panel of Figure 5.6, it is clear that the solution cannot remain on a curve with $K_{1o} > K_{1c}$, so that the solution must include a jump on the obstacle. After the jump, the solution must lie on the transcritical curve over the obstacle, since the flow is critically controlled. This serves uniquely to determine the point in phase space at which the jump must occur, labelled point B, with

layer depth displacement $\phi_-$ defined by

$$2\bar{\nu}^2\left(\phi_-^3-\phi_+^3-\bar{\Gamma}(\phi_-^2-\phi_+^2)\right)+2\left(3(\phi_-^2-\phi_+^2)-4\bar{\Gamma}(\phi_--\phi_+)\right) = K_{1c}-K_{1o} \quad (5.27)$$

where $\phi_+$, the layer depth displacement after the jump, is given by (5.9). Along this branch of the solution (critical over the obstacle), equation (5.15) may be integrated as before to reveal

$$x - x_0 = \frac{3\sqrt{2}}{\nu}\left(\phi + \frac{1}{3}\bar{\Gamma} + \frac{3}{\bar{\nu}^2}\right)^{1/2}. \quad (5.28)$$

At the edge of the obstacle, on evaluating the constant $K_2$ it is found that $K_2 > K_{2c}$, so that the solution now follows the same pattern as in regime V, with an hydraulic jump and wavetrain of limiting amplitude inertia-gravity waves downstream of the obstacle.

*Regime IVa solution*

In this case, $\bar{\Gamma} = 0.66$, $\bar{\nu} = 1.5$, and the solution is described by the bottom panels of Figure 5.6.

Here an hydraulic jump stands ahead of the obstacle. Before the jump, the flow is undisturbed so that $\phi_- = 0$, and from (5.9) the layer depth displacement immediately after the jump is given by $\phi_+ = 4/3\bar{\Gamma}$. The solution now follows a path of constant $K_0$ on the away from obstacle contours, with $K_0$ given by

$$K_0 = -\bar{\nu}^2(2\phi_+^3 - 2\bar{\Gamma}\phi_+^2),$$

until it reaches the point B at the edge of the obstacle ($x = 1, \phi = \phi_1$). Since the flow is critically controlled, point B is uniquely determined as it is the only possible point at which the solution may join the transcritical

curve over the obstacle. Therefore $\phi_1$ must satisfy

$$\sqrt{K_{1c} + \bar{\nu}^2(2\phi_1^3 - 2\bar{\Gamma}\phi_1^2) + 2(3\phi_1^2 - 4\bar{\Gamma}\phi_1)} + \sqrt{K_0 + \bar{\nu}^2(2\phi_1^3 - 2\bar{\Gamma}\phi_1^2)} - 2 = 0.$$

After reaching the edge of the obstacle, the solution follows the "above obstacle" contours with $K_1 = K_{1c}$, the solution being given explicitly by (5.28). After the obstacle, the solution behaves in the same way as the regime IVb solution described above.

*Regime boundary AG*

Regime IVa solutions have a jump ahead of the obstacle, whilst Regime IVb solutions have a jump on the obstacle. The limiting case, defining curve AG on Figure 5.5, is that in which a stationary jump is located exactly at the obstacle boundary. Transcritical flow with an upstream jump is possible only if the value $K_1$ from a stationary jump located exactly at the obstacle boundary $x = 1$ satisfies $K_1 \leq K_{1c}$, or

$$4 - \bar{\nu}^2\bar{\Gamma}^3\left(\frac{32}{27}\right) \leq \frac{8}{27}\bar{\Gamma}^3\bar{\nu}^2 + \frac{8}{3}\bar{\Gamma}^2.$$

The curve AG is determined by equality in the above expression, which may be rearranged to reveal

$$\bar{\nu}^2 = \frac{9}{10}\left(\frac{3 - 2\bar{\Gamma}^2}{\bar{\Gamma}^3}\right). \tag{5.29}$$

*Regime I solution*

In this case, $\bar{\Gamma} = -1$, $\bar{\nu} = 1$, and the solution is described by the top panels of Figure 5.7.

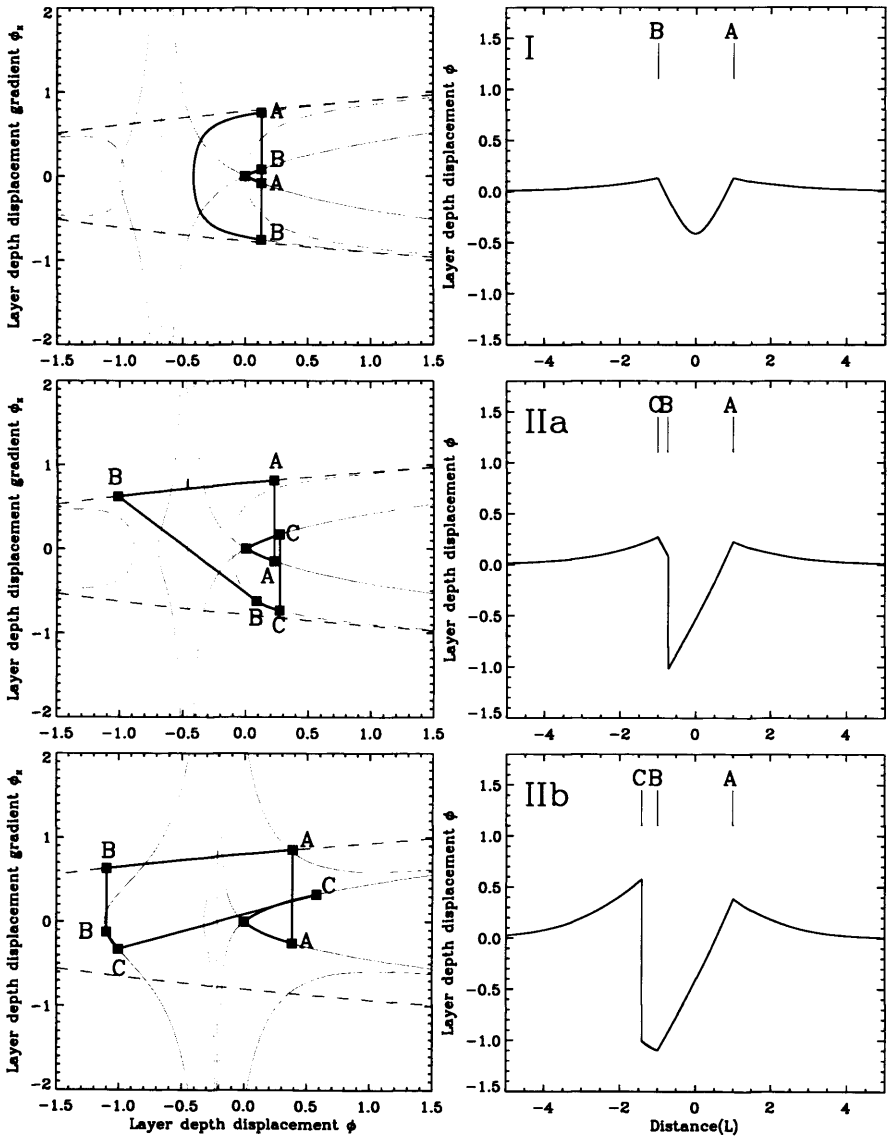


Figure 5.7: Illustrating the steady solutions as they appear in $(\phi, \phi_x)$ phase space (left-hand panels) and the layer depth displacement $\phi$ (right-hand panels) near to the obstacle. The values of the transcritical similarity parameter are as follows: (I) $\bar{\Gamma} = -1$; (IIa) $\bar{\Gamma} = -0.7$; (IIb) $\bar{\Gamma} = -0.32$. In each case, the rotation parameter is given by $\bar{\nu} = 1$. In the phase-space panels, the dashed grey contours are contours of constant $K_1$, and the solid grey contours of constant $K_0$ ($K_2$), with transcritical curves emphasised in bold. The thick black curve indicates the solution itself.

When the ambient flow is subcritical, since there are no closed "away from obstacle" curves on the subcritical side of the phase-space panels, as $x \to \pm\infty$ the flow must return to its undisturbed state with $\phi = \phi_x = 0$. Thus for each of the three subcritical flows to be discussed we must have

$$K_0 = K_2 = 0. \tag{5.30}$$

The regime I solution describes flow that is everywhere subcritical, and it is clear from the phase-space diagram that in this case the flow must be symmetric over the obstacle. Thus $\phi_1 = \phi_{-1}$, and in light of (5.30) we deduce that the entire solution must be symmetric about $x = 0$. The layer thickness displacement at the obstacle edges $\phi_1 = \phi_{-1}$ is then entirely determined by the condition that, solutions being symmetric, the minimum value $\phi_m$ on the "above obstacle" curves must occur at the obstacle crest. Thus

$$x(\phi_1) - x(\phi_m) = 1$$

where $x(\phi)$ is determined via the integral (5.17), and $\phi_m$ is the minimum value of $\phi$ along the curve with $K_1$ determined from (5.15).

*Regime boundary A'B*

The limiting case of purely subcritical solutions is that in which the flow is exactly critical at the obstacle crest. In this case, the condition that the minimum value of $\phi$ occurs at the obstacle crest becomes

$$x(\phi_1) - x\left(\frac{2}{3}\bar{\Gamma}\right) = 1,$$

whilst $\phi_1$ must also satisfy

$$\sqrt{K_{1c} + 2\left(3\phi_1^2 - 4\bar{\Gamma}\phi_1\right) + \bar{\nu}^2(2\phi_1^3 - 2\bar{\Gamma}\phi_1^2)} + \sqrt{2\bar{\nu}^2(\phi_1^3 - \bar{\Gamma}\phi_1^2)} - 2 = 0 \quad (5.31)$$

so that the solution joins the transcritical curve over the obstacle. Curve A'B, marking the boundary between purely subcritical and transcritical flows, is determined by numerical solution of the above equations using the secant method to find $\phi_1$ and $\bar{\Gamma}$ given $\bar{\nu}$, and thus determine the curve.

*Regime IIa solution*

In this case, $\bar{\Gamma} = -0.7$, $\bar{\nu} = 1$, and the solution is described by the middle panels of Figure 5.7.

The Regime IIa solution describes the case in which flow is transcritical over the obstacle, with a downstream recovery jump located over the obstacle. Thus $\phi = \phi_1$ at the upstream edge of the obstacle is determined by (5.31), which ensures that the solution joins the transcritical curve over the obstacle. The position at which the recovery jump must occur, labelled point B in Figure 5.7, is then determined by requiring that the solution join the "away from obstacle curve" with $K_2 = 0$ at the obstacle edge.

*Regime IIb solution*

In this case, $\bar{\Gamma} = -0.32$, $\bar{\nu} = 1$, and the solution is described by the bottom panels of Figure 5.7.

The Regime IIb solution describes the case in which flow is transcritical over the obstacle, but in this case the downstream recovery jump is found after the obstacle. Thus $\phi = \phi_1$ at the upstream edge of the obstacle is again determined by (5.31), which ensures that the solution joins the transcritical curve over the obstacle. The solution then remains on the transcritical curve

over the obstacle, and is given explicitly by (5.28). The position at which the downstream recovery jump must occur, labelled point C in Figure 5.7, is again determined by requiring that the solution join the "away from obstacle curve" with $K_2 = 0$ after the downstream jump.

*Regime boundary A'D*

Regime IIa solutions have a recovery jump over the obstacle, whilst regime IIb solutions have a recovery jump downstream of the obstacle. The limiting case, defining curve A'D on Figure 5.5, is that in which a stationary jump is located exactly at the downstream edge of the obstacle. In this case, $\phi_1$ must satisfy (5.31) so that the solution joins the transcritical curve over the obstacle, which is supplemented by the requirements that the obstacle is of length $2L$ and that the flow meets the "away from obstacle" curve with $K_2 = 0$ at the obstacle edge $x = -1$:

$$x(\phi_1) - x(\phi_{-1}) = 2; \tag{5.32}$$

$$\sqrt{K_{1+} + 2\left(3\phi_+^2 - 4\bar{\Gamma}\phi_+\right) + \bar{\nu}^2(2\phi_+^3 - 2\bar{\Gamma}\phi_+^2)} \tag{5.33}$$

$$+\sqrt{2\bar{\nu}^2(\phi_+^3 - \bar{\Gamma}\phi_+^2)} - 2 = 0. \tag{5.34}$$

Here, $\phi_+$ is determined from (5.9), with $\phi_- = \phi_{-1}$, and $K_{1+}$ is given by

$$K_{1+} = K_{1c} + 2\bar{\nu}^2\left(\phi_-^3 - \phi_+^3 - \bar{\Gamma}(\phi_-^2 - \phi_+^2)\right).$$

The above system of equations is solved numerically using the secant method to establish curve A'D of the regime diagram.

## 5.3 Comparison of weakly and fully nonlinear flows

In Figure 5.8 the regime diagram for steady flow over the parabolic obstacle (5.2) in the weakly nonlinear limit $M \to 0$ is compared with that of shallow-water flow (full nonlinearity) at finite obstacle height $M = 0.4$. Clearly, the most significant difference is that the weakly nonlinear limit precludes the possibility of hysteresis. Earlier it was noted that, for the parabolic obstacle (5.2), hysteresis occurs for $\mathcal{B}_m < 2$. Since $\mathcal{B}_m = \bar{\nu}^2/M^{1/2}$, in the limit $M \to 0$ with $\bar{\nu}$ constant the existence of hysteresis is necessarily precluded.

For $\bar{\nu} \gtrsim 1.125$, so that hysteresis is no longer present in the shallow-water equations, the $M = 0.4$ regime diagram is in reasonable agreement with its weakly nonlinear counterpart. Examining the diagrams more carefully, it appears that, in the weakly nonlinear limit, the region of parameter space for which transcritical flows occur is slightly overestimated, whilst transitions between the various transcritical flow regimes generally occur slightly closer to critical ($\bar{\Gamma} = 0$) than for the shallow-water flow.

Figure (5.9) compares the layer depth displacement $\phi = (\sigma - 1)/M^{1/2}$ in the weakly nonlinear limit with shallow-water flows at finite $M$, for representative flows with $\bar{\Gamma} > 0$. In each panel, the thick solid curve gives the weakly nonlinear layer depth displacement; shallow-water layer depth displacements for $M = 0.05$, $M = 0.1$, $M = 0.4$ are given by the dot-dash, dashed and dotted curves respectively. Vertical lines have been added to each panel to highlight the location of the obstacle edges at $x = \pm 1$. In each case, the rotation parameter $\bar{\nu} = 1.5$; the particular values of $\bar{\Gamma}$ for each panel are given in the figure caption. The location of each solution in $(\bar{\Gamma}, \bar{\nu})$ parameter space is indicated by a diamond in Figure 5.8.

The weakly nonlinear solutions are those discussed in the previous section. The shallow-water solutions are constructed in a similar 'semi-analytic'

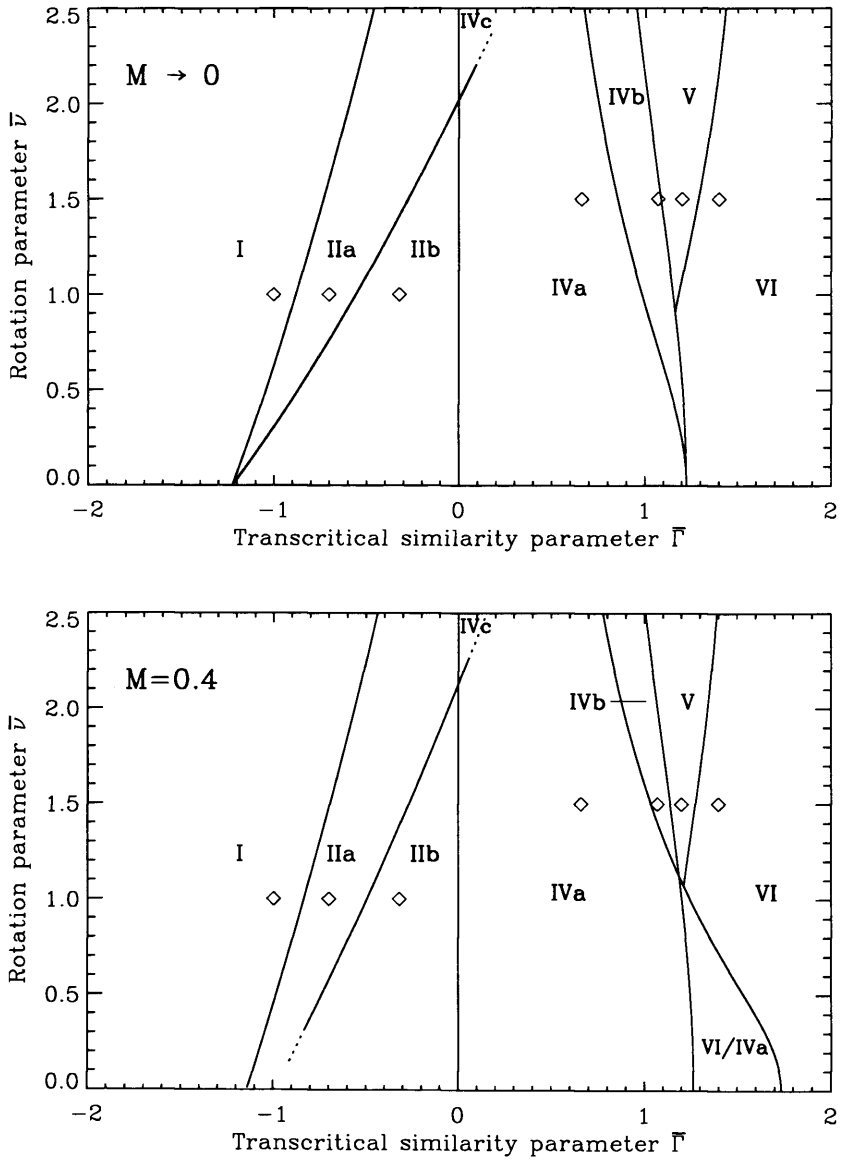


Figure 5.8: Transcritical similarity parameter / rotation parameter $(\bar{\Gamma}, \bar{\nu})$ regime diagrams for steady flow over the parabolic ridge (5.2). The flow regimes are as described previously. The upper panel corresponds to the weakly nonlinear limit described by (5.7); the lower panel corresponds to the shallow-water equations with finite obstacle height $M = 0.4$. Diamonds indicate the locations in parameter space of the example flows in Figures 5.9 & 5.10

fashion, described in detail by Esler *et al.* (2005).

When the flow over the obstacle remains supercritical, as is the case for solutions V and VI, the weakly nonlinear and finite $M$ layer depth displacements are barely distinguishable over most of the length of the obstacle. Some divergence is, however, apparent as the downstream edge of the obstacle is approached. The IVa solution, in which the flow over the obstacle is transcritical but jump free, indicates that in these circumstances the layer depth displacement over the obstacle is again well described by the weakly nonlinear theory, although here the divergence of the solutions is greater as the downstream edge of the obstacle is approached.

In the case that a jump stands over the obstacle, it is apparent from solution IVb that the discrepancies between the weakly nonlinear and finite $M$ layer depth displacements over the obstacle become significant. In the weakly nonlinear limit, the jump is located at approximately $x = 0.5$. As $M$ is increased, the jump moves toward the upstream edge of the obstacle and grows in amplitude, such that when $M = 0.4$ the jump stands just shy of the upstream edge of the obstacle. Interestingly, despite the jump amplitude and location differing appreciably, downstream of the point at which the jump in the weakly nonlinear solution occurs, the weakly nonlinear and finite $M$ solutions are again found to agree closely until the downstream edge of the obstacle is reached.

Downstream of the obstacle, the finite $M$ solutions are invariably less well described by the weakly nonlinear theory. The amplitude of the finite amplitude inertia-gravity wavetrain is consistently overestimated, and differences in the phase of solutions are apparent. When the downstream jump is the second of a pair of jumps (solutions IVa, IVb), its amplitude is underestimated by the weakly nonlinear theory. Conversely, for the regime

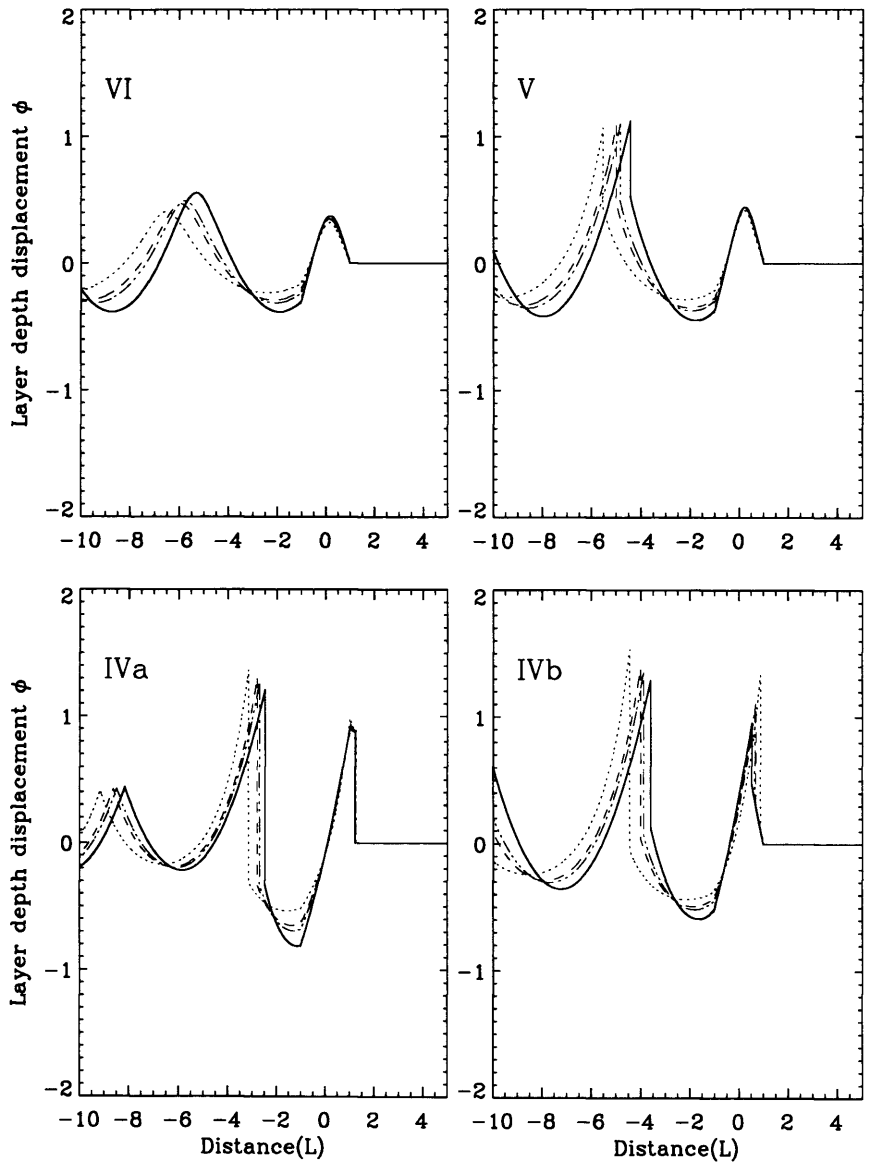


Figure 5.9: Comparing the layer depth displacement $\phi = (\sigma - 1)/M^{1/2}$ in the limit $M \to 0$ (described by equation (5.7)) with shallow-water layer depth displacements at finite obstacle heights $M$. In each panel the thick solid curve gives the $M \to 0$ displacement; the shallow-water displacements for $M = 0.05, 0.1, 0.4$ are given by the dot-dash, dashed and dotted curves respectively. Vertical lines in each panel indicate the obstacle edges, at $x = \pm 1$. The values of the transcritical similarity parameter are as follows: (VI) $\bar{\Gamma} = 1.4$; (V) $\bar{\Gamma} = 1.2$; (IVb) $\bar{\Gamma} = 1.07$; (IVa) $\bar{\Gamma} = 0.66$. In each case, the rotation parameter is given by $\bar{\nu} = 1.5$. The locations of each solution in $(\bar{\Gamma}, \bar{\nu})$ parameter space are indicated by diamonds in Figure 5.8.

V solution the amplitude of the downstream jump is overestimated. In either case, jumps downstream of the obstacle are invariably located further downstream for finite $M$ solutions than in the weakly nonlinear limit.

The weakly nonlinear theory is not always in error concerning jump location however. The upstream jumps of the IVa solutions match near-exactly between each of the solutions presented.

Figure 5.10 offers comparisons for representative flows with $\bar{\Gamma} < 0$. Here, the rotation parameter $\bar{\nu} = 1$ in each case; the particular values of $\bar{\Gamma}$ for each panel are given in the figure caption. The location of each solution in $(\bar{\Gamma}, \bar{\nu})$ parameter space is indicated by a diamond in Figure 5.8.

It is clear that for each possible flow configuration, subcritical flows with finite values of $M \leq 0.4$ are well described by the weakly nonlinear theory.

Partly, this is in accordance with our observations of flows with $\bar{\Gamma} > 0$: the weakly nonlinear theory performs best over the obstacle, and for subcritical oncoming flows the solution is largely confined to the immediacy of the obstacle. The greatest discrepancies are evident in the IIb solution - the only one of the three presented in which much of note happens downstream of the obstacle.

However, the precision with which the location and amplitude of hydraulic jumps are captured might still appear surprising. Reconsidering the supercritical flows, the upstream jump of the IVa solution is in fact described by the weakly nonlinear theory with good precision. Thus we conclude that it is the differences in wave length and amplitude of inertia-gravity waves between weakly nonlinear flows and 'similar' shallow-water flows at finite values of $M$ that result in the lesser accuracy of the weakly nonlinear approximation for supercritical oncoming flows.

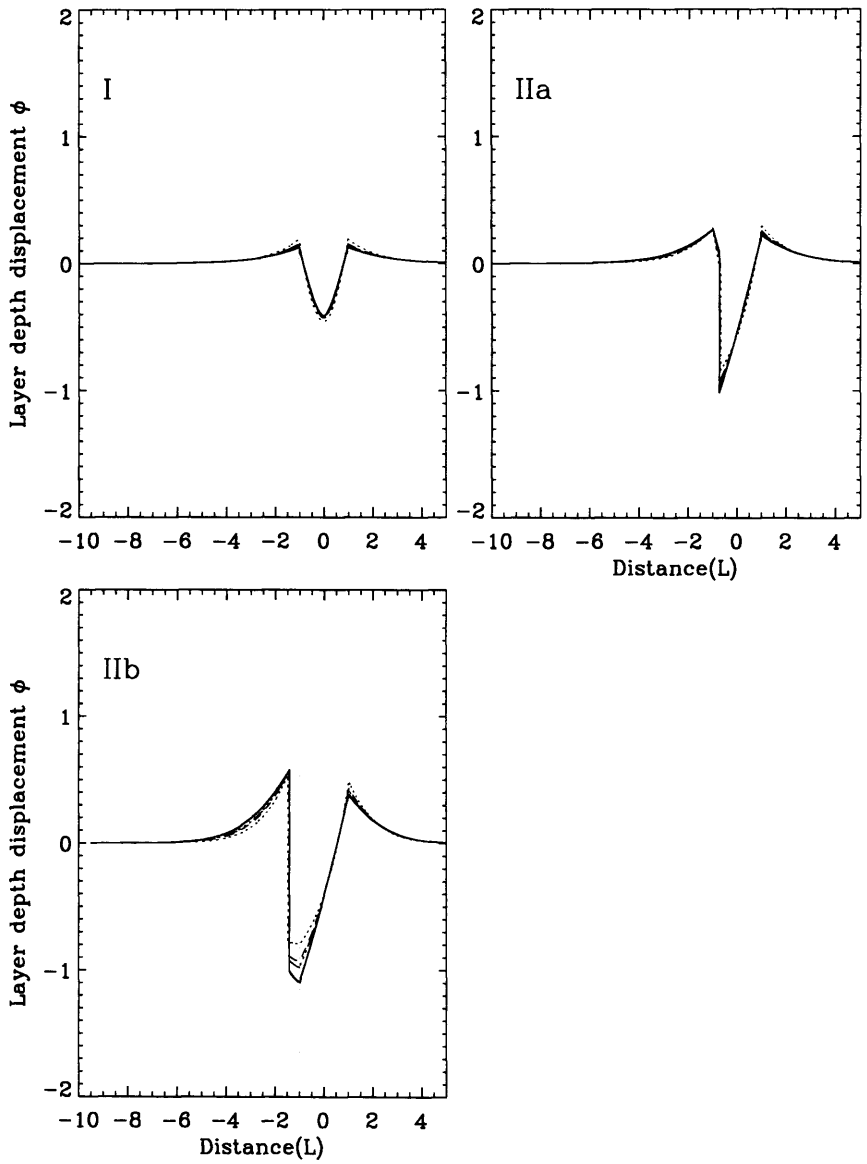


Figure 5.10: Comparing the layer depth displacement $\phi = (\sigma - 1)/M^{1/2}$ in the limit $M \to 0$ (described by equation (5.7)) with shallow-water layer depth displacements at finite obstacle heights $M$. In each panel the thick solid curve gives the $M \to 0$ displacement; the shallow-water displacements for $M = 0.05, 0.1, 0.4$ are given by the dot-dash, dashed and dotted curves respectively. Vertical lines in each panel indicate the obstacle edges, at $x = \pm 1$. The values of the transcritical similarity parameter are as follows: (I) $\bar{\Gamma} = -1$; (IIa) $\bar{\Gamma} = -0.7$; (IIb) $\bar{\Gamma} = -0.32$. In each case, the rotation parameter $\bar{\nu} = 1$. The locations of each solution in $(\bar{\Gamma}, \bar{\nu})$ parameter space are indicated by diamonds in Figure 5.8.

## 5.4 Conclusions

Solutions for steady flow over an infinite ridge with parabolic profile (5.2) have been discussed, in both the shallow-water equations and a weakly nonlinear limit appropriate for the transcritical regime.

Several important differences relative to non-rotating shallow-water flow over a ridge have been highlighted. In the absence of rotation, for sufficiently high obstacles the flow may become completely blocked; in the presence of rotation the oncoming flow is never blocked in the steady state. For sufficiently large values of the obstacle inverse Burger number $\mathcal{B}_m$, rotation acts to suppress the hysteresis encountered in non-rotating flow. Distinctive characteristics of rotating flow fields include the appearance of stationary hydraulic jumps both upstream and downstream of the obstacle, and the generation of an infinite wavetrain of nonlinear inertia-gravity waves downstream of an obstacle in initially supercritical flow.

The weakly nonlinear limit captures all the qualitative behaviour of solutions to the shallow-water equations, but for the region of hysteresis possible in the shallow-water system for sufficiently small values of $\mathcal{B}_m$. Both regime diagrams and flow fields also bear quantitative comparison with shallow-water flows at finite obstacle height $M$. Perhaps the greatest quantitative disparities result from the differing wavelengths and amplitudes of finite amplitude inertia-gravity waves between weakly nonlinear flows and 'similar' shallow-water flows at different values of $M$.

# Chapter 6

# Transcritical, rotating flow over topography

We now turn our attention to rotating flows over three-dimensional obstacles. Much of the work presented here appears in Esler *et al.* (2007*c*). In Chapter 2, it was shown that, in the limit of small $M$, transcritical, rotating shallow-water flow over topography is described by the rTSD equation (2.16), together with the equivalent aerofoil boundary condition. For convenience, both the equation and boundary condition are recalled:

$$(-2\Gamma - 3\phi_x)\,\phi_{xx} - \nu^2\phi + \phi_{YY} = 0, \quad \text{with} \quad \phi_Y(x,0) = K_x(x) \quad \text{on} \quad Y = 0. \tag{6.1}$$

In this limit, rotating shallow-water flow over an obstacle, which is a three-parameter $(M, F, B)$ problem, is reduced to the two parameter $(\Gamma, \nu)$ aerofoil problem.

In the discussion of solutions to the (non-rotating) TSD equation presented in Chapter 4, it was observed that flows over 'compact' and 'non-compact' obstacles presented distinct characteristics. In the current chap-

| Obstacle | $h(r)$ | $K(x)$ |
|---|---|---|
| Witch of Agnesi | $\frac{a^3}{(a^2+r^2)^{3/2}}$ | $\frac{a^3}{a^2+x^2}$ |
| $(a = 1/2)$ | | |
| Paraboloid | $1 - r^2$ | $\frac{2}{3}(1 - x^2)^{\frac{3}{2}}$ |
| | $(r < 1)$ | $(\|x\| < 1)$ |

Table 6.1: The 'Witch of Agnesi' and paraboloid obstacles, and corresponding 'equivalent aerofoils'.

ter, attention will be restricted to but one example of each case, namely the paraboloid and 'Witch of Agnesi' obstacles. To avoid excessive page turning, these obstacles, together with their 'equivalent aerofoils', are recalled in Table 6.1 above.

## 6.1 Transcritical rotating flows: the rTSD limit

In the previous chapter, it was demonstrated that the introduction of rotation produces a rich variety of 'new' flow configurations (relative to non-rotating flow), characterised by the appearance of multiple hydraulic jumps in the vicinity of the ridge. In the absence of rotation, at most one hydraulic jump is present in the vicinity of the ridge, so that the possibility of multiple jumps must be considered one of the fundamental qualitative consequences of rotation.

This difference is mirrored in the nature of solutions to the rTSD equation. Without rotation, solutions to the TSD equation may be either purely subcritical, purely supercritical or transcritical. For transcritical flows in which the oncoming flow is subcritical, there is a *single* embedded region of supercritical flow, located over the obstacle, which may or may not ex-

tend aft of the downstream edge of the obstacle. For transcritical flows in which the oncoming flow is supercritical, there is a *single* embedded region of subcritical flow, enclosing the upstream edge of the obstacle.

For subcritical oncoming flows, the presence of rotation in the rTSD equation introduces no further possible flow configurations; however, the location in parameter space of the transition from the embedded region of supercritical flow lying entirely over, or extending aft of, the obstacle is dependent on the rotation parameter $\nu$.

For supercritical oncoming flows the presence of rotation in the rTSD equation introduces a variety of possible flow configurations, which, as in the case of flow over a two-dimensional ridge, are characterised by the possibility of multiple hydraulic jumps, and their attendant embedded regions of subcritical flow.

First, a regime diagram describing the qualitative behaviour of transcritical rotating flow over a three-dimensional obstacle is constructed. Initially, the possible flow configurations are discussed for flow over the paraboloid obstacle. Although in Chapter 4 it was demonstrated that the transcritical theory performed better for the 'Witch of Agnesi' obstacle, solutions for flow over the paraboloid obstacle will be discussed in greater detail since it is possible to distinguish between configurations in which embedded regions of subcritical flow lie on or off the obstacle. Further, a direct comparison with the discussion of transcritical, rotating flow over the parabolic ridge of the previous chapter is possible. Subsequently, to ameliorate fears that the paraboloid obstacle might exhibit some rather singular behaviour, the corresponding regime diagram for the 'Witch of Agnesi' obstacle is briefly discussed.

### 6.1.1 *Regime diagram for the rTSD equation*

The upper panel of Figure 6.1 illustrates the regime diagram for the rTSD equation in transcritical similarity parameter / rotation parameter $(\Gamma, \nu)$ space for flow over the paraboloid obstacle. Regime boundaries are established through numerical solution of the rTSD equation (6.1). The regime diagram is to be examined in conjunction with Figure 6.2, in which steady-state free surface displacement fields $\eta$, illustrating various regimes in Figure 6.1, are contoured. Each panel in Figure 6.2 is labelled in its bottom right hand corner according to the regime of Figure 6.1 to which it belongs. Triangles in Figure 6.1 indicate the precise location of each example free surface displacement field in $(\Gamma, \nu)$ space.

In *regime I* of Figure 6.1, the flow is entirely subcritical throughout the domain. The solution is symmetric in $x$ and the effect of rotation is to cause the solution to decay rapidly away from the obstacle such that the lateral extent of the wave field is reduced relative to its non-rotating counterpart.

In *regime II*, the flow field contains an embedded region of supercritical flow. Fluid is accelerated smoothly from subcritical to supercritical over the obstacle (shaded region in panel), before decelerating back to subcritical abruptly via an hydraulic jump. Although the presence of rotation introduces no new flow configurations relative to the non-rotating case, the location of the transition from purely subcritical to transcritical flow (the functional $\Gamma_-$ discussed in Chapter 2) is affected, moving closer to critical flow ($\Gamma = 0$) as $\nu$ is increased. Thus the region of parameter space for which transcritical solutions exist in $\Gamma < 0$ is reduced. Regime II may be subdivided as follows. In *regime IIb* the region of embedded supercritical flow extends aft of the downstream edge of the obstacle, and the characteristic 'fishtail' system of jumps is observed (see, e.g. Chapman, 2000). In *regime*

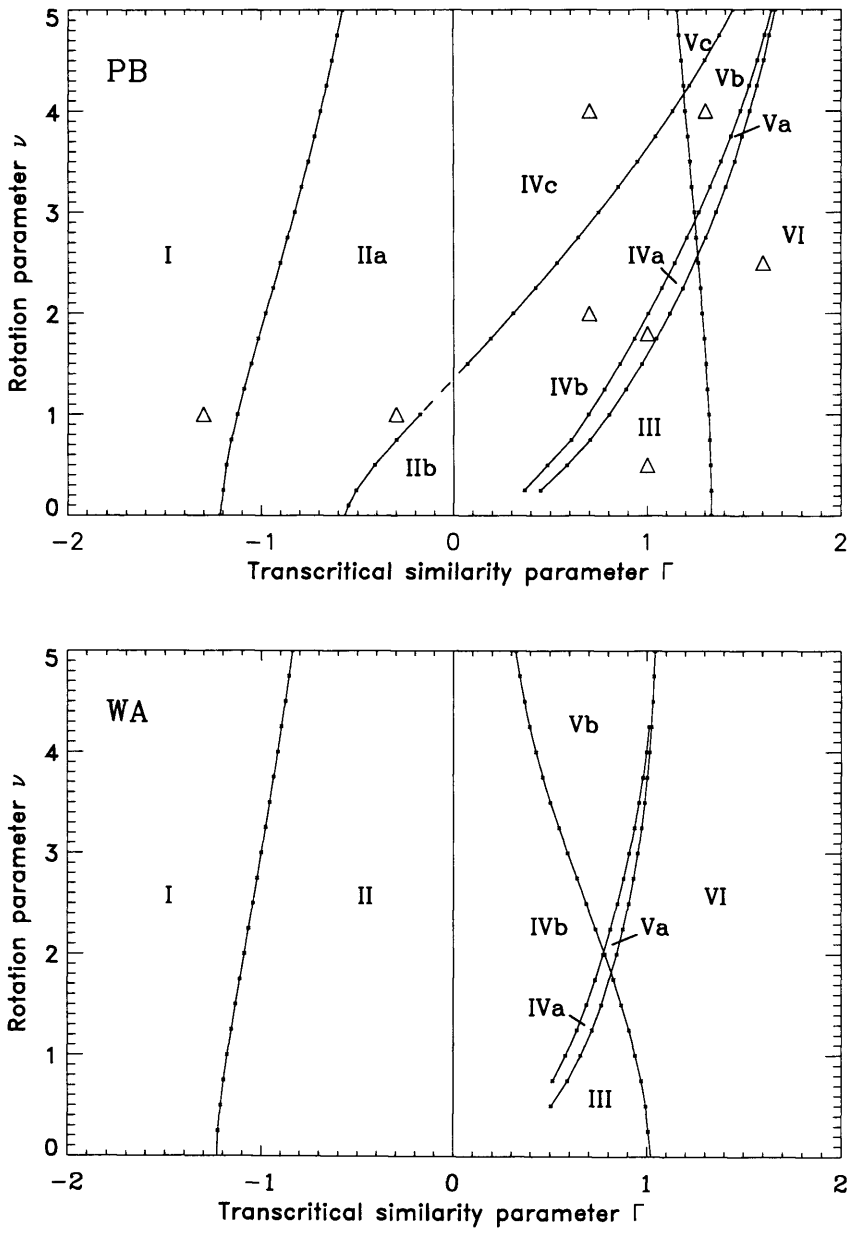


Figure 6.1: Transcritical similarity parameter/rotation parameter $(\Gamma, \nu)$ regime diagrams for steady solutions to the rTSD equation (6.1) corresponding to flow over the paraboloid (upper panel) and 'Witch of Agnesi' (lower panel) obstacles. Flow regimes labelled in the figure are described in the accompanying text. Triangles denote the location in $(\Gamma, \nu)$ space of the example free surface displacement fields given in Figure 6.2.

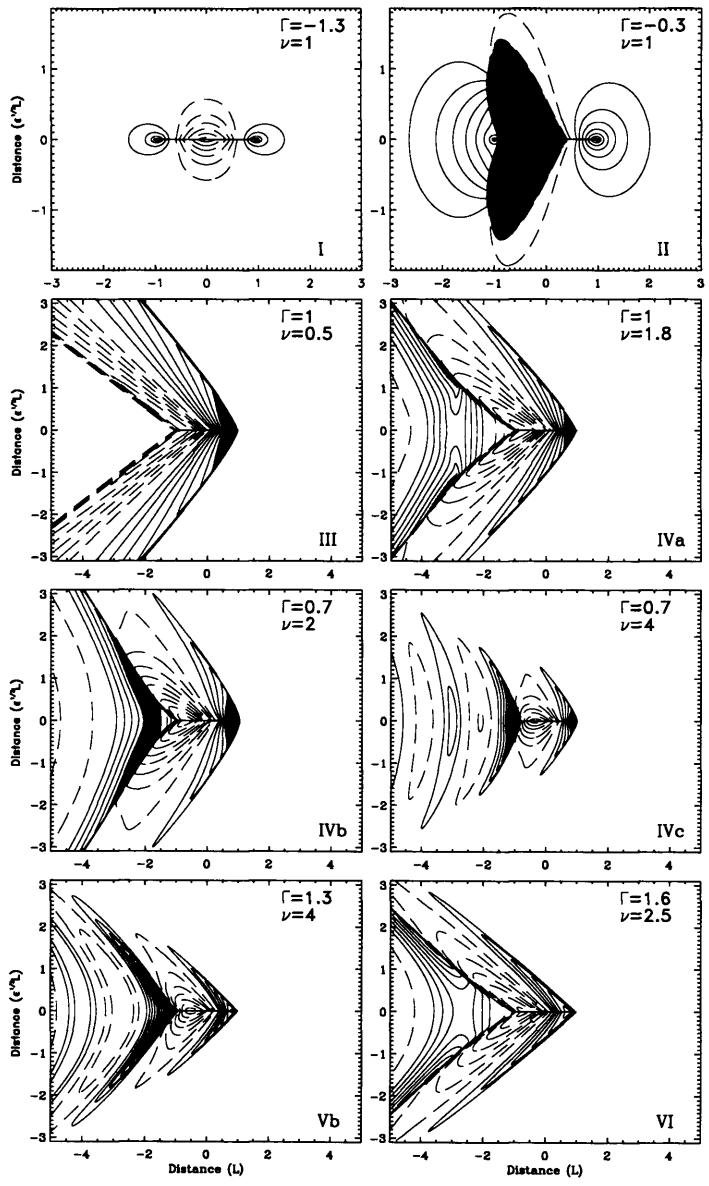


Figure 6.2: Steady state free surface displacement fields illustrating various regimes in the rTSD equation (6.1) discussed in the text. Results are for the paraboloid obstacle, and are derived from numerical solutions of the rTSD equation, with spatial resolution $\delta x = \delta y = 0.01L$. Contour intervals are $0.1\epsilon H$ in each panel ($\epsilon = M^{2/3}$). Values of $\Gamma$, $\nu$ are given in the top right of each panel; Roman numerals in the bottom right corner of each panel indicate to which region of the regime diagram (Figure 6.1) each solution belongs, the exact location of each solution being indicated in Figure 6.1 by a triangle. Regions of subcritical flow are shaded, except for the top right panel where the shaded region indicates supercritical flow.

*IIa* however, the effect of rotation is sufficiently strong that the embedded region of supercritical flow lies entirely over the obstacle, and the 'fishtail' system of jumps is destroyed.

For supercritical oncoming flow throughout *regime III*, the displacement field closely resembles that of non-rotating flow. A single embedded region of subcritical flow encloses the upstream edge of the obstacle; at the upstream boundary of this region is an hydraulic jump beyond which the flow is undisturbed. Downstream of the obstacle, the flow returns to its undisturbed state through a supercritical leap. Here, the distinction is made between an hydraulic jump (a jump connecting supercritical to subcritical flow), and a supercritical leap which connects two supercritical regions via a jump.

In *regime IV*, the flow field no longer resembles that of non-rotating flow. An embedded region of subcritical flow still encloses the upstream edge of the obstacle; however, further embedded regions of subcritical flow appear downstream of the obstacle. It is the nature of these further regions that leads to the subdivision into regimes IVa, IVb and IVc. In *regime IVa*, two further embedded regions of subcritical flow are found downstream of the obstacle either side of the centreline $Y = 0$, shown by the shaded regions in $x < 0$ in the corresponding panel of Figure 6.2. It is important to note that, for a fixed $0 < \Gamma < \Gamma_+$, these two further embedded regions of subcritical flow do not migrate from $x = -\infty$ toward $x = 0$ as the rotation parameter $\nu$ is increased, but rather appear at finite distance downstream of the obstacle as the boundary between regimes III and IVa is crossed. The jump to the rear of the obstacle, though continuous, changes from being a supercritical leap to an hydraulic jump as the embedded regions of subcritical flow are encountered.

As the rotation rate is further increased, this pair of embedded subcritical regions extend closer to the centreline $Y = 0$, until they meet to form a single embedded region of subcritical flow and a broad hydraulic jump lying downstream of the obstacle. This flow configuration is found throughout *regime IVb*. Along the centreline $Y = 0$, three jumps are now encountered, giving the 'fishtail' system of jumps to the rear of the obstacle seen in the corresponding panel in Figure 6.2. On further increasing the rotation parameter $\nu$, this single embedded region of subcritical flow to the rear of the obstacle moves closer to the downstream edge of the obstacle until the regime boundary is crossed into regime IVc. In *regime IVc*, the rotation is sufficiently strong that the rear embedded region of subcritical flow encloses the downstream edge of the obstacle. Along the centreline $Y = 0$, two jumps are again encountered, just as in non-rotating flow; but both jumps are now hydraulic jumps connecting regions of supercritical flow to regions of subcritical flow, whereas in the non-rotating scenario, this pair of jumps comprises a single hydraulic jump together with a supercritical leap.

In *regime V*, the hydraulic jump upstream of the obstacle, which gradually decreases in strength and lateral extent as rotation is increased, is finally destroyed. There is no longer a region of embedded subcritical flow enclosing the upstream edge of the obstacle. Embedded regions of subcritical flow are, however, still found downstream of the obstacle. The nature of these leads to a subdivision into regimes Va, Vb, and Vc in a manner analogous to that of regime IV. In *regime Va*, the downstream region of embedded subcritical flow is split into two parts about the centreline $Y = 0$. In *regime Vb* the two regions join to give a single region of embedded subcritical flow downstream of the obstacle; in *regime Vc* rotation becomes sufficiently strong that the embedded subcritical region is confined to lie entirely over the ob-

stacle. Since these subdivisions coincide with those of regime IV, Figure 6.2 includes an example only from regime Vb.

Finally, in *regime VI*, the flow is everywhere supercritical. Region VI flows are characterised by supercritical leaps that lie approximately along the 'Mach lines' emanating from the upstream and downstream edges of the obstacle. Note that the boundary between regimes III/V and VI represents the variation of the functional $\Gamma_+$ (discussed in Chapter 2) with $\nu$.

Throughout regimes IV, V & VI, a wavetrain analogous to the transcritical inertia-gravity waves discussed in the previous chapter is found downstream of the obstacle.

Also in the previous chapter, it was noted that the nature of the transition from purely supercritical to transcritical flow in the context of shallow water flows over a parabolic ridge is dependent on the obstacle inverse Burger number $\mathcal{B}_m$. For $\mathcal{B}_m < 2$, the supercritical transition was found to resemble that of the non-rotating case, whereas for $\mathcal{B}_m > 2$ the transition assumed a different character. This behaviour was also observed in the transcritical, rotating limit. Returning to the rTSD regime diagram for the paraboloid, and in the light of the above discussion, it is clear that the the character of the supercritical transition for transcritical rotating flow over a three-dimensional obstacle exhibits similar behaviour. For $\nu \lesssim 2.5$ the transition from purely supercritical to transcritical flow closely resembles that of non-rotating flow: the emergent region of subcritical flow appears first at the upstream edge of the obstacle. For $\nu > 2.5$ however, the supercritical transition takes on a new character, with a region of embedded subcritical flow first appearing downstream of the obstacle.

The lower panel of Figure 6.1 shows a similar regime diagram corresponding to the 'Witch of Agnesi' obstacle. Flow regimes are labelled in the

same manner as for the paraboloid obstacle, so that the above text describes the various flow regimes encountered. In the case of the 'Witch of Agnesi' obstacle, however, no distinction can be made between regions of embedded subcritical/supercritical flow lying on or off the obstacle since the obstacle is not compact. Therefore, the curves indicating transition to type 'c' regimes are absent. This aside, the regime diagram is qualitatively similar to that for the paraboloid obstacle. Perhaps the most notable difference between the two is that, for relatively high rotation rates - $\nu \gtrsim 2$ say - the transition from regime IV solutions which have jumps both ahead of and behind the obstacle, to regime V solutions in which only the rear jump is present, occurs at much lower values of $\Gamma$ for the 'Witch of Agnesi' obstacle. Further, the change in character of the supercritical transition noted above in this case occurs for $\nu \sim 1.7$ - significantly lower than for the paraboloid obstacle. Thus it could be argued that, although solutions for the paraboloid and 'Witch of Agnesi' obstacles are qualitatively similar, the effects of rotation for a given value of $\nu$ are felt more strongly by the 'Witch of Agnesi' obstacle than the paraboloid. Primarily, however, the 'Witch of Agnesi' regime diagram has been constructed in order to check that the regime diagram of the paraboloid is not a singular example.

### 6.1.2 *Variation of drag with rotation parameter $\nu$ in the rTSD limit*

As discussed in Chapter 2, an important aspect of the problem under consideration is the determination of the drag exerted on the flow by obstacles in the transcritical regime. Figure 6.3 shows the drag function $D(\Gamma)$ for fixed values of $\nu$ calculated from a series of steady numerical solutions to the rTSD equation (6.1) with values of $\Gamma$ in the range $[-1.5, 3]$. In the non-rotating case ($\nu = 0$) the drag curve rises steeply on the subcritical side,

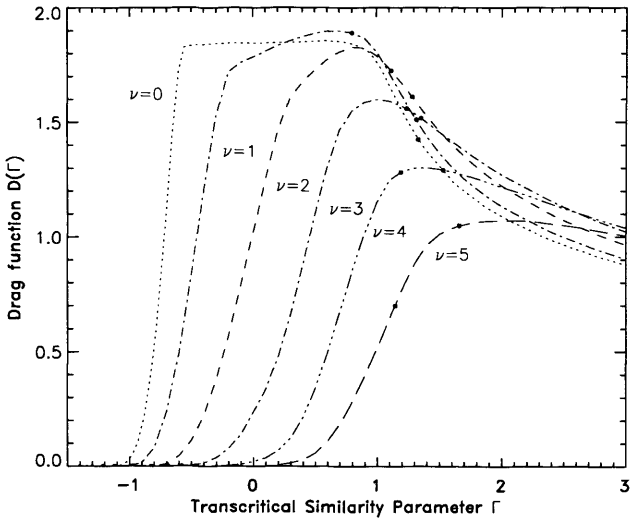


Figure 6.3: The drag function $D(\Gamma)$ as a function of the transcritical similarity parameter $\Gamma$ for various fixed values of the rotation parameter $\nu$, calculated from a series of steady numerical solutions of the rTSD equation (6.1) for the equivalent aerofoil corresponding to the paraboloid obstacle (PB).

plateaus close to its peak value $D_m$, then decays rather gradually on the supercritical side. In Chapter 4, it was seen that very similar drag curves were found for all the obstacles considered.

It is clear from Figure 6.3 that rotation has a strong and systematic effect on the drag exerted by the obstacle on the flow. As $\nu$ increases, the range of $\Gamma < 0$ for which significant drag is exerted decreases, to the extent that when $\nu = 5$ the drag exerted by the obstacle for $\Gamma < 0$ is negligible. Initially, the peak drag $D_m$ increases with increasing $\nu$ until $\nu \sim 2$, when $D_m$ roughly coincides with its non-rotating counterpart. $D_m$ then decreases with further increases in $\nu$. As $\nu$ increases, the value of $\Gamma > 0$ at which the peak drag $D_m$ occurs increases, as does the range of $\Gamma > 0$ for which $D(\Gamma)$ remains close to its maximum.

At all values of $\nu$ investigated, the drag is found to approximate to its

non-rotating value for sufficiently large $\Gamma$. Solid circles on each curve indicate the location of the regime boundaries of Figure 6.1. In some cases, these may be seen to pick out points of inflection on the corresponding drag curve.

## 6.2 Transcritical rotating flows: shallow-water

The question naturally arises as to what extent solutions to the rTSD equation represent those of the full rotating shallow-water theory. In Chapter 4, the corresponding theory without rotation was found to be reasonably accurate for $M \lesssim 0.4$ and $|\Gamma| \lesssim 1$. Do all the regimes present in the rTSD equation exist at finite obstacle height $M$ in the rotating shallow water equations? Are drag and regime boundary predictions still reasonable?

Figure 6.4 shows steady free surface displacement fields $\eta$ obtained from numerical integrations of the rotating shallow-water equations (1.15). For each panel, the obstacle is of height $M = 0.4$, with the values of the Froude number $F$ and inverse Burger number $B$ subsequently chosen to give the same values of $\Gamma$, $\nu$ as for the corresponding panels in Figure 6.2. The locations in ($\Gamma$,$\nu$) space of the panels correspond to the triangles in the regime diagram (Figure 6.1). Contour intervals have been scaled by $\epsilon$ for consistency with the transcritical asymptotic theory results shown in Figure 6.2, in which the $Y$-scale was chosen to allow exact comparison with Figure 6.4.

Comparison of Figures 6.2 and 6.4 reveals that each of the regimes identified in the rTSD equation persist at finite obstacle height $M = 0.4$, with the small caveat that in regime IVa (second from top right-hand panel of Figure 6.4) the embedded region of subcritical flow to the rear of the obstacle in $y > 0$ has disappeared. Further, each regime is identified within the expected region of parameter space in the regime diagram constructed

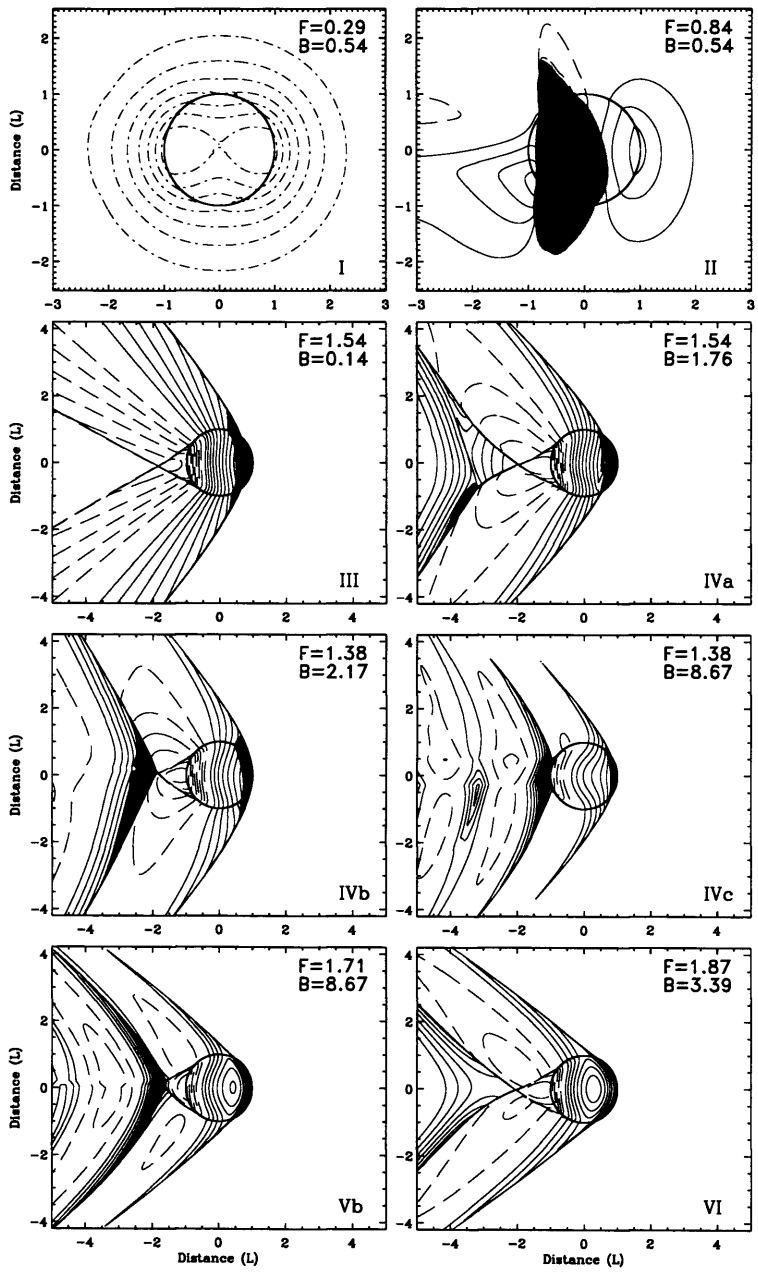


Figure 6.4: Steady state free surface displacement fields illustrating shallow water flow over the paraboloid obstacle with non-dimensional height $M = 0.4$. Results are derived from numerical solutions of the rotating shallow-water equations, with spatial resolution $\delta x = \delta y = 0.01L$. Contour intervals are $0.1\epsilon H$ in each panel, except for the top left panel in which the contour interval is $0.01\epsilon H$. Values of $F$, $B$ are given in the top right of each panel and correspond to the values of $\Gamma$,$\nu$ in Figure 6.2; Roman numerals in the bottom right corner of each panel indicate to which region of the regime diagram (Figure 6.1) each solution belongs, the exact location of each solution being indicated in Figure 6.1 by a triangle. Regions of subcritical flow are shaded, except for the top right panel where the shaded region indicates supercritical flow.

for the rTSD equation (Figure 6.1). In the case of purely subcritical flow (top left-hand panel of Figure 6.4), however, the solution to the full rotating shallow water equations is markedly different from the corresponding rTSD solution. This is unsurprising, since the disturbance to the free-surface elevation in the shallow-water solution is confined largely to being over the obstacle, whereas the rTSD solutions are formally valid only in the far field. The top right-hand panel of Figure 6.4 also seems to indicate significant vorticity generation at the jump, the mechanism for which has, in the absence of rotation, been discussed by Schär & Smith (1993b).

Qualitatively, the most obvious failing of the asymptotic theory is its inability to capture the asymmetry of the flow fields observed in Figure 6.4. Both this asymmetry and the vorticity generation noted above simply enter at higher order in the asymptotic development of Chapter 2.

Figure 6.5 is a plot of drag $\mathcal{D}$ scaled by $M^2$, against the Froude number $F$ of the oncoming flow, for the paraboloid obstacle. The top left panel shows non-rotating results ($\nu = 0$), the top right panel results for $\nu = 2$ and the bottom left panel results for $\nu = 5$. The bottom right panel repeats results for $\nu = 5$, in this case zoomed in on the dotted rectangle from the left hand panel, better to illustrate the behaviour close to $F = 1$ for the $M = 0.4$ solutions. In each case, the drags predicted by the asymptotic theory and linear rotating and non-rotating theories are compared with drags evaluated numerically from the shallow-water model. In Esler *et al.* (2007*b*), the linear rotating drag $\mathcal{D}$ for a general axisymmetric obstacle $h(r)$ is shown to be given by

$$\mathcal{D} = \frac{2\pi M^2}{F\sqrt{F^2-1}} f\left(\frac{|\sqrt{B}|}{\sqrt{F^2-1}}\right) \quad \text{with} \quad f(s) = \int_s^\infty \frac{\hat{h}(\kappa)^2\kappa^3}{\sqrt{\kappa^2-s^2}}d\kappa \,, \qquad (6.2)$$

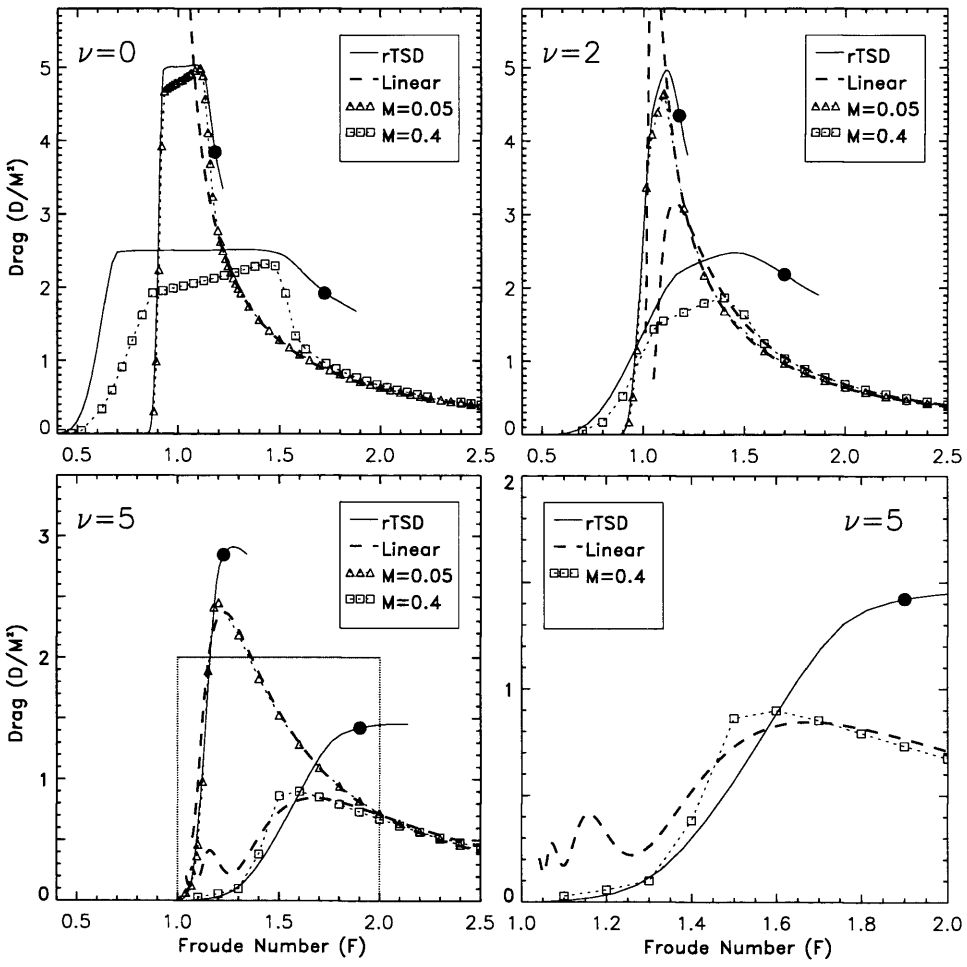


Figure 6.5: Drag $\mathcal{D}$, scaled by obstacle height $M^2$, as a function of Froude number $F$ for flow over the paraboloid obstacle with the rotation parameter $\nu$ = 0,2,5. Triangles and squares mark the results of shallow-water model results for $M = 0.05$ and 0.4 respectively. The solid lines show the transcritical similarity theory predictions for the drag in each case, derived from the rTSD numerical results, with the Froude number corresponding to the supercritical transition ($\Gamma = \Gamma_+$) marked as a solid circle. The dashed curves show the linear supercritical drags, given by equation (6.2).

| Obstacle | $h(r)$ | $\hat{h}(\kappa)$ | f(s) |
|---|---|---|---|
| Paraboloid | $1-r^2$ $(r<1)$ | $\frac{2}{\kappa^2}J_2(\kappa)$ | $\frac{1}{s^3}(6H_2(2s)-2sH_1(2s))$ |

Table 6.2: The Hankel (Fourier-Bessel) transform of the paraboloid obstacle, and the corresponding function f(s) giving the dependence of the drag $\mathcal{D}$ on the rotation rate. $J_2(z)$ is the Bessel function of the first kind of order 2; $H_n(z)$is the Struve function of order $n$.

where $\hat{h}(\kappa)$ is the Fourier transform of the obstacle $h(r)$. The functions $\hat{h}(\kappa)$ and $f(s)$ particular to the paraboloid obstacle are given in Table 6.2. The thick dashed curves in each picture are the linear supercritical drags, and the series of solid curves shows the rTSD predictions for transcritical drags. The rTSD drag curves are plotted for $\Gamma_- < \Gamma < 1.5$ in each case, with $\Gamma_+$ illustrated as a solid point on each curve. The rotating shallow-water numerical results for obstacle heights $M = 0.05$ and $M = 0.4$ are plotted as symbols (triangles and squares respectively). Recall that the value $B$ of the rotation parameter in the shallow-water equations scales with $M^{2/3}$, so that $\nu = constant$ requires that the value of $B$ is adjusted with obstacle height $M$ as necessary in the shallow-water computations. It is clear that for $\nu = 0$, the calculated drags follow the TSD prediction for Froude numbers $F$ satisfying $\Gamma_- < \Gamma \lesssim \Gamma_+$. For $F$ satisfying $\Gamma \sim \Gamma_+$, the calculated drags begin to diverge from the TSD prediction, and rapidly converge to the supercritical linear solution given by the thick dashed curve, which is accurate for values of $F$ corresponding to $\Gamma \gtrsim 1.5$. For $\nu = 2$, the calculated drags are again well described by the corresponding rTSD prediction for a range of values of $\Gamma$. However, the linear supercritical predictions given by the thick dashed curves now offer a more accurate prediction for a small range of values of $F$ satisfying $\Gamma < \Gamma_+$. That is, although a combination of the rTSD and linear

drag predictions still constitute a reasonable description of the observed drag behaviour at finite obstacle height, the range of Froude numbers for which the rTSD drag prediction is superior to its linear counterpart is reduced. This trend is continued to $\nu = 5$, when the $M = 0.4$ rTSD drag prediction appears to be reasonable for less than half of the range of Froude numbers $F$ satisfying $\Gamma < \Gamma_+$. However, the accompanying zoomed figure in the bottom right hand panel indicates that the rTSD drag can offer an improved estimate relative to its linear counterpart, albeit for a rather small range of $F$. In summary, if the rule of thumb 'we estimate the drag to be the minimum of the linear and transcritical predictions' were taken, a reasonable description of the observed behaviour at finite obstacle height would be achieved.

As discussed in Chapter 1, the location in obstacle height - Froude number $(M, F)$ space of the transitions from purely subcritical / supercritical flow to transcritical flow has, in the context of non-rotating shallow-water flow, received considerable attention. We now briefly consider the effects of rotation on the location of these boundaries. Figure 6.6 shows the calculated regime diagrams for the paraboloid obstacle, for both non-rotating ($\nu = 0$) and rotating flow with $\nu = 2$. The region of parameter space where purely supercritical flow is found is labelled SPC, subcritical flow SBC and transcritical flow TC. The locations in $(M, F)$ space where transition has been found to occur in shallow water numerical calculations are labelled with stars. The predictions from the transcritical theory, which are expected to be accurate for small $M$, are plotted as solid curves. The dotted curves show the corresponding results, valid for all $M$ but particular to the parabolic obstacle of Chapter 5, for one-dimensional flow over a ridge. For both rotating and non-rotating flows, the calculated locations of the transition curves diverge somewhat from the transcritical theory for values of $M$ approaching

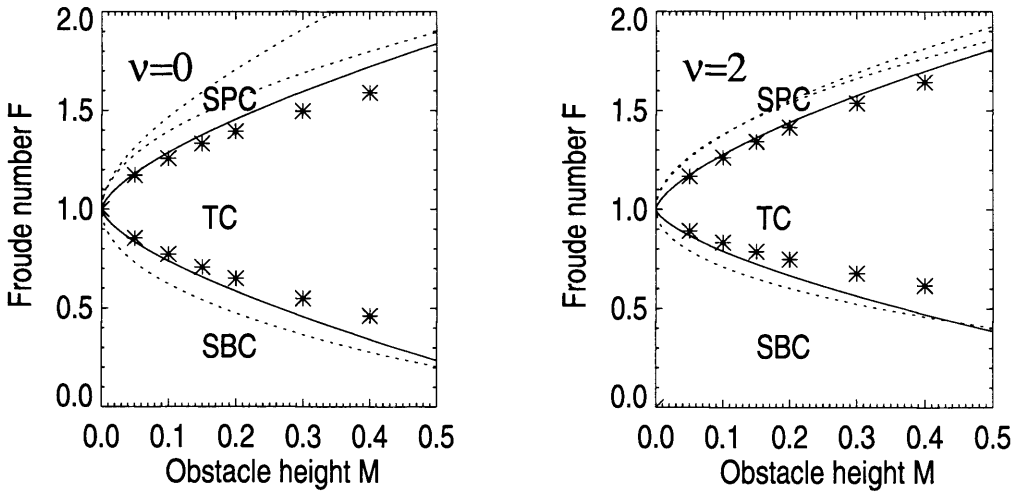


Figure 6.6: Illustrating the flow regimes (SBC - subcritical, TC - transcritical, SPC - supercritical), in obstacle height - Froude number ($M$,$F$) parameter space, for flow over the paraboloid obstacle with $\nu = 0,2$. The solid lines show the predictions for the supercritical and subcritical transitions calculated from the rTSD solutions ($F = 1 + \Gamma_+ M^{2/3}, F = 1 + \Gamma_- M^{2/3}$). The dotted curves show the corresponding results for one-dimensional obstacles, valid for all $M$ (c.f. Chapters 1 & 5). The stars show the location of the actual transitions found in each case from a sequence of steady numerical solutions of the shallow-water equations (1.15).

0.5, although this is unsurprising since, as noted in Chapter 4, the transcritical theory is less accurate when $|\Gamma|$ is relatively large, as it is in the region of the transition curves. The dashed curves corresponding to the one-dimensional transitions show a marked deviation between the rotating and non-rotating cases, which is not readily apparent in the corresponding predictions from the transcritical theory or indeed the calculated shallow-water transitions.

A peculiarity of the the transcritical asymptotic theory presented (c.f. Chapter 2) is that, despite the leading order free surface displacement $\eta$ and streamwise velocity $u$ fields being symmetric in $Y$, the corresponding leading order transverse velocity $v$ field diagnosed is not anti-asymmetric about $Y = 0$ (as it is in non-rotating flow). This is highlighted in Figure 6.7. The top left hand panel shows the $v$ field diagnosed from the rTSD flow around the equivalent aerofoil, and the lower left panel shows the $v$ field from the corresponding rotating shallow-water flow at obstacle height $M = 0.4$. Note that the $y$-axis and contour intervals in each panel have been scaled for consistency with the transcritical asymptotic theory. The upper right and lower right-hand panels show cross sections of the transverse velocity $v$ along $y = 1$ (solid line) and $y = -1$ (dashed line) for the rTSD and rotating shallow-water flows respectively. Again, results have been scaled for consistency with the transcritical asymptotic theory. Both the contour plots of the fields and the cross sections indicate that the transcritical theory offers a very reasonable qualitative diagnosis of the $v$ field, even at finite obstacle height $M = 0.4$.

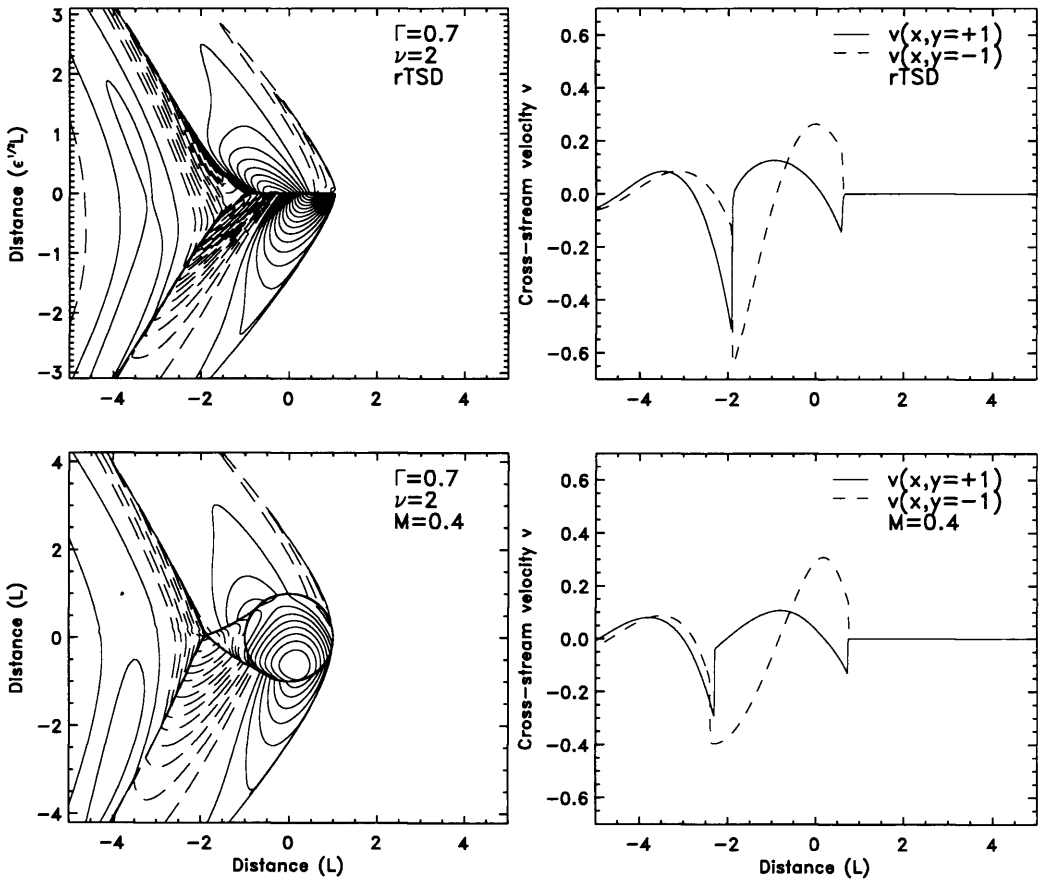


Figure 6.7: Upper panels: (Left) Contour plot of the leading order transverse velocity field $v_0^o(x, Y)$ as diagnosed from the rTSD solution for flow over the paraboloid obstacle with $\Gamma = 0.7$ and $\nu = 2$. The contour interval is $0.1\epsilon^{3/2}c$, (note that $\epsilon^{3/2} = M = 0.4$ allows comparison with the lower panel results). (Right) Cross sections of $v_0^o(x, Y)$ at $Y = 0.4^{1/3} \approx 0.7368$ (solid curves) and $Y = -0.4^{1/3}$ (dashed curve). (Note that these values of $Y$ are chosen to correspond to the edge of an obstacle of unit radius when $M = 0.4$ as below, and the $v$-axis is also scaled by $\epsilon^{3/2} = M = 0.4$). Lower panels: (Left) As for the upper panels but for $v(x, y)$, the solution of the rotating shallow-water equations for the PB obstacle with $M = 0.4$, $F = 1.3800$, $B = 2.1715$ (giving $\Gamma = 0.7$ and $\nu = 2$) with contour interval $0.04c$. (Right): Cross sections of v(x,y) at $y = 1$ (solid curve) and $y = -1$ (dashed curve).

## 6.3 Discussion

Rotating transcritical flows have been investigated in the simplified setting of the rTSD equation, derived in Chapter 2. Rich behaviour associated with the presence of rotation has been identified, characterised by the appearance of multiple embedded regions of subcritical flow and associated hydraulic jumps. Comparison with numerical solutions of the full rotating shallow-water equations indicates that the flow regimes investigated persist at least up to finite obstacle height $M = 0.4$. Drag predictions from the transcritical theory, together with its linear supercritical counterpart, combine to offer a reasonably complete description of the drag behaviour in the full problem.

# Chapter 7

# Supercritical, rotating flow over topography

In Chapter 2, an asymptotic theory describing the wake development with increasing distance $\mathcal{Y}_*$ from an axisymmetric obstacle in supercritical, rotating flow was introduced that is formally valid for $M \ll 1$ and $F-1 \gg M^{2/3}$. For convenience, we restate the far-field equation for the leading order free surface displacement field $\eta$ obtained, dropping sub and superscripts:

$$(2\gamma\eta\eta_{\mathcal{Y}_*} + 3\eta\eta_{\mathcal{X}})_{\mathcal{X}} - \hat{\nu}^2\eta = 0. \tag{7.1}$$

Equation (7.1) is the Ostrovsky-Hunter equation, with the 'stretched' space variable $\mathcal{Y}_*$ assuming the role of the time-like variable. The 'initial' condition for (7.1), determined by matching with an inner solution, is given by

$$\eta(\mathcal{X},0) = -\frac{1}{\gamma}\mathcal{X}G(\mathcal{X}) \quad \text{where} \quad G(\mathcal{X}) = \int_{|\mathcal{X}|}^{\infty} \frac{h'(r)}{\sqrt{r^2-\mathcal{X}^2}}\,dr. \tag{7.2}$$

The obstacles considered and the resulting functions $G(\mathcal{X})$ are recalled

in Table 7.1.

| Obstacle | $h(r)$ | $G(\mathcal{X})$ | $\beta_1$ | $\beta_2$ |
|---|---|---|---|---|
| Witch of Agnesi | $\frac{a^3}{(a^2+r^2)^{3/2}}$ | $\frac{-2a^3}{(\mathcal{X}^2+a^2)^2}$ | 0.20 | 0.0178 |
| $(a = 1/2)$ | | | | |
| Gaussian | $\exp\{-\frac{r^2}{a^2}\}$ | $-\frac{\sqrt{\pi}}{a}\exp\{-\frac{\mathcal{X}^2}{a^2}\}$ | 0.18 | 0.0481 |
| $(a = 1/\sqrt{2})$ | | | | |
| Cone | $1-\frac{r}{a}$ | $-\frac{1}{a}\cosh^{-1}\left\{\frac{a}{\lvert\mathcal{X}\rvert}\right\}$ | - | - |
| $(a = \sqrt{3/2})$ | $(r < a)$ | $(\lvert\mathcal{X}\rvert < a)$ | | |
| Hemi-ellipsoid | $\sqrt{1-\frac{r^2}{a^2}}$ | $-\frac{\pi}{2a}$ | - | - |
| $(a = \sqrt{3}/2)$ | $(r < a)$ | $(\lvert\mathcal{X}\rvert < a)$ | | |
| Paraboloid | $1-r^2$ | $-2\sqrt{1-\mathcal{X}^2}$ | - | - |
| | $(r < 1)$ | $(\lvert\mathcal{X}\rvert < 1)$ | | |

Table 7.1: Obstacle shapes investigated, 'initial condition' functions $G(\mathcal{X})$ and wave breaking bounds for the Ostrovsky-Hunter equation (7.3), discussed in the text.

Recalling the definition $\hat{\nu} = \sqrt{B/M}$, equation (7.1) together with (7.2) can be rescaled into the canonical problem

$$(u_{\bar{t}} + uu_{\mathcal{X}})_{\mathcal{X}} - u = 0, \quad \text{with} \quad u(\mathcal{X}, 0) \equiv u_0(\mathcal{X}) = -\beta\mathcal{X}G(\mathcal{X}), \tag{7.3}$$

with the initial condition amplitude $\beta$ being given by

$$\beta = \frac{3M}{B\sqrt{F^2-1}}. \tag{7.4}$$

Note that $\beta$ can be arbitrarily large without invalidating any of the assump-

tions of the theory of Chapter 2, since $B$ can be arbitrarily small. Clearly from (7.3), for a given obstacle, the supercritical, rotating obstacle wake is self-similar to the extent that its qualitative nature is a function solely of the non-dimensional parameter $\beta$.

## 7.1 The Ostrovsky-Hunter equation

In the absence of rotation, equation (7.3) reduces to the Hopf equation

$$u_{\bar{t}} + uu_{\mathcal{X}} = 0, \tag{7.5}$$

with an appropriately modified initial condition (c.f. Chapter 4). Using the method of characteristics (see, e.g. Whitham, 1974), it is easily demonstrated that if the initial condition $u(\mathcal{X}, \bar{t} = 0) \equiv u_0(\mathcal{X})$ is such that $u_{0\mathcal{X}}(\zeta) < 0$ for some $\zeta$, then solutions to the Hopf equation (7.5) break in finite time. Thus for localised or periodic boundary conditions, finite time wave breaking must always occur.

One fundamental question concerning the Ostrovsky-Hunter equation (7.3) is whether the low-wavenumber dispersion introduced by rotation can inhibit wave breaking. To answer this question in the context of the current work will require resort to solving the Ostrovsky-Hunter equation numerically. First, known results concerning the Ostrovsky-Hunter equation are briefly discussed.

The Ostrovsky-Hunter equation is but one example of a broad family of equations exhibiting low-wavenumber dispersion, first identified by Whitham in his book (Whitham, 1974, pp476-482) , which in general may

be written (Grimshaw and Rosales, personal communication)

$$u_{\bar{t}} + uu_{\mathcal{X}} = v, \tag{7.6}$$

where $u = u(\mathcal{X}, \bar{t})$ and either

$$v = K * u = \int_0^{2\pi} K(\mathcal{X} - y)u(y, \bar{t})dy, \tag{7.7}$$

or

$$v = K * u = \int_{-\infty}^{+\infty} K(\mathcal{X} - y)u(y, \bar{t})dy, \tag{7.8}$$

for some $K$. When (7.7) applies, it is taken that both $u$ and $K$ are periodic in $\mathcal{X}$. Whitham's motivation for introducing equations of this type was to describe waves both peaking and breaking.

As pointed out by Boyd (2005), the particular case of the Ostrovsky-Hunter equation exhibits both types of behaviour. First he notes that, on defining a moving coordinate $X \equiv \mathcal{X} - c\bar{t}$, the Ostrovsky-Hunter equation has a limiting-amplitude travelling wave solution of the peaked parabolic corner wave

$$u(X) = \frac{\pi^2}{9} - \frac{\pi}{3}|X| + \frac{1}{6}X^2 \ , \ X \in [-\pi, \pi] \ , \ c = \frac{\pi^2}{9}.$$

The above definition may be extended to all $X$ by spatial periodicity. Secondly, he points out that numerical experiments demonstrate that, for a given spatial period, solutions that exceed the maximum height of the corner wave will steepen and eventually break at some finite time $\bar{t}_b$. Perhaps more surprisingly, however, Boyd notes that the following dilation theorem ensures that initial conditions of arbitrarily small amplitude can break in the Ostrovsky-Hunter equation.

**Theorem 7.1** *Ostrovsky-Hunter dilation. Let $v(\mathcal{X},\bar{t})$ be a solution of the Ostrovsky-Hunter equation (7.3). Then for all $\lambda > 0$,*

$$u(\mathcal{X},\bar{t}) \equiv \frac{1}{\lambda^2} v(\lambda\mathcal{X}, \frac{1}{\lambda}\bar{t})$$

*is also a solution.*

Thus, as Boyd points out, for any given amplitude of the initial condition for the Ostrovsky-Hunter equation, wave breaking must always occur provided that the initial condition has sufficiently small spatial scale. Boyd dubs this concept 'microbreaking'.

This strongly suggests that it is not the amplitude of the given initial condition for the Ostrovsky-Hunter equation which determines whether wave breaking will occur, but rather the gradient of the initial condition. This indeed turns out to be the case; the following theorem has been proved by Grimshaw and Rosales (unpublished work, personal communication).

**Theorem 7.2** *Wave Breaking Theorem (Grismhaw and Rosales). Assume that the kernel $K$ in (7.7,7.8) is such that*

$$\|K * u\|_\infty \leq \kappa_1 \|u\|_\infty \quad \textit{and} \quad \|(K * u)_\mathcal{X}\|_\infty \leq \kappa_2 \|u\|_\infty$$

*for some $0 \leq \kappa_1, \kappa_2 < \infty$. Let $0 < \mathcal{A} = \|u_0\|_\infty < \infty$ be the $L_\infty$ norm of the initial data for (7.3) which is assumed to be smooth. Then for any fixed $0 < \mathcal{A} < \infty$, there is a constant $-\infty < \mathcal{B} < 0$ such that:*

$$\textit{If} \quad \frac{du_0}{d\mathcal{X}}(\mathcal{X}_0) < \mathcal{B} \quad \textit{for some} \quad -\infty < \mathcal{X}_0 < \infty,$$

*then a smooth solution cannot exist for all times. That is, there exists a finite time $0 < \bar{t}_b < \infty$ such that, for some $-\infty < \zeta < \infty$ one has $u_\mathcal{X}(\zeta, \bar{t}_b) = -\infty$.*

Consider now the particular case of the Ostrovsky-Hunter equation (7.3). On a periodic domain, the conditions of the theorem are clearly satisfied. Indeed, letting $M = ||u_0||_\infty$ and $m = -inf \partial_\mathcal{X} u_0(\mathcal{X})$, the following explicit breaking condition was first recognised by Hunter (1990): if

$$\frac{m^3}{4+m} > 4M,$$

then periodic solutions on $[0, 1]$ of the Ostrovsky-Hunter equation break in finite time.

On $\Re$ however, the infinity norm of the operator $K$ corresponding to the Ostrovsky-Hunter equation is unbounded, so that the conditions of the wave breaking theorem are not satisfied. To the best of the author's knowledge, the establishment of an analytic criterion for wave breaking in the Ostrovsky-Hunter equation on an infinite domain remains an open problem. However, at least for the 'zero-mass' class of initial conditions encountered in the

current work, the existence of such a condition seems highly probable. That is, a wave breaking bound may be established numerically such that, at least for the cases considered, the behaviour of solutions is consistent relative to that bound.

## 7.2 Numerical solution of the Ostrovsky-Hunter equation

Two facets of the solution of the Ostrovsky-Hunter equation (7.3) are to be investigated. In the first instance, the breaking bounds described above are to be determined numerically. Although in principle the finite volume method could be employed, the accuracy with which breaking bounds might be established would be questionable: first, a numerical wave breaking criterion would need to be established in an heuristic fashion; secondly, as $\beta$ is reduced, the amplitude of the initial condition is decreased so that solutions become increasingly difficult to resolve numerically. Fortunately, the following representation of the equation serves to remedy these issues.

The Ostrovsky-Hunter equation (7.3) may be rewritten in characteristic form as

$$\frac{\partial \mathcal{X}}{\partial \bar{t}} = u, \quad \frac{\partial u}{\partial \bar{t}} = \int^{\chi} u(\chi', \bar{t}) d\chi' \quad \text{on} \quad \zeta = \text{constant}, \tag{7.9}$$

where $\zeta = \chi$ at $\bar{t} = 0$. Differentiating with respect to $\zeta$ reveals the system

$$\frac{\partial}{\partial \bar{t}}(\mathcal{X}_\zeta) = u_\zeta, \quad \frac{\partial}{\partial \bar{t}}(u_\zeta) = u\mathcal{X}_\zeta, \tag{7.10}$$

subject to the initial conditions

$$\mathcal{X}_\zeta = 1, \quad u_\zeta = u_0'(\zeta) \quad \text{at} \quad \bar{t} = 0. \tag{7.11}$$

The advantage of this formulation is the following: when wave breaking occurs we have $u_\mathcal{X} \to -\infty$; in the parametric form above, since $u_\mathcal{X} = u_\zeta / \mathcal{X}_\zeta$ this corresponds to $\mathcal{X}_\zeta = 0$. Thus wave breaking may be diagnosed by an order one quantity passing through zero, as opposed to a numerical diagnosis of an increasingly under-resolved solution. System (7.10) together with the initial conditions (7.11) may be solved accurately and efficiently using a pseudospectral method (see, e.g. Boyd, 2005).

An analysis of the asymptotic theory requires that solutions of the Ostrovsky-Hunter equation be compared to those of the full shallow-water equations. Although the above technique is accurate and efficient for diagnosing breaking bounds, at the onset of wave breaking the parametric formulation allows waves to overturn, rather than fitting a shock. Thus, to facilitate a comparison with the results of the full shallow-water equations, the Ostrovsky-Hunter equation must be solved using a shock fitting code; this is implemented rather easily in CLAWPACK. For the purposes of implementing a finite volume scheme, equation (7.3) may first be integrated in $\mathcal{X}$, so that the equation to be solved can be regarded as the Hopf equation (7.5) with a source term. Similarly to the full shallow-water equations, the source term may be conveniently handled by the use of Strang splitting.

Figure 7.1 compares solutions of the Ostrovsky-Hunter equation (7.3) computed using the finite volume and pseudospectral parametric numerical formulations. The initial condition is that corresponding to the 'Witch of Agnesi' obstacle (see Table 7.1); $\beta = 1$ and solutions are shown for $\bar{t} = 2.6$.

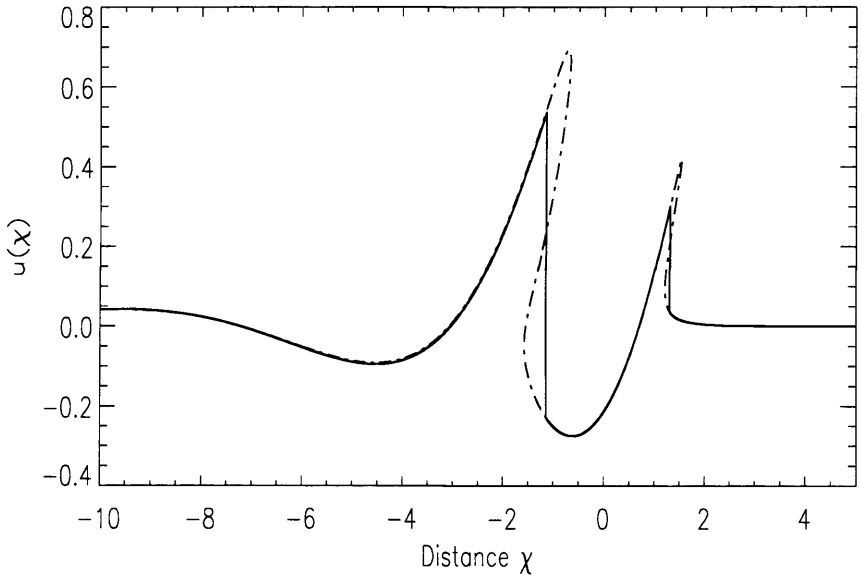


Figure 7.1: Comparison of numerical solutions to the Ostrovsky-Hunter equation (7.3) using pseudospectral and finite volume methods discussed in the text. The initial condition is that corresponding to the 'Witch of Agnesi' obstacle (see Table 7.1). The initial condition amplitude parameter $\beta = 1$, and the solution shown is for $\bar{t} = 2.6$. The solid line shows the CLAWPACK shock fitting solution, with spatial resolution $\delta\mathcal{X} = 0.00005$. The broken line shows the pseudospectral parametric solution, computed using 1024 Chebyshev nodes.

The solid line shows the CLAWPACK finite volume solution, with spatial resolution $\delta\mathcal{X} = 0.00005$, and the broken line shows the pseudospectral parametric solution, computed using 1024 Chebyshev nodes. The agreement between the solutions is excellent, and clearly demonstrates the 'equal areas' rule of shock fitting described by Whitham (1974).

### 7.2.1 *Breaking bounds*

Initial conditions corresponding to the obstacles introduced in Chapter 4, repeated in Table 7.1, are investigated. For the obstacles of compact sup-

port, the discontinuity in the first derivative of the initial condition $u_{0\mathcal{X}}(\mathcal{X})$ corresponding to the edge of the obstacle is found to result in wave breaking for arbitrarily small values of the parameter $\beta$. For initial conditions corresponding to the remaining obstacles, namely the 'Witch of Agnesi' and the Gaussian, numerically established threshold values of $\beta$ for wave breaking to occur are given in Table 7.1. The value $\beta_2$ corresponds to the bounds discussed previously: that is, for $\beta > \beta_2$, solutions to the Ostrovsky-Hunter equation (7.3) are invariably found to break in finite time; for values of $\beta$ less than $\beta_2$, solutions remain smooth for all time. Values of $\beta_2$ have been computed using the parametric pseudospectral numerical formulation, and are given to four decimal places. Further to the transition from solutions that break in finite time to smooth solutions, a transition from solutions exhibiting at most one wave breaking region (for all time) to solutions in which two wave breaking regions appear is also identified. Values of $\beta_1$ in Table (7.1) correspond to this second threshold. In this case, bounds have been established from finite volume solutions of (7.3), since the pseudospectral method is found to fail once the front shock becomes excessively steep; these bounds are likely to be less accurate than those computed using the pseudospectral method, and therefore are given to only 2 decimal places.

It is important to remember that all of these bounds have been computed numerically. Thus, the phrase "remain smooth for all time" must be treated with caution - any numerical solution necessarily encompasses only a finite time interval. However, extensive numerical tests have been performed so that such statements can be made with a degree of confidence; since these tests are of rather obvious importance, the results have been included in Appendix A.

Further to establishing these breaking bounds, a question of interest

concerns the 'order' in which wave breaking occurs: at the onset of wave breaking does the front shock or rear shock appear first? Is this order always preserved in the development of solutions with varying values of $\beta$? Although intuitively one might answer 'yes' to the latter, the previous chapter highlighted the fact that, in the steady transcritical limit, order is *not* preserved: for low rotation rates an hydraulic jump first appears at the leading edge of an obstacle, whereas for higher rotation rates an hydraulic jump first appears downstream of an obstacle. What happens in the case of the supercritical leaps of supercritical flow?

Figure 7.2 plots breaking times $\bar{t}_b$, as functions of the initial condition amplitude parameter $\beta$, for the initial conditions corresponding to the 'Witch of Agnesi' and Gaussian obstacles for $\beta$ in the range $[0.3, 4]$. In each panel, the solid line indicates the front shock and the dashed line the rear shock (to clarify, 'front' refers to the upstream side of the obstacle, 'rear' to the downstream side). For both obstacles it is seen that the order of breaking is the same for all values of $\beta$ considered: the rear shock always appears first. For solutions exhibiting only one wave breaking region, that is for $\beta_2 < \beta < \beta_1$, it is the rear shock that remains, the front shock having disappeared. Comparing breaking times between the two obstacles, the rear shocks show remarkably similar behaviour for the range of values of $\beta$ considered. For the front shocks, however, when $\beta < 1$ the breaking times for the 'Witch of Agnesi' obstacle are significantly longer than those for the Gaussian.

## 7.3 Comparison with shallow-water flows

To recapitulate, for small $M$ in non-dispersive, rotating, supercritical flow, the steady flow pattern away from the obstacle is described by the Ostrovsky-

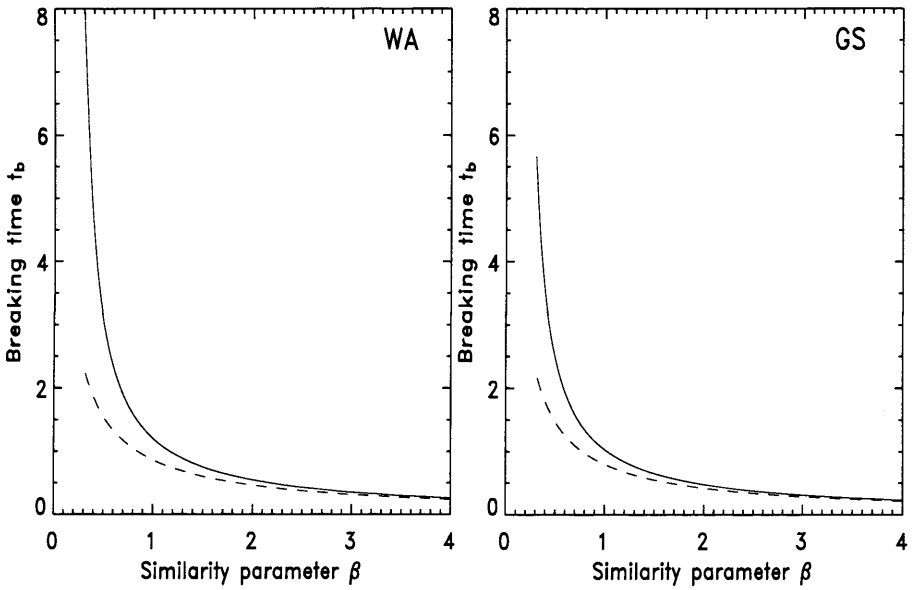


Figure 7.2: Breaking times $\bar{t}_b$ as a function of the initial condition amplitude amplitude parameter $\beta$, for initial conditions corresponding to the 'Witch of Agnesi' (WA) and Gaussian (GS) obstacles (see Table 7.1), derived from numerical solutions of the Ostrovsky-Hunter equation (7.3) using a pseudospectral parametric formulation. The solid line shows the breaking time for the front shock (ahead of the obstacle), and the dashed line the breaking time for the rear shock (downstream of the obstacle).

Hunter equation (7.3). In this limit, non-dispersive, rotating, supercritical shallow-water flow over an obstacle, which is a three-parameter problem $(M, F, B)$, is reduced to the single parameter $\beta$. Here the accuracy of predictions for the wake patterns and wave breaking are tested by comparison with numerical solutions of the full shallow-water equations with obstacles of finite height $M$.

Figure 7.3 shows a comparison of the steady free surface displacement field $\eta$ for shallow-water flow over the 'Witch of Agnesi' obstacle with $M = 0.1$, $F = 1.4$ and $B = 0.31$ so that $\beta = 1$, with the wake predicted by the asymptotic theory. The upper left and right panels correspond to the shallow

water solution, and show the steady state free surface displacement field $\eta$ and cross sections of $\eta$ along $y = +5$ (solid line) and $y = -5$ (dashed line) respectively. The lower panels show the corresponding solutions from the asymptotic theory. The lower left panel shows the steady state free surface displacement field $\eta$ reconstructed from solutions to the Ostrovsky-Hunter equation; since the asymptotic theory describes the wake development and is not expected to be accurate in the vicinity of the obstacle, contours in the interval $y \in (-1, 1)$ have been omitted. The lower right panel replots the cross sections of $\eta$ along $y = +5$ (solid line) and $y = -5$ (dashed line) from the shallow-water solution, together with the cross section of $\eta$ for $y = \pm 5$ from the asymptotic theory (thick line).

Comparing the free surface displacement fields, the asymptotic theory predicts the shallow water flow pattern rather well, excepting that the asymmetry evident in the shallow-water solution is not captured by the asymptotic theory. This is confirmed through comparison of cross sections of $\eta$, the cross section along $y = \pm 5$ from the asymptotic theory lying exactly in between the cross sections from $y = +5$ and $y = -5$ of the shallow-water solution. Considering the breaking bounds determined via numerical solutions of the Ostrovsky-Hunter equation, we see that in this case, for which $\beta = 1$, two wave breaking regions are expected; and indeed this is precisely what is observed.

Figure 7.4 shows a comparison of the steady free surface displacement field for shallow-water flow over the 'Witch of Agnesi' obstacle, here with $M = 0.2$, $F = 2$ and $B = 0.35$, so that again $\beta = 1$, with the wake predicted by the asymptotic theory. The individual panels are as described for Figure 7.3. Figure 7.5 shows a further comparison, again with $\beta = 1$, but now for $M = 0.1$, $F = 2$, $B = 0.17$. The arrangement of panels is as

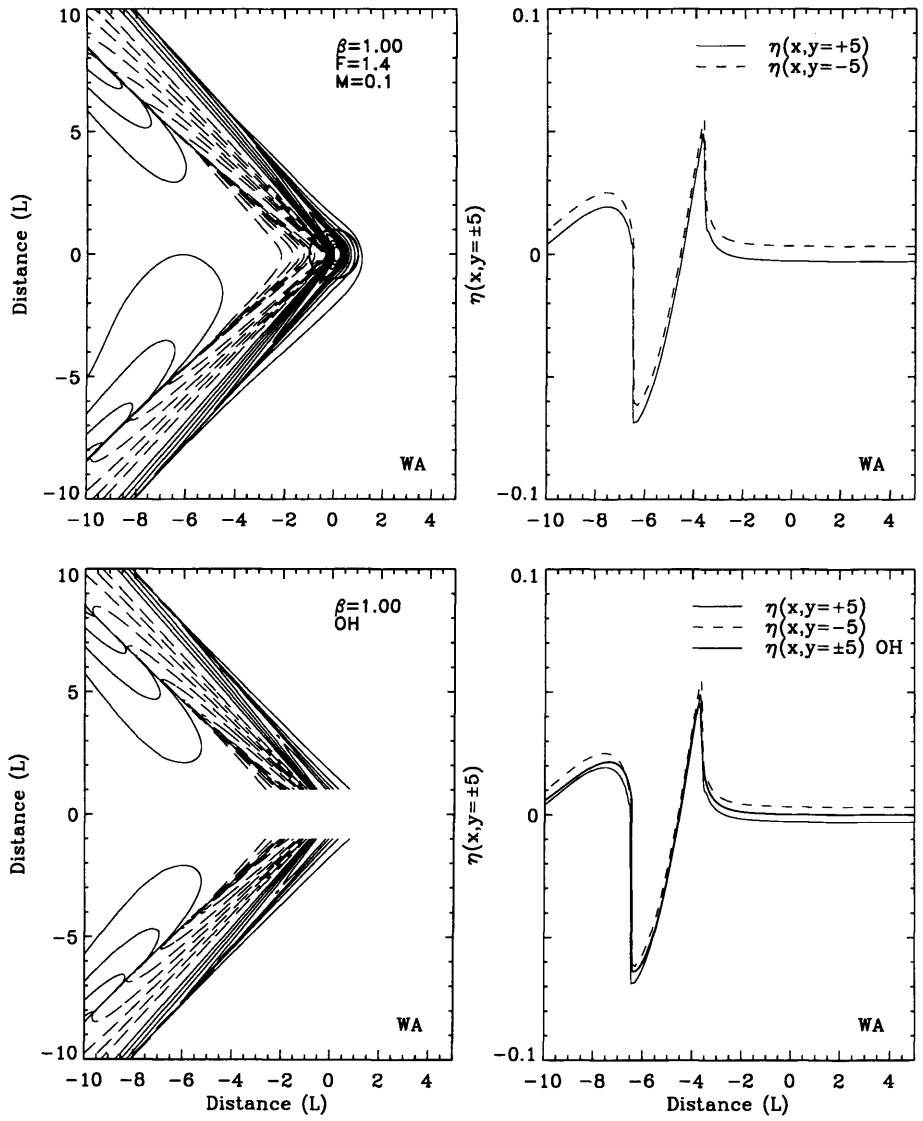


Figure 7.3: Illustrating the supercritical, rotating asymptotic theory for flow over the 'Witch of Agnesi' obstacle, with the similarity parameter $\beta = 1$. The top left panel shows the steady state free surface displacement field $\eta$ derived from numerical solution of the shallow-water equations, with spatial resolution $\delta x = 0.01$, $\delta y = 0.02$, for $F = 1.4$, $M = 0.1$ and $B = 0.31$. The lower left panel shows the corresponding steady free surface displacement field reconstructed from solutions to the Ostrovsky-Hunter equation (7.3), with spatial resolution $\delta \mathcal{X} = 0.00005$ and temporal resolution $\delta \bar{t} = 0.2$. Contour intervals are $0.01H$ in each panel. The upper right panel shows cross sections of $\eta$ along $y = +5$ (solid line) and $y = -5$ (dashed line) from the shallow-water solution. The lower right panel replots these cross sections, together with the cross section along $y = \pm 5$ derived from the Ostrovsky-Hunter solutions (thick line).

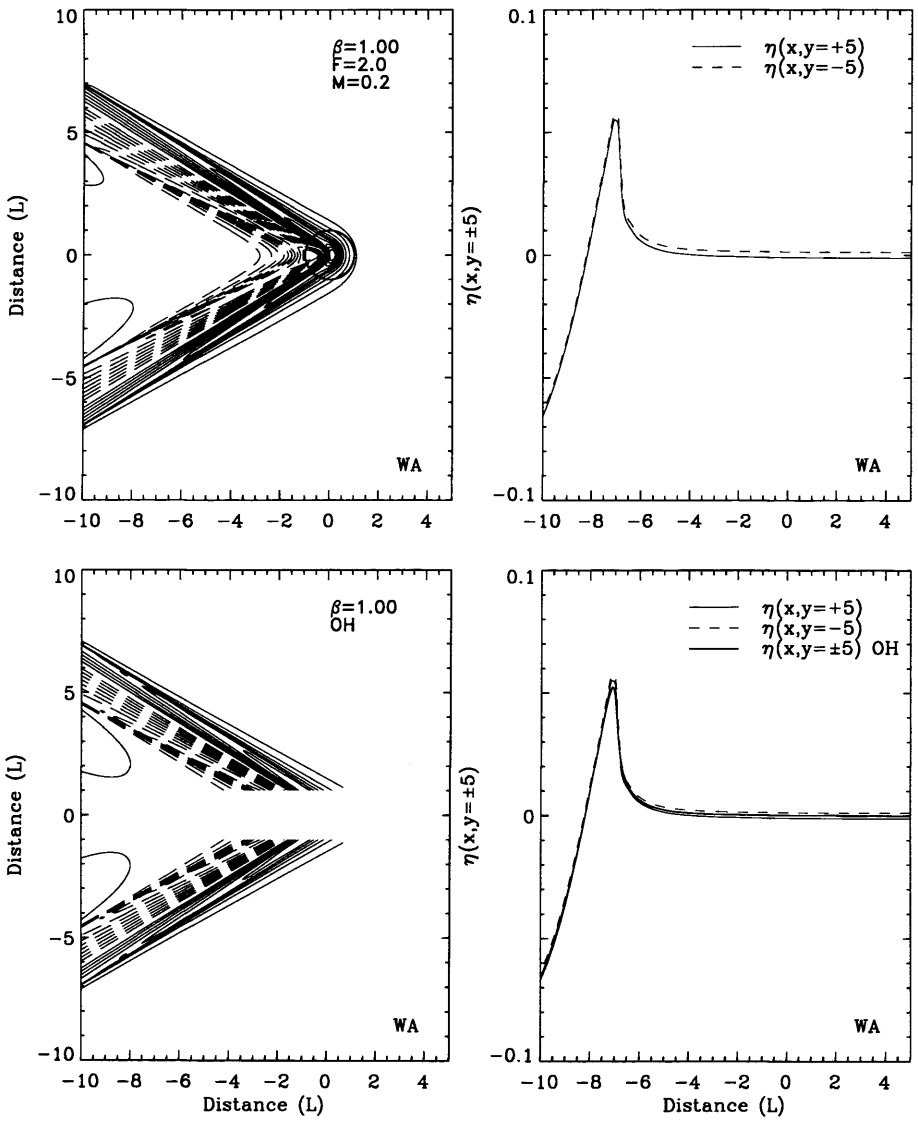


Figure 7.4: Illustrating the supercritical, rotating asymptotic theory for flow over the 'Witch of Agnesi' obstacle, with the similarity parameter $\beta = 1$. The top left panel shows the steady state free surface displacement field $\eta$ derived from numerical solution of the shallow-water equations, with spatial resolution $\delta x = 0.01$, $\delta y = 0.02$, for $F = 2.0$, $M = 0.2$ and $B = 0.35$. The lower left panel shows the corresponding steady free surface displacement field reconstructed from solutions to the Ostrovsky-Hunter equation (7.3), with spatial resolution $\delta \mathcal{X} = 0.00005$ and temporal resolution $\delta \bar{t} = 0.2$. Contour intervals are $0.01H$ in each panel. The upper right panel shows cross sections of $\eta$ along $y = +5$ (solid line) and $y = -5$ (dashed line) from the shallow-water solution. The lower right panel replots these cross sections, together with the cross section along $y = \pm 5$ derived from the Ostrovsky-Hunter solutions (thick line).

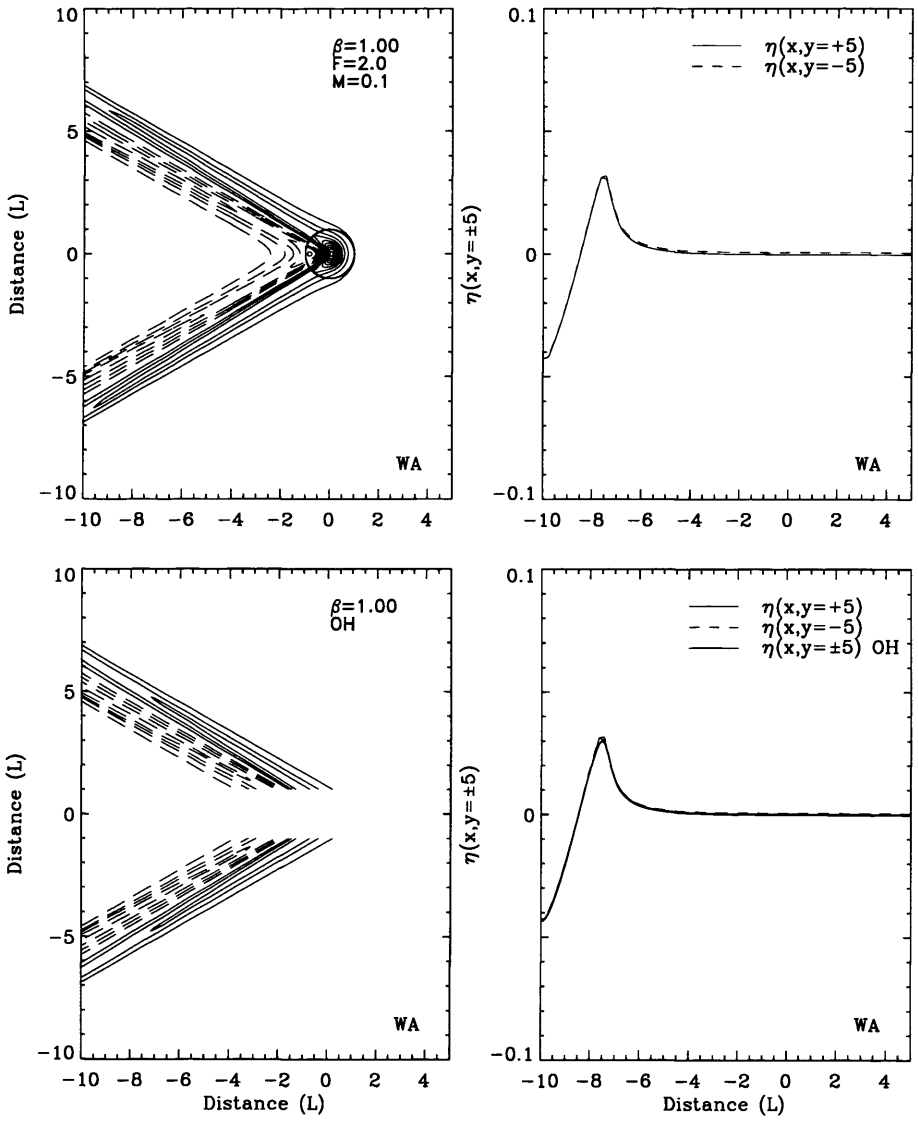


Figure 7.5: Illustrating the supercritical, rotating asymptotic theory for flow over the 'Witch of Agnesi' obstacle, with the similarity parameter $\beta = 1$. The top left panel shows the steady state free surface displacement field $\eta$ derived from numerical solution of the shallow-water equations, with spatial resolution $\delta x = 0.01$, $\delta y = 0.02$, for $F = 2.0$, $M = 0.1$ and $B = 0.17$. The lower left panel shows the corresponding steady free surface displacement field reconstructed from solutions to the Ostrovsky-Hunter equation (7.3), with spatial resolution $\delta \mathcal{X} = 0.00005$ and temporal resolution $\delta \bar{t} = 0.2$. Contour intervals are $0.01H$ in each panel. The upper right panel shows cross sections of $\eta$ along $y = +5$ (solid line) and $y = -5$ (dashed line) from the shallow-water solution. The lower right panel replots these cross sections, together with the cross section along $y = \pm 5$ derived from the Ostrovsky-Hunter solutions (thick line).

described previously. In both figures, the asymptotic theory again captures the shallow-water wake pattern rather well; for the three figures discussed so far, the asymptotic theory seems to perform equally well in each. Further, although wave breaking is not captured in the plotted domain of the latter two, two supercritical leaps are found in all three scenarios, as predicted by the asymptotic theory. The point of interest in comparing these figures lies in the fact that they illustrate the role of the parameter $\beta$. For all three flows $\beta = 1$; further, in all three cases the asymptotic form of the wake has been reconstructed from the same data set - that is, the same solutions of the Ostrovsky-Hunter equation. Thus the three solutions of the shallow-water equations, although they appear to be qualitatively different, are actually 'similar'.

Figure 7.6 compares the steady free surface displacement field $\eta$ for shallow-water flow over the 'Witch of Agnesi obstacle' with predictions from the asymptotic theory, the panels being as described previously. In this case, the combination $M = 0.1$, $F = 1.4$, $B = 3.06$ results in the value $\beta = 0.1$. Comparing this value with those in Table 7.1, we expect the flow to exhibit only one wave breaking region, and this turns out to be the case. The cross sections along $y = \pm 5$ pick out this wave breaking, a large amplitude supercritical leap being clearly visible. Similarly to the $\beta = 1$ cases discussed previously, the obstacle wake is well described by the asymptotic theory. This is particularly encouraging in light of the fact the the value of the inverse Burger number $B$ - assumed to scale with M in the derivation of the theory (c.f. Chapter 2) - is significantly larger than for the examples discussed previously.

Figure 7.7 shows a comparison of the steady free surface displacement fields for shallow-water flows over the 'Witch of Agnesi' and paraboloid ob-

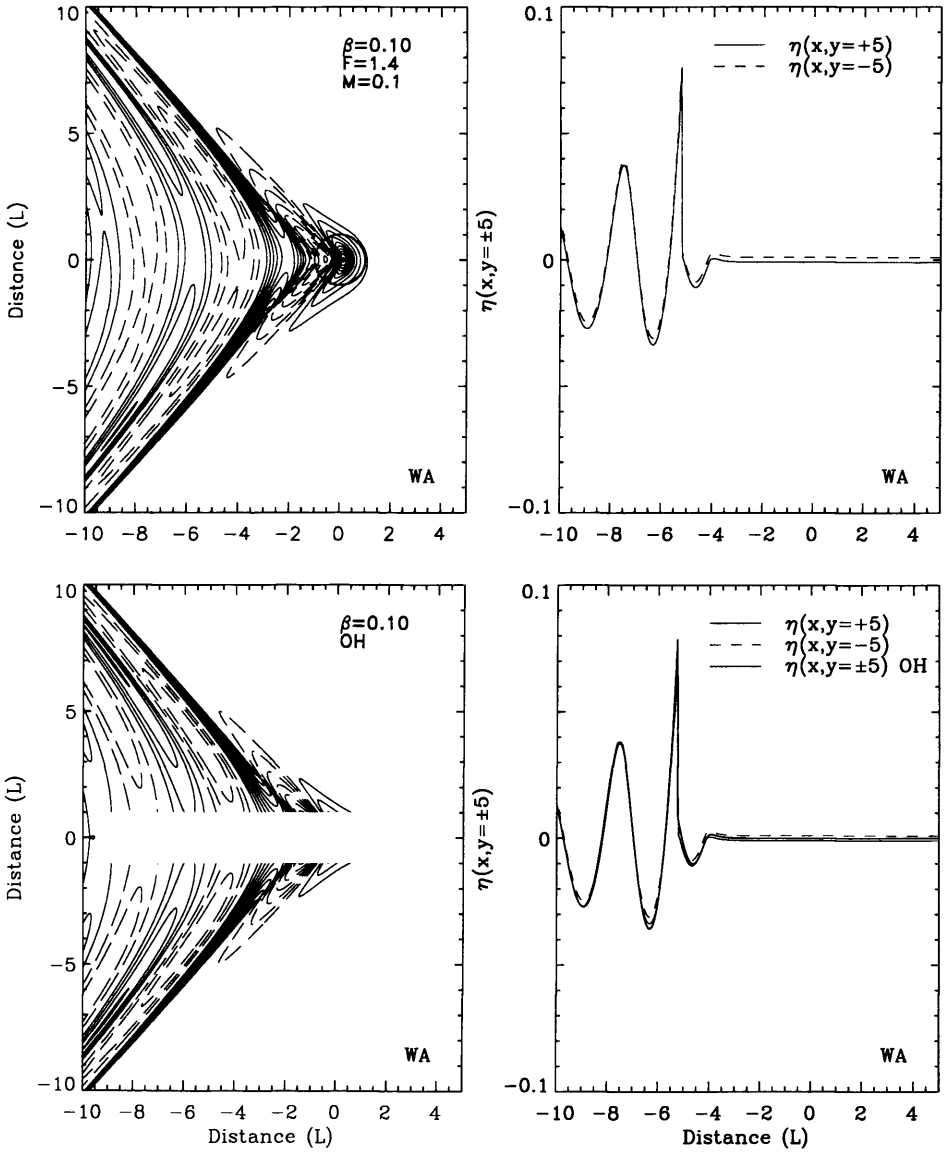


Figure 7.6: Illustrating the supercritical, rotating asymptotic theory for flow over the 'Witch of Agnesi' obstacle, with the similarity parameter $\beta = 0.1$. The top left panel shows the steady state free surface displacement field $\eta$ derived from numerical solution of the shallow-water equations, with spatial resolution $\delta x = 0.01$, $\delta y = 0.02$, for $F = 1.4$, $M = 0.1$ and $B = 3.06$. The lower left panel shows the corresponding steady free surface displacement field reconstructed from solutions to the Ostrovsky-Hunter equation (7.3), with spatial resolution $\delta \mathcal{X} = 0.00005$ and temporal resolution $\delta \bar{t} = 0.2$. Contour intervals are $0.01H$ in each panel. The upper right panel shows cross sections of $\eta$ along $y = +5$ (solid line) and $y = -5$ (dashed line) from the shallow-water solution. The lower right panel replots these cross sections, together with the cross section along $y = \pm 5$ derived from the Ostrovsky-Hunter solutions (thick line).

stacles with $M = 0.1$, $F = 1.4$ and $B = 30.62$, so that $\beta = 0.01$. The upper left and right panels correspond to flow over the 'Witch of Agnesi' obstacle, and show the steady state free surface displacement field $\eta$ and cross sections of $\eta$ along $y = +5$ (solid line) and $y = -5$ (dashed line) respectively. The lower panels show the corresponding solutions for flow over the paraboloid obstacle. In terms of capturing the behaviour of the obstacle wake, the asymptotic theory at this point fails; two possible explanations present themselves. First, recall that the asymptotic procedure introduces the coordinate variable $\mathcal{Y}_*$, describing flow along the 'Mach' lines and scaling with obstacle height $M$. That is, there is an implicit assumption that the flow varies more rapidly perpendicular to the 'Mach' lines than along them. Examining the free surface displacement fields $\eta$ in Figure 7.7, one immediately sees that this is not the case for these flows. Secondly, as noted in the previous paragraph, rotation is taken to scale with $M(= 0.1)$ in the theory, so that for such a large value of the inverse Burger number $B(= 30.62)$ one might anticipate the theory breaking down; but all is not lost. Solutions to the Ostrovsky-Hunter equation indicate that, for $\beta = 0.01$, flow over the 'Witch of Agnesi' obstacle should remain smooth throughout the flow domain - and this is found to be the case in the shallow-water solution. Further, from the asymptotic theory we expect flow over the paraboloid obstacle to exhibit wave breaking for arbitrarily small values of $\beta$. Examination of the shallow-water solution for the paraboloid (confirmed via higher resolution computations not shown) indicate that, at least for $\beta = 0.01$, wave breaking does occur.

Finally, recalling from Chapter 4 that the height and amplitude of the N-wave in the far field of the obstacle in the absence of rotation are relatively insensitive to the details of obstacle shape, the marked qualitative

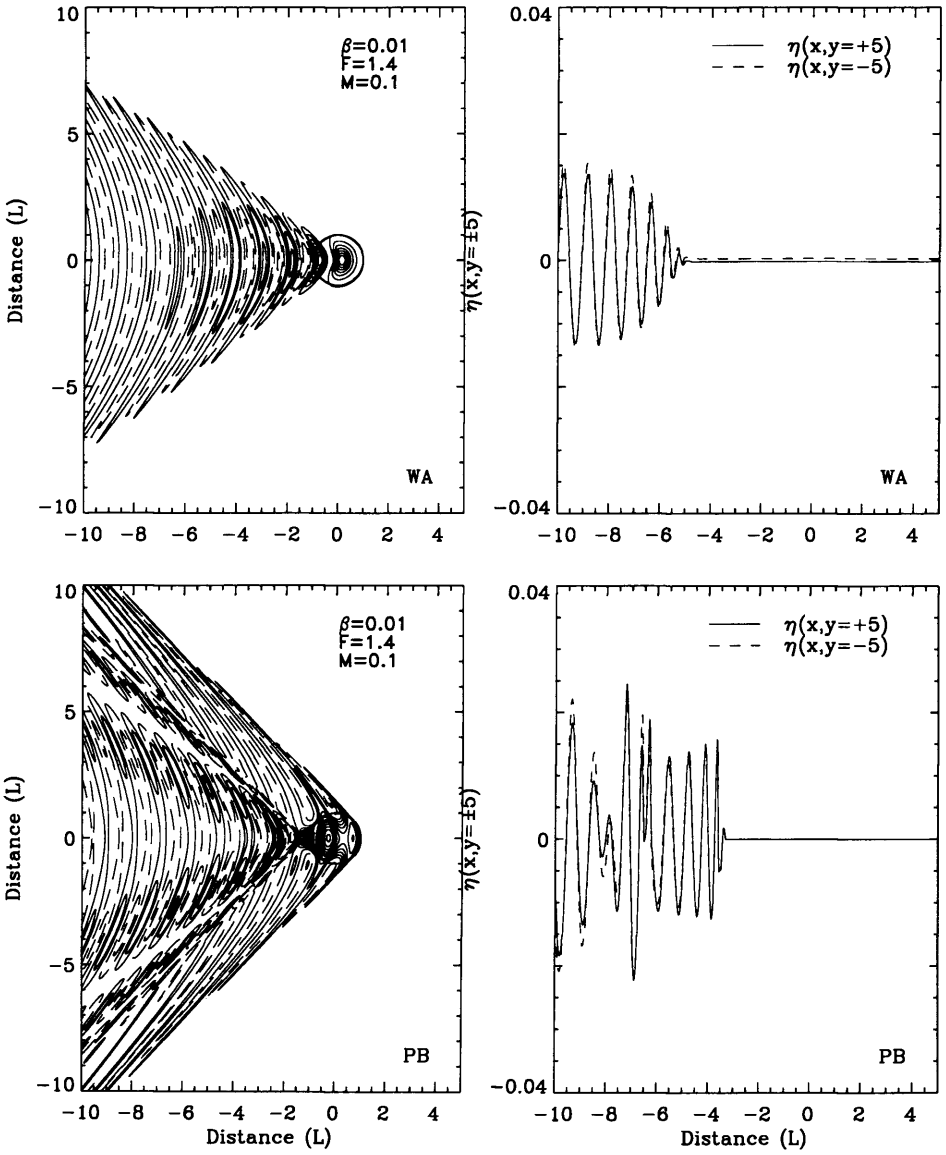


Figure 7.7: Comparison of rotating, supercritical, shallow-water flow over the 'Witch of Agnesi' and paraboloid obstacles. The left column shows the free surface displacement fields $\eta$ derived from numerical solutions of the shallow-water equations, with spatial resolution $\delta x = 0.01$, $\delta y = 0.02$, for $F = 1.4$, $M = 0.1$ and $B = 30.62$. The contour interval is $0.01H$ in both panels. The upper panel shows flow over the 'Witch of Agnesi' obstacle, the lower panel flow over the paraboloid obstacle. The right column shows the corresponding cross sections of $\eta$ along $y = +5$ (solid lines) and $y = -5$ (dashed lines). Again, the upper panel corresponds to the 'Witch of Agnesi' obstacle, the lower panel to the paraboloid obstacle.

difference for the rotating flows of Figure 7.7 over the 'Witch of Agnesi' and paraboloid obstacles indicate that the same cannot be said for rotating flows over topography.

## 7.4 Discussion

The main theme of this chapter has been an analysis of the asymptotic theory introduced in Chapter 2 describing the supercritical, rotating obstacle wake. The asymptotic theory has been seen, in most cases, to offer good qualitative, and quantitative, agreement with shallow-water flows at finite obstacle height $M$. The qualitative nature of the supercritical, rotating obstacle wake has been demonstrated to depend on the single parameter $\beta$.

# Chapter 8

# Qualitative effects of dispersion and experimental observations

So far, results have been presented in which the effects of short-wave dispersion have been neglected. In order to model the physical situation of breaking waves, both the shallow-water equations and asymptotic theories have been regularised by including the possibility of mass and momentum conserving hydraulic jumps. As discussed in Chapter 1, there is an implicit assumption that an unspecified dissipation acts on the (unresolved) horizontal scale of these jumps.

Although hydraulic jumps are sometimes a good model for the physical phenomena of breaking waves, they are an appropriate model only for those situations where the implicit dissipation dominates over dispersive effects on scales typical of the jump width (Mei (1989), Baines (1995)).

In many geophysical and laboratory situations, it is in fact dispersion that dominates, with nonlinear waves exhibiting solitary-wave-like behaviour.

Helfrich & Melville (2006), state in the abstract of their excellent recent review article

> "Over the past four decades, the combination of in situ and remote sensing observations has demonstrated that long nonlinear internal solitary-like waves are ubiquitous features of coastal oceans".

An extensive anthology of images of nonlinear internal waves may be found online at http:/www.internalwaveatlas.com.

An example of atmospheric solitary waves is afforded by flow past Guadalupe Island, Baja California. As described in Chapter 1, a low layer of stratocumulus cloud is moving at 6-10kts past the island, whose peaks reach $4500ft$ and thereby project through, and interfere with, the cloud layer. Figure 8.1 repeats the more recent of the two photographs of Guadalupe island given in Chapter 1 (a NASA photograph, taken on 11 July 2001). A parabolic bow wave spreads from the north end of the island; but, behind the initial bow wave, a further series of waves is visible because of cloud formation due to wave-induced uplift.

Johnson & Vilenski (2004) argue that this 'splitting' of the bow wave is due to the effects of dispersion, and show that the observed flow pattern may be reproduced with some success when modelled by the Kadomtsev Petviashvili (KP) (Kadomtsev & Petviashvili (1970)) equation. Further observations of multiple solitary waves in atmospheric flow upstream of islands, which are a distinctively dispersive phenomenon, are discussed by Li *et al.* (2004), Badgley *et al.* (1969) and Burk & Haack (1999).

An example of oceanic solitary waves may also be found near to Guadalupe island, in the Gulf of California. Figure 8.2, reproduced from Fu & Holt (1982), shows the surface signature of internal solitary waves generated by

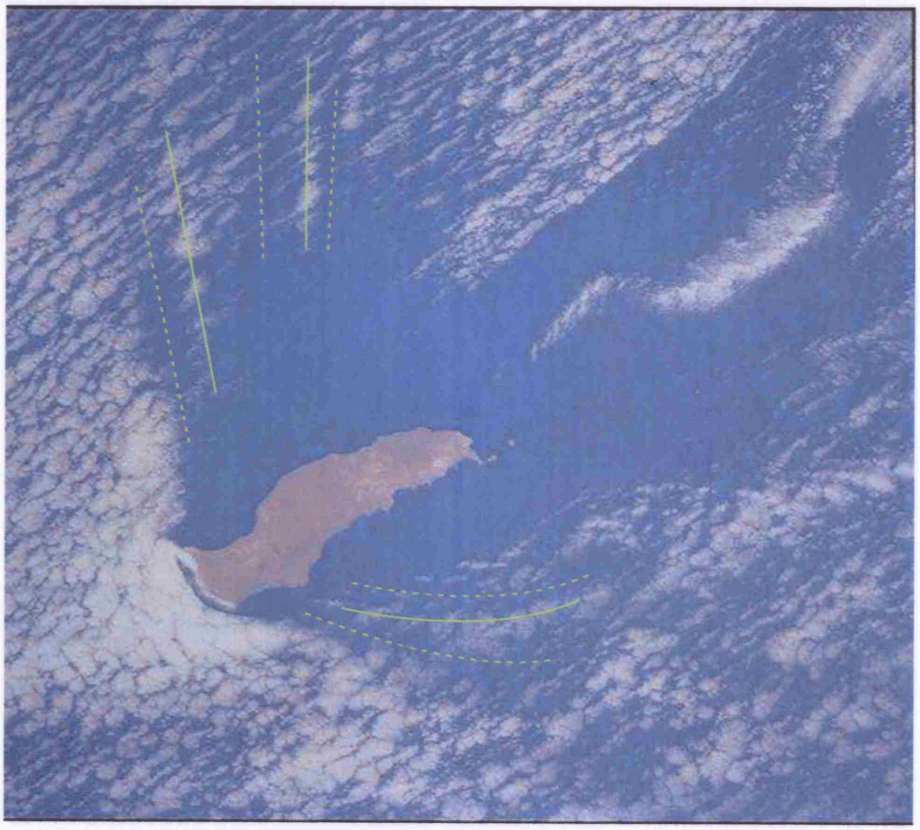

Figure 8.1: Cloud formation over Guadalupe Island, Baja California, due to wave-induced uplift. Solid lines indicate wave crests; dotted lines indicate wave troughs.

steep topography in the channels between Baja California and the nearby islands. As discussed by Helfrich & Melville (2006), at least eight wave packets are visible, showing up as alternating light and dark bands. The right-hand panel shows the bathymetry of the basin, and the letters indicate the location of the eight wave packets identified by Fu & Holt (1982).

In order to describe these dispersive phenomena, the ratio $\delta$ of the characteristic height and length scales of the flow must be treated as non-zero; but the typical length scales of many geophysical phenomena are such that, though it may not be appropriate to set $\delta$ to be zero, it is at least small.

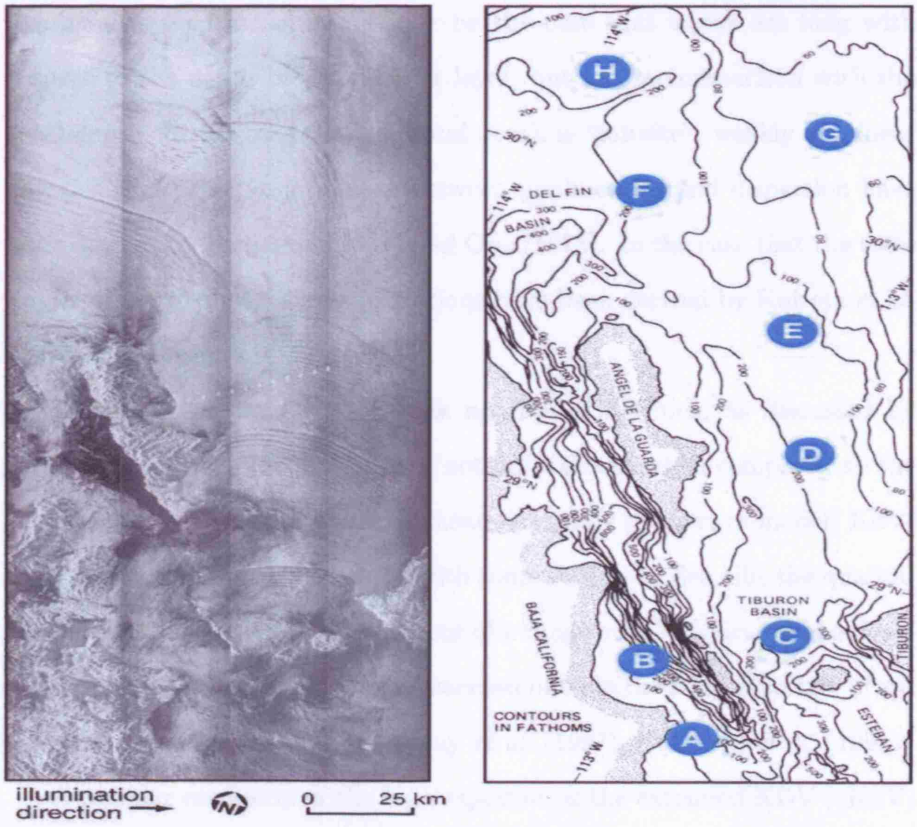


Figure 8.2: Reproduced from Fu & Holt (1982). SAR (synthetic aperture radar) images of the Gulf of California clearly show several internal wave packets, visible as alternating light and dark bands. The right-hand panel details the bathymetry of the basin, with the locations of the eight most apparent wave packets indicated by letters.

Various approximations to the full Euler equations are appropriate in the limit of small but non-zero $\delta$. In the weakly nonlinear limit (which in the current context of flow over topography implies that the obstacle height $M$ is small), progress can be made by assuming that nonlinearity and non-hydrostatic dispersion are both comparable and small. The canonical equations to describe such weakly nonlinear, weakly dispersive waves are the KdV equation and its two-dimensional relatives (Grimshaw & Smyth (1986), Kadomtsev & Petviashvili (1970), Akylas (1994)). In the case of flows that

exhibit a layered structure, it may be the case that waves are long with respect to the depth of a particular layer, but not in comparison with the total depth. In the case that the total depth is "infinite", weakly nonlinear theories that preserve a balance between nonlinearity and dispersion have been derived by Benjamin (1967) and Ono (1975). In the case that the total depth is intermediate, similar equations have been derived by Kubota *et al.* (1978) and Joseph (1977).

Despite the assumption of weak nonlinearity (which, as discussed by Helfrich & Melville (2006), is often not appropriate when compared to the observed scales of the geophysical phenomena they purport to model) KdV-type theories have been employed with some success to describe the qualitative, if not the quantitative, behaviour of a range of geophysical phenomena. The extent to which these theories succeed outside their formal range of validity has been discussed by Holloway *et al.* (1997), Holloway *et al.* (1999).

A popular extension of the KdV equation is the extended KDV (eKdV) equation, which retains the terms of the KdV equation, but includes *cubic* nonlinearity (Djordjevic & Redekopp (1978), Kakutani & Matsuuchi (1978), Lee & Beardsley (1974)). The way in which this cubic nonlinear term may arise is discussed in the following chapter, where the non-dispersive equivalent of the eKdV equation, termed the extended rotating transcritical small disturbance (erTSD) equation, is derived. As found by Stanton & Ostrovsky (1998), the eKdV equation offers good agreement with even highly nonlinear observed waves, to the extent that Helfrich & Melville (2006) claim that the eKdV equation "has been adopted as the phenomenological model of choice".

Analytic progress is also possible for finite amplitude (finite $M$ in the current context) waves. Choi & Camassa (1999) derive an equation to de-

scribe fully nonlinear internal waves in a two-fluid system, whilst Green & Naghdi (1976) derive a system of equations containing both full nonlinearity and weak dispersion. An alternative approach is simply to integrate the full Euler equations numerically.

## 8.1 Qualitative effects of dispersion in flows over topography

Grimshaw & Smyth (1986) and subsequent studies show that weakly dispersive flows over small obstacles are often unsteady, with solitary waves periodically propagating upstream from the obstacle. That is, the upstream propagating hydraulic jump found in non-dispersive flow (c.f. Chapter 1) is replaced by periodic upstream propagating cnoidal wavetrains in the corresponding dispersive flow.

Johnson & Vilenski (2004) consider the intermediate problem of flow over a quasi-three-dimensional obstacle (an obstacle that is elongated asymptotically in the cross-stream direction) in the context of the KP equation. Numerical results are used to categorise the resulting flow patterns into a supercritical V-wave regime, a soliton regime, an unsteady flow regime and a subcritical modulated-wavetrain regime as the Froude number of the oncoming flow is reduced. They note that, although it might prove problematic to establish the appropriate value of the coefficient of the dispersive term in the KP equation for a particular geophysical example, numerical simulations show that even quite large changes in the strength of the dispersion do not result in large qualitative changes in flow pattern. Rather, they conclude that it is the criticality parameter $\Gamma$ that has the strongest qualitative effect on the types of flow pattern seen.

### 8.1.1 *The equivalent aerofoil description*

A particular advantage of the equivalent aerofoil theory discussed in Chapter 2 is that, when extended to include the effects of weak dispersion, it may be used to describe weakly dispersive flows over a fully three-dimensional obstacle (Esler *et al.* (2007*a*)). Thus, although no new qualitative behaviour will be discovered relative to Johnson & Vilenski (2004), the 'equivalent aerofoil' description allows results to be associated with a definite, physical obstacle (in Johnson & Vilenski (2004) the obstacle's cross-stream dimension varies as $M^{-1/3}$).

The equivalent aerofoil description also allows a direct comparison of dispersive transcritical flows over three-dimensional obstacles and the corresponding non-dispersive flows (governed by the TSD equation), a comparison which seems not to have been previously made.

The derivation of the equivalent aerofoil theory including the effects of (weak) dispersion as in Esler *et al.* (2007*a*), but with the added ingredient of weak rotation, is reviewed in Appendix B. In the outer region, the leading order free surface displacement is found to be governed by the rKP equation

$$\left(2\eta^o_{0\tau} + 3\eta^o_0\eta^o_{0x} - 2\Gamma\eta^o_{0x} + \frac{\Delta^2}{3}\eta^o_{0xxx}\right)_x - \nu^2\eta^o_0 + \eta^o_{0YY} = F(x,Y), \quad (8.1)$$

where

$$F(x,Y) = -2\delta(Y)K_{xx}(x), \qquad K(x) = \int_0^\infty h(x,\hat{y})\,d\hat{y}, \quad (8.2)$$

and $\delta(Y)$ is Dirac delta function.

### 8.1.2 *Non-dispersive and dispersive flow over topography*

Figure 8.3 compares steady state free-surface displacement fields for non-dispersive and dispersive flows over the paraboloid obstacle. The upper

panels show non-dispersive flows, being solutions of the TSD equation (2.16) for $\Gamma = -0.3$ (left-hand panels) and $\Gamma = 0.5$ (right-hand panels). The lower panels show the corresponding steady solutions of the KP equation ((8.1), with $\nu = 0$) with $\Delta = 0.5$ (middle panels) and $\Delta = 0.25$ (lower panels). In the left-hand panels, shading indicates regions of supercritical flow, whereas in the right-hand panels shading indicates regions of subcritical flow.

First consider the case of subcritical oncoming flow ($\Gamma = -0.3$, left-hand panels). The non-dispersive flow is familiar, having been discussed in Chapter 4. Fluid accelerates smoothly to supercritical over the obstacle, before abruptly decelerating to subcritical flow through the 'fishtail' system of jumps to the rear of the obstacle. The corresponding dispersive flows bear only a passing resemblance to the non-dispersive flow. In both cases, the signature of the non-dispersive flow is (just) recognisable near to the obstacle, although the lateral extent of the disturbance is significantly reduced in the dispersive examples. Downstream of the obstacle, the expected dispersive wavetrain is found, which for both examples of dispersive flow is of sufficient amplitude that the flow oscillates from subcritical to supercritical within the phase of each wave. A weak dispersive wavetrain is found upstream of the obstacle in each of the dispersive flows.

The similarities between the supercritical oncoming flows ($\Gamma = 0.5$, right-hand panels) are much more compelling. For the dispersive flow with $\Delta = 0.5$, the bow hydraulic jump of the non-dispersive flow is replaced by a broad, large amplitude solitary-type wave. When $\Delta = 0.25$, the bow hydraulic jump is replaced by a pair of separate solitary waves of rather less width. In both the dispersive and non-dispersive flows, upstream of the initial nonlinear wave(s), the flow is undisturbed. In the non-dispersive flow the free surface displacement field decreases uniformly behind the upstream

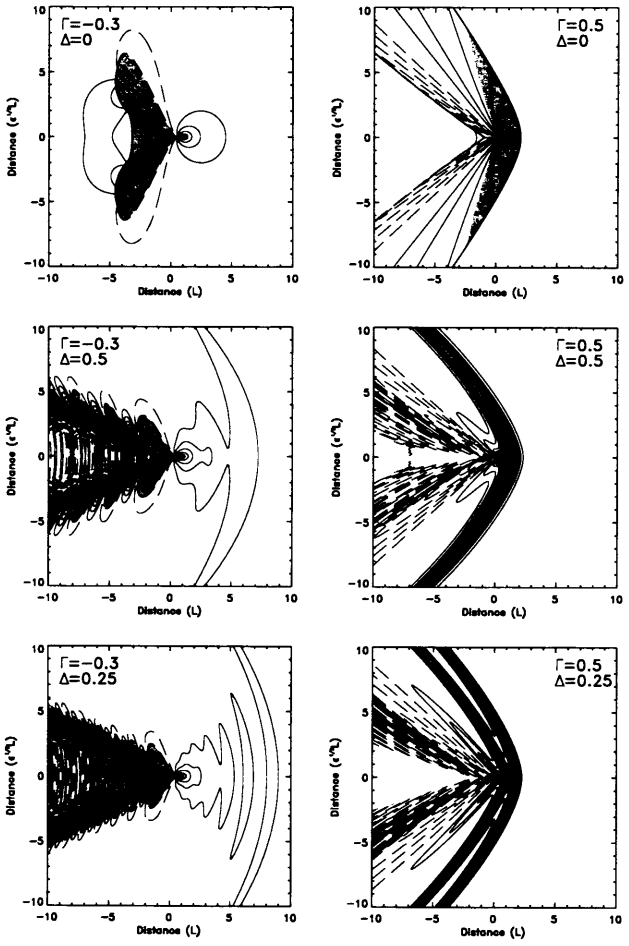


Figure 8.3: Comparison of non-dispersive and dispersive transcritical free surface displacement fields $\eta_0^o(x, Y)$ for steady flow around the paraboloid obstacle, in the transcritical limit. The top panels show the displacement field from numerical solutions of the TSD equation (2.16) for $\Gamma = -0.3$ (left) and $\Gamma = 0.5$ (right). The remaining panels show the corresponding results from numerical solutions of the (dispersive) KP equation ((8.1), with $\nu = 0$) for two values of the dispersion parameter $\Delta = 0.5, 0.25$. In each panel, the contour interval is $0.1M^{2/3}H$, negative contours are dashed and the zero contour is omitted. In the left panels, shading indicates supercritical flow, whereas in the right panels shading indicates subcritical flow.

jump, eventually becoming negative before returning to its equilibrium position through the downstream supercritical leap (the 'V-wave'). In the dispersive flows, the free surface displacement field remains almost constant behind the initial solitary wave(s). Behind this constant-displacement region, waves now spread dispersively; however, the lines tracing the centre of these waves are almost exactly coincident with the location of the downstream V-wave of the non-dispersive flow.

## 8.2 Experimental investigation of topographically generated nonlinear waves in rotating and non-rotating two-layer flow

Dispersive effects are also often important in experimental situations. Here, experimental observations of finite amplitude interfacial waves forced by a surface-mounted obstacle towed through a two-layer fluid are reported. In the current context, they are included to offer a 'practical' demonstration of some of the phenomena discussed in this thesis. For a more detailed discussion of these experiments, the interested reader may consult Johnson *et al.* (2006).

Experiments were performed at the LEGI-Coriolis Institute in Grenoble. The LEGI-Coriolis facility offers a large ($13m$ diameter) circular tank mounted on a turntable, so that flows in which the fluid is otherwise at rest and flows in which the fluid is otherwise rotating as a solid body may be studied. Thus, the experimental set-up closely recreates the 'experimental scenario' described in Chapter 1 (Figure 1.5).

The advantage of the LEGI-Coriolis facility is the large diameter of the tank. Analytical and numerical results presented thus far have been for

flow past an *isolated* obstacle, and it is this scenario that the experiments aimed to reproduce. As observed previously, the lateral extent of the wave field forced by obstacles towed at near-critical speeds is large, so that in a narrow tank the entire wave field might soon be dominated by reflection from the sidewalls (Ertekin *et al.*, 1986). Observations of the experiments performed using the LEGI-Coriolis facility confirm that here the tank is of a sufficiently large diameter that sidewall effects are negligible - at least until long after the dominant flow pattern has passed the measurement line. Thus the experimental set-up may be taken to be truly representative of flow past isolated topography.

### 8.2.1 *Experimental set-up*

A schematic of the experimental set-up is presented in Figure 8.4. The left-hand panel depicts a plan view of the 'basic premise' of the experiments: the obstacle $O$ is towed (or pushed) across a diameter of the tank by the carriage $C$, which rides along rigid rails $R$; the resulting wave field is recorded via a set of probes $P$.

In order that the experiments be effective, slightly more consideration must be given to their vertical structure, depicted in the right-hand panel of Figure 8.4. Two layers of density-contrasting fluid (in this case salty and fresh water) are arranged so that a thin upper layer, of depth $H_1 = 6cm$, overlays a much deeper layer of thickness $H_2 = 54cm$. Although a system to model an atmospheric flow might consist of a thin lower layer below a much deeper upper layer (c.f. Chapter 1), inverting the system offers two distinct advantages: first, experiments should not be adversely affected by bottom boundary layer effects at the obstacle; secondly, the upper layer can be readily refreshed with fresh water after each experiment.

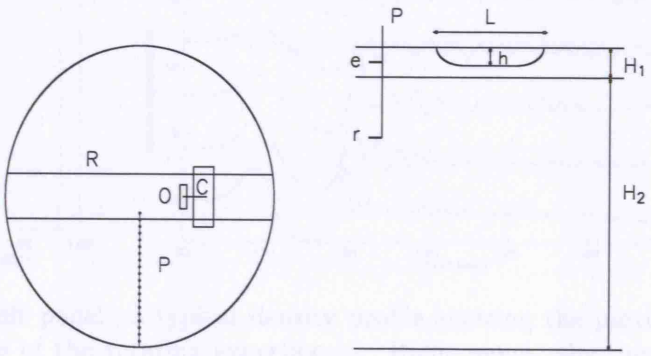


Figure 8.4: The experimental set-up. Left: plan view. Right: a vertical cut. The obstacle $O$ is moved along the upper layer by the carriage $C$ which rides along rigid rails $R$ sufficiently far above the surface to clear the spar supporting the interfacial probes $P$. Each probe consists of an ultrasonic emitter/receiver $e$ above the interface and a reflector $r$ below the interface.

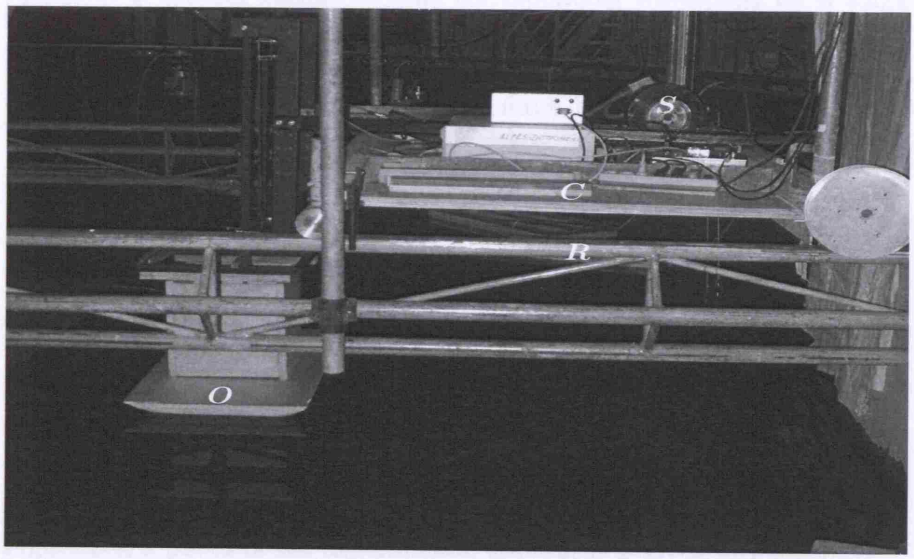


Figure 8.5: A side photograph of the experimental apparatus. The speed at which the carriage $C$ is moved along the rails $R$ is accurately controlled by the stepper motor $S$.

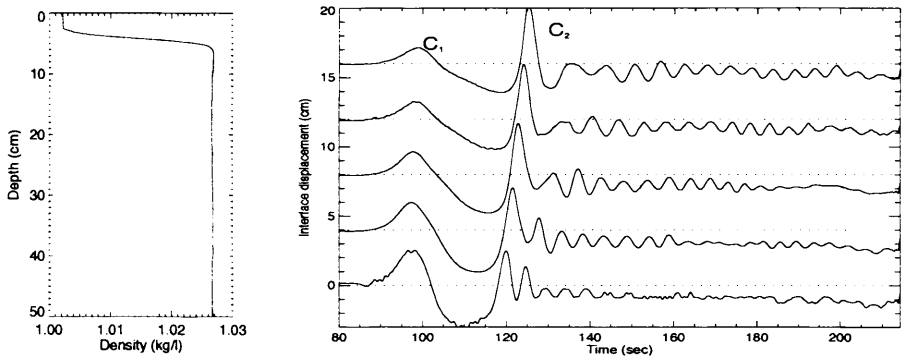


Figure 8.6: Left panel: a typical density profile showing the particularly sharp interface of the rotating experiments. Right panel: the time-series of interface displacements from the five innermost probes (in order from the closest at the bottom, with successive traces displayed upwards by $4cm$ to avoid overlap) for Figure 8.7 for rotating flow with towing speed $U = 10cms^{-1}$. The crest of the bow wave is marked $C_1$ and the more prominent sharp-crested lee wave is marked $C_2$.

For the results presented in the following, the density contrast between the two fluid layers is 2.5%, so that the interfacial long wavespeed $c = (g'H_1)^{1/2}$ is around $10cms^{-1}$. The corresponding wavespeed for a single layer of the same depth $c = (gH_1)^{1/2}$ is approximately six times greater, explaining the preference for a two-layer fluid: had a single fluid layer been used, the wave field would certainly have become swamped by the sidewall reflections mentioned above. Before proceeding to a description of the measurement system used, it should be noted that the wavespeed associated with the free surface is of the order of $2ms^{-1}$ so that an obstacle towed at close to the critical interfacial wavespeed ($\sim 10cms^{-1}$) results in the Froude number associated with the free surface being extremely small. Thus the upper surface acts as a rigid lid to the motion. Further to the schematics of Figure 8.4, a photo of the experimental apparatus is given in Figure 8.5.

Interface displacements were measured with a set of 20 acoustic probes (P in Figure 8.4 ) spaced $20cm$ apart along a spar transverse to, and to one

side of, the obstacle motion. The probes consisted of an ultrasonic pulse emitter ($e$ in Figure 8.4), positioned above the interface, and a reflector (a small metallic plate, $r$ in Figure 8.4), positioned below it. The piezo-electric emitter was also used as a receiver and the return time of the ultrasonic pulses measured. As the speed of sound is different in each layer, this return time varies linearly with interface displacement. The precision of measurement was $0.1mm$. The probe calibration was checked before each experiment by applying a vertical translation of $1cm$ to the whole spar of probes, using a stepping motor. Similar interfacial probes have been used previously by Ramirez & Renouard (1998). Figure 8.6 gives the time-series from a typical experimental run.

### 8.2.2 *Experimental results*

Results presented here are for the flat obstacle visible in Figure 8.5. An unfortunate feature of the experimental set-up (see Figure 8.4) was that the probes used to measure the interfacial disturbance could be mounted to only one side of the obstacle. Thus data for any given experiment could be gathered for only one half of the wave field. Runs were performed in both directions to establish the degree of symmetry about the centreline. Individual runs with the same parameters showed a high degree of reproducibility and runs with the same parameters in opposite directions showed good agreement: at the rotation rate (period $T = 120s$) presented in the following, the observed wave fields away from the direct wake region appeared to be reasonably symmetric about the centreline. Thus the interface elevations in Figure 8.7 are shown with data reflected about the centreline to represent the whole wave field. At higher rotation rates, however, the asymmetry of the flow became increasingly apparent. The absence of data in the band

near the centreline is due to the inner limit placed on the probe line to allow the obstacle to pass without obstruction. The gap between the innermost probe and the edge of the flat obstacle was $9cm$. Time-series of interface displacements from the probes, examples of which are given in Figure 8.6, were converted into the spatial plots of Figure 8.7 by assuming that the flow pattern was both symmetric and stationary relative to the obstacle.

Figure 8.7 shows contour plots of the experimentally observed interface displacements for the oblong obstacle towed at speeds $U = 7.5,\ 10,$ and $12.5cms^{-1}$. The left-hand column shows non-rotating flows, with towing speed increasing moving down the page. The right-hand column shows the equivalent experiments, now with the tank rotating with a period of $T = 120s$, so that the Rossby radius is approximately $1m$. The obstacle centre is marked by a '+' in each panel.

Consider first the upper panels, for which the towing speed $U = 7.5cms^{-1}$ suggests that the ambient flow is subcritical. For the non-rotating flow (left panel), a dispersive wavetrain of rather small amplitude waves is apparent upstream of the obstacle. Immediately downstream of the obstacle, a dispersive wavetrain of significantly larger amplitude waves is observed, suggesting that here the observed waves are essentially nonlinear in character. Thus the observed flow pattern is in fact rather reminiscent of the subcritical ($\Gamma = -0.3$) solutions of the KP equation in Figure 8.3. The flow field of the corresponding rotating flow (upper right-hand panel) is qualitatively similar; however, the lateral extent of the the wave field has been considerably reduced, and now extends to approximately the Rossby radius either side of the obstacle. Although it is evident that in the experiments dispersive effects are important, in Chapter 6 it was seen that a reduction of the lateral extent of the wave field was the main qualitative effect of rotation for

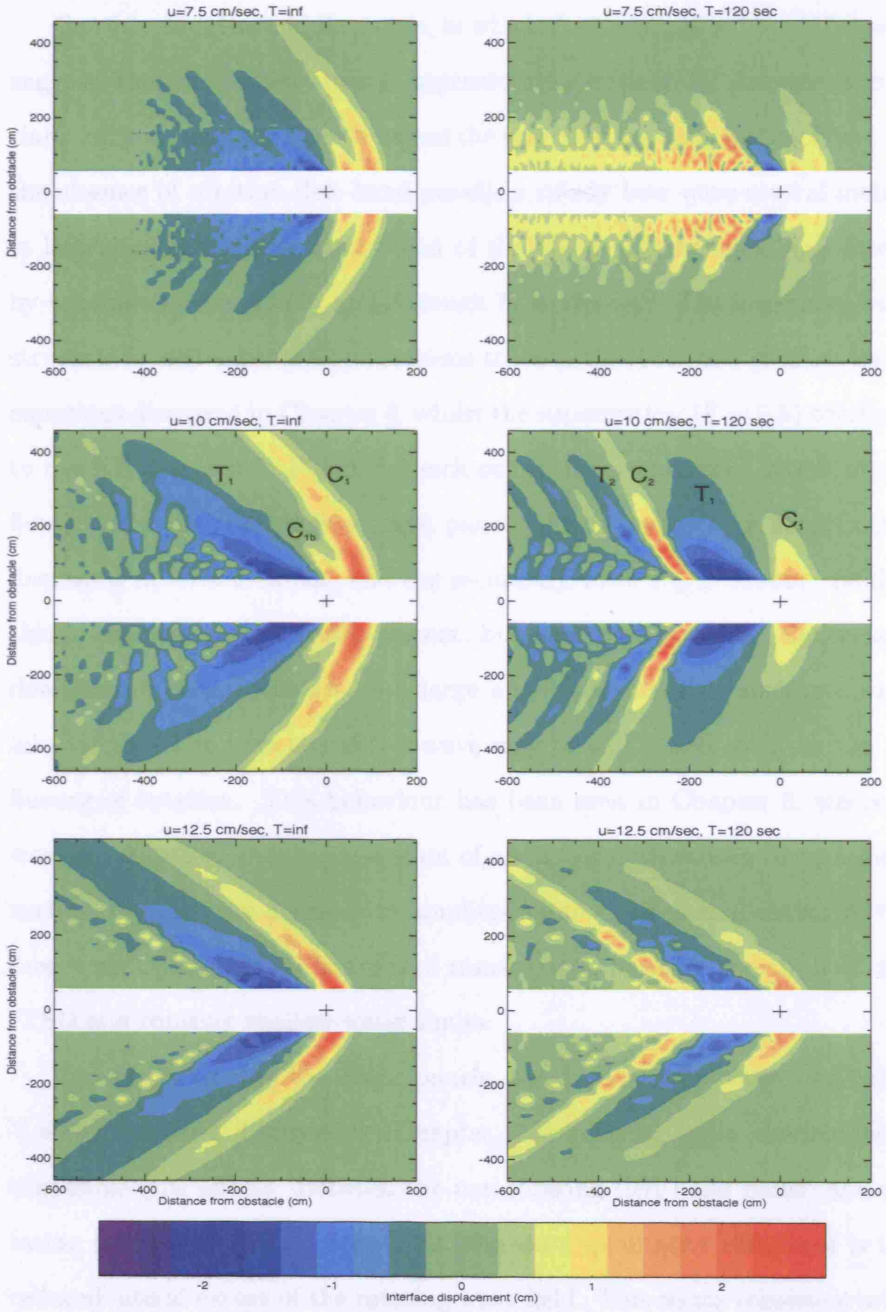


Figure 8.7: Observed experimental interface elevations for an oblong obstacle at towing speeds $U = 7.5,\ 10,$ and $12.5 cms^{-1}$. Left column: non-rotating. Right column: rotating with period $T = 120s$, giving a Rossby radius of approximately $1.0m$. The centre of the obstacle is indicated by the '+' at the origin. As in Figure 8.6, $C_1$ marks the crest of the bow wave, $C_2$ the more prominent sharp-crested lee wave and $T$, the long deep trough between them.

subcritical oncoming flows governed by the (non-dispersive) rTSD equation.

Consider now the middle panels, in which the towing speed $U = 10cms^{-1}$ suggests that the ambient flow is approximately critical. In this case, appreciable differences are evident between the non-rotating and rotating flows. In the absence of rotation (left-hand panel), a steady bow wave several metres in lateral extent is generated ahead of the obstacle (labelled $C_1$), followed by a smaller bow wave $C_{1b}$ and a trough $T_1$ to the rear. The basic bow-wave structure is well captured by solutions to both the TSD and shallow-water equations discussed in Chapter 4, whilst the supercritical ($\Gamma = 0.5$) solutions to the KP equation in Figure 8.3 pick out further qualitative details of the flow pattern. In rotating flow (right panel), the bow wave $C_1$ is significantly decreased in lateral extent, and the secondary wave $C_{1b}$ is absent. Behind this a broad trough $T_1$ is still present, but immediately behind the trough, downstream of the obstacle, is a large amplitude, narrow, nonlinear wave labelled $C_2$. The presence of this wave may be attributed solely to the influence of rotation. This behaviour has been seen in Chapter 6, where it was demonstrated that amplification of nonlinear downstream disturbances such as $C_2$, and the decrease in amplitude and cross-stream extent of the bow wave $C_1$ are typical features of transcritical, rotating flow, in both the rTSD and rotating shallow-water limits.

Finally, examining the lower panels, the familiar bow-wave - trough - V-wave structure discussed in Chapter 4 is evident, again overlaid with dispersive-type effects. Between the non-rotating (left-hand panel) and rotating (right-hand panel) flow fields, the main qualitative difference is the reduced lateral extent of the rotating wave field. This seems consistent with the observation in Chapter 6 that, in certain regions of $(\Gamma > 0, \nu)$ parameter space, non-rotating and rotating solutions of the rTSD equation remain

qualitatively similar, but for the reduced lateral extent of disturbances.

### 8.2.3 *Interpretation of experimental observations*

Although the experimentally observed flow fields of Figure 8.7 bear some comparison with results presented in the previous chapters, the question arises as to which of the various models discussed in the introduction to this chapter is most applicable to the experiments performed.

For a given experimental or geophysical scenario, this question is not easily answered. In atmospheric flows, if *horizontally* propagating internal waves are to exist, some form of 'trapping' mechanism is necessary to prevent the *vertical* propagation of energy. When such a mechanism exists, it is usually referred to as a waveguide. Rottman & Einaudi (1993) review the application of one-dimensional weakly nonlinear theory for two typical atmospheric scenarios. In the first, waves propagate within a strongly stratified waveguide, with relatively weak stratification elsewhere; a particular example is the marine atmospheric boundary layer. In this case, Rottman & Einaudi (1993) argue that the appropriate model is the Benjamin-Davis-Acrivos (BDA) theory.

The second scenario describes the situation in which the stratification is reasonably uniform throughout most of the depth of the fluid; in the atmospheric case, waves then occupy most of the troposphere, with the tropopause and strongly stable stratosphere acting as an upper boundary, to give an effectively finite-depth flow. In this case, the appropriate model is the KdV theory.

How prevalent are the atmospheric conditions necessary for each type of theory to 'really' be applicable? Rottman & Einaudi (1993) point out that the atmosphere often produces layers of nearly neutrally stratified air that

are sufficiently deep to provide effective trapping of solitary waves (the BDA case), but rarely produce a sufficiently large increase in buoyancy frequency to make a good reflector and effectively cap a stratified layer (the KdV case). They suggest, however, that the KdV equation may be relevant when there is sufficient vertical shear in the oncoming flow to reflect vertically propagating internal waves.

Returning to the experiments discussed here, Johnson *et al.* (2006) argue that, since the lower layer in the experiments is both deep and neutrally stable and the effective oncoming flow is unsheared, the experiments relate most closely to the BDA case. They interpret the experimental results in Figure 8.7, with a degree of success, via numerical integrations of the forced, rotating, weakly two-dimensional BDA equation (fr2dBDA).

Here, we shall content ourselves with the fact that the experiments performed, to a degree, confirm the qualitative features of the models discussed throughout this thesis.

## 8.3 Conclusions

Theories related to those considered in previous chapters, but in which the first effects of dispersion are retained, have been briefly discussed. The utility of the 'equivalent aerofoil' description in this context is twofold: first, results may be related directly to a particular, physical obstacle; secondly, a direct comparison between non-dispersive flows and their dispersive equivalents is facilitated. For subcritical oncoming flows, the differences between the two are great; but for supercritical oncoming flows there are some striking similarities.

Derived in the simplest possible way - from the Euler equations describing the flow of a single fluid layer of constant density (as in Appendix B)

- theories of KdV type may seem, though of interest, to have limited direct practical applications. The requirement of a rather particular balance between nonlinearity and dispersion might also cause concern.

The theories discussed in this chapter have a rather wider importance than the restriction to single-layer flow might suggest because, as has been pointed out in the context of two-dimensional flow (Grimshaw & Smyth (1986), Rottman & Einaudi (1993)), many results in the transcritical regime exactly correspond to those obtained for stratified flows where a single trapped vertical mode is near resonance.

For the second concern, Johnson (1997) notes that for any value of the aspect ratio $\delta$, as the 'amplitude parameter' $\epsilon \to 0$ ($M$ in our scenario), there always exists a region of space-time where the required balance between nonlinearity and dispersion comes about. Thus, in the absence of competing effects, it is likely that an initial disturbance will generate KdV-type solitary waves somewhere, provided only that the disturbance amplitude $\epsilon$ is small.

Ultimately however, neither the non-dispersive models discussed in the majority of this thesis, nor the dispersive models discussed in this chapter, are completely satisfactory as models of observed wave motions. In the first case, waves of arbitrarily small amplitude eventually break (at least in the absence of rotation), whereas in the latter, waves never break. A reduced equation that describes both solitary waves, wave breaking, and wave peaking (c.f. Chapter 5) can be considered a desirable goal, since 'real world' flows may exhibit all three behaviours.

# Chapter 9

# Conclusions and further work

The majority of this thesis has been concerned with the transcritical and supercritical regimes of non-dispersive shallow-water flow over an isolated obstacle of small height.

The transcritical similarity theory described in Chapter 2 gives precision to the well known analogy between the shallow-water equations and the equations of compressible gas dynamics: transcritical shallow-water flow over an obstacle of small height is isomorphic to transonic flow over a thin 'equivalent aerofoil' with thickness proportional to the cross-sectional area of the obstacle.

In Chapter 4, the range of validity of the transcritical theory has been explored numerically. The theory offers a reasonable description of transcritical shallow-water flows for obstacle heights $M \lesssim 0.4$. It is hoped that insights gained into the behaviour of the drag exerted by the obstacle on the flow in the transcritical regime, in which the peak drag is exerted, may be of use to those concerned with drag parameterisation in global scale circulation

models.

When the Froude number of the oncoming flow is such that $\Gamma \gtrsim 1.5$, the transcritical theory becomes inaccurate. However, the supercritical asymptotic theory described in the latter half of Chapter 2 is seen rapidly to become valid thereafter, so that, taken together, the transcritical and supercritical theories offer a reasonably complete description of shallow-water flows over obstacles of height $M \lesssim 0.4$.

A second major concern has been the effects of rotation on topographically forced flows. In Chapter 5, results presented in Esler *et al.* (2005) pertaining to flow over an infinite 'one-dimensional' ridge without sidewalls were reviewed and compared with the results of a weakly nonlinear theory. The theory captures all of the behaviour found in the shallow-water equations but for the possibility of hysteresis. In Chapter 6, rotating flow over three-dimensional obstacles was discussed, again comparing results of the transcritical similarity theory with shallow-water flows at finite obstacle height $M$.

These studies indicate that rotation has a robust, predictable effect on topographically forced flows, which persists regardless of the geometry of the obstacle. Rotating flows are characterised by the appearance of stationary hydraulic jumps both ahead of and downstream of the obstacle. Frequently, the amplitude of the downstream hydraulic jump can exceed that of its upstream counterpart; indeed, flow regimes in which only one hydraulic jump is present, lying downstream of the obstacle, are possible. This leads to a clear distinction between supercritical transitions at low and high rotation rates. When the oncoming flow is supercritical, the flow downstream of the obstacle is characterised by an infinite wavetrain of finite-amplitude inertia-gravity waves.

That these stationary, highly nonlinear waves occurring downstream of an obstacle are physically realisable has been verified through the rotating tank experiments described in Chapter 8, which make evident the effects of non-hydrostatic dispersion, a feature of many geophysical phenomena. In Esler *et al.* (2007*a*), the derivation of the 'equivalent aerofoil' theory retains the first effects of non-hydrostatic dispersion. A particular advantage of the 'equivalent aerofoil' description is that it allows a direct comparison between dispersive and non-dispersive flows. Striking similarities are apparent in the case when the oncoming flow is supercritical, but little comparison can be sustained when the oncoming flow is subcritical.

In Chapter 7 it is shown that supercritical, rotating shallow-water flows for small obstacle height $M$ may be characterised by a single parameter $\beta$. This leads naturally to a discussion of another important effect of rotation - its ability to suppress the wave breaking otherwise inherent in non-dispersive flows.

Although the material described in this thesis might be extended in numerous ways, just two possibilities will be briefly explored. First, the consequences of relaxing the assumption that the obstacle is axisymmetric are discussed; secondly, the rTSD equation is extended to include cubic nonlinearity so that it might describe the baroclinic mode of a two-layer fluid.

## 9.1 Non-axisymmetric obstacles

### 9.1.1 Analytic expressions for linear, non-rotating, super-critical drag

Linearising the non-rotating shallow-water equations reveals

$$\begin{aligned} Fu_x &= \eta_x, \\ Fv_x &= \eta_y, \\ u_x - F\eta_x + MFh_x + v_y &= 0, \end{aligned} \tag{9.1}$$

so that the linearised free surface displacement $\eta$ satisfies

$$(F^2-1)\eta_{xx} - \eta_{yy} = MF^2 h_{xx}.$$

Using Green's functions techniques, Jiang & Smith (2000) obtained the general solution (adapted here for right-to-left flow)

$$\eta(x,y) = -\frac{MF^2}{2\gamma}\left\{\int_{-\infty}^{y} h_x(x+\gamma(y-\tilde{y}),\tilde{y})\,d\tilde{y} + \int_{y}^{\infty} h_x(x-\gamma(y-\tilde{y}),\tilde{y})\,d\tilde{y}\right\}, \tag{9.2}$$

where $\gamma = \sqrt{F^2-1}$. At this stage the rotated coordinate system $(\mathcal{X}_\pm, \mathcal{Y}_\pm) = (x \pm \gamma y, y \mp \gamma x)/F$ for the regions $y > 0$ and $y < 0$ respectively is introduced. In $y > 0$, the new coordinate system is rotated anti-clockwise through an angle $\tan^{-1}\gamma$, so that $\mathcal{X}_+$ measures distance perpendicular to the Mach lines, $x + \gamma y = constant$, and $\mathcal{Y}_+$ the distance along these Mach lines. A similar, but clockwise, rotation occurs for the coordinates in $y < 0$. In terms of these new coordinates, Johnson & Vilenski (2004) noted that, provided the obstacle height decays sufficiently rapidly at large distances, then as

$y \to \pm\infty$ the solution (9.2) converges to

$$\lim_{y\to\pm\infty} \eta(x,y) = -\frac{MF^2}{2\gamma^2} \int_{-\infty}^{\infty} \begin{cases} h_x\left(\xi, \frac{(F\mathcal{X}_+ - \xi)}{\gamma}\right) d\xi & y \to +\infty \\ h_x\left(\xi, \frac{(\xi - F\mathcal{X}_-)}{\gamma}\right) d\xi & y \to -\infty \end{cases} . \quad (9.3)$$

Equation (9.3) shows that the linear solution away from the obstacle tends to a function of the single coordinate $\mathcal{X}_\pm$, with sign taken according to whether we are looking at $y \to \pm\infty$.

Now consider the drag exerted on the flow by the obstacle. Upstream, the oncoming flow is uniform and in the $x$ direction. Downstream the $x$-momentum is in deficit by an amount equal to the sum of the northward and southward fluxes of $x$-momentum due to the outgoing waves. The force that effects this change in momentum is the drag $\mathcal{D}$ exerted on the flow by the obstacle.

The flux of $x$-momentum into each outgoing wave is given by

$$\mathcal{F} = \int_{-\infty}^{\infty} uv dx,$$

so that in view of (9.1) the northward flux of $x$-momentum is

$$\mathcal{F}_N = \frac{\gamma}{F} \int_{-\infty}^{\infty} \eta^2(\chi_+) d\chi_+, \quad (9.4)$$

and the southward flux of $x$-momentum is

$$\mathcal{F}_S = \frac{\gamma}{F} \int_{-\infty}^{\infty} \eta^2(\chi_-) d\chi_-, \quad (9.5)$$

with $\eta(\chi_\pm)$ given by (9.3). The drag $\mathcal{D}$ is then

$$\mathcal{D} = \mathcal{F}_N + \mathcal{F}_S.$$

### 9.1.2 *Linear supercritical drag due to an axisymmetric obstacle*

Before considering non-axisymmetric obstacles, it is useful briefly to review the derivation of the expression for the drag $\mathcal{D}$ for the case of an axisymmetric obstacle. This illustrates the general procedure employed, after which results will simply be stated.

In the case that the obstacle is axisymmetric, the flow field is symmetric so that $\mathcal{F}_N = \mathcal{F}_S$, and we choose to evaluate $\mathcal{F}_N$. Thus, from (9.3), consider

$$\eta(\chi_+) = -\frac{MF^2}{2\gamma^2}\int_{-\infty}^{\infty} h_x\left(\xi, \frac{(F\chi_+ - \xi)}{\gamma}\right) d\xi. \tag{9.6}$$

Since $h \equiv h(r)$, $h_x = h'(r)x/r$ so that

$$\eta(\chi_+) = -\frac{MF^2}{2\gamma^2}\int_{-\infty}^{\infty} \frac{\xi h'(r(\xi))}{r(\xi)} d\xi.$$

Now

$$r^2 = \xi^2 + \left(\frac{F\chi_+ - \xi}{\gamma}\right)^2,$$

which may be rearranged to reveal

$$r^2 - \chi_+^2 = \zeta^2 \quad \text{where} \quad \zeta = \frac{F}{\gamma}\xi - \frac{\chi_+}{\gamma}.$$

Then

$$\eta(\chi_+) = -\frac{MF}{2\gamma}\int_{-\infty}^{\infty} \frac{(\frac{\gamma}{F}\zeta + \frac{\chi_+}{F})h'(r(\zeta))}{r(\zeta)} d\zeta = -\frac{M}{\gamma}\int_0^{\infty} \frac{\chi_+ h'(r(\zeta))}{r(\zeta)} d\zeta$$

because $r$ is an even function of $\zeta$. A change of variable in the integral then reveals

$$\eta(\chi_+) = -\frac{M}{\gamma}\int_{|\chi_+|}^{\infty} \frac{\chi_+ h'(r)}{\sqrt{r^2 - \chi_+^2}} dr. \tag{9.7}$$

Finally, substituting into equation (9.4) reveals that the drag $\mathcal{D}$ is given by

$$\mathcal{D} = c_d \frac{M^2}{F\sqrt{F^2-1}}, \tag{9.8}$$

where $c_d$ is constant for a given obstacle, defined as

$$c_d = 2\int_{-\infty}^{\infty} \chi_+^2 G(\chi_+)^2 d\chi_+ \tag{9.9}$$

with

$$G(\chi_+) = \int_{|\chi_+|}^{\infty} \frac{h'(r)}{\sqrt{r^2-\chi_+^2}} dr. \tag{9.10}$$

The functionals $G(\chi)$ and values $c_d$ for each of the obstacles discussed throughout this work have been given previously in Chapter 4; for convenience they are recalled here in Table 9.1.

### 9.1.3 *Linear supercritical drag due to an elliptical obstacle*

In order to relate results as closely as possible to those for circular obstacles, we again consider obstacles of the form $h = h(r)$ detailed in Table 9.1. In order that the obstacles be elliptical however, we now take

$$r = \sqrt{\mathcal{E}x^2 + \frac{1}{\mathcal{E}}y^2}$$

to be the 'radial' coordinate, where $\mathcal{E}$ describes the eccentricity of an obstacle. This form has been chosen so that the volume of the obstacle is preserved under changes in eccentricity $\mathcal{E}$. To make the algebra more lucid, the eccentricity parameter $\mathcal{E}$ is not the 'usual' one $\bar{\mathcal{E}}$, but relates to it thus:

$$\mathcal{E} = \sqrt{1-\bar{\mathcal{E}}}.$$

| Obstacle | $h(r)$ | $G(\mathcal{X})$ | $c_d$ |
|---|---|---|---|
| Witch of Agnesi | $\frac{a^3}{(a^2+r^2)^{3/2}}$ | $\frac{-2a^3}{(\mathcal{X}^2+a^2)^2}$ | $\frac{\pi a}{2}$ |
| $(a = 1/2)$ | | | |
| Gaussian | $\exp\{-\frac{r^2}{a^2}\}$ | $-\frac{\sqrt{\pi}}{a}\exp\{-\frac{\mathcal{X}^2}{a^2}\}$ | $a\left(\frac{\pi}{2}\right)^{3/2}$ |
| $(a = 1/\sqrt{2})$ | | | |
| Cone | $1 - \frac{r}{a}$ | $-\frac{1}{a}\cosh^{-1}\{\frac{a}{\lvert\chi\rvert}\}$ | $\frac{4a}{3}(2c_t - 1)$ |
| $a = \sqrt{3/2}$ | $(r < a)$ | $(\lvert\mathcal{X}\rvert < a)$ | |
| Hemi-ellipsoid | $\sqrt{1 - \frac{r^2}{a^2}}$ | $-\frac{\pi}{2a}$ | $\frac{\pi^2 a}{3}$ |
| $(a = \sqrt{3}/2)$ | $(r < a)$ | $(\lvert\mathcal{X}\rvert < a)$ | |
| Paraboloid | $1 - r^2$ | $-2\sqrt{1 - \mathcal{X}^2}$ | $\frac{32}{15}$ |
| | $(r < 1)$ | $(\lvert\mathcal{X}\rvert < 1)$ | |

Table 9.1: Obstacle shapes, functionals $G(\chi)$ and linear supercritical drag coefficients $c_d$. $c_t$ is Catalan's constant ($\approx 0.916$).

As in the case of a circular obstacle, the flow field is symmetric about $y = 0$. Following the same procedure reveals that the drag exerted on the flow by an elliptical obstacle is given by

$$\mathcal{D} = \frac{M^2\mathcal{E}^{3/2}F^2 c_d}{\gamma(\mathcal{E}^2\gamma^2 + 1)^{3/2}}, \tag{9.11}$$

where $c_d$ is the same constant as for the corresponding circular obstacle, given in Table 9.1.

In the upper panel of Figure 9.1, normalised drag $\mathcal{D}/M^2$ is plotted against the eccentricity parameter $\mathcal{E}$ for the particular case of the paraboloid obstacle with the Froude number of the oncoming flow $F = 2$. Stars in the figure indicate drags derived from numerical integrations of the shallow-

water equations with obstacle height $M = 0.1$. Essentially, this plot is included as a check on the algebra necessary in the derivation of (9.11); similar checks have been made against the 'Witch of Agnesi' obstacle. Two further observations can be made.

First, from (9.11), the value of the eccentricity parameter for which peak drag is exerted on the flow by the obstacle is given by $\mathcal{E}_m = 1/\gamma$. The value $\mathcal{E}_m$ is indicated by the dashed line in the upper panel of Figure 9.1. The dotted lines highlight the location of the circular obstacle in the figure. When the obstacle is somewhat elongated in the streamwise direction ($\mathcal{E} < 1$), the drag exerted by the obstacle can exceed that exerted by the corresponding circular obstacle; however, when the obstacle is sufficiently elongated in the streamwise direction, the drag is seen to fall below that of its circular counterpart. When the obstacle is elongated in the transverse direction ($\mathcal{E} > 1$), the drag exerted on the flow is less than that exerted by the corresponding circular obstacle. Is this behaviour generic?

The lower panel of Figure 9.1 plots the eccentricity $\mathcal{E}_m$ for which peak drag is exerted on the flow by an obstacle as a function of the Froude number $F$. The dotted line corresponds to $\mathcal{E} = 1$, in which case an obstacle is circular. Clearly the behaviour described above is not generic. When $F = \sqrt{2}$, peak drag is exerted by a circular obstacle. When $F < \sqrt{2}$, peak drag is exerted by an obstacle that is elongated in the transverse direction, whereas for $F > \sqrt{2}$ peak drag is exerted by an obstacle which is elongated in the streamwise direction.

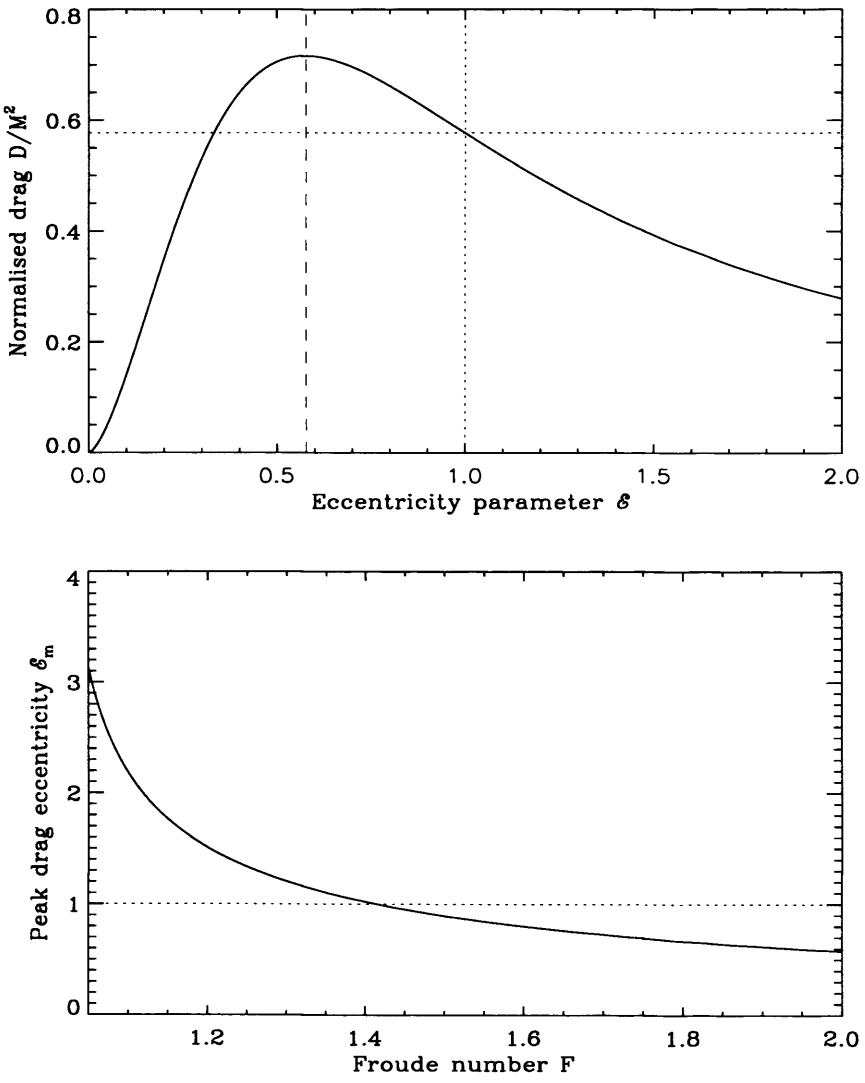


Figure 9.1: Upper panel: variation of normalised drag $\mathcal{D}/M^2$ with eccentricity parameter $\mathcal{E}$ for flow over the paraboloid obstacle with oncoming Froude number $F = 2$. Dotted lines highlight the situation in which the obstacle is circular; the dashed line indicates the eccentricity $\mathcal{E}_m$ for which peak drag is exerted on the flow by the obstacle. Lower panel: eccentricity $\mathcal{E}_m$ of an obstacle for which peak drag is exerted on the flow, as a function of oncoming Froude number $F$. The dotted line highlights the point at which the obstacle is circular.

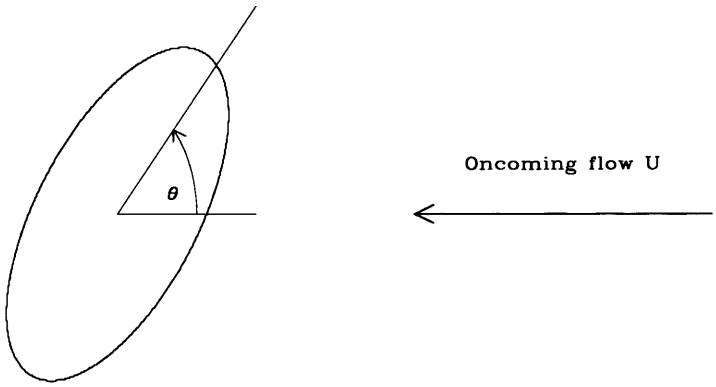


Figure 9.2: Schematic of the scenario of oncoming flow from right to left over an elliptical obstacle aligned at an angle $\theta$ to the oncoming flow.

### 9.1.4 *Linear supercritical drag due to an elliptical obstacle at an angle to the oncoming flow*

We now consider the most interesting case to be described, that in which an elliptical obstacle is aligned at an angle to the oncoming flow. A schematic of the situation is depicted in Figure 9.2: oncoming flow from right to left over an obstacle at an angle $\theta$ to the oncoming flow.

As before, consider an obstacle of the form $h = h(r)$, where the 'radial' coordinate is now given by

$$r = \sqrt{\mathcal{E}(x\cos\theta + y\sin\theta)^2 + \frac{1}{\mathcal{E}}(y\cos\theta - x\sin\theta)^2}.$$

In this case the flow is no longer symmetric about $y = 0$. Following the same procedure as that described for the axisymmetric obstacle, it can be

shown that the northward and southward $x$-momentum fluxes are given by

$$\mathcal{F}_N = \frac{M^2\sqrt{2}\mathcal{E}^{3/2}F^2 c_d}{\gamma\big((1+\mathcal{E}^2)F^2 + (\mathcal{E}^2-1)\{(\gamma^2-1)\cos 2\theta - 2\gamma\sin 2\theta\}\big)^{3/2}}, \tag{9.12}$$

$$\mathcal{F}_S = \frac{M^2\sqrt{2}\mathcal{E}^{3/2}F^2 c_d}{\gamma\big((1+\mathcal{E}^2)F^2 + (\mathcal{E}^2-1)\{(\gamma^2-1)\cos 2\theta + 2\gamma\sin 2\theta\}\big)^{3/2}}, \tag{9.13}$$

respectively, where, as before, $c_d$ is the constant for the corresponding circular obstacle, given in Table 9.1. The drag exerted on the flow by the obstacle is given by

$$\mathcal{D} = \mathcal{F}_N + \mathcal{F}_S.$$

Since the flow field is in this case asymmetric, the flow is also subject to a 'lift' force $\mathcal{L}$, given by

$$\mathcal{L} = \gamma(\mathcal{F}_N - \mathcal{F}_S).$$

.

In the upper panel of Figure 9.3, normalised drag $\mathcal{D}/M^2$ is plotted against the angle $\theta$ of the obstacle relative to the oncoming flow, for the particular case of the paraboloid obstacle with the Froude number of the oncoming flow $F = 2$ and the eccentricity parameter $\mathcal{E} = 0.5$. In the lower panel, normalised lift $\mathcal{L}/M^2$ is plotted against the angle $\theta$ of the obstacle relative to the oncoming flow. Stars indicate normalised drags and lifts derived from numerical integrations of the shallow-water equations with obstacle height $M = 0.1$, and serve as a check on the algebra involved in the derivation of (9.12,9.13). As might be anticipated, drag is symmetric with respect to $\theta$ whilst lift is antisymmetric. Peak drag occurs when $\theta$ is slightly greater than $\pi/8$, with peak lift being almost coincident with peak drag.

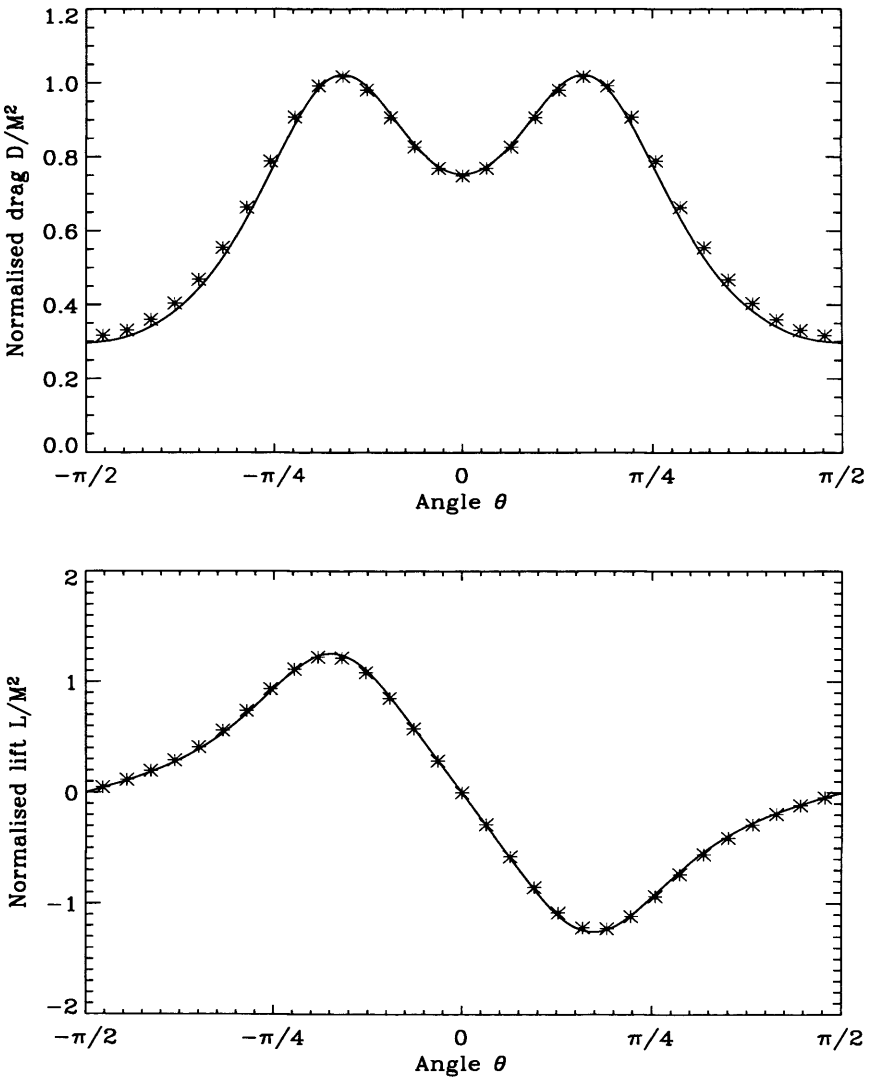


Figure 9.3: Upper panel: variation of normalised drag $\mathcal{D}/M^2$ with the angle $\theta$ of the obstacle to the oncoming flow for the paraboloid obstacle with oncoming Froude number $F = 2$ and eccentricity $\mathcal{E} = 0.5$. Lower panel: normalised lift $\mathcal{L}/M^2$. Stars indicate normalised drags and lifts derived from numerical integrations of the shallow-water equations with obstacle height $M = 0.1$.

Perhaps more surprisingly, it is clear that, at least in this case, for $\theta$ close to the angle at which peak drag is attained, the lift exerted on the flow can exceed the drag.

Figure 9.4 highlights the sensitivity of the drag and lift, as functions of the angle $\theta$, to the Froude number $F$ of the oncoming flow. The eccentricity parameter is fixed, $\mathcal{E} = 0.5$, and in each panel the solid curve describes the normalised drag factor $\mathcal{D}/(M^2 c_d)$, whilst the dashed curve describes the normalised lift factor $\mathcal{L}/(M^2 c_d)$. The general structure between both the drag and lift curves in each panel is similar: both peak drag and (necessarily) peak lift are exerted by an obstacle aligned at a nontrivial angle to the oncoming flow. When $F = 1.3$, the drag exerted on the flow by an obstacle at *any* nontrivial angle to the oncoming flow exceeds that exerted by an obstacle that is aligned with the oncoming flow (dotted line in each panel). Peak drag and lift are attained at very nearly the same angle $\theta$, with the peak drag being over 50% greater than the peak lift.

As the Froude number of the oncoming flow is increased, several trends are apparent. First, the angles at which peak drag and lift are exerted are seen to decrease, whilst the difference in angle at which these peak drags and lifts are exerted increases. Secondly, drag exerted by an obstacle at any nontrivial angle to the oncoming flow need no longer exceed that exerted by an obstacle aligned with the oncoming flow; for an increasing range of values of $\theta$ with increasing $F$, the drag exerted by an obstacle at an angle to the oncoming flow can be less than that exerted by an obstacle aligned with the flow. Thirdly, though both drag and lift decrease with increasing Froude number $F$, the drag exerted decreases more rapidly than the lift such that when $F = 1.7, F = 1.9$ the peak lift exerted by the flow exceeds the peak drag.

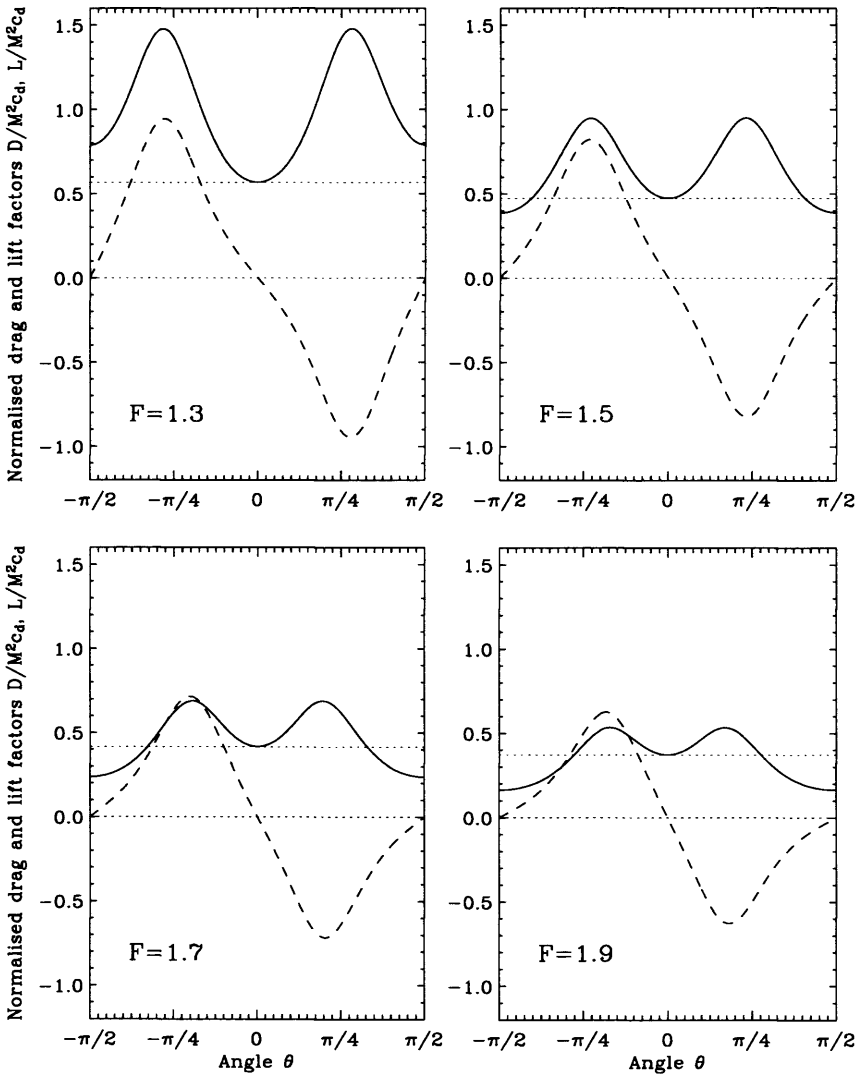


Figure 9.4: Illustrating the sensitivity of drag and lift exerted by an obstacle on the flow, as a function of the angle at which the obstacle is aligned to the oncoming flow $\theta$, to the Froude number $F$ of the oncoming flow. The eccentricity parameter is $\mathcal{E} = 0.5$, and in each panel the solid curve describes the normalised drag factor $\mathcal{D}/(M^2 c_d)$ whilst the dashed curve describes the normalised lift factor $\mathcal{L}/(M^2 c_d)$.

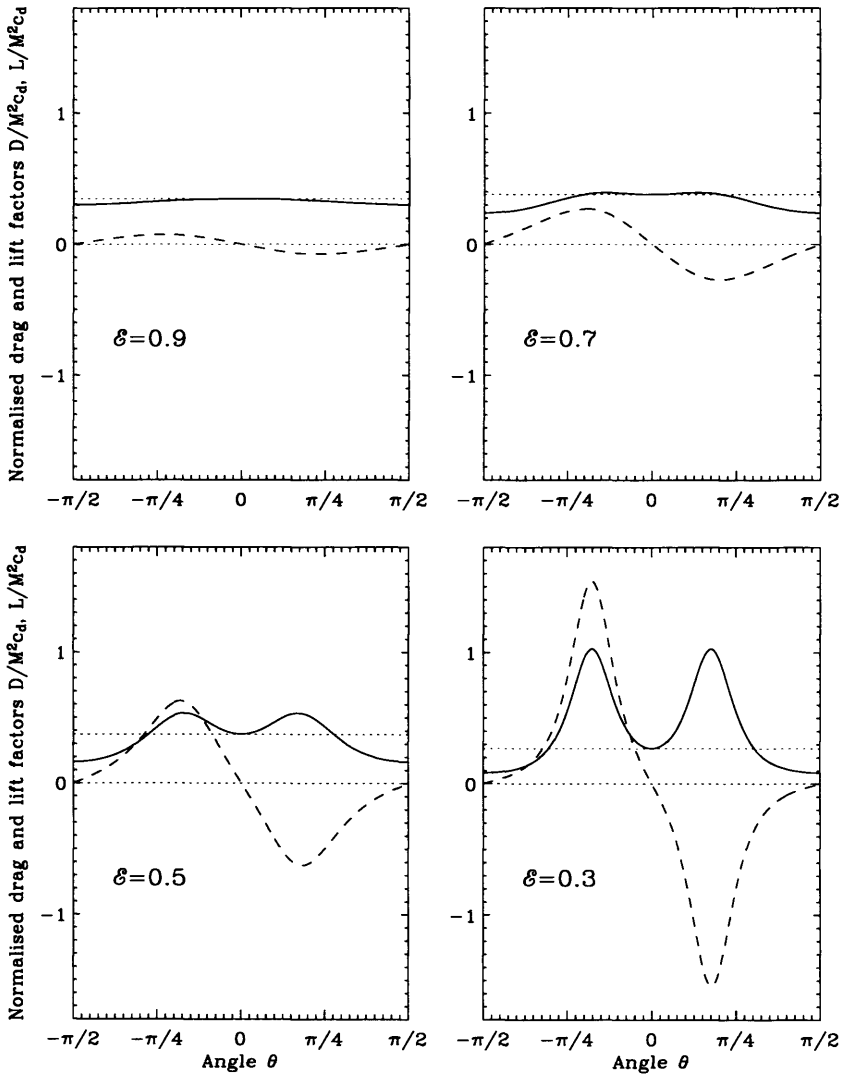


Figure 9.5: Illustrating the sensitivity of drag and lift exerted by an obstacle on the flow, as a function of the angle at which the obstacle is aligned to the oncoming flow $\theta$, to the eccentricity $\mathcal{E}$ of the obstacle. The Froude number is $F = 1.9$, and in each panel the solid curve describes the normalised drag factor $\mathcal{D}/(M^2 c_d)$ whilst the dashed curve describes the normalised lift factor $\mathcal{L}/(M^2 c_d)$.

Figure 9.5 highlights the sensitivity of the drag and lift, as a function of the angle $\theta$, to the eccentricity $\mathcal{E}$ of the obstacle. The Froude number of the oncoming flow is fixed, $F = 1.9$, and in each panel the solid curve describes the normalised drag factor $\mathcal{D}/(M^2 c_d)$, whilst the dashed curve describes the normalised lift factor $\mathcal{L}/(M^2 c_d)$. When $\mathcal{E} = 0.9$, so that the obstacle is nearly circular, drag is, unsurprisingly, insensitive to the angle $\theta$ of the obstacle relative to the oncoming flow, and the lift exerted is small. The peak drag is exerted when the obstacle is aligned with the oncoming flow. As the eccentricity of the obstacle is increased (decreasing $\mathcal{E}$), the familiar structure of peak drag being exerted by an an obstacle at a nontrivial angle to the oncoming flow is recovered, and the peak lift exerted by the flow increases rapidly such that when $\mathcal{E} = 0.5$ peak lift exceeds peak drag. The angles at which peak drag and lift are attained however, seem relatively insensitive to changes in eccentricity $\mathcal{E}$.

Similar figures (not shown) have been constructed for other fixed values of the oncoming Froude number $F$. When the oncoming Froude number of the flow is lower, $F = 1.3$ say, though the peak lift exerted by an obstacle increases as $\mathcal{E}$ decreases, peak lift appears never to exceed peak drag. Thus we infer that the Froude number of the oncoming flow is the critical parameter in determining whether peak lift can exceed peak drag.

### 9.1.5 *The 'equivalent aerofoil' paradigm*

Could the 'equivalent aerofoil' theory introduced in Chapter 2 be applied to the case of an elliptical obstacle aligned at an angle to the oncoming flow? Since in this case the flow field is anticipated to be asymmetric, the relevant

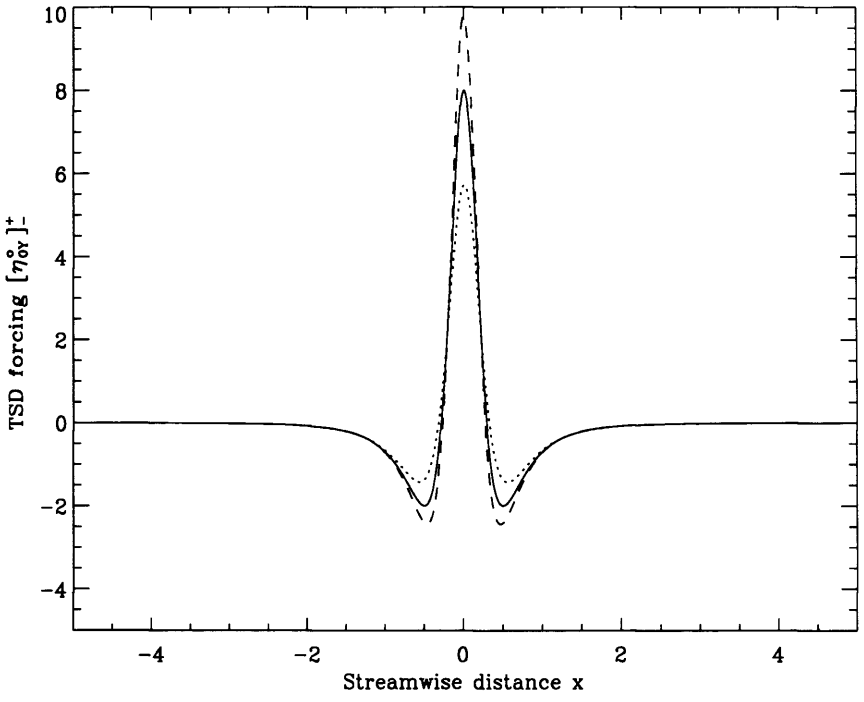


Figure 9.6: TSD equation forcings $[\eta^o_{0Y}]^+_-$ for the 'Witch of Agnesi' obstacle. Solid line, axisymmetric obstacle. Dashed and dotted lines are for the corresponding elliptical 'Witch of Agnesi' obstacle, with eccentricity parameter $\mathcal{E} = 0.5$, aligned at angles $\theta = \pi/4$ (dotted line) and $\theta = \pi/3$ (dashed line) to the oncoming flow.

boundary condition for the TSD equation is given by

$$[\eta^o_{0Y}]^+_- = -\int_{-\infty}^{\infty} h_{xx}(x, \hat{y}) d\hat{y}.$$

Figure 9.6 plots the forcing function in the above boundary condition for the particular case of the 'Witch of Agnesi' obstacle. The solid line indicates the forcing when the obstacle is radially symmetric. The dashed and dotted lines indicate the forcings for the corresponding elliptical 'Witch of Agnesi' obstacle, with eccentricity parameter $\mathcal{E} = 0.5$, aligned at angles $\theta = \pi/4$ (dotted line) and $\theta = \pi/3$ (dashed line) to the oncoming flow. The limi-

tations of the 'equivalent aerofoil' as a description of flow over an obstacle aligned at an angle to the oncoming flow are immediately apparent: the asymmetry of the flow is not captured by the appropriate boundary condition, so that solutions to the TSD equation cannot capture the asymmetry of shallow-water flows. For this reason, the TSD limit to describe this scenario will not considered further here. However, it is possible that the 'equivalent aerofoil' theory might still offer reasonable drag predictions.

## 9.2 Two-Layer Flows: the erTSD equation

Consider the physical scenario of two density contrasting layers of inviscid fluid under a rigid lid, subject to gravity $g$, with undisturbed depths $H_I$ and $H_{II}$ and densities $\rho_I$, $\rho_{II}$ in the upper and lower layers respectively, initially rotating as a solid body with angular frequency $f/2$ but otherwise quiescent. An obstacle of finite volume, with maximum height $h_m$ and radial scale $L$, is towed through the lower layer at uniform speed $U$ from left to right. A schematic of this flow configuration is given in Figure 9.7

In dimensional form, the shallow-water equations corresponding to this scenario are as follows (see, e.g. Plougonven & Zeitlin, 2003)

$$\begin{aligned}
u_{I_t} + (u_I - U)u_{I_x} + v_I u_{I_y} - f v_I &= -\rho_I^{-1}\pi_x, \\
v_{I_t} + (u_I - U)v_{I_x} + v_I v_{I_y} + f u_I &= -\rho_I^{-1}\pi_y, \\
u_{II_t} + (u_{II} - U)u_{II_x} + v_{II} u_{II_y} - f v_{II} &= -(\rho_{II}^{-1}\pi_x + g'(\sigma + h)_x), \\
v_{II_t} + (u_{II} - U)v_{II_x} + v_{II} v_{II_y} + f u_{II} &= -(\rho_{II}^{-1}\pi_y + g'(\sigma + h)_y),
\end{aligned}$$

$$\begin{aligned}
(H - (\sigma + h))_t + ((H - (\sigma + h))(u_I - U))_x + ((H - (\sigma + h))v_I)_y &= 0, \\
\sigma_t + (\sigma(u_{II} - U))_x + (\sigma v_{II})_y &= 0.
\end{aligned}$$

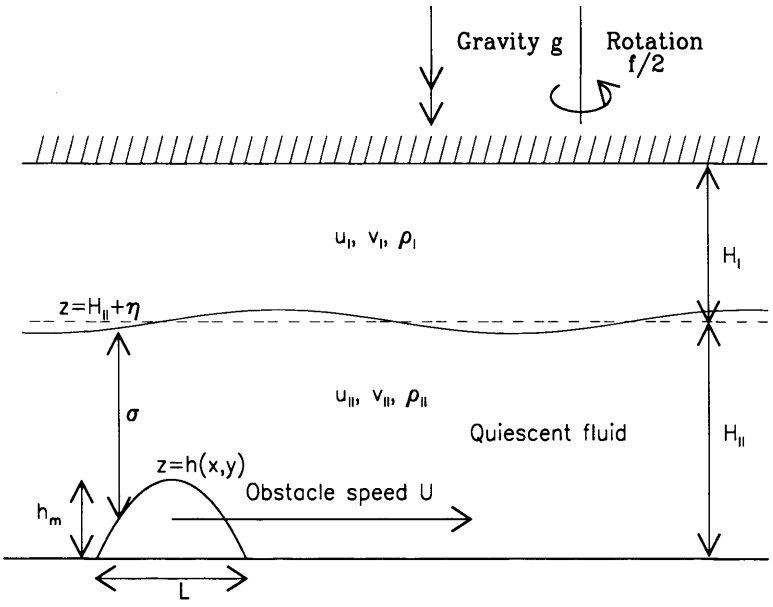


Figure 9.7: Schematic showing the physical scenario of an obstacle towed from left to right, at speed $U$ through the lower layer of a two layer fluid under a rigid lid.

Here: $u_j, v_j$, $j = I, II$ are the velocities in the upper and lower layers respectively; $\pi$ is the barotropic pressure imposed by the rigid lid; $\sigma$ is the thickness of the lower layer; $H_I$ and $H_{II}$ are the heights of the two layers at rest (away from the obstacle) so that $H = H_I + H_{II}$ is the total fluid depth; $f$ is the Coriolis parameter and $g'$ is the reduced gravity, defined by $g' = g(\rho_{II} - \rho_I)/\rho_{II}$.

To proceed, non-dimensionalise velocities with respect to the long interfacial gravity wavespeed, $c_e = \sqrt{g'H_e}$ where $r = \rho_I/\rho_{II}$ is the ratio of the densities of the layers and $H_e$ is the 'equivalent depth' $H_e = \frac{H_I H_{II}}{H_I + rH_{II}}$. Depths are non-dimensionalised with respect to the lower layer depth $H_{II}$, lengths with respect to the obstacle length scale $L$ and time with the ad-

vection time $L/c_e$. Under these scalings, having eliminated the barotropic pressure $\pi$, the following system is revealed:

$$\begin{aligned} r\{u_{I_t} + (u_I - F)u_{I_x} + v_I u_{I_y} - \sqrt{B}v_I\} &= \\ u_{II_t} + (u_{II} - F)u_{II_x} + v_{II}u_{II_y} - \sqrt{B}v_{II} + (1 + \frac{r}{\mathcal{H}})\eta_x; & \\ r\{v_{I_t} + (u_I - F)v_{I_x} + v_I v_{I_y} + \sqrt{B}u_I\} &= \\ v_{II_t} + (u_{II} - F)v_{II_x} + v_{II}v_{II_y} + \sqrt{B}u_{II} + (1 + \frac{r}{\mathcal{H}})\eta_y; & \end{aligned} \tag{9.14}$$

$$\begin{aligned} -\eta_t + [(u_I - F)(\mathcal{H} - \eta)]_x + [v_I(\mathcal{H} - \eta)]_y &= 0; \\ \eta_t + [(u_{II} - F)(1 + \eta - Mh)]_x + [v_{II}(1 + \eta - Mh)]_y &= 0. \end{aligned}$$

In the above, $\eta$ is the interface displacement and the five non-dimensional parameters which appear are: the Froude number $F = U/c_e$; the non-dimensional obstacle height $M = h_m/H_{II}$; an inverse Burger number $B$, $B = f^2L^2/c_e^2$; the density ratio $r = \rho_I/\rho_{II}$ and the layer depth ratio $\mathcal{H} = H_I/H_{II}$.

As a preliminary estimate, consider the equation obtained when the scalings of 'one-and-a-half' layer, rotating, transcritical flow over an obstacle with small height $M \ll 1$ of Chapter 2 are employed. The non-dimensional parameters

$$\Gamma = (F - 1)M^{-2/3}, \qquad \nu = B^{1/2}M^{-1/3}, \tag{9.15}$$

are taken to be of order unity.

Introducing the small parameter $\epsilon = M^{2/3}$ and seeking solutions of (9.14) that evolve on a 'slow' time scale $\tau = \epsilon t$, the variables $u_j, v_j$ and $\eta$ are

expanded in powers of $\epsilon^{1/2}$ as follows

$$\begin{aligned} u_j &= \epsilon(u_{j_0} + \epsilon^{1/2}u_{j_1} + \epsilon u_{j_2} + \dots), \\ v_j &= \epsilon^{3/2}(v_{j_0} + \epsilon^{1/2}v_{j_1} + \epsilon v_{j_2} + \dots), \\ \eta &= \epsilon(\eta_0 + \epsilon^{1/2}\eta_1 + \epsilon\eta_2 + \dots). \end{aligned} \tag{9.16}$$

Ignoring two-dimensional and rotational effects, and further ignoring the topographic forcing term, the above scalings result in the equation

$$2\eta_{0\tau} - 2\Gamma\eta_{0x} + 3\left(\frac{\mathcal{H}^2 - r}{\mathcal{H}(\mathcal{H}+r)}\right)\eta_0\eta_{0x} = 0 \tag{9.17}$$

for the leading order interface displacement $\eta_0$. Clearly, when $r = \mathcal{H}^2$ - when the *critical depth* is achieved - the nonlinear term vanishes from equation (9.17). In these circumstances, the flow is not adequately described by equation (9.17).

To remedy the problem, a further parameter $\mathcal{R}$ is introduced to represent the deviation from the critical depth. The criticality and rotation parameters must also be rescaled, so that we consider the limit in which

$$\Gamma = (F-1)M^{-1}, \quad \nu = B^{1/2}M^{-1/2}, \quad \mathcal{R} = (r - \mathcal{H}^2)M^{-1/2}, \tag{9.18}$$

remain finite as $M \to 0$.

Now taking $\epsilon = M$ to be the small parameter, and seeking solutions of (9.14) that evolve on the 'slow' time scale $\tau = \epsilon t$, the variables $(u_j, v_j)$ and

$\eta$ are expanded in powers of $\epsilon^{1/2}$ as follows

$$\begin{aligned} u_j &= \epsilon^{1/2}(u_{j_0} + \epsilon^{1/2}u_{j_1} + \epsilon u_{j_2} + \dots), \\ v_j &= \epsilon(v_{j_0} + \epsilon^{1/2}v_{j_1} + \epsilon v_{j_2} + \dots), \\ \eta &= \epsilon^{1/2}(\eta_0 + \epsilon^{1/2}\eta_1 + \epsilon\eta_2 + \dots). \end{aligned} \tag{9.19}$$

Note that in this case, the interface displacement $\eta$ scales with $M^{1/2}$, whereas in the 'one-and-a-half' layer scenario discussed in Chapter 2, $\eta$ scaled with $M^{2/3}$. Similarly to the derivation of the rTSD equation, the expansions (9.19) may now be used to match leading order asymptotic solutions of (9.14) in two separate regions defined by their cross-stream distance from the centre of the obstacle at $y = 0$.

*Inner region*

In the inner region, which describes flow on streamlines that pass over or near to the obstacle, the cross-stream coordinate is taken to be $y$. Denoting inner region variables with the superscript $i$ and inserting the expansion (9.19) in (9.14), at leading order it is established that

$$u^i_{I_0} = -\frac{1}{\mathcal{H}}\eta^i_0(x), \quad u^i_{II_0} = \eta^i_0(x). \tag{9.20}$$

The leading order solution is therefore described by an (as yet) undetermined $y$-independent function $\eta^i_0(x)$, except for the leading order cross-stream velocities $v^i_{I_0}$,$v^i_{II_0}$. At the next order in the expansion the relation

$$v^i_{II_0y} - \mathcal{H}^2 v^i_{I_0y} = -h_x$$

is revealed. Integrating in $y$ gives

$$v^i_{II_0} - \mathcal{H}^2 v^i_{I_0} = V(x) - \int_0^y h_x(x,\hat{y})d\hat{y}, \tag{9.21}$$

where $V(x)$ is an undetermined function. The velocities $v^i_{I_0}$,$v^i_{II_0}$ are related to the interface displacement through

$$-v^i_{II_0x} + \mathcal{H}^2 v^i_{I_0x} + (1+\mathcal{H})\nu\eta^i_0 = -(1+\mathcal{H})\eta^i_{1y}. \tag{9.22}$$

Proceeding to higher order, it becomes clear that $\eta^i_0(x)$ will not be determined by the inner region expansion alone. Furthermore, the solution becomes invalid away from the obstacle where $|y| \sim O(\epsilon^{-1/2})$. At these distances, higher order terms in the series expansion become comparable with those at leading order. This indicates that $\eta^i_0$ must be determined by matching with an outer region solution which is valid for $|y| \sim O(\epsilon^{-1/2})$.

*Outer region*

In the outer region, the variable $Y = \epsilon^{1/2}y$ is introduced to capture the cross-stream scale on which the leading order interface displacement and streamwise velocities vary in the direction perpendicular to the oncoming flow. The influence of the obstacle is experienced through the boundary condition at $Y = 0$ only. Throughout the rest of the domain in the rescaled coordinates the bottom boundary is taken to be flat. In the outer region far-field asymptotic solutions are sought, denoted by the superscript $o$, of (9.14) by substituting

$$u_{I_0} = u^o_{I_0}(x, Y, \tau) \quad \text{etc.}$$

for each term in the series expansion (9.19). At leading order

$$u^o_{I_0} = -\frac{1}{\mathcal{H}}\eta^o_0, \qquad u^o_{II_0} = \eta^o_0,$$

together with

$$v^o_{II_0x} - \mathcal{H}^2 v^o_{I_0x} = (1+\mathcal{H})\nu\eta^o_0 + (1+\mathcal{H})\eta^o_{0Y}. \tag{9.23}$$

From the next order, the following relations will be required:

$$\begin{aligned} -\mathcal{H}^2 u^o_{I_{1x}} + u^o_{II_{1x}} - (1+\mathcal{H})\eta^o_{1x} &= 0; \\ \mathcal{H}u^o_{I_{1x}} + \eta^o_{1x} + \frac{1}{\mathcal{H}}(\eta^{o^2}_0)_x &= 0; \\ u^o_{II_{1x}} - \eta^o_{1x} + (\eta^{o^2}_0)_x &= 0. \end{aligned} \tag{9.24}$$

From the $x$-momentum and continuity equations, the following relations between the $0(\epsilon^{3/2})$ terms are obtained

$$\begin{aligned} -\mathcal{H}^2 u^o_{I_{2x}} + u^o_{II_{2x}} - (1+\mathcal{H})\eta^o_{2x} &= -\mathcal{H}^2 u^o_{I_{0\tau}} - \mathcal{H}^2(u^o_{I_0}u^o_{I_1})_x + \\ \mathcal{H}^2\Gamma u^o_{I_{0x}} + \mathcal{H}^2\nu v^o_{I_0} - \mathcal{R}u^o_{I_0}u^o_{I_{0x}} &+ \mathcal{R}u^o_{I_{1x}} + u^o_{II_{0\tau}} + (u^o_{II_0}u^o_{II_1})_x - \Gamma u^0_{II_{0x}} \\ &\quad -\nu v^o_{II_0} + \frac{\mathcal{R}}{\mathcal{H}}\eta^o_{1x}, \\ \mathcal{H}u^o_{I_{2x}} + \eta^o_{2x} &= \eta^o_{0\tau} + (u^o_{I_1}\eta^o_0)_x + (u^o_{I_0}\eta^o_1)_x - \Gamma\eta^o_{0x} - \mathcal{H}v^o_{I_{0Y}}, \\ u^o_{II_{2x}} - \eta^o_{2x} &= -\eta^o_{0\tau} - (u^o_{II_1}\eta^o_0)_x - (u^o_{II_0}\eta^o_1)_x + \Gamma\eta^o_{0x} - v^o_{II_{0Y}}. \end{aligned}$$

Substituting into the $x$-momentum equation from the continuity equations, and subsequently employing relations (9.24), (9.23) to eliminate terms in-

volving $\eta_1^o$, $v_{j_0}^o$, the following equation is revealed

$$\left(2\eta_{0\tau}^o - 2\Gamma\eta_{0x}^o - \frac{3\mathcal{R}}{\mathcal{H}^2(\mathcal{H}+1)}\eta_0^o\eta_{0x}^o - \frac{2}{\mathcal{H}}(\eta_0^{o^3})_x\right)_x - \nu^2\eta_0^o + \eta_{0YY}^o = 0. \quad (9.25)$$

Equation (9.25) is the dispersionless extended rKP equation, as might have been anticipated for the outer region. In the context of the current work, for consistency with previous results, it will be referred to as the extended, rotating transcritical small disturbance equation (erTSD).

### 9.2.1 *Matching conditions - the equivalent aerofoil*

Matching between the inner and outer regions results in the following conditions

$$\begin{aligned}
\eta_0^i(x) &= \lim_{Y\to 0}\eta_0^o(x,Y), \\
\lim_{y\to\pm\infty}\eta_{1y}^i(x,y) &= \lim_{Y\to 0^\pm}\eta_{0Y}^o(x,Y), \\
\lim_{y\to\pm\infty}v_{I_0}^i(x,y) &= \lim_{Y\to 0^\pm}v_{I_0}^o(x,Y), \\
\lim_{y\to\pm\infty}v_{II_0}^i(x,y) &= \lim_{Y\to 0^\pm}v_{II_0}^o(x,Y).
\end{aligned} \quad (9.26)$$

Using (9.21) and (9.22) the matching conditions may be replaced by the single condition

$$[\eta_{0Y}^o]_-^+ = -\int_{-\infty}^{\infty} h_{xx}(x,\hat{y})\,d\hat{y}, \quad (9.27)$$

where the square brackets denote the difference between evaluation at $Y \to 0^+$ and $Y \to 0^-$.

### 9.2.2 *Jump conditions for the erTSD equation*

In an analogous manner to the rTSD equation discussed in Chapter 2, solutions to the erTSD equation (9.25) must be regularised by the inclusion

of hydraulic jump discontinuities. However, in the context of a two-layered fluid, determining the appropriate form of these jump conditions presents considerable difficulties.

Mathematically speaking, problems stem from the fact that the 'flux function' for the erTSD equation is non convex. In this case, the Lax criterion, which (loosely) states that characteristics must impinge on a jump discontinuity, can be violated in a physically meaningful way, so that characteristics may in fact emanate from a jump.

The problem of jump closure for the erTSD equation has been addressed recently by Kluwick *et al.* (2007), who consider a variant of the eTSD equation in which the effects of both weak dispersion and weak dissipation are retained. Subsequently, they show that the possible jump discontinuities that emerge in the limit of weak dispersion and dissipation depend crucially on the ratio of dispersion and dissipation maintained during the limit process.

## 9.3 Summary

Explicit expressions for the linear, non-rotating drag exerted by an obstacle that is both elliptic and aligned at an angle to the oncoming flow have been introduced. The extension of the 'equivalent aerofoil' theory to the description of the baroclinic mode of a two-layered fluid has been described. Many further extensions are, of course, possible. To give just one example, Cole & Cook (1986) discuss transonic flow over an aerofoil in which the oncoming flow is sheared in the $y$-direction, showing that the required modification is $\Gamma = \Gamma(Y)$. Presumably the same modification would result from an analysis of the corresponding problem of shallow-water flow over an isolated obstacle of small height.

# Appendix A

# Numerical determination of breaking bounds for the Ostrovsky-Hunter equation

With the Ostrovsky-Hunter equation (7.3) expressed in the parametric form (7.10), with initial conditions (7.11), wave breaking occurs when $\mathcal{X}_\zeta = 0$. Here we detail the numerical establishment of the bound $\beta_2$, which describes the transition from solutions that exhibit finite time wave breaking to solutions that remain smooth for all time. Equations (7.10), together with the initial conditions (7.11), are integrated in time using a pseudospectral method similar to that discussed by Boyd (2005).

Aside from errors associated with the numerical discretisation itself, three factors might affect the accuracy of numerically established breaking bounds for the Ostrovsky-Hunter equation (7.3).

- Numerical resolution.
- The time span of the integration.

- The effects of domain truncation. The Ostrovsky-Hunter equation (7.3) is posed on an infinite domain, yet numerical solutions discussed here encompass only a finite domain.

Each factor is examined, for initial conditions corresponding to both the 'Witch of Agnesi' and Gaussian obstacles (c.f. Table 7.1), in the following series of tables.

| $\beta_2$ | $inf(\mathcal{X}_\zeta)$ | $n$ |
|---|---|---|
| 0.017865 | 0.004 | 512 |
| 0.017866 | -0.0047 | 512 |
| 0.017901 | 0.0076 | 1024 |
| 0.017902 | -0.0023 | 1024 |
| 0.017906 | 0.0055 | 2048 |
| 0.017907 | -0.0036 | 2048 |

Table A.1: Sensitivity of the wave breaking bound $\beta_2$ to the number of Chebyshev nodes ($n$ in the table) used in solving equation (7.10) with a pseudospectral method. The initial condition (7.11) corresponds to the 'Witch of Agnesi' obstacle, and is given in Table 7.1. For each integration, the spatial domain encompasses $\zeta \in [-5, 5]$, and the integration spans $\bar{t} \in [0, 1000]$.

Tables A.1, A.2 & A.3 highlight the sensitivity of the wave breaking bound $\beta_2$ to the numerical resolution (number of Chebyshev nodes), time span of the numerical integration and to domain truncation respectively, for the initial condition (7.11) corresponding to the 'Witch of Agnesi' obstacle (c.f. Table 7.1). Examining these tables, we conclude that to four decimal places, we can state that for the 'With of Agnesi' obstacle $\beta_2 = 0.0178$ with a good degree of confidence.

Tables A.4, A.5 & A.6 highlight the sensitivity of the wave breaking bound $\beta_2$ to the numerical resolution (number of Chebyshev nodes), time

| $\beta_2$ | $inf(\mathcal{X}_\zeta)$ | $\bar{t}_{max}$ |
|---|---|---|
| 0.017901 | 0.0076 | 1000 |
| 0.017902 | -0.0023 | 1000 |
| 0.017862 | 0.011 | 2000 |
| 0.017863 | -0.0032 | 2000 |
| 0.017841 | 0.0165 | 3000 |
| 0.017842 | -0.0033 | 3000 |
| 0.017841 | 0.0165 | 4000 |
| 0.017842 | -0.0033 | 4000 |
| 0.017841 | 0.00165 | 5000 |
| 0.017842 | -0.0033 | 5000 |

Table A.2: Sensitivity of the wave breaking bound $\beta_2$ to the time span of the integration, $(0, \bar{t}_{max})$, used in solving equation (7.10) with a pseudospectral method. The initial condition (7.11) corresponds to the 'Witch of Agnesi' obstacle, and is given in Table 7.1. For each integration, the spatial domain encompasses $\zeta \in [-5, 5]$ and is covered by 1024 Chebyshev nodes.

span of the numerical integration and to domain truncation respectively, for the initial condition (7.11) corresponding to the Gaussian obstacle (c.f. Table 7.1). Examining these tables, we conclude that to four decimal places, we can state that for the Gaussian obstacle (rounding down) $\beta_2 = 0.0481$ with a good degree of confidence.

| $\beta_2$ | $inf(\mathcal{X}_\zeta)$ | $\zeta$, $n$ |
|---|---|---|
| 0.017841 | 0.0168 | $\zeta \in [-5,5]$ , $n = 1024$ |
| 0.017842 | -0.0033 | |
| 0.017841 | 0.0242 | $\zeta \in [-10,10]$ , $n = 2048$ |
| 0.017842 | -0.0159 | |

Table A.3: Sensitivity of the wave breaking bound $\beta_2$ to the range of $\zeta$ used in solving equation (7.10) with a pseudospectral method. The initial condition (7.11) corresponds to the 'Witch of Agnesi' obstacle, and is given in Table 7.1. Each integration encompasses the time span $\bar{t} \in [0, 5000]$; $n$ is the number of Chebyshev nodes covering the range of $\zeta$.

| $\beta_2$ | $inf(\mathcal{X}_\zeta)$ | $n$ |
|---|---|---|
| 0.048208 | 0.00702 | 512 |
| 0.048209 | -0.00005 | 512 |
| 0.048238 | 0.001445 | 1024 |
| 0.048239 | -0.004498 | 1024 |
| 0.048238 | 0.001922 | 2048 |
| 0.048239 | -0.0040 | 2048 |

Table A.4: Sensitivity of the wave breaking bound $\beta_2$ to the number of Chebyshev nodes ($n$ in the table) used in solving equation (7.10) with a pseudospectral method. The initial condition (7.11) corresponds to the Gaussian obstacle, and is given in Table 7.1. For each integration, the spatial domain encompasses $\zeta \in [-5, 5]$, and the integration spans $\bar{t} \in [0, 1000]$.

| $\beta_2$ | $inf(\mathcal{X}_\zeta)$ | $\bar{t}_{max}$ |
|---|---|---|
| 0.048238 | 0.001922 | 1000 |
| 0.048239 | -0.0040 | 1000 |
| 0.048196 | 0.00529 | 2000 |
| 0.048197 | -0.00474 | 2000 |
| 0.048182 | 0.00344 | 3000 |
| 0.048183 | -0.0122 | 3000 |
| 0.048179 | 0.012 | 4000 |
| 0.048180 | -0.004 | 4000 |
| 0.048179 | 0.0089 | 5000 |
| 0.048180 | -0.00859 | 5000 |
| 0.048176 | 0.01747 | 6000 |
| 0.048177 | -0.0016 | 6000 |
| 0.048175 | 0.00163 | 7000 |
| 0.048176 | -0.080966 | 7000 |
| 0.048175 | 0.00163809 | 8000 |
| 0.048176 | -0.0080 | 8000 |
| 0.048174 | 0.037728 | 9000 |
| 0.048175 | -0.0042 | 9000 |
| 0.048174 | 0.0377 | 10000 |
| 0.048175 | -0.0420 | 10000 |
| 0.048174 | 0.0377 | 11000 |
| 0.048175 | -0.0420 | 11000 |
| 0.048174 | 0.0377 | 12000 |
| 0.048175 | -0.0420 | 12000 |

Table A.5: Sensitivity of the wave breaking bound $\beta_2$ to the time span of the integration, $(0, \bar{t}_{max})$, used in solving equation (7.10) with a pseudospectral method. The initial condition (7.11) corresponds to the Gaussian obstacle, and is given in Table 7.1. For each integration, the spatial domain encompasses $\zeta \in [-5, 5]$ and is covered by 1024 Chebyshev nodes.

| $\beta_2$ | $inf(\mathcal{X}_\zeta)$ | $\zeta$, $n$ |
|---|---|---|
| 0.048174 | 0.0377 | $x \in [-5,5]$ , $n = 1024$ |
| 0.048175 | -0.0420 | |
| 0.048174 | 0.0761 | $x \in [-10,10]$ , $n = 2048$ |
| 0.048175 | -0.0623 | |

Table A.6: Sensitivity of the wave breaking bound $\beta_2$ to the range of $\zeta$ used in solving equation (7.10) with a pseudospectral method. The initial condition (7.11) corresponds to the Gaussian obstacle, and is given in Table 7.1. Each integration encompasses the time span $\bar{t} \in [0, 12000]$; $n$ is the number of Chebyshev nodes covering the range of $\zeta$.

# Appendix B

# 'Equivalent aerofoil' theory with dispersion

Consider the 'experimental scenario', depicted in Figure 1.5, in which an obstacle is towed at speed $U$, from left to right, through a single layer of rotating fluid which is otherwise quiescent. The non-dimensional Euler equations for this scenario are

$$\begin{aligned} \frac{Du}{Dt} - \sqrt{B}v &= -p_x, \\ \frac{Dv}{Dt} + \sqrt{B}u &= -p_y, \\ \delta^2 \frac{Dw}{Dt} &= -(p_z + 1), \\ u_x + v_y + w_z &= 0, \end{aligned} \tag{B.1}$$

where the advective derivative, $D/Dt = \partial_t + (u - F)\partial_x + v\partial_y + w\partial_z$ contains a contribution from the mean flow. The set (B.1) is subject to the boundary

conditions

$$\begin{aligned} \eta_t + (u-F)\eta_x + v\eta_y &= w, \qquad \text{on} \quad z = 1+\eta(x,y,t), \\ M[(u-F)h_x + vh_y] &= w, \qquad \text{on} \quad z = Mh(x,y), \\ p &= 0, \qquad \text{on} \quad z = 1+\eta(x,y,t). \end{aligned} \tag{B.2}$$

The four non-dimensional parameters are as before: the aspect ratio $\delta = H/L$, the Froude number $F = U/c$, the Burger number $B = f^2L^2/c^2$, and the non-dimensional obstacle height $M = h_m/H$.

Following Esler *et al.* (2007*a*) and the scalings of Chapter 2, the non-dimensional parameters

$$\Gamma = (F-1)M^{-2/3}, \qquad \Delta = \delta M^{-1/3}, \qquad \nu = \sqrt{B}M^{-1/3}, \tag{B.3}$$

are taken to be of order unity. The parameters $\Gamma$ and $\nu$ are as described previously. The parameter $\Delta$ is a measure of the importance of dispersion in the system, with the non-dispersive limit corresponding to $\Delta = 0$, and the weakly dispersive limit given by $\Delta \to 0$.

As previously, introducing a small parameter $\epsilon = M^{2/3}$, and seeking solutions of (B.1–B.2) that evolve on a 'slow' time scale $\tau = \epsilon t$, the variables $(u, v, w)$, $p$ and $\eta$ may be expanded in powers of $\epsilon^{1/2}$ as follows

$$\begin{aligned} u &= \epsilon\left(u_0 + \epsilon^{1/2}u_1 + \epsilon u_2 + ....\right) \\ v &= \epsilon^{3/2}\left(v_0 + \epsilon^{1/2}v_1 + \epsilon v_2 + ....\right) \\ w &= \epsilon\left(w_0 + \epsilon^{1/2}w_1 + \epsilon w_2 + ....\right) \\ p &= 1 - z + \epsilon\left(p_0 + \epsilon^{1/2}p_1 + \epsilon p_2 + ....\right) \\ \eta &= \epsilon\left(\eta_0 + \epsilon^{1/2}\eta_1 + \epsilon\eta_2 + ....\right). \end{aligned} \tag{B.4}$$

The expansions (B.4) are used to match leading order asymptotic solutions of (B.1–B.2) in two separate regions defined by their cross-stream distance from the centre of the obstacle at $y = 0$.

In the inner region, which describes flow on streamlines that pass over or near to the obstacle, the cross-stream co-ordinate is taken to be $y$. Denoting inner region variables with the superscript $i$ and inserting the expansion (B.4) in (B.1–B.2), at leading order it is established that

$$u_0^i = p_0^i = \eta_0^i(x), \qquad w_0^i = -\eta_{0x}^i z. \tag{B.5}$$

The leading order solution is therefore described by an (as yet) undetermined $y$-independent function $\eta_0^i(x)$, except for the leading order cross-stream velocity $v_0^i$. At the next order in the expansion

$$u_1^i = p_1^i = \eta_1^i(x,y), \qquad w_1^i = -\left(\eta_{1x}^i + v_{0y}^i\right) z - h_x. \tag{B.6}$$

Inserting the above expression for $w_1^i$ into the kinematic condition at the free surface gives $v_{0y}^i = -h_x$. Integrating in $y$ gives

$$v_0^i(x,y) = V(x) - \int_0^y h_x(x,\hat{y})\, d\hat{y}, \tag{B.7}$$

where $V(x)$ is an undetermined function, with the velocity $v_0^i$ being related to the free surface height through

$$-v_{0x}^i + \nu\eta_0^i = -\eta_{1y}^i. \tag{B.8}$$

In the outer region the variable $Y = \epsilon^{1/2} y$ is introduced to capture the cross-stream scale on which the leading order free surface height and streamwise velocity vary in the direction perpendicular to the oncoming

flow. The influence of the obstacle is experienced only through the boundary condition at $Y = 0$. Throughout the rest of the domain in the rescaled coordinates the bottom boundary is taken to be flat. In the outer region we seek far field asymptotic solutions, denoted by superscript $o$, of (B.1–B.2) by substituting

$$u_0 = u_0^o(x, Y, z, \tau) \quad \text{etc.}$$

for each term in the series expansion (B.4). At leading order

$$u_0^o = p_0^o = \eta_0^o(x, Y), \qquad w_0^o = -\eta_{0x}^o z, \tag{B.9}$$

together with

$$v_{0x}^o = \eta_{0Y}^o + \nu\eta_0^o. \tag{B.10}$$

At the next order, $u_1^o$, $v_1^o$, $w_1^o$, $p_1^o$, $\eta_1^o$ are found to satisfy an identical set of equations to (B.9-B.10), and hence may be set to zero without loss of generality. To obtain an equation for $\eta_0^o$ we must proceed to $O(\epsilon^2)$, thereby introducing nonlinear terms. The derivation from here follows the standard derivation of the rKP equation. The following relations between the $O(\epsilon^2)$ terms are obtained

$$\begin{aligned}
p_2^o &= \eta_2^o + \frac{\Delta^2}{2}\eta_{0xx}^o\left(1 - z^2\right), \\
u_{2x}^o &= \eta_{2x}^o + \frac{\Delta^2}{2}\eta_{0xxx}^o\left(1 - z^2\right) - \nu v_0^o + \eta_{0\tau}^o - \Gamma\eta_{0x}^o + \eta_0^o\eta_{0x}^o, \\
w_2^o &= z\left[-\eta_{2x}^o - \frac{\Delta^2}{2}\eta_{0xxx}^o + \nu v_0^o - v_{0Y}^o - \eta_{0\tau}^o + \Gamma\eta_{0x}^o - \eta_0^o\eta_{0x}^o\right] + z^3\frac{\Delta^2}{6}\eta_{0xxx}^o.
\end{aligned} \tag{B.11}$$

Inserting the above expression for $w_2^o$ into the kinematic condition at the

free surface reveals that terms involving $\eta_2$ cancel, to give

$$\left(2\eta^o_{0\tau} + 3\eta^o_0\eta^o_{0x} - 2\Gamma\eta^o_{0x} + \frac{\Delta^2}{3}\eta^o_{0xxx}\right)_x - \nu^2\eta^o_0 + \eta^o_{0YY} = 0, \qquad \text{(B.12)}$$

where $v^o_0$ has been eliminated using (B.10). Equation (B.12) is the rKP equation, as might be anticipated for the outer region. The novel component introduced in Esler *et al.* (2007*a*) is the derivation of the appropriate boundary condition on $Y = 0$, which is obtained by matching with the inner solution as follows.

Matching between the inner and outer regions results in the following conditions

$$\begin{aligned} \eta^i_0(x) &= \lim_{Y\to 0}\eta^o_0(x,Y), \\ \lim_{y\to\pm\infty}\eta^i_{1y}(x,y) &= \lim_{Y\to 0^\pm}\eta^o_{0Y}(x,Y), \\ \lim_{y\to\pm\infty}v^i_0(x,y) &= \lim_{Y\to 0^\pm}v^o_0(x,Y). \end{aligned} \qquad \text{(B.13)}$$

Using (B.7) and (B.8) the matching conditions may be replaced by the single condition

$$[\eta^o_{0Y}]^+_- = -\int_{-\infty}^{\infty} h_{xx}(x,\hat{y})\,d\hat{y}, \qquad \text{(B.14)}$$

where the square brackets denote the difference between evaluation at $Y \to 0^+$ and $Y \to 0^-$. Note that for obstacles symmetric about $y = 0$, including axisymmetric obstacles, the boundary condition (B.14) for equation (B.12) can be replaced by a 'line-charge' forcing term on the right-hand side of (B.12) of the form

$$F(x,Y) = -2\delta(Y)K_{xx}(x), \quad \text{where } K(x) = \int_0^{\infty} h_(x,\hat{y})\,d\hat{y}, \qquad \text{(B.15)}$$

and $\delta(Y)$ is the Dirac delta function.

# Bibliography


AKYLAS, T. R. 1994 Three-dimensional long water-wave phenomena. *Ann. Rev. Fluid Mech.* **26**, 191–210.

ALBERT, J. P. 1997 Nonlinear nonlocal equations in the theory of waves. *Bulletin of the American Mathematical Society* **34**, 95–99.

BADGLEY, P. C., MILOY, L. & CHILDS, L. 1969 *Oceans from Space*. Gulf Publishing.

BAINES, P. G. 1995 *Topographic Effects in Stratified Flows*. Cambridge: Cambridge University Press.

BAINES, P. G. & LEONARD, B. P. 1989 The effects of rotation on flow of a single layer over a ridge. *Q. J. R. Meteorol. Soc.* **115**, 293.

BAINES, P. G. & WHITEHEAD, J. A. 2003 On multiple states in single-layer flows. *Phys. Fluids* **15**, 298.

BALLHAUS, W. F. & GOORJIAN, P. M. 1977 Implicit finite-difference computations of unsteady transonic flows about airfoils. *AIAA J.* **15**, 1728–1735.

BALLHAUS, W. F., JAMESON, A. & ALBERT, J. 1978 Implicit approximate factorisation schemes for steady transonic flow problems. *AIAA J.* **16**, 573–579.

BENJAMIN, T. B. 1967 Internal waves of permanent form in fluids of great depth. *J. Fluid Mech.* **25**, 559–92.

BOYD, J. P. 2005 Microbreaking and polycnoidal waves in the Ostrovsky-Hunter equation. *Physics Letters A* **338**, 36–43.

BRANDT, A. 1977 Multi-level adaptive solutions to boundary value problems. *Math. of Comp.* **31**, 333–390.

BURK, S. D. & HAACK, T. 1999 The dynamics of wave clouds upwind of coastal orography. *Mon. Weath. Rev.* **28**, 1438–1455.

CHAPMAN, C. J. 2000 *High Speed Flow*. Cambridge: Cambridge University Press.

CHOI, W. & CAMASSA, R. 1999 Fully nonlinear internal waves in a two-fluid system. *J. Fluid Mech.* **396**, 1–36.

COLE, J. D. & COOK, P. 1986 *Transonic Aerodynamics*. New York: North-Holland.

DJORDJEVIC, V. D. & REDEKOPP, L. G. 1978 The fission and disintegration of internal solitary waves moving over two-dimensional topography,. *J. Phys. Oceanogr.* **8**, 1016–24.

ENGQUIST, B. & OSHER, S. 1980 Stable and entropy satisfying approximations for transonic flow calculations. *Math. Comp.* **34**, 45–75.

ERTEKIN, W. C., WEBSTER, R. C. & WEHAUSEN, J. V. 1986 Waves caused by moving disturbance in a shallow channel of finite width. *J. Fluid Mech.* **169**, 275–292.

ESLER, J. G., RUMP, O. J. & JOHNSON, E. R. 2005 Steady rotating flows over a ridge. *Phys. Fluids* **17**, 116601.

ESLER, J. G., RUMP, O. J. & JOHNSON, E. R. 2007*a* Nondispersive and weakly dispersive single layer flow over an axisymmetric obstacle: The equivalent aerofoil formulation. *J. Fluid Mech.* **574**, 209–237.

ESLER, J. G., RUMP, O. J. & JOHNSON, E. R. 2007*b* Supercritical rotating flow over topography. In preparation.

ESLER, J. G., RUMP, O. J. & JOHNSON, E. R. 2007*c* Transcritical rotating flow over topography. J. Fluid Mech. In press.

FU, L. L. & HOLT, B. 1982 Seasat view oceans and sea ice with synthetic aperture radar. NASA/JPL Publ. 821-120.

GOORJIAN, P. M. & VAN BUSKIRK, R. 1981 Implicit calculations of transonic flows using monotone methods. *AIAA J.* **81-0331**.

GREEN, A. E. & NAGHDI, P. M. 1976 A derivation of equations for wave propagation in water of variable depth. *J. Fluid Mech.* **78**, 237–246.

GRIMSHAW, R. H. J. & MELVILLE, W. K. 1989 On the derivation of the modified Kadomtsev-Petviashvili equation. *Stud. Appl. Maths* **80**, 183–203.

GRIMSHAW, R. H. J., OSTROVSKY, L. A., SHRIRA, V. I. & STEPANYANTS, Y. A. 1998 Long nonlinear surface and internal gravity waves in a rotating ocean. *Surv. Geophys.* **19**, 289–338.

GRIMSHAW, R. H. J. & SMYTH, N. 1986 Resonant flow of a stratified fluid over topography. *J. Fluid Mech.* **169**, 429–464.

HALL, M. G. 1981 Computational fluid dynamics - a revolutionary force in aerodynamics. In *5th Computational Fluid Dyn. Conf.*, pp. 176–188.

HELFRICH, K. R. & MELVILLE, W. K. 2006 Long nonlinear internal waves. *Annu. Rev. Fluid Mech.* **38**, 395–425.

HIRSCH, C. 1988 *Numerical Computation of Internal and External Flows.* New York: Wiley.

HOLLOWAY, P. E., PELINOVSKY, E. & TALIPOVA, T. 1999 A generalized Korteweg-de Vries model of internal tide transformation in the coastal zone. *J. Geophys. Res.* **104**, 18333–50.

HOLLOWAY, P. E., PELINOVSKY, E., TALIPOVA, T. & BARNES, B. 1997 A nonlinear model of internal tide transformation on the Australian north west shelf. *J. Phys. Oceanogr.* **27**, 871–896.

HOLST, T. L. 2000 Transonic flow computations using nonlinear potential methods. *Progress in Aerospace Sciences* **36**, 1–61.

HOUGHTON, D. D. 1969 Effect of rotation on the formation of hydraulic jumps. *J. Geophys. Res.* **74**, 1351.

HOUGHTON, D. D. & KASAHARA, A. 1968 Nonlinear shallow fluid flow over an isolated ridge. *Comm. Pure Appl. Math.* **21**, 1.

HUNTER, J. K. 1990 Numerical solutions of some nonlinear dispersive wave equations. *Lectures in Applied Mathematics* **26**, 301–316.

JAMESON, A. 1979 Acceleration of transonic potential flow calculations on arbitrary meshes by the multiple grid method. *AIAA Paper* **79**, 1979–1458.

JAMESON, A. 1986 *Numerical solution of nonlinear partial differential equations of mixed type.* Oxford: North-Holland.

JIANG, Q. & SMITH, R. B. 2000 V-waves, bow shocks, and wakes in supercritical hydrostatic flow. *J. Fluid Mech.* **406**, 27–53.

JOHNSON, E. R., ESLER, J. G., RUMP, O. J., SOMMERIA, J. & VILENSKI, G. G. 2006 Orographically generated nonlinear waves in rotating and nonrotating two-layer flow. *Proc. Roy. Soc. Lond. Ser. A.* **462**, 3–20.

JOHNSON, E. R. & VILENSKI, G. G. 2004 Flow patterns and drag in near-critical flow over isolated orography. *J. Atmos. Sci.* **61**, 2909–2918.

JOHNSON, R. S. 1997 *A Modern Introduction to the Mathematical Theory of Water Waves*. Cambridge: Cambridge University Press.

JOSEPH, R. I. 1977 Solitary waves in finite depth fluids. *J. Phys. A.* **10**, 1225–1227.

KADOMTSEV, B. B. & PETVIASHVILI, V. I. 1970 On the stability of solitary waves in weakly dispersing media. *Sov. Phys. Dokl.* **15**, 539–541.

KAKUTANI, T. & MATSUUCHI, T. R. 1978 Solitary waves on a two-layer fluid. *J. Phys. Soc. Jpn.* **45**, 674–79.

KLEMP, J. B., ROTUNNO, R. & SKAMAROCK, W. C. 1997 On the propagation of internal bores. *J. Fluid Mech.* **331**, 81–106.

KLUWICK, A., SCHEICHL, S. & COX, E. 2007 Near-critical hydraulic flows in in two-layered fluids. *J. Fluid Mech.* **575**, 187–219.

KNECHTEL, E. D. 1959 Experimental investigation at transonic speeds of pessure distributions over wedge and circular-arc airfoil sections and evaluations of perforated-wall interference. NASA technical report TN D-15.

KRUPP, J. A. & COLE, J. D. 1976 Studies in transonic flow IV, unsteady transonic flow. In *UCLA Engineering Department Report No. 76/04*.

KUBOTA, T., KO, D. R. S. & DOBBS, L. D. 1978 Weakly-nonlinear long internal waves in a stratified fluid of finite depth. *J. Hydronaut.* **12**, 157–65.

LAMB, V. R. & BRITTER, R. E. 1984 Shallow flow over an isolated obstacle. *J. Fluid Mech.* **147**, 291–313.

LEE, C. Y. & BEARDSLEY, R. C. 1974 The generation of long nonlinear internal waves in a weakly stratified shear flow. *J. Geophys. Res.* **79**, 453–62.

LEVEQUE, R. J. 2002 *Finite Volume methods for Hyperbolic Problems.* Cambridge: Cambridge University Press.

LI, X. F., DONG, C. M., CLEMENTE-COLON, P., PICHEL, W. G. & FRIEDMAN, K. S. 2004 Synthetic aperture radar observation of the sea surface imprints of up- stream atmospheric solitons generated by flow impeded by an island. *J. Geophys. Res.* **209**, C02016.

MEI, C. C. 1989 *The applied dynamics of ocean surface waves.* Singapore: World Scientific.

MURMAN, E. M. & COLE, J. D. 1971 Calculations of plane steady transonic flows. *AIAA J.* **9**, 114–121.

ONO, H. 1975 Algebraic solitary waves in stratified fluids. *J. Phys. Soc. Japan* **39**, 1083–1091.

OSTROVSKY, L. A. 1978 Nonlinear internal waves in a rotating ocean. *Oceanology* **18**, 181–191.

PIERREHUMBERT, R. T. 1984 Linear results on the barrier effects of mesoscale mountains. *J. Atmos. Sci.* **41**, 1356.

PLOUGONVEN, R. & ZEITLIN, V. 2003 On periodic inertia-gravity waves of finite amplitude propagating without change of form at sharp-density gradient interfaces in the rotating fluid. *Phys. Lett. A* **314**, 140.

PRESS, W. H., FLANNERY, B. P., TEULOSKY, S. A. & VETTERLING, W. T. 2001 *Numerical recipes in C++: the art of scientific computing.* Cambridge: Cambridge University Press.

QUENEY, P. 1948 The problem of airflow over mountains. A summary of theoretical studies. *Bull. Am. Meteorol. Soc.* **29**, 16.

RAMIREZ, C. & RENOUARD, D. 1998 Generation of internal waves over a shelf. *Dyn. Atmos. Oceans* **28**, 107–125.

ROE, P. L. 1981 Approximate Riemann solvers, parameter vectors, and difference schemes. *J. Comput. Phys.* **43**, 357–372.

ROTTMAN, J. W. & EINAUDI, F. 1993 Solitary waves in the atmosphere. *J. Atmos. Sci.* **50**, 2116–2136.

SAMBUCO, E. & WHITEHEAD, J. A. 1976 Hydraulic control by a wide weir in a rotating fluid. *J. Fluid Mech.* **73**, 521.

SCHÄR, C. & SMITH, R. B. 1993a Shallow water flow past an isolated topography. Part I: Vorticity production and wake formation. *J. Atmos. Sci.* **50**, 1373–1400.

SCHÄR, C. & SMITH, R. B. 1993b Shallow water flow past an isolated topography. Part II: Transition to vortex shedding. *J. Atmos. Sci.* **50**, 1401–1412.

SHRIRA, V. I. 1986 On long strongly nonlinear waves in a rotating ocean. *IAPO* **22**, 298–305.

SPREITER, J. R. & ALKSNE, A. Y. 1958 Thin aerofoil theory based on approximate solution of the trasonic flow equation. NASA technical report TN 1359.

SPREITER, J. R., ALKSNE, A. Y. & HYETT, B. J. 1958 Theoretical pressure disturbances for several related nonlifting airfoils at high subsonic speeds. NASA technical report TN 4148.

STANTON, T. P. & OSTROVSKY, L. A. 1998 Observations of highly nonlinear solitons over the continental shelf. *Geophys. Res. Lett.* **25**, 2695–98.

STEVENSON, R. E. 1969 *The 200-mile fishline. In Oceans from space (ed. P.C. Badgley, L. Miloy & L.F. Childs).* Houston: Gulf Publishing Company.

STOKER, J. J. 1948 The formation of breakers and bores. *Comm. Pure and App. Math.* **1**, 1–87.

VILENSKI, G. G. & JOHNSON, E. R. 2004 Near critical free-surface rotating flow over topography. *Proc. R. Soc. Lond. A* **460**, 2865–2881.

WHITCOMB, R. T. 1956 A study of the zero-lift drag-rise characteristics of wing-body combinations near the speed of sound. *Tech. Rep.* 1273. NASA.

WHITHAM, G. B. 1974 *Linear and Nonlinear Waves*. New York: Wiley.